Politecnico di Milano
Department of Aerospace Science and Technology
Doctoral Programme In Aerospace Engineering

Multi-Phase Mission Analysis and Design for Satellite Constellations with Low-Thrust Propulsion

Doctoral Dissertation of:
Simeng Huang

Supervisor:
Prof. Camilla Colombo

Academic year 2020/21 – Cycle XXXII

Doctoral Dissertation of:		Simeng Huang
Supervisor:	Prof.	Camilla Colombo
External Reviewer:	Prof.	Alessandro A. Quarta
External Reviewer:	Prof.	Matteo Ceriotti
Coordinator of the Doctoral Program:	Prof.	Pierangelo Masarati
Tutor:	Prof.	Michèle Lavagna

Huang, S. (2021), *Multi-Phase Mission Analysis and Design for Satellite Constellations with Low-Thrust Propulsion*, Ph.D. Thesis, Politecnico di Milano, Supervisor: Colombo, C.

Sommario

Poiché la domanda di servizi dallo Spazio è sempre più importante per la vita sulla Terra, l'interesse internazionale per le costellazioni satellitari è sempre più in crescita. Ad esempio, negli ultimi anni, molte grandi costellazioni, che sono composte da centinaia a migliaia di satelliti, sono state o verranno schierate in orbita terrestre bassa (LEO), per fornire servizi di telecomunicazioni ad alta velocità alla Terra con copertura globale. L'ondata di costellazioni porta varie sfide agli studi sulle costellazioni, come il costo elevato, la minaccia alla sicurezza per lo spazio e il considerevole sforzo di calcolo per progettare missioni di costellazioni contenenti molti satelliti. Per rispondere a queste sfide, questa dissertazione esegue l'analisi della missione e la progettazione delle quattro fasi chiave del ciclo di vita della costellazione.

Una prima fase è la fase pre-missione della costellazione - progettazione della costellazione. Non esistono regole generali per la progettazione delle costellazioni; invece, i progettisti di costellazioni devono considerare i vari fattori di costo. Viene eseguito un progetto di costellazione multicriterio, in cui vengono valutate quantitativamente sette proprietà della costellazione, ciascuna delle quali rappresenta una prestazione o un costo critico della costellazione. Il presente progetto fornisce un approccio sistematico per trovare costellazioni ottimali a livello globale per determinate missioni.

Una seconda fase è il dispiegamento a bassa spinta della costellazione attraverso le perturbazioni J_2 della Terra, dove si concentra lo spiegamento di più piani orbitali con un solo lancio. Basato sul metodo di distribuzione tradizionale che sfrutta solo l'effetto J_2, viene aggiunta una fase di spinta fuori dal piano per accelerare la separazione in Ascensione retta del nodo ascendente (RAAN). Viene eseguita una progettazione di distribuzione analitica, in cui le soluzioni analitiche vengono prima derivate per il trasferimento circolare a bassa spinta soggetto a leggi di controllo predefinite, quindi vengono sviluppati metodi analitici per determinare i tempi assegnati alle fasi di distribuzione separate, consentendo il tempo totale e il consumo di carburante per separazione RAAN da ridurre al minimo allo stesso tempo. Il presente progetto fornisce un approccio computazionalmente efficiente per ridurre i costi scambiando i ricavi di una distribuzione più rapida e il costo di

un maggiore consumo di carburante.

Una terza fase è il deorbitamento di una costellazione LEO a bassa spinta attraverso perturbazioni naturali, dove vengono studiate due diverse strategie di deorbitazione: una usa la spinta per abbassare l'altitudine del perigeo, l'altra usa la spinta per raggiungere una condizione specifica che può portare al decadimento orbitale sotto l'effetto accoppiato dell'oblazione della Terra e della pressione di radiazione solare. Per ogni strategia, viene sviluppata una legge di controllo a circuito chiuso, che si è dimostrata stabile, basata sul metodo del controllo di feedback di Lyapunov. Successivamente, il movimento medio a bassa spinta governato dalle leggi di controllo proposte viene derivato con una tecnica di media orbitale. Propagando il movimento medio a bassa spinta per la deorbitazione dall'intera regione LEO, le mappe che mostrano il budget Δv, il tempo di deorbitazione e le condizioni di applicazione delle due strategie sono ottenute. Leggendo le mappe, i progettisti della missione possono scegliere la loro strategia preferibile in base alle condizioni e ai requisiti della missione.

Oltre alle tre fasi indipendenti di cui sopra, viene studiato anche il trasferimento planare a bassa spinta (cioè innalzamento dell'orbita e deorbitazione planare) per i satelliti complanari, prendendo la collisione autoindotta, cioè la collisione causata dai satelliti dalla stessa costellazione, in considerazione. Come primo passo dello studio, viene sviluppata una legge di controllo Blended Error-Correction a circuito chiuso mescolando leggi di controllo che possono modificare in modo efficiente gli elementi orbitali planari e compensando l'errore dell'orbita osculante rispetto all'orbita target. Quindi il problema di evitare la collisione autoindotta viene convertito nel problema di massimizzare la distanza relativa minima tra i satelliti, che a sua volta viene affrontata programmando correttamente i tempi per avviare il trasferimento per ogni satellite.

Abstract

As the demand for services from Space is more and more important to life on the Earth, the international interest in satellite constellations is increasingly growing. For example, in the recent years, many large constellations, which are composed of hundreds to thousands of satellites, are being or to be deployed in Low Earth Orbit (LEO), to provide high-speed telecommunications services to the global Earth. The surge in constellations brings various challenges to constellation studies, such as the expensive cost, the safety threat to space, and the considerable computational effort to design constellation missions containing many satellites. In order to respond to these challenges, this dissertation performs mission analysis and design for four key phases of constellation life cycle.

A first phase is the constellation pre-mission phase – constellation design. No general rules exist for constellation design; instead, constellation designers have to consider various cost drivers in a trade-off way. A multi-criteria constellation design is performed, in which seven constellation properties are quantitatively assessed, each property representing a critical constellation performance or cost. The present design provides a systematic approach to find globally optimal constellations for given missions.

A second phase is constellation low-thrust deployment through the Earth J_2 perturbations, where the deployment of multiple orbital planes by one launch is focused. Based on the traditional deployment method which exploits the J_2 effect only, an out-of-plane thrusting phase is added to accelerate the separation in Right Ascension of the Ascending Node (RAAN). An analytical deployment design is performed, in which analytical solutions are first derived for circular low-thrust transfer subject to predefined control laws, and then analytical methods are developed to determine the times allocated to separate deployment phases, allowing the total time and fuel consumption for RAAN separation to be minimised at the same time. The present design provides a computationally efficient approach to reduce cost by trading off the revenue of a quicker deployment and the cost of higher fuel consumption.

A third phase is LEO constellation low-thrust de-orbiting through natural perturbations, where two different de-orbiting strategies are investigated: one is using thrust to lower the perigee altitude, the other is using thrust to reach a specific condition that can lead to orbital decay under the coupled effect of the Earth oblateness and Solar Radiation Pressure. For each strategy, a closed-loop control law, which is proved to be stable, is developed based on the method of Lyapunov feedback control. Subsequently, the averaged low-thrust motion governed by the proposed control laws are derived with an orbital averaging technique. By propagating the averaged low-thrust motion for de-orbiting from the entire LEO region, maps that show the Δv-budget, de-orbiting time, and application conditions of the two strategies are obtained. By reading the maps, mission designers can choose their preferable strategy according to mission conditions and requirements.

In addition to the above three independent phases, the planar low-thrust transfer (i.e. orbit raising and planar de-orbiting) for co-planar satellites is also studied, by taking the self-induced collision, that is, the collision caused by satellites from the same constellation, into consideration. As the first step of the study, a closed-loop Blended Error-Correction control law is developed by blending control laws which can efficiently change the planar orbital elements, and by offsetting the error of the osculating orbit relative to the target orbit. Then the problem of avoiding the self-induced collision is converted to the problem of maximising the minimum relative distance between satellites, which in turn is addressed by properly scheduling the timing to start transfer for every satellite.

To my mother

"All that I am, or hope to be, I owe to my angel mother."

— *Abraham Lincoln*

献给我的母亲

"无论现在或将来，我所拥有的一切都归功于我的母亲。"

— 亚伯拉罕 • 林肯

Acknowledgements

First of all, I would like to express my sincere gratitude to my supervisor Prof. Camilla Colombo. Thanks for all your efforts to make this doctoral dissertation possible, from the selection of the topic to the finalisation of the thesis. Your patience and encouragement helped me overcome the difficulties in the first year, and guided me, step by step, to become a true researcher. Not only did you teach me how to do academic research, you have also been my firm partner who would defend for my work and unselfishly pave the way for my future career.

I would like to acknowledge my thesis reviewers, Prof. Alessandro A. Quarta and Prof. Matteo Ceriotti. Thanks to you, I got the certainty that at least two people read this work in its entirety.

Many thanks go to Prof. Franco Bernelli-Zazzera and his wife Vittoria. Thank you for taking care of me in both study and daily life. I would like to express my gratitude to all the academic, administrative, and technical staffs of the Department of Aerospace Science and Technology at Politecnico di Milano, for creating a friendly and comfortable environment.

I am grateful to all my colleagues from “Camilla’s army”. Thank you Davide, Matteo, and Stefan, who were there from the beginning. I will never forget the happy days we took classes and did homework together. Thanks to our post-doctors Ioannis, Elisa (visiting researcher), Juan, Narcís, Mirko, and Gabriella, and to our Ph.D. students Marco, Giacomo, Francesca, and Alessandro. I learned a lot from each of you. I would also like to thank Tong and Lincheng, who stayed with us for short time. It has been a enjoyable time to work in such an excellent and harmonised team.

I want to thank my best friends Yiqing and Kai. I cannot imagine how I could have faced these four years without your accompanying. I would also like to thank Yang for his kind help with the course reports.

Together with my supervisor Prof. Camilla Colombo, we would like to acknowledge Mr. Thomas J. Lang for his kind help sharing his work “Optimal Low Earth Orbit Constellations for Continuous Global Coverage”, which was used in Chap. 3 to determine the central angle of coverage for Walker constellation. And we would like to thank Dr. Chengyu Ma from Imperial College London for his support in low-thrust technologies, as well as Dr. Tomer Shtark for his kind help in reviewing the work in Chap. 5. I would also like to acknowledge Dr. Elisa Maria Alessi for her precious advice in passive de-orbiting technologies and for performing numerical simulations in Chap. 5.

Last but not least, I want to give my biggest thanks to my family. 谢谢妈妈，谢谢您无私的爱，谢谢您尊重并支持我所做的每一个决定。Thank you Zhili, living in two continents with seven hours time difference for four years has been difficult, but we know we are family and best friends. I cannot express how I appreciate your unconditional support, either emotional or financial, with words, just like the lyrics: "*I am strong when I am on your shoulders. You raise me up, to more than I can be.*"

The doctoral research presented in this thesis has received funding from the European Research Council (ERC) under the European Union's Horizon 2020 research and innovation programme as part of project COMPASS (Grant agreement No 679086), and from the Chinese Government Scholarship awarded by the Chinese Scholarship Council.

Contents

List of Figures

List of Tables

Nomenclature

Acronyms

AoL	Argument of Latitude
BEC	Blended Error-Correction
ECI	Earth Centred Inertial
EoL	End-of-Life
GPS	Global Positioning System
IADC	Inter-Agency Space Debris Coordination Committee
LEO	Low Earth Orbit
MEO	Medium Earth Orbit
ODE	Ordinary Differential Equation
PU	Pattern Unit for Walker constellation
RAAN	Right Ascension of the Ascending Node
SoC	Street-of-Coverage
SRP	Solar Radiation Pressure
ToF	Time of Flight

Constants

Earth gravitational parameter $\mu \approx 3.9860 \times 10^5$ km^3/s^2

Earth mean equatorial radius $R_\oplus \approx 6378.16$ km

Earth second zonal harmonics $J_2 \approx 0.0011$

Standard gravity $g_0 \approx 9.8066$ m/s^2

Greek Symbols

θ	angular radius of the footprint, rad or deg
α	pitch angle, rad or deg
β	yaw angle, rad or deg
Δm_p	fuel consumption, kg
Δv	change in velocity, km/s
Δv_{eol}	change in velocity of a constellation for EoL disposal, km/s
Δv_{keep}	change in velocity of a constellation for station-keeping, km/s
$\Delta\circ$	change in $\circ$
$\delta\circ$	difference in $\circ$ between two orbits or between two satellites
$\Delta\circ_{\mathrm{rev}}$	change in $\circ$ after one revolution
ϵ	elevation angle, rad or deg
η_{eng}	thruster engine efficiency, %
κ	satellite-pair angular miss distance, rad or deg
ν	true anomaly, rad or deg
Ω	RAAN, rad or deg
ω	argument of perigee, rad or deg
ϕ_{fpa}	flight path angle, rad or deg
ϕ_{site}	latitude of the launch site, rad or deg
ψ	terminal condition
ϑ	central angle of coverage, rad or deg
K	constellation angular miss distance, rad or deg

Latin Symbols

I_{sp}	thruster specific impulse, s
P_{eng}	thruster engine input power, W
$\hat{\boldsymbol{f}}$	unit vector of the low-thrust acceleration
$\boldsymbol{f}$	low-thrust acceleration vector, km/s^2
$\boldsymbol{J}$	objective vector
a	semi-major axis, km
A/m	area-to-mass ratio, m^2/kg

C_j^{θ}	half-width of SoC with j-fold continuous coverage, rad or deg
C_j^{ϑ}	minimum half-width of SoC with j-fold continuous coverage, rad or deg
cov	excess coverage
D_{miss}	constellation miss distance, km
d_{miss}	satellite-pair miss distance, km
E	eccentric anomaly, rad or deg
e	eccentricity
F	phasing parameter for Walker constellation
F	thrust magnitude, N
f	magnitude of the low-thrust acceleration vector, km/s^2
f_{θ}	transversal component of the low-thrust acceleration vector, km/s^2
f_h	out-of-plane component of the low-thrust acceleration vector, km/s^2
f_r	radial component of the low-thrust acceleration vector, km/s^2
h	altitude, km
h_{am}	angular momentum, km^2/s
h_p	perigee altitude, km
i	inclination, rad or deg
J	objective function
j	coverage fold
lch_h	index of the launch property, km
lch_i	index of the launch property, rad or deg
m	spacecraft mass, kg
M	mean anomaly, rad or deg
$m/C_D A$	ballistic coefficient, kg/m^2
N	number of satellites
n	mean motion, rad/s
n_S	apparent mean motion of the Sun measured on the ecliptic plane, rad/s
opp	unit collision opportunity, s^{-1}
P	number of orbital planes

p	semilatus rectum, km
pct	average percentage of the Earth's surface visible to $(j+1)$ satellites over one orbit period, %
r	orbit radius, km
r_p	perigee radius, km
S	number of satellites per orbital plane
T	orbit period, s
t	time, s
u	AoL, rad or deg
V	candidate Lyapunov function

Other Symbols

$\circ$	generic variable
$\circ_0$	initial value of $\circ$
$\circ_{\text{des}}$	desired value of $\circ$
$\circ_{\text{req}}$	requirement on $\circ$
$\circ_f$	final value of $\circ$
$\circ_{J_2}$	J_2 effect on $\circ$
$\circ_T$	thrust effect on $\circ$
$\dot{\circ}$	time rate of change of $\circ$
$\dot{\circ}_{J_2}$	time rate of change of $\circ$ due to the secular effect of J_2 perturbations
$\dot{\bar{\circ}}$	average time rate of change of $\circ$
$\text{sgn}_\circ$	sign of $\circ$

Subscripts

co	co-rotating interface
counter	counter-rotating interface
inter	inter-plane
intra	intra-plane
lb	lower bound
LEO	LEO constellation
man	manoeuvring satellite

MEO	MEO constellation
ref	reference satellite
tan	tangential thrusting
tra	transversal thrusting
ub	upper bound

Superscripts

str1	perigee decrease strategy
str2	de-orbiting corridor strategy

CHAPTER 1

Introduction

In the recent years, the surge in constellations brings the fore various challenges to constellation studies. This thesis will respond to the challenges by performing mission analysis and design for several key phases of constellation life cycle.

This chapter is organised as follows. Sec. 1.1 introduces the term "satellite constellation" and gives the study scope of the thesis. Sec. 1.2 presents the motivations and objectives of the research. Sec. 1.3 reviews the previous work that was undertaken to achieve the objectives. Sec. 1.5 provides a summary of the methodologies developed and implemented. Sec. 1.5 explains the structure of the dissertation. Finally, the contributions of this work in the form of publications are listed in Sec. 1.6.

1.1 Satellite Constellations and Problem Definition

The satellite constellation, as defined by Wood [1], is "*composed by a certain number of similar satellites, of a similar type and function, designed to be in similar complementary orbits for a shared purpose, under shared control.*" It is well known that the characteristics of different constellations vary dramatically, and constellations can fall into various categories depending on the type of coverage (continuous/intermittent), the type of coverage region (global/zonal), the type of orbit (circular/elliptical/hybrid), the altitude of implementation (low/medium/-geosynchronous Earth orbit), etc. In this thesis we are focused on global coverage constellations, which are often used for telecommunications, positioning and navigation, and other similar functions [2, pp. 671], and particularly, we are interested in circular-orbit and continuous coverage constellations in which all satellites are placed at common altitude and inclination.

An Earth-orbiting constellation can be used for surveillance and reconnaissance, telecommunications, positioning and navigation, military defence, etc. For continuous global coverage constellations, depending on the service to be offered, the required coverage fold can be from one to four, where the coverage fold refers to the minimum number of satellites continuously visible to every point on the Earth's surface. In general, most of the missions in Low Earth Orbit (LEO) require 1-fold continuous global coverage to offer surveillance and reconnaissance, and telecommunications services, whereas the missions in Medium Earth Orbit (MEO) usually require 4-fold continuous global coverage to offer positioning and navigation services. A coverage fold higher than required can enhance the constellation's robustness to satellite failures, however on the other hand, it also implies a higher redundancy of satellite utility, which in turn increase the system cost; this concept will be demonstrated in Sec. 3.3.2.

A constellation in its life cycle will experience the following phases: launch, deployment, station-keeping, replacement (or replenishment), and End-of-Life (EoL) disposal [3]. Prior to these phases, the constellation's size and structure, which strongly affect the system cost and performance, must be carefully designed [2, pp. 673].

Over the past decades, the major trends in the development of constellations are the increase in the number of satellites and consequently, the more and more complicated constellation configuration. For example, many large constellations, which are composed of hundreds to thousands of satellites are being or to be deployed in LEO, to provide high-speed telecommunications services to the global Earth, even the most rural areas. Moreover, the low-thrust technologies have become more and more popular with constellations due to the high specific impulse.

The aforementioned trends bring various challenges to constellation studies, including but not limited to:

- the reduction of cost, which is one of the most crucial problems for constellation builders;
- the safety threat to the space environment, especially to the already congested LEO region;
- the great computational effort involved in the mission analysis and design for constellations containing a large number of satellites.

As a result, constellation studies have become considerable current work and will continue to grow in importance, both as constellations become more achievable and as the challenges become more critical.

In order to respond to the challenges, the major goal of this dissertation is to study methodologies and techniques for mission analysis and design of the following four key phases of constellation life cycle:

- constellation design (the pre-mission phase)
- constellation deployment
- constellation de-orbiting
- constellation planar transfer considering self-induced collision avoidance

where the self-induced collision is the collision caused by satellites from the same constellation. Note that, different than the first three topics, the last topic is not an independent phase but focused on tackling the self-induced collision problem when multiple co-planar satellites in the constellation perform planar manoeuvres together during the deployment and de-orbiting phases. Moreover, it has to be noted that, although the other phases, such as launch and station-keeping, are not specifically studied as independent topics, they are encompassed in the first topic – constellation design.

For the last three phases, the low-thrust propulsion is used. As a preliminary study, we assume that the thrust can be continuously applied. However, it has to be noted that in real missions, a low-thrust propulsion system cannot thrust in eclipse, and most cannot thrust continuously due to heating and power.

1.2 Research Motivations and Objectives

This research is motivated by the need to respond to the challenges to constellation studies.

Because constellations are inherently very expensive, the prime objective of the research is to reduce cost and meanwhile, to increase revenue. No general rules exist for constellation design [2, Chap. 13]. Instead, it is a complicated trade-off process during which various cost drivers that dominate constellation performances and costs have to be taken into account. Therefore, this research aims to study methodologies for the design of constellations, which allows maximising constellation performances and minimising costs. Moreover, the design is desired to be done in a systematic way such that it can be generalised to any missions with different requirements. In parallel, to start revenue flow as early as possible, this research is focused on the study of rapid deployment techniques.

As the surge in constellations is posing a severe safety threat to Space, the second objective of the research is to reduce the negative impact of constellations on the space environment since the early stage of constellation mission design. Within the scope of the four phases concerned, this objective indicates the need to reduce collision hazards in the constellation operational phase and to fast remove constellations after their end of life. For these reasons, the inter-satellite collision probability should be considered during the constellation design process; also, a proper de-orbiting strategy, which can lead to quick re-entry, should be selected, and the low-thrust de-orbiting is desired to be time-optimal. In addition, due to the fact that the co-planar satellites usually perform planar manoeuvres, such as orbit raising and de-orbiting, at the same time, while a low-thrust transfer may consist of hundreds to thousands of revolutions, it is also necessary to minimise the collision risk between co-planar satellites during planar transfer.

For constellations, the low-thrust trajectory design is not a stand-alone problem, but it is integrated with the optimisation of one or more mission performance indexes. For example, the performance of a deployment mission is evaluated not only by the Δv-budget of low-thrust transfer but also by the total deployment time. Therefore, the last objective of the research is to study techniques that can be rapidly implemented for the integrated design of constellation mission using low-thrust propulsion. In this context, it is desired to develop an analytical closed-loop control law, which is computationally efficient and can be directly applied to every satellite in the constellation for potential real-time autonomous guidance.

Moreover, to further reduce the computational load of propagating low-thrust motion, this research aims to study techniques for analytical and semi-analytical solutions of low-thrust transfer.

To sum up, each of the four phases is involved in separate objectives, viz.,

- objective 1: to reduce cost and to increase revenue;
- objective 2: to reduce the negative impact on space environment, especially the LEO region;
- objective 3: to study techniques that can be rapidly implemented for the integrated design of constellation missions using low-thrust propulsion.

For clarity, Table 1.1 summarises the research objectives for the four phases, where the symbol × means the objective is contained. It has to be noted that the blank table cell does not mean the objective is not considered at all. For example, in the design of de-orbiting phase, in addition to the de-orbiting time, the candidate de-orbiting strategies are also assessed from the aspect of Δv-budget so as to find an economic solution, which to some extent, is related to the reduction of cost, i.e. the first objective.

Table 1.1: *Summary of the research objectives for the four phases*

Phase	Objective 1	Objective 2	Objective 3
Constellation design	×	×	
Constellation deployment	×		×
Constellation de-orbiting		×	×
Constellation planar transfer considering self-induced collision avoidance		×	×

1.3 Literature Review

In this section, Sec. 1.3.1 reviews the previous work undertaken to address the four constellation mission phases, and Sec. 1.3.5 reviews the technologies of low-thrust trajectory design.

1.3.1 Constellation Design

Over the past decades, different types of circular-orbit constellations have been proposed, such as Walker, Street-of-Coverage, and Flower.

The Walker constellation was first published by Walker [4–7] in 1970s. It is also reported in Ref. [8] that Mozhaev [9, 10] had independently proposed the similar constellation in 1968. The Walker constellation is characterised by a globally symmetrical structure, in which all satellites and orbital planes are uniformly distributed. Then researchers such as Ballard, Lang, and Adams [11–14] conducted fruitful work, finding the optimal Walker constellations providing continuous global coverage with a minimum number of satellites.

The Street-of-Coverage (SoC) constellation was developed based on a SoC concept, where the term SoC refers to a swath on the ground with continuous coverage. At the early stage of SoC constellation design, the orbits were evenly spaced along the equatorial plane, and some work [15–17] was devoted to finding the optimal number of orbits and inclinations required to cover the zone of interest [14].

In 1978, Beste [18] proposed the polar SoC constellation in which polar orbits were unevenly spaced; compared to an early work by Lüders [15], Beste reduced the number of satellites by 15% for 1-fold continuous global coverage [18]. Then Rider [19] carried out a further study to find the optimal polar SoC constellations providing continuous global coverage with a minimum number of satellites. However, the polar SoC constellation does not suit practical applications because all orbits cross at the poles, thus may leading to high collision hazards. In order to address this problem, Ulybyshev [8] proposed the near-polar SoC constellation by transforming the original polar constellations to a new class of inclined ones.

The Flower constellation was proposed by Mortari et al. [20] in 2004. It is a theoretical framework that allows the design of symmetrical constellations whose satellites all move on the same trajectory with respect to a rotating reference frame. Based on the original Flower constellation, the 2D and 3D Lattice Flower constellations were developed [21, 22], encompassing the Walker constellation and some other symmetrical constellations with elliptical orbits.

Traditionally, the prime design criterion for continuous global coverage constellations is the coverage performance. A good coverage performance can guarantee the quality of communications between ground and constellation, and it usually indicates fewer satellites required, thus reducing the system cost. However, the mono-criterion design may not suit practical applications, because the design of constellations is a complicated trade-off process during which various cost drivers have to be taken into account.

Draim and Kacena [23] discussed the impacts on constellation design from various aspects: launch vehicle, orbit maintenance, debris, etc. Lang and Adams [14] compared the Walker, polar SoC, and Draim constellations in terms of coverage, launch vehicle capability, spare strategy, crosslinking, and space debris mitigation and collision avoidance. Lansard and Palmade [24] proposed a multi-criteria approach, highlighting and handling three driving criteria: coverage performance, operational availability, and life-cycle costs of the system. Lansard et al. [25] incorporated the robustness consideration and some additional coverage constraints, and designed a new type of constellation which was resistant to satellite failures by using an optimisation tool based on genetic algorithms. Keller et al. [26] examined the polar and near-polar constellations for the use of intersatellite links. Ferringer and Spencer [27] studied two pairs of trade-offs – sparse-coverage trade-off and resolution trade-off – using multi-objective evolutionary computation. Li et al. [28] proposed a general evaluation criterion for the coverage of LEO constellations, which was applicable to different constellation configurations. Shtark and Gurfil [29] developed a LEO constellation optimisation method for regional positioning, and examined the figures of merit of total coverage time, revisit time, and geometric dilution of precision percentiles. Buzzi et al. [30] described the process of constellation and orbit design for the TROPICS mission, in which the following figures of merit were assessed: coverage, cost, constellation robustness, lifetime, and deployment.

It has to be noted that the aforementioned work is not limited to the study scope of this paper, viz. circular-orbit continuous global coverage constellations, but they are reviewed for the purpose of identifying the critical criteria for constellation design along with the approaches of modelling the criteria.

1.3.2 Constellation Deployment

The traditional deployment method, which requires a dedicated launch for one orbital plane, may not suit constellations consisting of many orbital planes.

King and Beidleman [31] patented a method of exploiting the Earth J_2 perturbations to deploy a set of satellites into one or more desired orbital planes. In this method, satellites are sequentially raised from the initial orbit to their respective final orbits at predetermined time intervals to achieve the desired separation in the Right Ascension of the Ascending Node (RAAN). In 2006, the FORMOSAT-3/COSMIC mission [32] demonstrated the J_2 method by deploying six satellites into six orbital planes with one launch vehicle. An obvious advantage of the J_2 method is the low fuel consumption.

Some studies of constellation low-thrust deployment using the J_2 method were performed. Jenkins et al. [33] investigated a 180 deg separation in the RAAN between two CubeSats, where the RAAN separation was obtained by increasing the semi-major axis of one satellite, drifting in a higher orbit, and returning to the original semi-major axis; in the meanwhile, the other satellite stayed in its original orbit. A simulation of hybrid transfer was performed, in which the RAAN was actively changed in the drift orbit by thrust. It was concluded that the active RAAN change was far less efficient than J_2, due to the limited capability of the low-thrust technology considered for this study, in which each thruster produced a thrust of 150 μA and a specific impulse of 760 s. McGrath and Macdonald [34] also investigated the RAAN separation between a manoeuvring satellite and a non-manoeuvring satellite through the similar three-phase manoeuvre as the one by Jenkins et al. [33], but the drift orbit in this study was lower than the original one so as to achieve a more efficient deployment. Moreover, this study considered another strategy by simultaneously manoeuvring two satellites, achieving a minimum-time deployment by optimising the propellant distribution between the two manoeuvring satellites. Cerf [35] solved a minimum-fuel transfer between circular orbits based on the Edelbaum averaged dynamics equations. In this work, the transfer was composed of three phases: a thrusting phase to lower the orbit, a coasting phase to passively change the RAAN by J_2, and another thrusting phase to reach the final semi-major axis and inclination. The results obtained by this work have potentiality for constellation deployment.

Chow et al. [36] proposed an alternative method for LEO constellation deployment by taking advantage of the complex dynamical behaviour near the Earth-Moon L_1 Lagrange point. In this method, several carrier vehicles, each carrying a set of satellites to be deployed into a single orbital plane, are sent to L_1 and inserted to a Lissajous or Halo orbit by a single large launch vehicle. At L_1, the carrier vehicles wait as long as necessary to access separate Earth return trajectories leading to different orbital planes. When approaching the Earth, the carrier vehicles perform an aerocapture manoeuvre with the aid of ballutes to slow and enter into the final orbit. Chase et al. [37] performed a preliminary analysis in terms of the launch cost, demonstrating that compared to the traditional method (one launch per orbital plane), the L_1 method could realise a significant cost saving by 42% – 74%. Following the previous studies, Nadoushan et al. [38] designed more accurate trajectories based on the three-body model using the stable and unstable manifolds of the Halo orbit around L_1 and the multiple shooting method. This work confirmed the results by Chow et al. [36] in terms of the required Δv and demonstrated that the L_1 method would take only 20 days to deploy a constellation of six orbital planes spaced along the equatorial plane at intervals of 60 deg, while the J_2 method would take 1.5 years. However, the use of multiple carrier vehicles and ballutes would require additional system development and lead to an increase in mass by a factor of 2.1 for each satellite weighting 100 kg [39], thus limiting the application of the L_1 method to constellations containing many satellites.

Nowadays, the high uncertainty of the actual demand (e.g. the expected number and activity level of users) may need constellations to be deployed in a staged manner, such that the constellation configuration can dynamically adapt to the evolution of the market [40]. For this reason, a technique that can rapidly provide optimal solutions for deployment without great computational effort would be desired. Appel et al. [41] proposed a combined algorithm based on the neighbouring-extremal algorithm and the first-order gradient algorithm to solve a minimum-fuel low-thrust transfer problem, where all satellites were required to reach the desired positions at the same time. de Weck et al. [42] developed an auction algorithm to assign multiple satellites into designated slots with a minimum total Δv. However, both work used numerical methods such might not be computationally efficient enough for constellations containing many satellites. In pursuit of rapid computation, analytical solutions for the low-thrust transfers involved in the deployment would be preferred. Kechichian [43] derived analytical solutions for near-circular low-thrust transfer. McGrath and Macdonald [34, 44] used a general perturbation method, which took into account the conversion between mean and osculating orbital elements, to obtain analytical solutions for circular low-thrust transfer with high accuracy. However, both work assumed a constant thrust acceleration, thus limiting the accuracy of the analytical solutions, and they were focused on the tangential thrusting (the thrust direction tangent to the trajectory) only. As a matter of fact, Burt [45] had considered the variation in thrust acceleration for the tangential thrusting and for the yaw thrusting (the thrust direction normal to the orbital plane) in 1967, but the analytical solutions derived here were for the semi-major axis and inclination only.

1.3.3 Low Earth Orbit Constellation De-Orbiting

A pioneering work on low-thrust de-orbiting from LEO was done by Pollard [46], where two strategies were investigated. One is to lower the perigee altitude to the drag dominated region and then the drag will lower the apogee altitude until re-entry happens. The other is to move spacecraft to graveyard altitudes between 2,000 and 2,500 km that are rarely used because of the intense radiation, however not guaranteeing the complete removal of spacecraft from orbit. By comparing the Δv-budgets of the two strategies (assuming that the perigee altitude was lowered to 250 km), Pollard recommended to use the perigee decrease strategy for initial altitudes lower than 1,250 km and the graveyard strategy for initial altitudes higher than $1,250$ km.

With the development of materials and manufacturing technology, more and more passive de-orbiting devices (e.g. drag and solar sail, drag balloon, and electrodynamic tether) have been considered for passive de-orbiting. Over the past years, considerable feasibility studies on passive de-orbiting devices have been performed, demonstrating that such devices can enhance the passive de-orbiting from high-altitude LEO, by exploiting the orbital resonances due to the coupled effect of the Earth oblateness and Solar Radiation Pressure (SRP) [47–52]. However, a feasible technology for passive de-orbiting device can be achieved only if the conditions of orbital resonances, which can be described by a certain combination of orbital elements, are satisfied. Natural de-orbiting can take place along resonance lines, but this will take a longer time than a direct manoeuvre, since manifold dynamics is exploited [47, 49]. In order to better exploit the orbital resonances, a strategy to move spacecraft to the conditions of orbital resonances with impulsive thrust were investigated in Refs. [53, 54].

1.3.4 Low Earth Orbit Constellation Self-Induced Collision Avoidance

With more and more constellations injected to the already congested LEO region, a lot of attention have been drawn to the constellation relevant collision problem. To the author's knowledge, most of the work was focused on modelling, computing, and analysing the impact of constellations on the space environment [55–57].

Concerning the problem of self-induced collision, i.e., the collision between satellites from the same constellation, Lang [14] took it as a criterion for constellation design. In this work, the self-induced collision risk was quantitatively evaluated by an angular miss distance, which is the minimum angular separation between satellites. For circular-orbit constellations in which all satellites are placed at a common altitude, the angular separation is linked to the linear distance but independent of the orbit radius, thus simplifying the problem. For the self-induced collision during low-thrust transfer, Lee et al. [58] addressed the collision problem by conducting sub-optimal control for the cooperative collision-free transfer of multiple satellites using continuous thrust.

1.3.5 Low-Thrust Trajectory Design

Indirect and Direct Methods

In general, methods for low-thrust trajectory optimisation are classified into indirect and direct approaches [59, 60].

Indirect methods solve a Two-Point Boundary Value Problem by means of the shooting method. However, for long-duration transfer, the optimal solutions are usually difficult to obtain because of the small convergence domain. In order to address this problem, the homotopic approach was studied by Refs. [61–63], to search for initial costates for fixed-time minimum-fuel transfers, and the results indicated that the homotopic approach would still take few hours to obtain the optimal solutions.

Direct methods, on the other side, convert the optimal control problem into a parameter optimisation problem, which is then solved by nonlinear programming. Compared to indirect methods, direct methods have a larger convergence domain and thus are feasible to handle long-duration transfer. Scheel and Conway [64] solved a planar transfer with $1,027$ variables through a Runge-Kutta parallel-shooting transcription approach. Betts [65] proposed a direct sequential quadratic programming method to solve a 578 revolutions' transfer with $416,123$ variables. As seen from the previous work, direct methods are usually computationally expensive due to the large number of optimisation variables.

Heuristic Methods

Heuristic methods, which can be orders of magnitude faster than indirect and direct methods [66], have also received some attention. Heuristic methods generally fall into two categories [66].

One category is involved in blending the control laws which can instantaneously optimise the time rates of change of orbital elements. Spencer and Culp [67] developed three optimal control laws for the semi-major axis, inclination, and perigee radius, separately, and sequentially employed these control laws in a LEO to Geosynchronous Earth Orbit (GEO) transfer. Kluever and Oleson [68] blended the optimal control laws for the semi-major axis, eccentricity, and inclination, and optimised the weights allocated to these control laws with direct methods. Then taking the results in Ref. [68] as reference trajectories and based on those optimal control laws, Kluever [69,70] proposed two guidance schemes suitable for on-board implementation. Gao [71] employed three control laws over different orbital arcs, two optimal for the semi-major axis and inclination and one near-optimal for the eccentricity, and then optimised the starting and ending points of orbital arcs with direct methods.

The other category is based on the Lyapunov stationary theory, where a candidate Lyapunov function must be properly defined to ensure convergence. Petropoulos [66,72] proposed a Q-Law algorithm based on a Lyapunov candidate function Q, which was a proximity quotient to quantify the proximity of the osculating orbit to the target orbit. Then the divergence problem exhibited in Ref. [72] was addressed in Ref. [66] by introducing penalty functions. Hernandez and Akella [73] used the Lyapunov method to solve planar transfer and rendezvous problems, where the proposed candidate Lyapunov functions were able to give rise to asymptotically stabilising control laws. However, one problem for the Lyapunov method is that there does not exist a well-defined method to select controller gains [74], and some researchers have to resort to stochastic methods, such as genetic algorithm [75,76], which in turn increase the computational load.

In a constellation low-thrust transfer problem, the low-thrust trajectory is required for every satellite. So it would be preferable to develop an analytical closed-loop control law that can be directly applied to every satellite for potential real-time autonomous guidance. Ruggiero et al. [77] proposed closed-loop guidance laws by simultaneously offsetting the instantaneous errors in orbital elements. Zhang et al. [78] managed to derive the analytical near-time-optimal and near-fuel-optimal control laws for GEO transfers by optimising two objective functions, which were properly constructed based on the instantaneous variations of orbit elements and the cumulative effects of thrust, separately.

The techniques for solar sail trajectory design can also be applied to low-thrust because both of them are characterised by small thrust. Ceriotti and McInnes [79] generated the optimal trajectories for Earth hybrid pole sitters by firstly obtaining the local-optimal control law with a semi-analytical inverse method and then using them as a first guess in the subsequent indirect method. Mengali and Quarta [80] solved an orbit raising problem from LEO with solar sail, in which an analytical control law that maximised the time rate of change of the semi-major axis at any instant of the trajectory was found; such control law depended on the ratio between local aerodynamic pressure and SRP on the sail.

Orbital Averaging Technique for Low-Thrust Trajectory Design

Because of the low thrust-to-mass ratio, a low-thrust transfer usually consists of many revolutions and may take several months or even up to few years. The computational load of precisely integrating a long-duration transfer is quite high, let alone in constellation mission design we are dealing with many satellites. To reduce the computational load, an orbital averaging technique is often used, with which the short-term oscillations can be filtered out. Kechichian [43] investigated the low-thrust orbit raising problem due to tangential thrusting, where the analytical expressions of the incremental changes in orbital elements were obtained with the aid of Taylor series expansion; however, the results were only valid for eccentricity up to 0.2. Gao and Kluever [81] worked on the same subject but in a different way by introducing an approximation to the elliptic integrals, and the results were also valid for large eccentricity.

1.4 Methodologies Developed and Implemented

For each of the four constellation mission phases, the methodologies developed and implemented are devoted to the major objectives as described in Sec. 1.2.

1.4.1 Constellation Design

A first phase addressed in this thesis is the design of circular-orbit continuous global coverage constellations, with the major objective to develop a systematic constellation design method to maximise constellation performances and to minimise costs. The development of this method is generally divided into three steps.

First, we choose two classical types of circular-orbit constellations: Walker and SoC, and perform a thorough review of their characteristics; this choice is justified by the fact that many practical applications (e.g. the Galileo [82] and Iridium [83, 84] constellations) are of these types. Based on the review, a set of characteristic parameters, which can determine the configuration of a Walker or SoC constellation, are identified. A contribution of this work to the literature is deriving the necessary condition for continuous global coverage for the SoC constellation.

Then by widely reviewing the previous work on constellation design, we select seven constellation properties as design criteria, each of them representing a particular constellation performance or cost, reported in Table 1.2. Because these performances and costs are constellation's inherent qualities, they are collectively called here as constellation properties. For each property, one or two indexes are proposed with valid reasons, and the indexes are modelled as functions of the characteristic parameters that having been identified. In this way, we can quantitatively establish the relationship between constellation configuration and properties through mathematical formulae, and furthermore, analyse the trade-offs between properties; recall that the constellation configuration is represented by the characteristic parameters.

Table 1.2: *Constellation properties.*

Property	Description
Coverage	Performance to offer required coverage
Robustness	Performance to offer required coverage if satellite fails
Self-induced collision avoidance	Performance to avoid self-induced collision
Launch	Cost to deliver constellation to mission orbit
Build-up	Period to build up constellation
Station-keeping	Cost to maintain constellation structure
EoL disposal	Cost to remove constellation from mission orbit

Finally, taking the constellation properties as objectives and taking the characteristic parameters as design variables, a multi-objective optimisation problem is formulated, in which the mission-related parameters can be replaced according to given mission requirements. As a multi-objective optimisation problem is set, the solution is found in terms of a set of non-dominated solutions belonging to the Pareto-front, and further, the globally optimal constellations can be found. The multi-objective optimisation implemented for this work uses the formulation proposed by Vasile [85].

1.4.2 Constellation Deployment

A second phase addressed in this thesis is the constellation deployment, with the objectives of rapid deployment to start revenue flow as early as possible and of reducing the computational effort for the integrated design of a deployment mission with low-thrust control. In this thesis, the deployment of multiple orbital planes by one launch is focused.

In light of the strengths and drawbacks of the J_2 and L_1 methods, it is decided to investigate the use of the J_2 method due to the saving in cost. In order to accelerate the deployment, on the basis of the traditional J_2 method which exploits the J_2 effect only for RAAN separation, this research adds an out-of-plane thrusting phase to actively change the RAAN by thrust.

Two simple but efficient control laws are used for the deployment: an in-plane tangential thrusting to change the semi-major axis and an out-of-plane yaw thrusting to change the RAAN. Under a reasonable assumption that all satellites remain in circular orbits throughout the deployment, the analytical solutions for circular low-thrust transfer due to the tangential and yaw thrusting are derived. A difficulty for deriving the analytical solutions is that the motion of orbital elements is coupled by short-term oscillations. In order to decouple the motion, we employ the orbital averaging technique to filter out the short-term oscillations and keep the long-term and secular motion.

Because the out-of-plane thrusting is inherently expensive, two parameters are introduced to control the fuel consumption: one to adjust the contributions of J_2 and thrust effects to the RAAN separation, and the other to adjust the length of burning arcs per revolution in the out-of-plane thrusting phase. With the analytical solutions having been derived, the time and fuel consumption for RAAN separation can be analytically expressed in terms of the parameters. Then a multi-objective optimisation problem is formulated, in which the design variables are the two parameters and the objectives to be minimised are the time and fuel consumption for RAAN separation. Through a mapping from the design variable space to the objective space, the optimal design variables are found to be the solution of singular transformation, and they can be analytically described by setting the determinant of the transformation matrix to zero. With these optimal design variables, we can further determine the optimal times to be allocated to separate phases of the RAAN separation in an analytical way.

In general, the proposed method provides an analytical-optimal solution for low-thrust deployment exploiting the J_2 effect, enabling a rapid deployment with low fuel consumption.

1.4.3 Low Earth Orbit Constellation De-Orbiting

A third phase addressed in this thesis is the de-orbiting of LEO constellations, with the objectives of rapid de-orbiting to minimise the negative impact on the LEO environment and of reducing the computational effort for the integrated design of de-orbiting mission using low-thrust propulsion.

To this end, two strategies, which are applicable to de-orbiting from LEO, are investigated. The first strategy is the traditional perigee decrease strategy that have been widely used in practical applications. It consists of a low-thrust phase to lower the perigee altitude to the drag-dominated region and a passive de-orbing phase in which the drag effect will lower the apogee altitude until re-entry happens. The second strategy exploits the natural coupled effect of the Earth oblateness and SRP, named here as the de-orbiting corridor strategy. It contains a low-thrust phase to move the spacecraft to the condition of orbital resonances due to the coupled effect and a passive de-orbiting phase in which the coupled effect will provoke orbital decay, provided a passive de-orbiting device with large enough area-to-mass ratio.

In light of the strengths and drawbacks of different low-thrust trajectory design methods, it is decided to use the Lyapunov method to develop closed-loop control laws. For each strategy, a candidate Lyapunov function, which is zero at the final state and positive elsewhere, is built based on the terminal condition of the low-thrust phase as described. Given the objective of rapid de-orbiting, the control law is designed to send the candidate Lyapunov function to zero at the fastest rate by minimising the time derivative of the candidate Lyapunov function. Subsequently, the stability analysis is performed to prove that the proposed control law is robust to any initial conditions such that it can be directly applied to every satellite in the constellation without need for off-line design.

In order to assess the strategy performance, maps are drawn to show the Δv-budget and de-orbiting time for de-orbiting from any near-circular LEO using the two strategies, based on which, maps that indicate the application conditions of the two strategies are obtained. Besides, to reduce the computational load of propagating a series of initial conditions for the entire LEO region, the averaged low-thrust dynamics models, i.e. the semi-analytical solutions of low-thrust transfer, governed by the proposed control laws are firstly derived with the orbital averaging technique.

1.4.4 Low Earth Orbit Co-Planar Satellites Planar Transfer Considering Self-Induced Collision Avoidance

A last problem tackled in this thesis is the self-induced collision avoidance during the planar orbit raising and de-orbiting transfers for co-planar satellites in LEO constellations. The objectives are to reduce collision risk for the purpose of minimising negative impact on LEO environment and to reduce computational effort for the integrated design of multi-satellite planar transfer mission using low-thrust propulsion.

Inspired by the previous work of Refs. [68,71,77], it is decided to investigate the use of heuristic methods to develop a closed-loop control law. A Blended Error-Correction (BEC) control law is proposed, in which two types of control laws are blended: a tangential thrusting to change the semi-major axis in the optimal way [86] and an inertial thrusting to change the eccentricity in the near-optimal way [87]. A weighting parameter, which offsets the error of the osculating orbit to the target orbit, is assigned to each control law. Then to ensure the thrust direction following the desired one, a normalisation procedure is performed.

This work quantitatively models the self-induced collision risk as the miss distance between satellites. In this way, the problem of self-induced collision avoidance is converted to the maximisation of miss distance, which in turn can be solved by properly scheduling the timing to start transfer for every satellite. Because in every trial to find the transfer starting time we need to propagate low-thrust motion for all satellites. To reduce the computational load, the averaged low-thrust dynamics model, i.e. the semi-analytical solutions of low-thrust transfer, is firstly derived.

For the orbit raising mission, it is found that the close proximity is caused by a phenomenon of latitude resonance. Based on this discover, we identify the safe transfer starting time difference between two successive transfer, such that the miss distance can be ensured larger than a given threshold. For the de-orbiting mission in which the orbit is more elliptical, we resort to multi-objective optimisation techniques and get the optimal transfer starting times that can maximise the miss distance while minimise the total mission time.

1.5 Dissertation Organisation

This dissertation is, after the introduction chapter, divided into six chapters. Chap. 3 to Chap. 6 are dedicated to the design of the four phases concerned, while Chap. 2 and Chap. 7 are dedicated to the introduction of the fundamentals and conclusion, respectively.

Chap. 2 explains the fundamentals of orbital dynamics and low-thrust trajectory design that will be used in Chap. 3 to Chap. 6. Sec. 2.1, Sec. 2.2, and Sec. 2.3 show the coordinate systems, orbital elements, and dynamics model, respectively. Sec. 2.4 introduces some simple and efficient control laws. Finally, an introduction to the orbital averaging technique is presented in Sec. 2.5.

Chap. 3 performs a multi-criteria design for continuous global coverage constellations through quantitative assessments of seven important constellation properties. Sec. 3.1 presents a thorough review of continuous global coverage Walker and SoC constellations. Sec. 3.2 quantitatively assesses the constellation properties and analyses the trade-offs between properties. A multi-objective optimisation problem to find globally optimal constellations for given missions is formulated in Sec. 3.3. Finally, the optimisation results are presented and discussed in Sec. 3.4.

Chap. 4 proposes an analytical approach for constellation low-thrust deployment through J_2 perturbations. Sec. 4.1 introduces the deployment scheme. Sec. 4.2 derives the analytical solutions for circular low-thrust transfer. Then in Sec. 4.3 and Sec. 4.4, analytical methods are developed to determine the times allocated to different phases for the separation in RAAN and Argument of Latitude, respectively. Finally in Sec. 4.5, two case studies of large constellation deployment are presented to show how the proposed approach is used.

Chap. 5 investigates the low-thrust de-orbiting through natural perturbations for LEO constellations, where two strategies are considered: the perigee decrease strategy and the de-orbiting corridor strategy. Sec. 5.1 introduces the two strategies and gives the terminal conditions of low-thrust transfer. Sec. 5.2 develops the closed-loop control laws and performs the stability analyses, following which, the averaged low-thrust dynamics models are derived in Sec. 5.3. Finally in Sec. 5.4, numerical simulations are performed to validate the control laws and averaged dynamics models, and to obtain the de-orbiting maps.

Chap. 6 analyses the low-thrust planar transfer problems, i.e. orbit raising and planar de-orbiting, while taking the self-induced collision avoidance into consideration. Sec. 6.1 develops the closed-loop control law, following which, the averaged low-thrust dynamics models are derived in Sec. 6.2. The self-induced collision avoidance problem is addressed in Sec. 6.3, where the transfer starting times are scheduled for the orbit raising and de-orbiting missions, separately.

Finally, Chap. 7 concludes this dissertation with a summary of the findings, the limitations of the method and potential future work.

1.6 Contributions

The contents of this dissertation have been published in one journal paper and in four stand-alone but highly related conference papers, and have been submitted to journals.

The results of Chap. 3 were presented in 2017 at the 68th International Astronautical Congress in Adelaide, Australia [88], and were submitted to Acta Astronautica in August 2020 (the revision was submitted in January 2021).

The results of Chap. 4 were submitted to Journal of Guidance, Control, and Dynamics in January 2021.

The results of Chap. 5 were presented at two conferences and were submitted to Acta Astronautica in January 2021. The preliminary results of near-polar orbits de-orbiting were presented in January 2019 at the 29th AAS/AIAA Space Flight Mechanics Meeting in Ka'anapali, Hawaii, United States of America [89]. The complete results were presented in July 2019 at the 10th International Workshop on Satellite Constellations and Formation Flying in Glasgow, United Kingdom [90]. In particular, the results of Sec. 5.4.2 are the outcome of a joined work with Dr. Elisa Maria Alessi, who performed the numerical simulations for passive de-orbiting.

The results of Chap. 6 were presented in 2018 at the 4th IAA Conference on Dynamics and Control of Space Systems in Changsha, China [91], and were published in November 2020 in Aerospace Science and Technology [92].

Journal Publications

- Huang S., Colombo C., and Bernelli-Zazzera F., "Low-Thrust Planar Transfer for Co-Planar Low Earth Orbit Satellites Considering Self-Induced Collision Avoidance", *Aerospace Science and Technology*, Vol. 106, November 2020, doi: 10.1016/j.ast.2020.106198.
- Huang S., Colombo C., and Bernelli-Zazzera F., "Multi-Criteria Design of Continuous Global Coverage Walker and Street-of-Coverage Constellations Through Property Assessment". Submitted to *Acta Astronautica* in August 2020 (revision submitted in January 2021).
- Huang S. and Colombo C., "An Analytical Approach for Circular-Orbit Constellation Low-Thrust Deployment Exploiting Earth Oblateness". Submitted to *Journal of Guidance, Control, and Dynamics* in January 2021.
- Huang S., Colombo C., Alessi E. M., and Wang Y., "Low Earth Orbit Constellation Low-Thrust De-Orbiting Through Natural Perturbations". Submitted to *Acta Astronautica* in January 2021.

Conference Publications

- Huang S., Colombo C., and Bernelli-Zazzera F., "Comparative Assessment of Different Constellation Geometries for Space-Based Application", *68th International Astronautical Congress*, 25-29 September 2017, Adelaide, Australia, IAC-17, C1, IP, 31, x41252.
- Huang S., Colombo C., and Bernelli-Zazzera F., "Orbit Raising and De-Orbit for Coplanar Satellite Constellations with Low-Thrust Propulsion", *4th IAA Conference on Dynamics and Control of Space Systems*, 21-23 May 2018, Changsha, China, IAA-AAS-DyCoSS4-1-15, AAS 18-508.
- Huang S., Colombo C., Alessi E. M., and Hou Z., "Large Constellation De-Orbiting with Low-Thrust Propulsion", *29th AAS/AIAA Space Flight Mechanics Meeting*, 13-17 January 2019, Ka'anapali, Hawaii, United States of America, AAS 19-480.
- Huang S., Colombo C., and Alessi E. M., "Trade-Off Study on Large Constellation De-Orbiting Using Low-Thrust and De-Orbiting Balloons", *10th International Workshop on Satellite Constellations and Formation Flying*, 16-19 July 2019, Glasgow, United Kingdom, IWSCFF 19-1953.

CHAPTER 2

Fundamentals of Orbital Dynamics and Low-Thrust Trajectory Design

This chapter explains the fundamentals of orbital dynamics and low-thrust trajectory design that will be used in the subsequent chapters for the four constellation mission phases.

2.1 Coordinate Systems

2.1.1 Earth Centred Inertial Coordinate System

The Earth Centred Inertial (ECI) coordinate system is an Earth-based system, originating at the centre of the Earth [93, Sec. 3.3]. It will be used in Sec. 3.1 to show the configuration of a constellation in space. Fig. 2.1 shows this coordinate system, where the three axes are defined as follows [93, Sec. 3.3]:

- the $\hat{I}$ axis points towards the vernal equinox;
- the $\hat{J}$ axis is 90 deg easterly (measured from the $\hat{I}$ axis) in the equatorial plane;
- the $\hat{K}$ axis extends through the North Pole, completing the right-handed coordinate system.

2.1.2 Gauss Coordinate System

The Gauss coordinate system is a satellite-based system that moves with the satellite [93, Sec. 3.3]. It is used in this thesis to study spacecraft motion due to the low-thrust effect. Fig. 2.2 shows this coordinate system, where the three axes are defined as follows [93, Sec. 3.3].

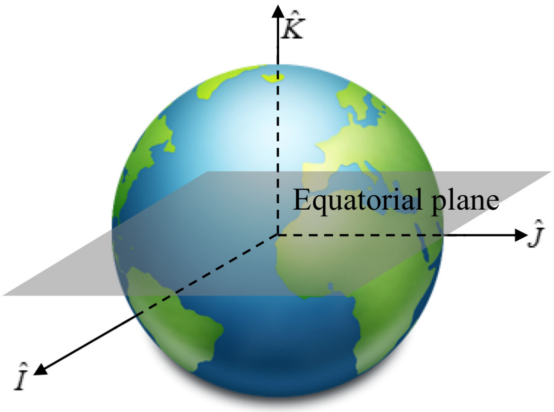

Figure 2.1: *Earth Centred Inertial coordinate system.*

- the $\hat{r}$ axis points out from the satellite along the Earth's radius vector to the satellite;
- the $\hat{\theta}$ axis lies in the orbital plane, perpendicular to the $\hat{r}$ axis and in the direction of, but not necessarily parallel to, the velocity vector;
- the $\hat{h}$ axis is normal to the orbital plane, completing the right-handed coordinate system.

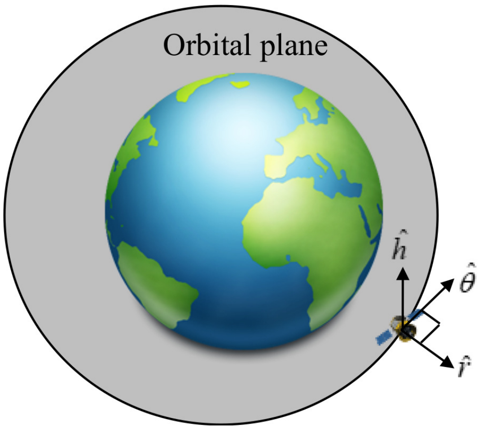

Figure 2.2: *Gauss coordinate system.*

2.2 Classical Orbital Element

In principle, the state of a satellite can be defined by six classical orbital elements [93, Sec. 2.4.1]:

- the semi-major axis a
- the eccentricity e
- the inclination i
- the Right Ascension of the Ascending Node (RAAN) Ω
- the argument of perigee ω
- the true anomaly ν

As a matter of fact, the semi-major axis and eccentricity determine the size and shape of the orbit [93, Sec. 2.4.1]; the inclination, RAAN, and argument of perigee determine the orientation of the orbit in space; the true anomaly determines the satellite's in-plane position relative to the orbital perigee [93, Sec. 2.4.1], and it can be replaced by the eccentric anomaly E or the mean anomaly M. ν, E, and M are related by by [93, pp. 51-56]

$$\sin\nu = \frac{\sin E\sqrt{1-e^2}}{1-e\cos E}, \quad \cos\nu = \frac{\cos E - e}{1-e\cos E} \tag{2.1}$$

$$M = E - e\sin E \tag{2.2}$$

For orbits of zero inclination, the RAAN is not defined. However, as the scope of this thesis is continuous global coverage constellations whose inclinations are usually is not zero, the use of classical orbital elements is reasonable. For orbits with zero eccentricity, the argument of perigee is also not defined. In this case, we make use of the Argument of Latitude (AoL) u, an in-plane angle measured from the ascending node to the satellite's position in the direction of satellite's motion [93, Sec. 2.4.1].

2.3 Dynamics Model

The Gauss form of the variational equations is a convenient technique to address low-thrust problems because it allows the time rates of change of orbital elements to be explicitly expressed in terms of perturbing accelerations [93, Sec. 9.3.2]. If we only consider the low-thrust perturbing acceleration, the equations of motion can be stated in Gauss form as [94, Sec. 10.3]:

$$\dot{a} = \frac{2a^2}{h_{\text{am}}}\left(e\sin\nu f_r + \frac{p}{r}f_\theta\right) \tag{2.3a}$$

$$\dot{e} = \frac{1}{h_{\text{am}}}\left\{p\sin\nu f_r + \left[(p+r)\cos\nu + re\right]f_\theta\right\} \tag{2.3b}$$

$$\dot{i} = \frac{r\cos(\omega+\nu)}{h_{\text{am}}}f_h \tag{2.3c}$$

$$\dot{\Omega} = \frac{r\sin(\omega+\nu)}{h_{\text{am}}\sin i}f_h \tag{2.3d}$$

$$\dot{\omega} = \frac{1}{h_{\text{am}}e}\left[-p\cos\nu f_r + (p+r)\sin\nu f_\theta\right] - \frac{r\sin(\omega+\nu)}{h_{\text{am}}\tan i}f_h \tag{2.3e}$$

$$\dot{\nu} = \frac{h_{\text{am}}}{r^2} + \frac{1}{h_{\text{am}}e}\left[p\cos\nu f_r - (p+r)\sin\nu f_\theta\right] \tag{2.3f}$$

or

$$\dot{E} = \frac{na}{r} + \frac{1}{nae}\left[(\cos\nu - e)f_r - \left(1+\frac{r}{a}\right)\sin\nu f_\theta\right] \tag{2.3g}$$

$$\dot{M} = n + \frac{1}{na^2e}\left[(p\cos\nu - 2re)f_r - (p+r)\sin\nu f_\theta\right] \tag{2.3h}$$

where $\dot{\circ}$ represents the time derivative of the generic variable $\circ$, f_r f_θ, and f_h are the radial, transversal, and out-of-plane components, respectively, of the low-thrust acceleration vector. In the preceding equations, n is the osculating mean motion, p is the semilatus rectum, h_{am} is the angular momentum, and r is the orbit radius; they are given by

$$n = \sqrt{\mu/a^3}, \quad p = a(1-e^2), \quad h_{\mathrm{am}} = \sqrt{\mu p}, \quad r = \frac{p}{1+e\cos\nu} \tag{2.4}$$

where $\mu \approx 3.9860 \times 10^5$ km^3/s^2 is the Earth gravitational parameter.

In this thesis, for the convenience of employing the orbital averaging technique, we would prefer to express the equations of motion in terms of the eccentric anomaly E:

$$\dot{a} = \sqrt{\frac{a^3}{\mu}} \frac{2}{1-e\cos E}\left(e\sin E f_r + \sqrt{1-e^2} f_\theta\right) \tag{2.5a}$$

$$\dot{e} = \sqrt{\frac{a\left(1-e^2\right)}{\mu}} \frac{1}{1-e\cos E}\left[\sqrt{1-e^2}\sin E f_r + \left(2\cos E - e - e\cos^2 E\right) f_\theta\right] \tag{2.5b}$$

$$\dot{i} = \sqrt{\frac{a}{\mu}}\left(\frac{\cos E - e}{\sqrt{1-e^2}}\cos\omega - \sin E\sin\omega\right) f_h \tag{2.5c}$$

$$\dot{\Omega} = \sqrt{\frac{a}{\mu}}\left(\frac{\cos E - e}{\sqrt{1-e^2}}\sin\omega + \sin E\cos\omega\right)\frac{f_h}{\sin i} \tag{2.5d}$$

$$\dot{\omega} = \sqrt{\frac{a}{\mu}}\frac{1}{e\left(1-e\cos E\right)}\left[\sqrt{1-e^2}\left(e-\cos E\right) f_r + \left(2-e^2-e\cos E\right)\sin E f_\theta\right] - \cos i\dot{\Omega} \tag{2.5e}$$

$$\dot{E} \approx \sqrt{\frac{\mu}{a^3}}\frac{1}{1-e\cos E} \tag{2.5f}$$

where $\dot{E}$ is approximated as a two-body problem, because the low-thrust acceleration is very small compared to the gravitational acceleration [95].

In addition to the low-thrust effect, the secular effects due to the second zonal harmonics, $J_2 \approx 1.0826 \times 10^{-3}$, are also considered, given by [93, Sec. 9.6.1]:

$$\dot{a}_{J_2} = \dot{e}_{J_2} = \dot{i}_{J_2} = 0 \tag{2.6a}$$

$$\dot{\Omega}_{J_2} = -\frac{3nR_\oplus^2 J_2}{2p^2}\cos i \tag{2.6b}$$

$$\dot{\omega}_{J_2} = \frac{3nR_\oplus^2 J_2}{4p^2}(4-5\sin^2 i) \tag{2.6c}$$

$$\dot{M}_{J_2} = -\frac{3nR_\oplus^2 J_2\sqrt{1-e^2}}{4p^2}(3-2\sin^2 i) \tag{2.6d}$$

where $R_\oplus \approx 6378.16$ km is the Earth mean equatorial radius.

2.4 Control Law

A control law can describe the time history of the magnitude and direction of the low-thrust acceleration vector.

In this thesis, we consider a constant ejection velocity propulsion model [96, Sec. 1.1], where the low-thrust engine input power P_{eng}, the low-thrust engine efficiency η_{eng}, and the specific impulse I_{sp} are assumed constant. Under this assumption, the thrust F and the mass flow rate $\dot{m}$ are also constant, given by [96]

$$F = \frac{2\eta_{\text{eng}} P_{\text{eng}}}{g_0 I_{\text{sp}}}, \quad \dot{m} = -\frac{2\eta_{\text{eng}} P_{\text{eng}}}{g_0^2 I_{\text{sp}}^2} \tag{2.7}$$

where $g_0 = 9.8066$ m/s^2 is the standard gravity. Accordingly, the magnitude of the thrust acceleration is

$$f = \frac{F}{m} = \frac{2\eta_{\text{eng}} P_{\text{eng}}}{m g_0 I_{\text{sp}}} \tag{2.8}$$

where m is the spacecraft mass.

Generally speaking, the thrust direction can be determined by two steering angles: an in-plane steering angle α and an out-of-plane steering angle β, which are called pitch angle and yaw angle, respectively. Here we define the pitch and yaw angles in the Gauss coordinate system, as shown in Fig. 2.3. The thrust components are therefore

$$\begin{aligned} f_r &= f \cos\beta \sin\alpha \\ f_\theta &= f \cos\beta \cos\alpha \\ f_h &= f \sin\beta \end{aligned} \tag{2.9}$$

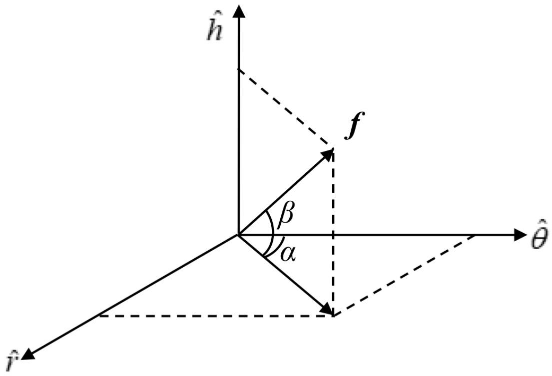

Figure 2.3: *Definition of the pitch and yaw angles in the Gauss coordinate system for low-thrust control.*

An objective of this research is to develop closed-loop control laws to directly apply to every satellite in the constellation. Thus, it is necessary to review some commonly used closed-loop control laws which can efficiently change orbital elements.

2.4.1 Tangential Thrusting

The tangential thrusting is the optimal in-plane control law to the change semi-major axis [86]; the thrust direction is tangent to the trajectory, i.e. parallel to the velocity vector. This control law is obtained by solving $\partial \dot{a} / \partial \alpha = 0$ and can be expressed in terms of E as [81]

$$\begin{aligned} f_r &= \pm f \frac{e \sin E}{\sqrt{1 - e^2 \cos^2 E}} \\ f_\theta &= \pm f \frac{\sqrt{1 - e^2}}{\sqrt{1 - e^2 \cos^2 E}} \\ f_h &= \ \ 0 \end{aligned} \tag{2.10}$$

where the sign + and − represent the cases of semi-major increase and decrease, respectively.

2.4.2 Transversal Thrusting

The transversal thrusting is another commonly used in-plane control law to change the semi-major axis; the thrust direction is perpendicular to the orbit radius vector; that is to say, only the transversal thrust component f_θ exists. This control law is given in the form of

$$\begin{aligned} f_r &= \ \ 0 \\ f_\theta &= \pm f \\ f_h &= \ \ 0 \end{aligned} \tag{2.11}$$

where the sign + and − represent the cases of semi-major increase and decrease, respectively.

The transversal thrusting is efficient when the eccentricity is small, because in this case the thrust direction is close to the one of the tangential thrusting.

2.4.3 Inertial Thrusting

The inertial thrusting, according to Ref. [87], is a near-optimal in-plane control law to change the eccentricity [71]; the thrust direction is perpendicular to the line of apsides. This control law can be expressed in terms of the true anomaly ν as [71]

$$\begin{aligned} f_r &= \pm \sin \nu \\ f_\theta &= \pm \cos \nu \\ f_h &= \ \ 0 \end{aligned} \tag{2.12}$$

and from the relation between the true and eccentric anomalies in Eq. (2.1), it can also expressed in terms of E as

$$\begin{aligned} f_r &= \pm f \frac{\sin E \sqrt{1 - e^2}}{1 - e \cos E} \\ f_\theta &= \pm f \frac{\cos E - e}{1 - e \cos E} \\ f_h &= \ \ 0 \end{aligned} \tag{2.13}$$

where the sign + and − represent the cases of eccentricity increase and decrease, respectively.

2.4.4 Yaw Thrusting

The yaw thrusting sets the yaw angle to 90 deg such that only the out-of-plane thrust component f_h exists. This control law is given in the form of

$$\begin{aligned} f_r &= \quad 0 \\ f_\theta &= \quad 0 \\ f_h &= \pm f \end{aligned} \tag{2.14}$$

where the sign $+$ and $-$ indicate that the thrust direction is along and opposite, respectively, to the $\hat{h}$ axis.

The yaw thrusting is the optimal way to change the inclination and RAAN, because $\dot{i}$ and $\dot{\Omega}$ are governed by f_h only. It has to be noted that the thrust direction must invert at $\omega + \nu = \pm\pi/2$ for i and at $\omega + \nu = 0$ for Ω, otherwise there will be a nearly null change in each of them [45].

2.5 Orbital Averaging

An orbital averaging technique is often used in low-thrust trajectory design to reduce the high computational load for the integration of the exact dynamics model. By using this technique, we can derive the averaged dynamics model in which the short-term oscillations are filtered out while the long-term and secular motion are kept.

Let x denote any of the orbital elements to be averaged. Due to the fact that the thrust acceleration is small, typically on the order of $10^{-4} g_0$ or less [43], all orbital elements except A can be assumed constant within a single revolution, where A is a proxy of ν, E, M, and u. Under this assumption, the incremental change in x over one revolution can be obtained by integrating $\mathrm{d}x/\mathrm{d}A$ in A:

$$\Delta x = \int_{A_{\mathrm{on}}}^{A_{\mathrm{off}}} \frac{\mathrm{d}x}{\mathrm{d}A} \mathrm{d}A \tag{2.15}$$

where A_{on} and A_{off} are the starting and ending points of the burning arc in a single revolution.

This incremental change occurs during a time period of $2\pi/\dot{A}$. The averaged time rate of change of x is therefore

$$\dot{\tilde{x}} = \frac{\dot{A}}{2\pi} \Delta x \tag{2.16}$$

where $\dot{\tilde{\circ}}$ represents the average time derivative of the generic variable $\circ$. Because the major perturbing effects, such as low-thrust and J_2, are every small compared to the Earth gravitational effect, $\dot{A}$ can be approximated as

$$\dot{A} \approx n \tag{2.17}$$

recalling that $n = (\mu/a^3)^{1/2}$ is the osculating mean motion.

Note that the implementation of the orbital averaging technique requires the control law explicitly expressed in terms of orbital elements, i.e. the closed-loop control law, otherwise it will be impossible to carry out the analytical integration for Δx. In some previous work (e.g. Refs. [97, 98]), the averaged dynamics model is also referred to as the semi-analytical solutions because the expression of Δx is analytical, and then it is inserted into a numerical Ordinary Differential Equation (ODE) solver to be numerically integrated.

2.6 Summary

This chapter explained the fundamentals of the ECI and Gauss coordinate systems, of the classical orbital elements, and of the Gauss equations of motion. Several control laws were introduced. Particularly,

- the tangential thrusting will be used in Chap. 4 and Chap. 6;
- the transversal thrusting will be used in Chap. 5;
- the inertial thrusting will be used in Chap. 6;
- the yaw thrusting will be used in Chap. 4.

An introduction to the orbital averaging technique was presented. It will be employed in Chap. 4 to derive the analytical solutions and in Chap. 5 and Chap. 6 to derive the semi-analytical solutions, i.e. averaged dynamics model, of low-thrust transfer.

CHAPTER 3

Multi-Criteria Constellation Design Through Property Assessment

This chapter presents a systematic method for the design of continuous global coverage Walker and SoC constellations, by taking seven critical constellation properties (coverage, robustness, self-induced collision avoidance, launch, build-up, station-keeping, and end-of-life disposal) as design criteria. In this method, a set of characteristic parameters, which can determine the constellation configuration, are first identified based on the review of Walker and SoC constellations. Then a series of indexes are proposed and modelled as functions of the characteristic parameters, to quantitatively assess the constellation properties. Through the quantitative assessment, the influence of constellation configuration on constellation properties are revealed, and the trade-offs between constellation properties are analysed. Finally, taking the characteristic parameters and constellation properties as the design variables and objectives, a multi-objective optimisation problem is formulated to find the globally optimal constellations for given missions.

Note that this study analyses the prograde-orbit constellations containing no more than 200 satellites. However, for large constellations with more than 200 satellites, the properties considered here may not be priorities for constellation design, e.g. coverage and robustness. Besides, due to space limitations, in this chapter we only present the results for 1- and 4-fold coverage LEO and MEO constellations. However, the systematic constellation design method developed can also be applied to 2- or 3-fold coverage and to geosynchronous constellations.

3.1 Review of Walker and Street-of-Coverage Constellations for Continuous Global Coverage

The Walker and SoC constellations are two typical types of constellations that have been widely studied. The common characteristics of these two types of constellations are:

- the constellation, containing a total of N satellites, is composed of S satellites evenly spaced on each of P orbital planes;
- all satellites are placed in circular orbits at the same altitude h and at the same inclination i.

On the other hand, the essential difference between these two types of constellations is the distribution of orbital planes, which will be shown in the following sections.

3.1.1 Walker Constellations

The Walker constellation is globally symmetrical in terms of the geometrical configuration. When describing a Walker constellation, a Pattern Unit (PU) is used to measure angular distances within the constellation, with 1 PU $= 2\pi/N$ rad [5].

The characteristics of a Walker constellation are defined as follows [5].

- All the P orbital planes are evenly spaced along the equatorial plane at intervals of S PUs (i.e. of $2\pi/P$ rad).
- In each orbital plane, the S satellites are evenly spaced at intervals of P PUs (i.e. of $2\pi/S$ rad).
- When a satellite is at its ascending node, some satellite in the adjacent orbital plane towards east has an AoL of F PUs (i.e. of $2\pi F/N$ rad), where F is an integer which may have any value from 0 to $(P-1)$[1].

To summarise, the distribution of orbital planes and satellites for a Walker constellation can be described by

$$\delta\Omega = S, \quad \delta u_{\text{intra}} = P, \quad \delta u_{\text{inter}} = F \tag{3.1}$$

where the symbol $\delta\circ$ represents the difference in the generic variable $\circ$ between two orbits or between two satellites, $\delta\Omega$ is the RAAN spacing between adjacent orbital planes, δu_{intra} is the intra-plane AoL spacing between adjacent satellites in a single orbital plane, and δu_{inter} is the inter-plane AoL spacing between successive satellites in adjacent orbital planes, with the term “successive” referring to satellites *successively* passing their respective ascending nodes. Fig. 3.1 gives the illustration of $\delta\Omega$, δu_{intra}, and δu_{inter}, assuming $S = 8$, $P = 3$, and $F = 1$. In the plots, the x- and y-axis indicate the RAAN and AoL, respectively, of satellite. Fig. 3.1 (a) shows the satellite distribution in PUs and Fig. 3.1 (b) shows in degrees; in the present example 1 PU $= 360/(8 \times 3) = 15$ deg.

A Walker constellation can be designated in shorthand notation as i: $N/P/F$ [5], and there is $S = N/P$. Two typical Walker constellations are the 55 deg: 24/6/2 Global Positioning System (GPS) constellation [99] and the 56 deg: 24/3/1 Galileo constellation [82].

---

[1] F can also be equal to or larger than P, but then the configuration of the constellation will be the same as $F = F - P$.

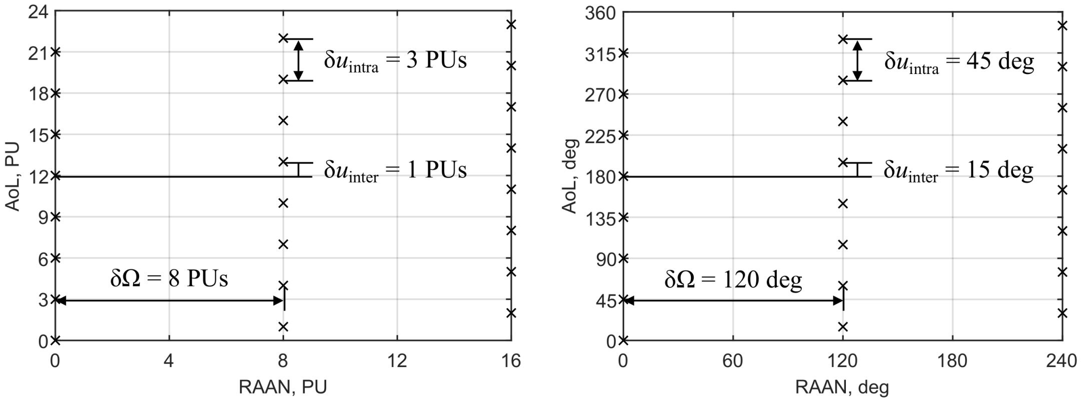

(a) RAAN versus AoL in PUs. (b) RAAN versus AoL in degrees.

Figure 3.1: *Illustration of* $\delta\Omega$, δu_{intra}, *and* δu_{inter}, *assuming* $S = 8$, $P = 3$, *and* $F = 1$.

3.1.2 Street-of-Coverage Constellations

The SoC constellation is a class of asymmetrical constellations in terms of the geometrical configuration, in which orbital planes are unevenly spaced either along the equatorial plane or along half of the equatorial plane [8, 18, 19]. It has been demonstrated by Ulybyshev [8] that the former configuration generally consists of more orbital planes with fewer satellites per orbital plane than the latter one. In this study we focus on the latter configuration, i.e., orbital planes unevenly spaced along half of the equatorial plane, for the reason that we will take into account the build-up property for the present constellation design, and this property degrades with the number of orbital planes (see Sec. 3.3.5).

Geometrical Configuration

The SoC constellation was developed based on a Street-of-Coverage (SoC) concept. Fig. 3.2 illustrates the coverage geometry of SoC for a single orbital plane containing S evenly spaced satellites, where the circles with an angular radius of θ are the footprints projected onto the Earth's surface. As shown in Fig. 3.2 (a), if $\theta \geq j\pi/S$, the coverage will be j-fold continuous along the swath with a half-width of C_j^θ (in Fig. 3.2 (a) $j = 1$), and such swath is called the Street-of-Coverage, indicated by the shadow area. θ and C_j^θ are related by [19]

$$\cos\theta = \cos C_j^\theta \cos\left(j\pi/S\right) \tag{3.2}$$

Fig. 3.2 (b) shows that the higher the coverage fold, the narrower the SoC will be.

There exist two types of interfaces between orbital planes in the SoC constellation: the co-rotating interface and the counter-rotating interface. The co-rotating interface is such that satellites in adjacent orbital planes move in the same direction. The counter-rotating interface is such that satellites in adjacent orbital planes move in the opposite directions [8]. Fig. 3.3 shows an illustrative example of a polar SoC constellation (i.e. $i = 90$ deg) consisting of four orbital planes, where the arrows indicate the direction of satellite motion and $\Delta\Omega_{\text{co}}$, $\Delta\Omega_{\text{counter}}$

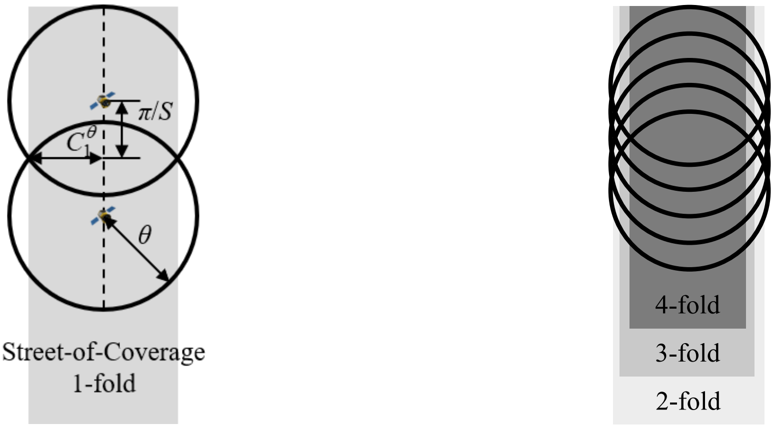

(a) Single-fold continuous coverage.

(b) Multiple-fold continuous coverage.

Figure 3.2: *Coverage geometry of SoC.*

are the RAAN spacings between adjacent orbital planes with co- and counter-rotating interfaces, respectively. As shown in the figure, the co-rotating interfaces exist between plane 1 and 2, plane 2 and 3, and plane 3 and 4, whereas the counter-rotating interface exists between plane 4 and 1. Having the concept of co- and counter-rotating interfaces, the superiority of the SoC constellation can be described as follows: the coverage overlap on the co-rotating interface is minimised at the maximum perpendicular distance between adjacent orbital planes, where the maximum perpendicular distance occurs at 90 deg on either side of the intersection of two orbits [2, Sec. 13.1].

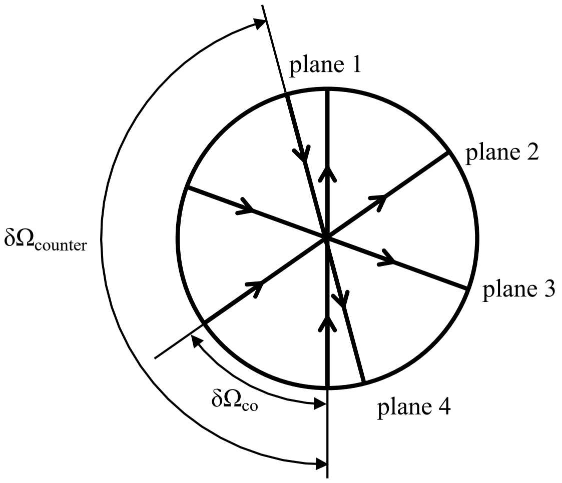

Figure 3.3: *Illustration of the co- and counter-rotating interfaces from polar view, assuming a polar SoC constellation consisting of four orbital planes.*

Fig. 3.4 illustrates the coverage geometry of the co- and counter-rotating interfaces for j-fold continuous coverage, where the arrows along the dashed lines indicate the direction of satellite motion and the shadow areas indicate the co- and counter-rotating interfaces. In the figures, the circles with an angular radius of ϑ

are the smallest footprints required for j-fold continuous global coverage, called here as the central angle of coverage, and C_j^ϑ is the corresponding minimum half-width of SoC. ϑ and C_j^ϑ are related by

$$\cos\vartheta = \cos C_j^\vartheta \cos\left(j\pi/S\right) \tag{3.3}$$

As a matter of fact, the central angle of coverage is a shared concept for both Walker and SoC constellations, and it will be discussed in detail in Sec. 3.1.3.

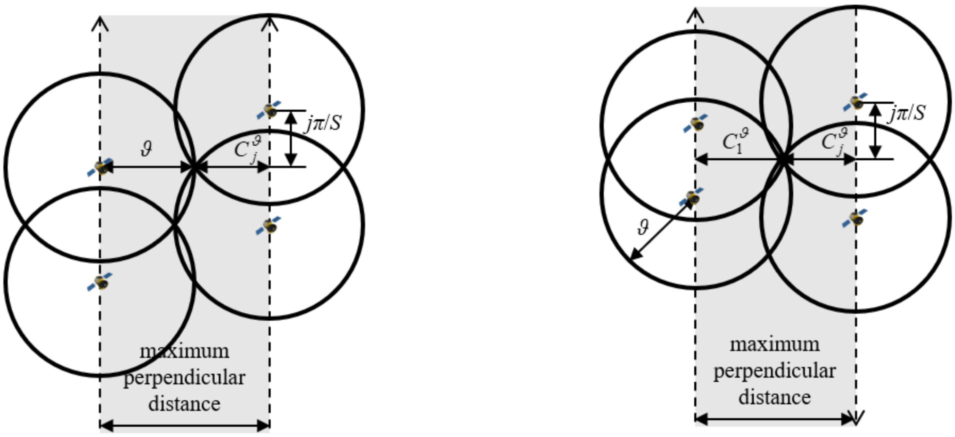

(a) Co-rotating interface.

(b) Counter-rotating interface.

Figure 3.4: *Coverage geometry of the co- and counter-rotating interfaces.*

For the co-rotating interface, as shown in Fig. 3.4 (a), the relative positions of satellites do not change over time, and thus the coverage dips can always be offset by the coverage bulges if the perpendicular angular separation between orbital planes are set to $(\vartheta + C_j^\vartheta)$. For the counter-rotating interface, as shown in Fig. 3.4 (b), the relative positions of satellites change over time, and thus to ensure the coverage being continuous along the interface, the perpendicular angular separation between orbital planes has to be narrowed to $(C_1^\vartheta + C_j^\vartheta)$, although leading to large coverage overlaps. Here the perpendicular angular separation is not the RAAN spacing but is an arc on the great circle 90 deg from the intersection of two orbits [2, Sec. 13.1]; the RAAN spacing $\delta\Omega$ and the perpendicular angular separation D are related by [2, Sec. 13.1]

$$\sin\tfrac{\delta\Omega}{2} = \sin\tfrac{D}{2} / \sin i \tag{3.4}$$

It is of note that C_j^θ given in Eq. (3.2) is the real half-width of SoC, while C_j^ϑ represents the minimum half-width of SoC required for j-fold continuous coverage. Fig. 3.5 shows the difference between the real and minimum half-width of SoC.

The characteristics of a SoC constellation are defined as follows.

- The RAAN spacings between adjacent orbital planes with co- and counter-rotating interfaces, denoted by $\delta\Omega_{\text{co}}$ and $\delta\Omega_{\text{counter}}$, are given by [8] [2, Sec. 13.1]

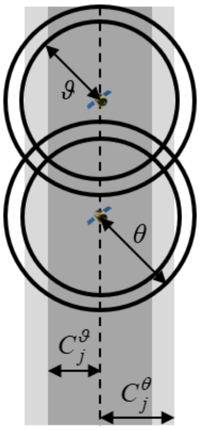

Figure 3.5: *Difference between the real and minimum half-widths of SoC.*

$$\delta\Omega_{\text{co}} = 2\sin^{-1}\left(\sin\frac{\vartheta + C_j^{\vartheta}}{2} \Big/ \sin i\right) \tag{3.5a}$$

$$\delta\Omega_{\text{counter}} = 2\sin^{-1}\left(\sin\frac{\pi - C_1^{\vartheta} - C_j^{\vartheta}}{2} \Big/ \sin i\right) \tag{3.5b}$$

In addition, there is a geometrical constraint for $\delta\Omega_{\text{co}}$ and $\delta\Omega_{\text{counter}}$ [8]:

$$\delta\Omega_{\text{counter}} = (P-1)\,\delta\Omega_{\text{co}} \leq \pi \tag{3.6}$$

because all orbital planes have to be placed within half of the equatorial plane; if $\delta\Omega_{\text{counter}} = \pi$, then the two orbital planes with counter-rotating interface will intersect at the equatorial plane [8].

- In each orbital plane, the S satellites are evenly spaced at intervals of $2\pi/S$ rad, i.e.:

$$\delta u_{\text{intra}} = 2\pi/S \tag{3.7}$$

- When a satellite is at its ascending node, some satellite in the adjacent orbital plane towards east has an AoL of [8]

$$u = \delta u_{\text{inter}} = j\pi/S - 2\cos^{-1}\left(\cos\frac{\delta\Omega_{\text{co}}}{2} \Big/ \cos\frac{\vartheta + C_j^{\vartheta}}{2}\right) \tag{3.8}$$

such that the coverage dips on the co-rotating interface can always be offset by the coverage bulges.

A SoC constellation in this study is designated in shorthand notation as i: N/P, and there is $S = N/P$. A typical SoC constellation is the 86.4 deg: 66/6 Iridium constellation [83, 84].

Necessary Condition for Continuous Global Coverage

One significant advantage of the SoC constellation is the superiority in terms of the coverage overlap, which however, imposes a constraint on the number of orbital planes. In the following a demonstration of this concept will be given.

Supposing that a polar SoC constellation with N satellites and P orbital planes is able to offer j-fold continuous global coverage, there must be

$$S\vartheta \geq j\pi \tag{3.9}$$

$$(P-1)(\vartheta + C_j^{\vartheta}) \leq \pi \tag{3.10}$$

where the first inequality implies that the coverage is continuous along the SoC for every orbital plane, and the second inequality is derived by substituting Eq. (3.5a) into Eq. (3.6) (assuming $i = 90$ deg), indicating that all orbital planes are placed within half of the equatorial plane. From Eq. (3.9) and Eq. (3.10), the following inequality holds:

$$S\vartheta \geq j(P-1)(\vartheta + C_j^{\vartheta}) \tag{3.11}$$

Replacing S with N/P, after some manipulations, Eq. (3.11) becomes

$$[N - jP(P-1)]\,\vartheta \geq jP(P-1)\,C_j^{\vartheta} \tag{3.12}$$

Observing from Eq. (3.12) that the right-hand side is non-negative, so the left-hand side must be non-negative too. Thus, we have

$$jP(P-1) \leq N \tag{3.13}$$

Eq. (3.13) is a necessary condition for a polar SoC constellation able to offer j-fold continuous global coverage; that is to say, if a polar SoC constellation does not satisfy Eq. (3.13), then it cannot offer the required coverage[2]. Since a polar SoC constellation is always more efficient in terms of the coverage performance than the inclined ones with the same number of satellites and orbital planes [8], if a polar SoC constellation cannot offer the required coverage, neither can the similar inclined ones. To conclude, the SoC constellation that does not satisfy Eq. (3.13) should be removed during the preliminary design.

3.1.3 Central Angle of Coverage

Fig. 3.6 illustrates the coverage geometry of a single satellite, where θ is the angular radius of the footprint, ϑ is the minimum angular radius of the footprint required for a specified fold of continuous global coverage, called here as the central angle of coverage, and ϵ is the elevation angle measured at the edge of the footprint, representing the worst communication condition from the ground. h, θ, and ϵ are related by

$$\frac{\cos(\theta+\epsilon)}{\cos\epsilon} = \frac{R_\oplus}{h + R_\oplus} \tag{3.14}$$

Note that θ must be less than 90 deg otherwise h will be infinite.

Different than θ which is relevant to h, ϑ is independent of h but can be uniquely determined for a Walker constellation with given N, P, F, i, or for a SoC constellation with given N, P, and i. Once ϑ is determined, from Eq. (3.14), the lower bound for h required for a specified fold of continuous global coverage can be obtained, if ϵ is given:

$$h \geq h_{\text{lb}} = \left[\frac{\cos\epsilon}{\cos(\vartheta+\epsilon)} - 1\right] R_\oplus \tag{3.15}$$

---

[2] If a proposition is true, then its converse-negative proposition must be true.

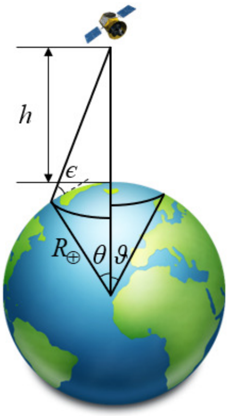

Figure 3.6: *Coverage geometry of a single satellite.*

Traditionally, the efficiency of a constellation can be evaluated by the central angle of coverage. As indicated in Fig. 3.6: for a fixed elevation angle, a small central angle of coverage will allow a low altitude, saving the costs such as launch and de-orbiting; for a fixed altitude, a small central angle of coverage will allow a large elevation angle, improving the observation performance [14]. Thus, the smaller the central angle of coverage, the more efficient the constellation will be.

In the following we will introduce the approaches to determining ϑ for Walker and SoC constellations.

Walker Constellations

For the Walker constellation, there are two typical approaches to determining ϑ: the "circumcircle" approach [4–6, 11] and the "test point" approach [13].

In the "circumcircle" approach, the Earth's surface is divided into a series of non-overlapping triangles, each triangle formed by three sub-satellite points, and the combination of non-overlapping triangles changes over time. At each time interval, the angular radii of the circumcircles of non-overlapping triangles can be computed. Then the size of the central angle of coverage can be determined by the largest circumcircle over all time intervals in one orbit period. However, the work of finding non-overlapping triangles for every time interval is computationally expensive, and thus the "circumcircle" approach does not suit constellations containing large numbers of satellites.

Compared to the "circumcircle" approach, the "test point" approach is more computationally efficient. In the "test point" approach, a virtual Earth[3], which rotates at the same rate as the constellation, is introduced, and any Walker constellation can be regarded as "geosynchronous" with respect to the virtual Earth. Due to the symmetry of the Walker constellation, the surface of the virtual Earth can be divided into several regions by the groundtracks of the "geosynchronous" constellation, all regions having the same coverage pattern. Thus, only one of the regions needs to be considered. Then generating a set of test points in any of the regions and within that region, computing the angular distances between

---

[3] If the global Earth can be continuously covered by a constellation, then it will be continuously covered independent of the Earth's rotational rate [13].

the test points and sub-satellite points for all time intervals in one orbit period, the central angle of coverage can be determined by the minimum angular distance that ensures all test points visible at any instant.

Fig. 3.7 shows the evolution of the central angle of coverage required for 4-fold continuous global coverage with the inclination for the GPS-like constellation ($N = 24$, $P = 6$, $F = 2$) and for the Galileo-like constellation ($N = 24$, $P = 3$, $F = 1$), indicated by the dashed and solid lines, respectively. It can be seen that ϑ does not monotonically change with i. Instead, the minimum ϑ for given N and P is provided by a medium i, that is, 59 deg for the GPS-like constellation and 55.5 deg for the Galileo-like constellation, and these numbers are close to the real inclination of the GPS and Galileo constellations, implying good efficiency of these two constellations.

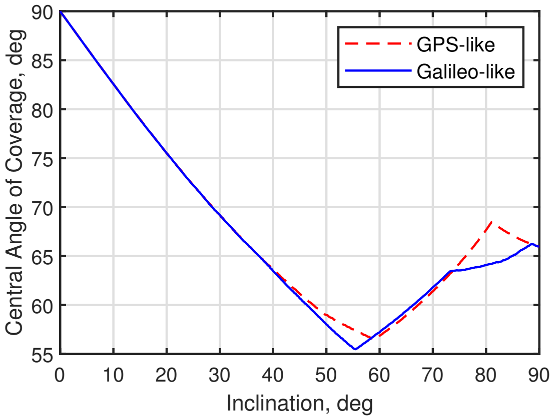

Figure 3.7: *Evolution of the central angle of coverage required for 4-fold continuous global coverage with the inclination for the GPS- and Galileo-like Walker constellations.*

Fig. 3.8 shows the minimum central angles of coverage required for 1- and 4-fold continuous global coverage for given numbers of satellites and orbital planes, for the Walker constellation. Here the minimum ϑ for given N and P is obtained by varying F from 0 to P and by varying i from 0 deg to 90 deg. In other words, each point of the plots represents a particular i: $N/P/F$ Walker constellation, whose ϑ is the smallest among the constellations with the same N and P. As shown in the figures, the minimum central angle of coverage, or the lower bound for the altitude (see Eq. (3.15)), generally decreases with the number of satellites and orbital planes.

Street-of-Coverage Constellations

For the SoC constellation, ϑ can be determined by solving the following equation

$$(P-1)\sin^{-1}\left(\sin\frac{\vartheta+C_j^\vartheta}{2}/\sin i\right)=\sin^{-1}\left(\sin\frac{\pi-C_1^\vartheta-C_j^\vartheta}{2}/\sin i\right) \tag{3.16}$$

which is derived by substituting Eq. (3.5) into Eq. (3.6). C_j^ϑ is a function of ϑ, j, and S (see Eq. (3.3)). If N, P, i, and j are given, Eq. (3.16)'s only unknown parameter will be ϑ, and it can be rapidly solved with the support of numerical optimisers such as the MATLAB nonlinear solver *fsolve* [100]. Note that

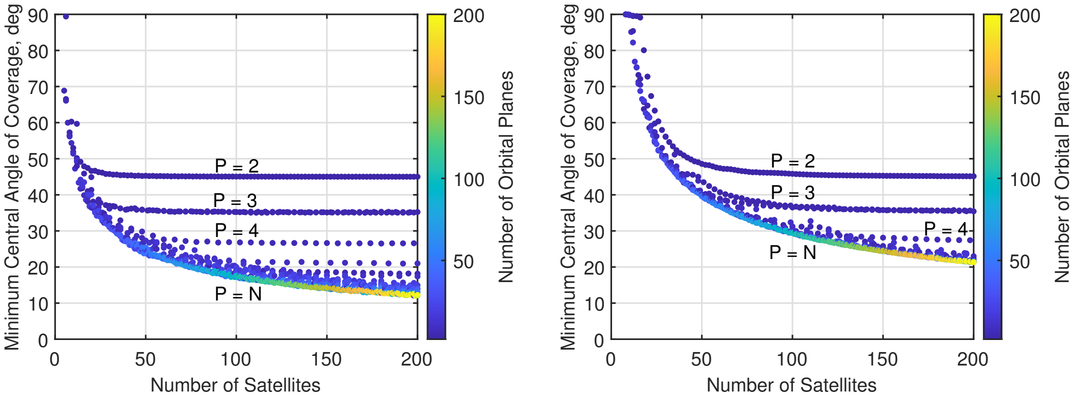

(a) 1-fold continuous global coverage.

(b) 4-fold continuous global coverage.

Figure 3.8: *Minimum central angles of coverage for given numbers of satellites and orbital planes, for the Walker constellation (the number of orbital planes increasing as the colour from dark to light).*

Eq. (3.16) will not have solution if Eq. (3.13), the necessary condition for the SoC constellation able to offer a specified fold of continuous global coverage, is not satisfied.

Fig. 3.9 shows the evolution of the central angle of coverage required for 1-fold continuous global coverage with the inclination for the Iridium-like SoC constellation ($N = 66$). It can be seen that:

- the more the orbital planes, the smaller the central angle of coverage will be;
- when $P > 2$, ϑ monotonically decreases with i, and this is the reason why the polar SoC constellation is always more efficient than the inclined ones with the same number of satellites and orbital planes;
- when $P = 2$, ϑ is independent of i, because in this case, from Eq. (3.16), ϑ is determined by

$$\vartheta + C_1^\vartheta + 2C_j^\vartheta = \pi \tag{3.17}$$

recalling from Eq. (3.3) that C_j^ϑ is not relevant to i.

Besides, Fig. 3.9 also implies that the Iridium constellation has good efficiency because it contains six orbital planes with high inclination, which can lead to a small central angle of coverage.

Figs. 3.10 shows the minimum central angles of coverage required for 1- and 4-fold continuous global coverage for given numbers of satellites and orbital planes, for the SoC constellation. Here the minimum ϑ for given N and P is always provided by the polar SoC constellation, because the central angle of coverage of a polar SoC constellation is always smaller than those of the inclined ones with the same number of satellites and orbital planes [8] (see also Fig. 3.9). In other words, each point of the plots represents a particular 90 deg: N/P SoC constellation. As shown in the figures, the minimum central angle of coverage, or the lower bound for the altitude (see Eq. (3.15)), generally decreases with the number of satellites and orbital planes.

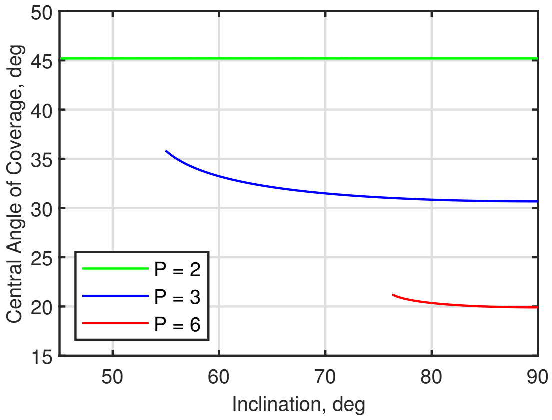

Figure 3.9: *Evolution of the central angle of coverage required for 1-fold continuous global coverage with the inclination for the Iridium-like SoC constellation.*

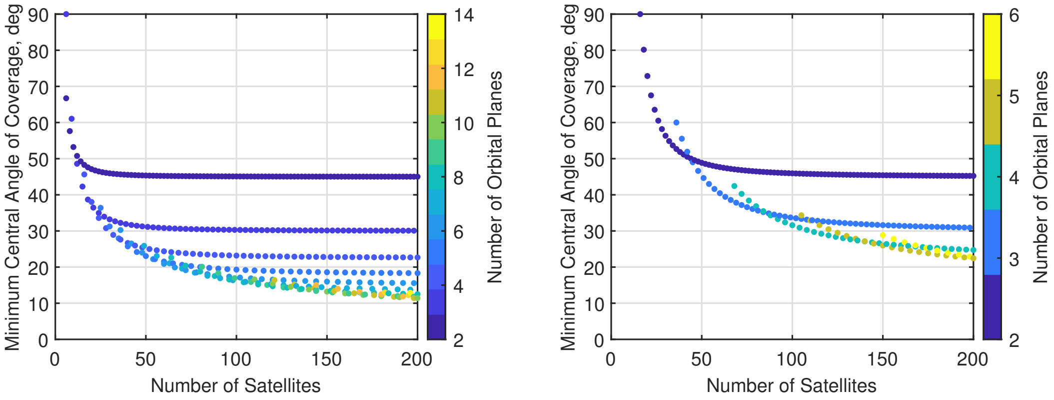

(a) 1-fold continuous global coverage.

(b) 4-fold continuous global coverage.

Figure 3.10: *Minimum central angles of coverage for given numbers of satellites and orbital planes, for the SoC constellation (the number of orbital planes increasing as the colour from dark to light).*

3.2 Characteristic Parameters of Walker and Street-of-Coverage Constellations

Based on the review in Sec. 3.1, a set of characteristic parameters, which can determine the configuration of a Walker or SoC constellation, are identified, reported in Table 3.1; they are: the number of satellites N, the number of orbital planes P, the phasing parameter F (for the Walker constellation only), the inclination i, and the altitude h. With these parameters, all geometrical information, such as the distribution of orbital planes, the relative positions of satellites, and the central angle of coverage, can be obtained. Note that in this study the elevation angle is assumed constant; this assumption defines a lower bound for communication quality between ground and constellation. As indicated the in table, compared to the Walker constellation, the SoC constellation lacks of a design parameter F, due to the design logic to minimise the coverage overlap on the co-rotating interface at the maximum perpendicular distance between adjacent orbital planes. In the followings we will show how to obtain the depended geometrical parameters from the characteristic parameters, taking as example the GPS, Galileo, and Iridium constellations.

Table 3.1: *Characteristic parameters.*

Parameter	Symbol	Constellation
Number of satellites	N	Walker, SoC
Number of orbital planes	P	Walker, SoC
Phasing parameter	F	Walker
Inclination	i	Walker, SoC
Altitude	h	Walker, SoC

Table 3.2 gives the geometrical information of the GPS and Galileo constellations offering 4-fold continuous global coverage. In the table:

- the characteristic parameters are taken from Ref. [99] and Ref. [82];
- $\delta\Omega$, δu_{intra}, and δu_{inter} are derived from Eq. (3.1);
- ϑ is determined using the “test point” approach presented in Sec. 3.1.3;
- θ is derived from Eq. (3.14), assuming $\epsilon = 5$ deg.

Table 3.2: *Geometrical information of the GPS and Galileo constellations.*

Parameter	Symbol	Value	
		GPS	Galileo
Number of satellites	N	24	24
Number of orbital planes	P	6	3
Number of satellites per plane	S	4	8
Phasing parameter	F	2	1
Inclination	i	55 deg	56 deg
Altitude	h	$20,200$ km	$23,222$ km
RAAN spacing	$\delta\Omega$	4 PU (60 deg)	8 PU (120 deg)
Intra-plane AoL spacing	δu_{intra}	6 PU (90 deg)	3 PU (45 deg)
Inter-plane AoL spacing	δu_{inter}	2 PU (30 deg)	1 PU (15 deg)
Central angle of coverage	ϑ	57.6 deg	55.7 deg
Angular radius of the footprint	θ	71.2 deg	72.6 deg

Fig. 3.11 (a) and (b) show the configurations of the GPS and Galileo constellations, respectively, in the ECI coordinate system, where the round markers and lines indicate the satellites and orbital planes, respectively.

Table 3.3 gives the geometrical information of the Iridium constellation offering 1-fold continuous global coverage. In the table:

- the characteristic parameters are taken from Ref. [83] and Ref. [84];
- $\delta\Omega_{\text{co}}$, $\delta\Omega_{\text{counter}}$, δu_{intra}, and δu_{inter} are derived from Eqs. (3.5) – (3.8), and they are consistent with the data in Ref. [83] and Ref. [84];
- ϑ is determined by solving Eq. (3.16);
- θ is derived from Eq. (3.14), assuming $\epsilon = 5$ deg.

Fig. 3.12 shows the configuration of the Iridium constellation in the ECI coordinate system, where the round markers and lines indicate the satellites and orbital planes, respectively.

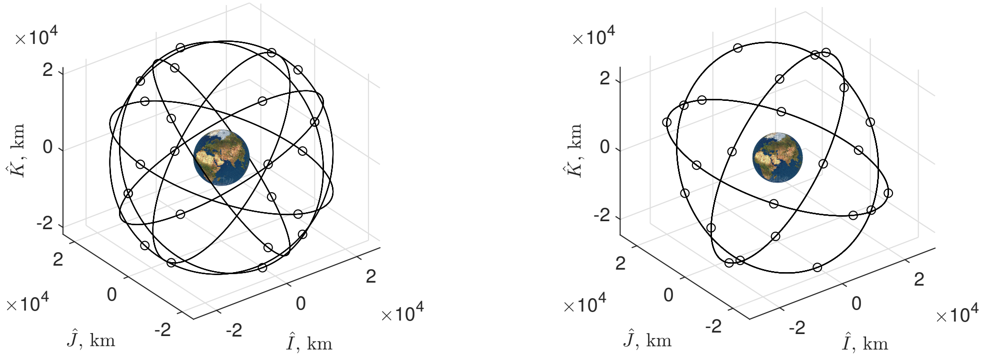

(a) GPS constellation.

(b) Galileo constellation.

Figure 3.11: *Configurations of the GPS and Galileo constellations.*

Table 3.3: *Geometrical information of the Iridium constellation.*

Parameter	Symbol	Value
Number of satellites	N	66
Number of orbital planes	P	6
Number of satellites per plane	S	11
Inclination	i	86.4 deg
Altitude	h	781 km
RAAN spacing for co-rotating interface	$\delta\Omega_{\text{co}}$	31.6 deg
RAAN spacing for counter-rotating interface	$\delta\Omega_{\text{counter}}$	158.0 deg
Intra-plane AoL spacing	δu_{intra}	32.7 deg
Inter-plane AoL spacing	δu_{inter}	14.3 deg
Central angle of coverage	ϑ	20.0 deg
Angular radius of the footprint	θ	22.4 deg

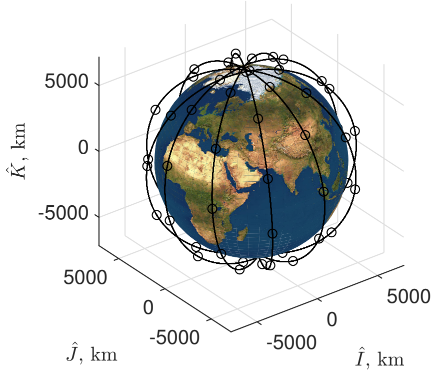

Figure 3.12: *Configuration of the Iridium constellation.*

3.3 Constellation Property Assessment and Trade-off Analysis

In this section, seven constellation properties reported in Table 1.2 will be quantitatively assessed using the characteristic parameters identified in Sec. 3.2, and the trade-offs between properties will be analysed.

3.3.1 Coverage

Traditionally, the coverage performance is the prime criterion for constellation design since coverage is the original motive that constellations were created [2, pp. 674]. Here the coverage performance refers to whether the required coverage is provided and how efficient it is. For continuous global coverage Walker and SoC constellations, the required coverage can be guaranteed if the altitude is higher than the lower bound given in Eq. (3.15). So the coverage property to be discussed in the followings is the coverage efficiency.

A common approach to assessing the coverage efficiency for continuous global coverage constellations is the excess coverage, cov, which evaluates the total coverage available as a percentage of the total coverage required [2, pp. 726]. Here, the total coverage required is the area of the Earth's surface multiplied by the required coverage fold, and for a circular-orbit constellation in which all satellites are placed at the same altitude, the total coverage available is the area of a single footprint multiplied by the number of satellites. cov is given by [2, pp. 726]

$$cov = \frac{N \times 2\pi R_{\oplus}^2 \left(1 - \cos\theta\right)}{4\pi R_{\oplus}^2 \times j} = \frac{N\left(1 - \cos\theta\right)}{2j} \tag{3.18}$$

where θ can be derived from h using Eq. (3.14) and a given ϵ.

A small excess coverage indicates small coverage overlaps and low redundancy of satellite utility, hence high coverage efficiency. Thus, the lower the value of cov, the higher the coverage efficiency will be. From Eq. (3.18), the coverage efficiency can be improved by decreasing the number of satellites and altitude, as θ is directly linked to h, if ϵ is fixed.

For a particular i: $N/P/F$ Walker or i: N/P SoC constellation, the highest coverage efficiency achievable is represented by the minimum value of cov, denoted by $cov_{\min}$. $cov_{\min}$ is obtained by setting $\theta = \vartheta$, i.e.:

$$cov_{\min} = \min_{\theta} cov = \frac{N\left(1 - \cos\vartheta\right)}{2j} \tag{3.19}$$

recalling that the central angle of coverage is the minimum angular radius of the footprint required for a specified fold of continuous global coverage. In other words, one can always link $cov_{\min}$ to ϑ, and analogous to ϑ, $cov_{\min}$ is independent of h but can be determined if N, P, F (Walker only), and i are known. Moreover, $cov_{\min}$ also sets the lower bound for cov, i.e.:

$$cov \geq cov_{\mathrm{lb}} \coloneqq cov_{\min} \tag{3.20}$$

If a constellation's cov_{lb} is too high, then the constellation can already be excluded from the optimal design because it will not be able to achieve a good enough coverage efficiency.

Fig. 3.13 shows the highest coverage efficiency achievable by Walker and SoC constellations for given numbers of satellites, for 1- and 4-fold continuous global coverage. In the plots, each point represents a class of coverage-optimal constellations sharing a particular set of N, P, F (Walker only), and i, whose $cov_{\min}$ is smaller than all other similar constellations with the same N, and accordingly, the y-axis represents the smallest $cov_{\min}$ for a given N.

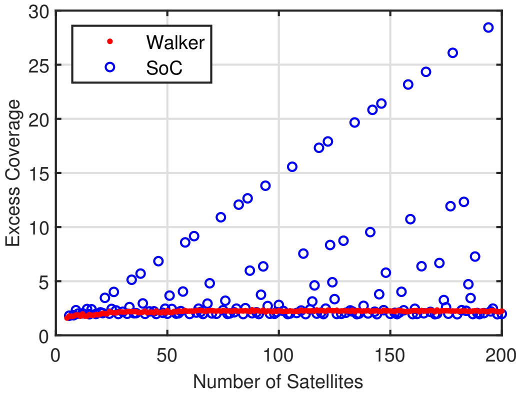

(a) 1-fold continuous global coverage.

(b) 4-fold continuous global coverage.

Figure 3.13: *Highest coverage efficiency achievable by Walker and SoC constellations for given numbers of satellites (dot: Walker, circle: SoC).*

As shown in Fig. 3.13, for a given N, the highest coverage efficiency achievable by the Walker constellation is always better than that by the SoC constellation, apart from some cases when $N \geq 20$ for 1-fold continuous global coverage. One possible reason is that for the SoC constellation, as demonstrated by Eq. (3.13), there exists a constraint on the number of orbital planes. Taking as example a constellation with 66 satellites, the Walker constellation can have 66 orbital planes, while the SoC constellation can have at most six orbital planes. If we fix the number of orbital planes as a relatively small value, e.g. $P = 6$, the SoC constellation will be able to achieve better highest coverage efficiency than the Walker constellation, as shown in Fig. 3.14, which is consistent with the SoC constellation's advantage in terms of the coverage overlap. In the plots, each point represents a class of coverage-optimal constellations sharing a particular set of N, P (here $P = 6$), F (Walker only), and i, whose cov_{min} is smaller than all other similar constellations with the same N and P, and accordingly, the y-axis represents the smallest cov_{min} for given N and P.

It is of note that, although the coverage performance is a principle design criterion, the coverage-optimal constellations may not suit practical applications. Here are the reasons.

- Most of the coverage-optimal Walker constellations in Fig. 3.13 are characterised by $P = N$, whose central angles of coverage are smaller than those of the similar constellations with the same numbers of satellites, as shown in Fig. 3.8. However, such constellations may lead to a high self-induced collision risk and a long build-up period; a demonstration of this concept will be given in Sec. 3.3.3 and Sec. 3.3.5.
- All the coverage-optimal SoC constellations in Fig. 3.13 and Fig. 3.14 are characterised by $i = 90$ deg, whose central angles of coverage are smaller than those of the similar inclined constellations with the same numbers of satellites and orbital planes [8]. However, such constellations will lead to a high self-induced collision risk and a high launch cost; a demonstration of this concept will be given in Sec. 3.3.3 and Sec. 3.3.4.

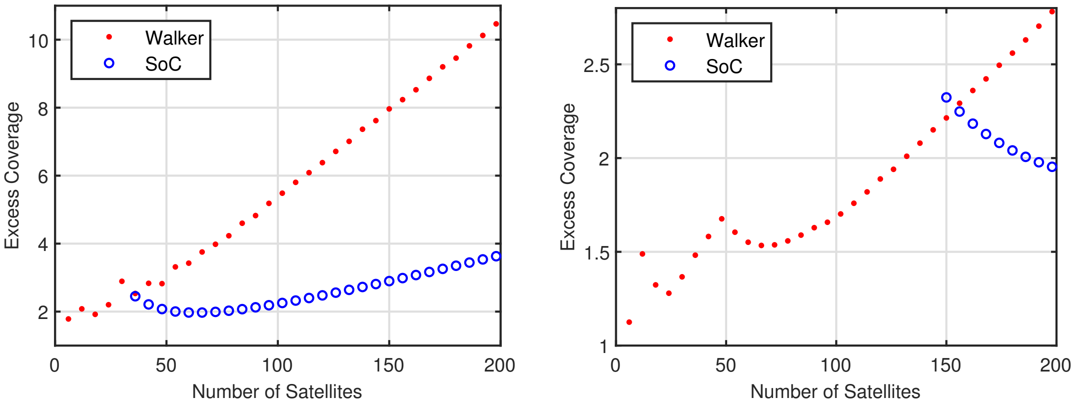

(a) 1-fold continuous global coverage.

(b) 4-fold continuous global coverage.

Figure 3.14: *Highest coverage efficiency achievable by Walker and SoC constellations consisting of six orbital planes for given numbers of satellites (dot: Walker, circle: SoC).*

In the following sections we will show the other properties for the coverage-optimal constellations, to demonstrate the need of performing trade-off during constellation design.

3.3.2 Robustness

In this study, the robustness property is defined as the constellation performance to offer normal services, should one satellite fails. It is assessed by the average percentage of the Earth's surface visible to $(j+1)$ satellites over one orbit period, denoted by pct, where j is the required coverage fold. The physical meaning of pct is that once a satellite fails and no matter which one it is, there will be pct-percent of the Earth's surface visible to at least j satellites, i.e., the required j-fold continuous global coverage can be maintained over pct-percent of the Earth's surface. Thus, the higher the value of pct, the stronger the robustness will be.

Here is the logic flow to compute pct.

- Generating a set of test points on the Earth's surface.
- Computing the locations of sub-satellite points at small time steps in one orbit period.
- Computing the number of test points enclosed by at least $(j+1)$ footprint circles as the percentage of the total number of test points at each time step.
- Averaging the percentages over all time steps in one orbit period.

pct is a function of the characteristic parameters, the number of test points, and the size of time step; the more the test points and the shorter the time step, the more accurate pct will be.

Fig. 3.15 shows the robustness of the coverage-optimal Walker and SoC constellations for given numbers of satellites at their lowest allowable altitudes, for 1- and 4-fold continuous global coverage, with the y-axis representing the value of pct. Here the lowest allowable altitude is the altitude's lower bound given by Eq. (3.15), assuming $\epsilon = 5$ deg. In the computation, the test points are selected along latitudes and longitudes at intervals of 1 deg, and the time step is set to

$T/10^3$, where

$$T = 2\pi\sqrt{\frac{(h + R_\oplus)^3}{\mu}} \tag{3.21}$$

is the unperturbed orbit period.

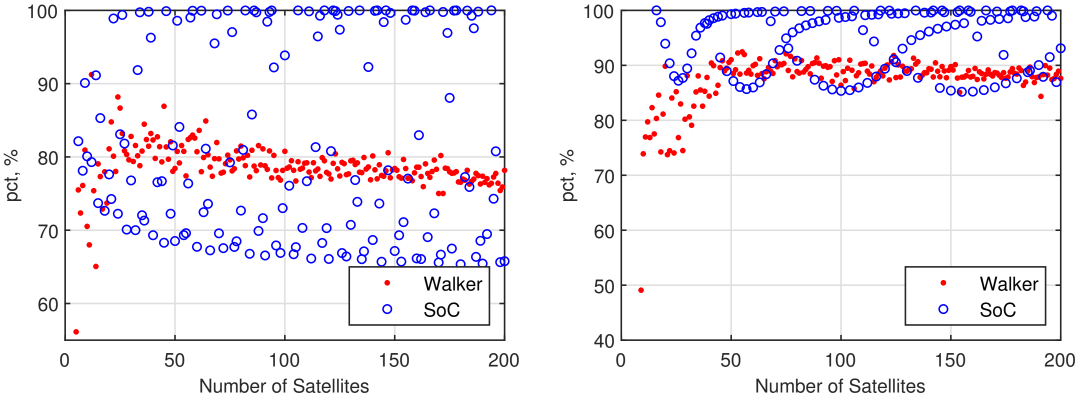

(a) 1-fold continuous global coverage.

(b) 4-fold continuous global coverage.

Figure 3.15: *Robustness of the coverage-optimal Walker and SoC constellations for given numbers of satellites at lowest allowable altitudes (dot: Walker, circle: SoC).*

Intuitively, the robustness property, which would benefit from large coverage overlaps and high redundancy of satellite utility, should be in contrast with the coverage property. However, comparing Fig. 3.15 with Fig. 3.13, it is observed that these two properties are not completely contrary with each other. Particularly, for 4-fold continuous global coverage, the coverage-optimal SoC constellations do not always show a stronger robustness than the coverage-optimal Walker constellations at their lowest allowable altitudes. One possible reason is due to the SoC constellation's design logic; the minimised coverage overlap on the co-rotating interface will lead to a larger area of outage.

By widely checking different combinations of characteristic parameters, we find that the robustness can be enhanced by increasing the number of satellites and orbital planes, increasing the altitude, using a medium inclination for the Walker constellation, and increasing the inclination for the SoC constellation.

3.3.3 Self-Induced Collision Avoidance

As the outer space is becoming more and more densely populated by satellites, collision avoidance is a critical issue that must be taken into consideration at the design stage. In this study we focus on the self-induced collision caused by satellites from the same constellation. If one collision happens within a constellation, it will be of high possibility to trigger a chain reaction, not only destroying the constellation itself but also posing severe safety hazards to the other operational spacecraft. In this study, the self-induced collision avoidance property is defined as the constellation performance to avoid collision without performing any manoeuvre. It is assessed from two aspects: the collision opportunity and the angular miss distance.

Collision Opportunity

In Ref. [2, pp. 709], the collision opportunity was defined as an incident where two satellites may approach each other within a distance lower than the sum of the radii of these two satellites. Supposing satellite A and satellite B in different orbital planes, satellite A passes through the plane of satellite B twice per revolution, and so does satellite B. Thus, each satellite in a constellation consisting of P orbital planes passes through the other planes $2\,(P-1)$ times per revolution. For a constellation with N satellites and P orbital planes, it will have $2N\,(P-1)$ collision opportunities per revolution. Take as example the Iridium constellation having 66 satellites and 6 orbital planes with approximately 14.3 revolutions per day. In a 10-year-lifetime, the Iridium constellation has 3.5×10^7 collision opportunities. If a less than 1% collision probability in 10 years is desired, then the probability of a collision in any single opportunity should be less than 10^{-9}, and even less than 10^{-11}, considering the catastrophic consequence of a collision [2, pp. 710].

In this study we introduce an unit collision opportunity, *opp*, to evaluate the collision opportunities per unit time. It is defined by

$$opp = \frac{2N\,(P-1)}{T} = \frac{\sqrt{\mu}}{\pi}\frac{N\,(P-1)}{(h+R_{\oplus})^{3/2}} \tag{3.22}$$

Apparently, the lower the value of *opp*, the better the constellation performance to avoid self-induced collision. From Eq. (3.22), the unit collision opportunity can be reduced by decreasing the number of satellites and orbital planes, and by increasing the altitude.

Angular Miss Distance

In Ref. [14], the angular miss distance, κ, was defined as the minimum angular separation between a pair of satellites. Speckman et al. [101] derived the analytical solution of κ for circular-orbit constellations in which all satellites are placed at the same altitude and inclination:

$$\cos\kappa = \cos^2\kappa_1 - \kappa_2 \sin^2\kappa_1 \tag{3.23}$$

where

$$\begin{aligned} \kappa_1 &= \delta u_{\mathrm{pair}}/2 + \tan^{-1}\left[\tan\left(\delta\Omega_{\mathrm{pair}}/2\right)\cos i\right] \\ \kappa_2 &= \cos^2 i + \sin^2 i \cos\delta\Omega_{\mathrm{pair}} \end{aligned} \tag{3.24}$$

with $\delta\Omega_{\mathrm{pair}}$ and δu_{pair} being the relative RAAN and AoL, respectively, between a pair of satellites.

In this study we introduce the constellation angular miss distance, K, to assess the constellation as a whole. It is the minimum value of κ for all pairs of satellites of a constellation, given by

$$K = \min_{A,\ B} \kappa_{AB} \tag{3.25}$$

where κ_{AB} is the angular miss distance between the Ath and Bth satellites, with $1 \leq A \leq N$, $1 \leq B \leq N$, and $A \neq B$. Apparently, the larger the constellation angular miss distance, the better the constellation performance to avoid self-induced collision.

Fig. 3.16 and Fig. 3.17 show the constellation angular miss distances of the coverage-optimal Walker and SoC constellations, respectively, for given numbers of satellites and orbital planes, for 1- and 4-fold coverage. In the plots, the constellations having a zero K are highlighted with red dots.

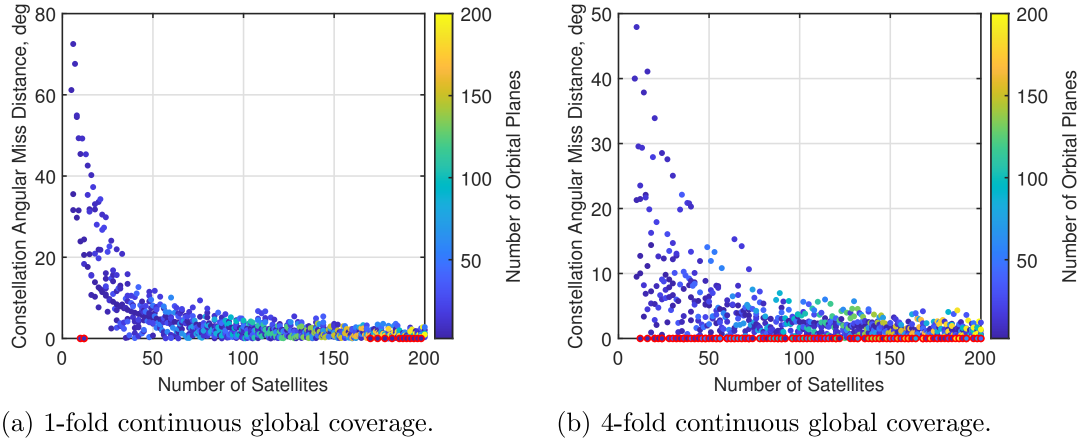

(a) 1-fold continuous global coverage.

(b) 4-fold continuous global coverage.

Figure 3.16: *Constellation angular miss distances of the coverage-optimal Walker constellations for given numbers of satellites and orbital planes (the number of orbital planes increasing as the colour from dark to light).*

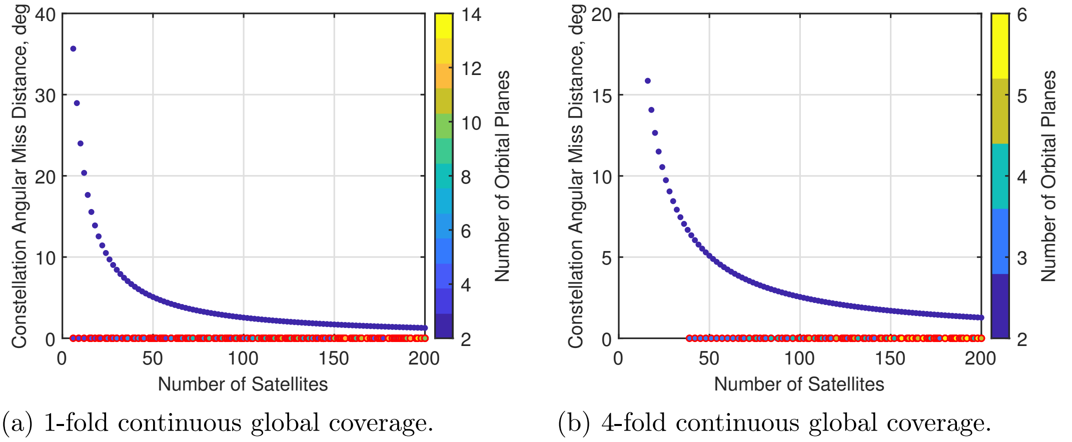

(a) 1-fold continuous global coverage.

(b) 4-fold continuous global coverage.

Figure 3.17: *Constellation angular miss distances of the coverage-optimal SoC constellations for given numbers of satellites and orbital planes (the number of orbital planes increasing as the colour from dark to light).*

As shown in the figures, the constellation angular miss distance generally decreases with the number of satellites and orbital planes. Especially, for the coverage-optimal SoC constellations, i.e., the polar ones, that have more than two orbital planes, collision will definitely happen at the poles because the satellite distribution will repeat itself every other orbital plane. This is the reason why the polar SoC constellation cannot be used for practical applications.

3.3.4 Launch

In this study, the launch property is defined as the launch cost to deliver the constellation into the mission orbit by an arbitrary launcher. Generally speaking, there are two approaches to delivering a spacecraft to the mission orbit: the direct injection and the indirect injection [102, Sec. 18.2]. The direct injection is such that the spacecraft is directly injected into the mission orbit by the launcher. The indirect injection is such that the spacecraft is first injected into a parking orbit by the launcher and then sent to the mission orbit either by the launcher's upper stage or by the spacecraft on-board propulsion system.

As summarised in Ref. [2, Table 13-2], the launch cost is determined by three factors: altitude, inclination, and spacecraft mass. For a general study of constellation design, the spacecraft mass can be replaced by the number of satellites of a constellation, the latter representing the total payload weight to launch. In the following we will present two indexes to assess the launch cost.

For direct injection, the launch cost can be assessed by the total Δv-budget of all satellites of a constellation, because it represents the total amount of fuel required. For indirect injection, the Δv-budget is affected by the parking orbit, and thus there does not exist a general formula to evaluate the Δv-budget. As a study focused on the design of constellation configuration, the selection of parking orbit will not be specifically discussed because it depends on the mission requirement and the system design of launcher and satellite. Nonetheless, due to the fact that the Δv-budget is proportional, although not strictly, to the number of satellites and altitude, here we propose

$$lch_h = Nh \tag{3.26}$$

as one index to assess the launch cost. lch_h is consistent with the principle option for constellation design reported in Ref. [2, Table 13-2], in terms of reducing the launch cost.

For the purpose of employing the Earth's rotation effects, the inclination of a prograde-orbit (i.e. $i \leq 90$ deg) constellation must not be lower than the latitude of the launch site ϕ_{site} [102, Sec. 6.4], where the launch site has to be located in the northern hemisphere. Moreover, the higher the inclination, the less the launch benefits from the Earth's rotation effects, because the velocity gained by the Earth's rotation effects is $v = v_{\oplus} \cos i$, where $v_{\oplus} \approx 464.5$ m/s is the velocity of the Earth's rotation at the equator [102, Sec. 6.4]. From the aforementioned reasons, Ref. [14] inferred that the launcher's payload capability decreases as the inclination increases above the latitude of the launch site, where the launcher's payload capability refers to the launcher's capability to boost a necessary amount of payloads to the mission orbit [102, Sec. 18.2]; a low difference between i and ϕ_{site} will allow a large margin for the amount of payloads. Therefore, we propose

$$lch_i = i - \phi_{\text{site}} \tag{3.27}$$

as another index to assess the launch cost. lch_i is a monotonically decreasing function of the velocity gained by the Earth's rotation effect.

Fig. 3.18 shows the inclinations of the coverage-optimal Walker constellations for given numbers of satellites, for 1- and 4-fold continuous global coverage. It is observed that in most cases the inclinations of the coverage-optimal Walker constellations is relatively high, indicating that if the launch site is at a low latitude, a good coverage property will lead to a bad launch property. This implies the need to perform a trade-off between the coverage and launch properties when selecting the inclination. For the SoC constellation, such trade-off is also necessary because the coverage-optimal SoC constellations are always the polar ones.

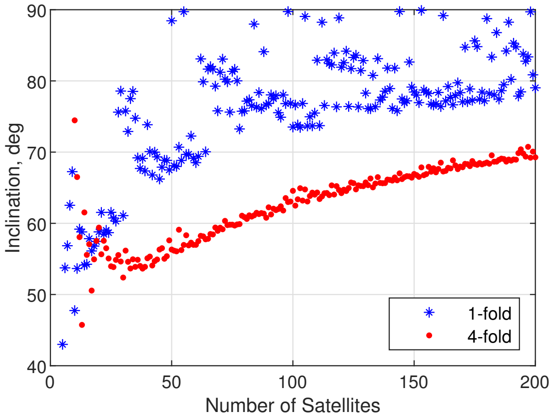

Figure 3.18: *Inclinations of the coverage-optimal Walker constellations for given numbers of satellites, for 1- and 4-fold continuous global coverage (asterisk: 1-fold, dot: 4-fold).*

From Eq. (3.26) and Eq. (3.27), the launch cost can be reduced by decreasing the number of satellites, altitude, and inclination. Note that, although in this section some simplifications are introduced, they would be necessary and useful by providing a simplified version of a complicated topic.

3.3.5 Build-Up

Due to the long duration from the testing of the early-launched satellites to the launching of all satellites, a constellation may spend a great part of its lifetime in an incomplete configuration [2, pp. 718]. If the build-up process is very slow, the early-launched satellites may become non-operational in orbit before the expected performances are achieved. In this case, the spares will have to be launched to take over the non-operational satellites, increasing the system cost and the difficulty of orbit operation. Thus, the period of building up a full constellation is an important cost driver. In this study, the build-up property is defined as the build-up period.

In real missions, the detailed process of building up a full constellation is unique and strongly related to the launch system, i.e., the choice of launcher, the number of satellites that can be placed in orbit by a single launch, etc. [2, pp. 719] Recalling that this is a general study focused on the design of constellation configuration, the launch system will not be specifically discussed. If irrespective of the launch system, the build-up period can be considered an increasing function of the number of orbital planes.

So far, the technology of injecting multiple satellites into a single orbital plane is mature. For example, India has successfully launched 104 satellites at once in February 2017 [103]. Without loss of generality, suppose that the orbital planes are built up one by one and there is no limit on the number of satellites by a single launch nor the time interval of launch. Then the number of orbital planes can be used to evaluate the build-up period; the less the orbital planes, the better the build-up property will be. The following index is proposed:

$$bld = P \tag{3.28}$$

3.3.6 Station-Keeping

In this study, the station-keeping property is defined as the cost to maintain the overall constellation configuration. The major purpose of station-keeping for constellations is to allow normal services provided and to avoid self-induced collision [2, Sec. 13.4]. Generally speaking, there are two alternative approaches to station-keeping [2, Sec. 13.4]. One is the absolute station-keeping by maintaining the absolute position of a satellite within a predefined station-keeping box. The other is the relative station-keeping by maintaining the relative positions of satellites with respect to each other. The station-keeping for constellations belongs to the latter approach [2, Sec. 13.4]. In this study we consider the J_2 and drag effects only. Because all satellites of a Walker or SoC constellation are placed in circular orbits at the common altitude and inclination, the secular rates of nodal regression and apsidal procession due to J_2 are the same for every satellite. In this case the only parameter that needs to be maintained is the altitude, which will decay under the drag effect. Thus, the station-keeping cost can be quantitatively assessed by the cost of altitude maintenance, which in turn can be evaluated in terms of the total Δv-budget of all satellites of the constellation. It is important to multiply the Δv-budget of a single satellite by the total number of satellites, because the total Δv-budget is proportional to the total amount of fuel carried by all satellites, which is proportional to the mass carried by the launcher and, as a result, affects the launch cost. Note that the altitude maintenance is required only by the constellations in LEO, where the drag effect cannot be neglected.

Supposing the altitude maintenance can be achieved via a 2-burn Hohmann transfer, the total Δv-budget is given by

$$\Delta v_{\text{keep}} = N\left[\left(\sqrt{\frac{2\mu}{a_f} - \frac{2\mu}{a_n + a_f}} - \sqrt{\frac{\mu}{a_f}}\right) + \left(\sqrt{\frac{\mu}{a_n}} - \sqrt{\frac{2\mu}{a_n} - \frac{2\mu}{a_n + a_f}}\right)\right] \tag{3.29}$$

where a_n is the semi-major axis of the nominal orbit, a_f is the final semi-major axis after altitude decay. a_f can be obtained by integrating the differential equation [93, pp. 525–529]

$$\frac{\mathrm{d}a}{\mathrm{d}t} = -\frac{C_D A}{m}\rho\sqrt{\mu a} \tag{3.30}$$

where $m/C_D A$ is the ballistic coefficient, ρ is the atmospheric density, given by the exponential model

$$\rho = \rho^* \exp\left(-\frac{a - a^*}{h_s}\right) \tag{3.31}$$

with ρ^* being the reference atmospheric density, a^* being the reference semi-major axis, and h_s being the scale height.

For a fixed frequency of altitude maintenance operation, the lower the value of Δv_{keep}, the lower the station-keeping cost will be. From Eq. (3.29), the station-keeping cost can be reduced by decreasing the number of satellites and by increasing the altitude, because the drag effect is weak at high altitudes.

3.3.7 End-of-Life Disposal

In this study, the EoL disposal property is defined as the cost to remove the constellation from the nominal orbit. According to the international regulation, non-operational spacecraft must be removed from the nominal orbit after end of life. Specifically, spacecraft in LEO should be de-orbited to a disposal orbit with low enough perigee so as to quickly re-enter under the drag effect, while spacecraft in MEO should be raised to a graveyard orbit higher than the nominal one so as not to interfere with other operational spacecraft [2, pp. 723]. As a matter of fact, a MEO constellation can also re-enter to the Earth if all satellites of the constellation are equipped with passive de-orbiting devices (e.g. solar/drag sail) and moved to the condition of orbital resonances that can provoke rapid orbital decay [47, 49]. However, we consider here the graveyard orbit strategy for the purpose of carrying out a general study of constellation design. Analogous to station-keeping, the EoL disposal cost is also quantitatively evaluated in terms of the total Δv-budget of all satellites of the constellation.

For LEO constellations, supposing the de-orbiting can be achieved via a tangential burn, the total Δv-budget is given by

$$(\Delta v_{\text{eol}})_{\text{LEO}} = N\left(\sqrt{\frac{\mu}{a_n}} - \sqrt{\frac{2\mu}{a_n} - \frac{2\mu}{a_n + r_{pd}}}\right) \tag{3.32}$$

where $r_{pd} = h_{pd} + R_\oplus$ is the perigee radius of the disposal orbit, with h_{pd} being the perigee altitude; lower than h_{pd} the drag will be strong enough to quickly lower the apogee and lead to re-entry.

For MEO constellations, supposing the orbit raising can be achieved via a 2-burn Hohmann transfer, the total Δv-budget is given by

$$(\Delta v_{\text{eol}})_{\text{MEO}} = N\left[\left(\sqrt{\frac{2\mu}{a_g} - \frac{2\mu}{a_n + a_g}} - \sqrt{\frac{\mu}{a_g}}\right) + \left(\sqrt{\frac{\mu}{a_n}} - \sqrt{\frac{2\mu}{a_n} - \frac{2\mu}{a_n + a_g}}\right)\right] \tag{3.33}$$

where a_g is the semi-major axis of the graveyard orbit.

Apparently, the smaller the total Δv-budget, the lower the EoL disposal cost will be. From Eq. (3.32), for a given disposal perigee altitude, the EoL disposal cost for LEO constellations can be reduced by decreasing the number of satellites and altitude. From Eq. (3.33), for a given semi-major axis increment, the EoL disposal cost for MEO constellations can be reduced by decreasing the number of satellites and by increasing the altitude.

3.3.8 Trade-off Analysis

Table 3.4 summarises the influence of the characteristic parameters on the constellation properties. In the table, the up and down arrows indicate that the properties benefit from increasing and decreasing, respectively, the characteristic parameters, whereas the symbol "–" indicates that the characteristic parameters do not show explicit impacts on the properties, if using the assessment methods proposed. Note that for the Walker constellation, the robustness property can be enhanced by using medium inclination, and for the SoC constellation, the inclination must not be 90 deg if there are more than two orbital planes, otherwise collision will happen.

Table 3.4: *Influence of the characteristic parameters on the constellation properties.*

					i	
Property	Index	N	P	h	Walker	SoC
Coverage	cov	↓	–	↓	–	–
Robustness	pct	↑	↑	↑	Medium	↑
Self-induced collision avoidance	opp	↓	↓	↑	–	–
Self-induced collision avoidance	K	↓	↓	–	–	$\neq 90$ deg ($P > 2$)
Launch	lch_h	↓	–	↓	–	–
Launch	lch_i	–	–	–	↓	↓
Build-up	bld	–	↓	–	–	–
Station-keeping	Δv_{keep}	↓	–	↑	–	–
EoL disposal for LEO constellations	$(\Delta v_{\text{eol}})_{\text{LEO}}$	↓	–	↓	–	–
EoL disposal for MEO constellations	$(\Delta v_{\text{eol}})_{\text{MEO}}$	↓	–	↑	–	–

Some conclusions can be drawn from the table.

- There are trade-offs between the robustness property and the other properties in terms of the number of satellites and orbital planes, i.e., the other properties benefit from small N and P while the robustness property benefit from large N and P.
- There are trade-offs between properties in terms of the altitude, e.g., between coverage and robustness properties, between robustness and launch property, between launch and station-keeping properties, etc.
- There is a trade-off between the robustness and launch properties in terms of the inclination.

3.4 Multi-Objective Optimisation for Constellation Design

In the next two sections we will find the globally optimal constellations for given missions by taking the seven constellation properties investigated in Sec. 3.3 as design criteria. A multi-objective global optimiser will be used to search for the Pareto-front solutions through a multi-agent-based search approach hybridised with a domain decomposition technique [85].

3.4.1 Mission Scenarios

Two different missions are considered: a 1-fold LEO mission and a 4-fold MEO mission; the former is usually used for Earth's observation or telecommunications (e.g. the Iridium constellation), and the latter can be applied to navigation and positioning (e.g. the GPS and Galileo constellations). For both missions, the elevation angle is fixed as $\epsilon = 10$ deg, and the latitude of the launch site is set to $\phi_{\text{site}} = 6$ deg. It is assumed that the altitude maintenance for the

LEO mission is performed once per year, and the ballistic coefficient is set to $m/C_D A = 83.33\ \mathrm{kg/m^2}$ for all satellites. Concerning the EoL disposal, the LEO mission will be de-orbited to a disposal perigee altitude of $h_{pd} = 250$ km, lower than which satellites can quickly re-enter due to the drag effect, whereas the MEO mission will be moved to a graveyard altitude which is 500 km higher than the nominal one.

3.4.2 Design Variables

In this study, the design variables are simply the characteristic parameters given by Table 3.1, and the design variable vectors for Walker and SoC constellations are therefore

$$\boldsymbol{x}_{\mathrm{Walker}} = \{N,\ P,\ F,\ h,\ i\}^\top \tag{3.34a}$$

$$\boldsymbol{x}_{\mathrm{SoC}} = \{N,\ P,\ h,\ i\}^\top \tag{3.34b}$$

Table 3.5 gives the bounds for the design variables, where the lower bound for N indicates the minimum number of satellites that can offer the required fold of continuous global coverage within the given altitude range. Besides, there are also some other constraints on the design variables.

- P should be an integer divisor of N. For the SoC constellation, P should also satisfy Eq. (3.13).
- For the Walker constellation, F should be an integer between 0 and $(P - 1)$.
- h should be higher than the lower bound given by Eq. (3.15), where the central angle of coverage ϑ, which is determined by the design variables, must be less than 90 deg.
- The design variables that lead to a zero constellation angular miss distance should be excluded.

Table 3.5: *Bounds for the design variables.*

Constellation	Parameter	Symbol	Bound			
			1-fold LEO mission		4-fold MEO mission	
			Lower	Upper	Lower	Upper
Walker	Number of satellites	N	30	200	15	200
SoC	Number of satellites	N	28	200	22	200
Walker, SoC	Inclination	i	ϕ_{site}	$\pi/2$ rad	ϕ_{site}	$\pi/2$ rad
Walker, SoC	Altitude	h	600 km	2000 km	2000 km	35786 km

3.4.3 Objective Functions

In this multi-objective optimisation problem, each of the seven constellation properties is to be modelled as an objective function and then minimised. The objective functions are defined as follows.

$$J_1 = cov \tag{3.35a}$$

$$J_2 = -\frac{pct}{10} \tag{3.35b}$$

$$J_3 = \frac{\log\left(\frac{\pi}{\sqrt{\mu}} opp\right) - \log\left(\frac{\pi}{\sqrt{\mu}} opp_{\mathrm{lb}}\right)}{\log\left(\frac{\pi}{\sqrt{\mu}} opp_{\mathrm{ub}}\right) - \log\left(\frac{\pi}{\sqrt{\mu}} opp_{\mathrm{lb}}\right)} + \frac{\frac{\pi}{2} - K}{\frac{\pi}{2}} \tag{3.35c}$$

$$J_4 = \frac{\log\ lch_h - \log\left(lch_h\right)_{\mathrm{lb}}}{\log\left(lch_h\right)_{\mathrm{ub}} - \log\left(lch_h\right)_{\mathrm{lb}}} + \frac{i - \phi_{\mathrm{site}}}{\frac{\pi}{2} - \phi_{\mathrm{site}}} \tag{3.35d}$$

$$J_5 = bld \tag{3.35e}$$

$$J_6 = \log \Delta v_{\mathrm{keep}} \tag{3.35f}$$

$$\left(J_7\right)_{\mathrm{LEO}} = \log\left(\Delta v_{\mathrm{eol}}\right)_{\mathrm{LEO}}, \quad \left(J_7\right)_{\mathrm{MEO}} = \log\left(\Delta v_{\mathrm{eol}}\right)_{\mathrm{MEO}} \tag{3.35g}$$

where J_1, J_2, J_3, J_4, J_5, and J_6 are the objective functions of the coverage, robustness, self-induced collision avoidance, launch, build-up, and station-keeping properties, respectively, $(J_7)_{\mathrm{LEO}}$ and $(J_7)_{\mathrm{MEO}}$ are the objective functions of the EoL disposal property for the LEO and MEO missions, respectively. In Eq. (3.35c) and Eq. (3.35d), the subscripts lb and ub represent the lower and upper bounds, respectively, for opp and lch_h, which are given by the means of

$$\begin{gathered} opp_{\mathrm{lb}} = \frac{\sqrt{\mu}}{\pi} \frac{\min\left[N\left(P-1\right)\right]}{\left(2000 + R_{\oplus}\right)^{3/2}}, \quad opp_{\mathrm{ub}} = \frac{\sqrt{\mu}}{\pi} \frac{\max\left[N\left(P-1\right)\right]}{\left(600 + R_{\oplus}\right)^{3/2}} \\ \left(lch_h\right)_{\mathrm{lb}} = \left(\min N\right) \times 600, \quad \left(lch_h\right)_{\mathrm{ub}} = \left(\max N\right) \times 2000 \end{gathered} \tag{3.36}$$

for the 1-fold LEO mission, and

$$\begin{gathered} opp_{\mathrm{lb}} = \frac{\min\left[N\left(P-1\right)\right]}{\left(35786 + R_{\oplus}\right)^{3/2}}, \quad opp_{\mathrm{ub}} = \frac{\max\left[N\left(P-1\right)\right]}{\left(2000 + R_{\oplus}\right)^{3/2}} \\ \left(lch_h\right)_{\mathrm{lb}} = \left(\min N\right) \times 2000, \quad \left(lch_h\right)_{\mathrm{ub}} = \left(\max N\right) \times 35786 \end{gathered} \tag{3.37}$$

for the 4-fold MEO mission; the minimum and maximum values of $N\left(P-1\right)$ and N can be obtained based on the bounds for the design variables given in Sec. 3.4.2.

The rationale behind the definitions of the objective functions is explained as follows.

- All the properties are optimised by minimising their respective objective functions. Recall that the properties refer to performances or costs, where the performances are to be maximised and the costs are to be minimised. For the performances which are improved by increasing the corresponding indexes, a minus sign should be accordingly added. In Eq. (3.35b) and Eq. (3.35c), the robustness and self-induced collision avoidance properties are improved by increasing the indexes pct and K, so a minus sign is added to these two indexes.
- For the self-induced collision avoidance and launch properties, each of them is assessed by two different indexes, and the two indexes should be properly scaled according to their respective lower and upper bounds such that they can be formulated together as a single objective. To be specific:

  - the upper and lower bounds for opp and lch_h are given by Eq. (3.36) and Eq. (3.37);
  - the upper and lower bounds for i are given in Table 3.5;
  - the upper and lower bounds for K are 0 and $\pi/2$ rad, respectively.
- For the indexes related to h, i.e., opp, lch_h, Δv_{keep}, $(\Delta v_{\text{eol}})_{\text{LEO}}$, and $(\Delta v_{\text{eol}})_{\text{MEO}}$, their values may vary from 10^{-4} to 10^{6}. In order to reduce the impact by h and to enhance the convergence of the optimisation process, the base 10 logarithm is therefore used.

Finally, the objective vectors for the LEO and MEO missions are

$$\boldsymbol{J}_{\text{LEO}} = \{J_1,\ J_2,\ J_3,\ J_4,\ J_5,\ J_6,\ (J_7)_{\text{LEO}}\}^{\top} \tag{3.38a}$$

$$\boldsymbol{J}_{\text{MEO}} = \{J_1,\ J_2,\ J_3,\ J_4,\ J_5,\ \qquad (J_7)_{\text{MEO}}\}^{\top} \tag{3.38b}$$

Note that $\boldsymbol{J}_{\text{MEO}}$ does not include J_6 because the altitude maintenance is required only by LEO constellations.

3.5 Optimisation Results and Discussion

3.5.1 1-Fold LEO Mission

Fig. 3.19 shows the Pareto-front solutions for the 1-fold LEO mission, each point representing an optimal constellation. In the plots, the three axes indicate the number of satellites, the inclination, and the altitude, and the colour bar indicates the number of orbital planes.

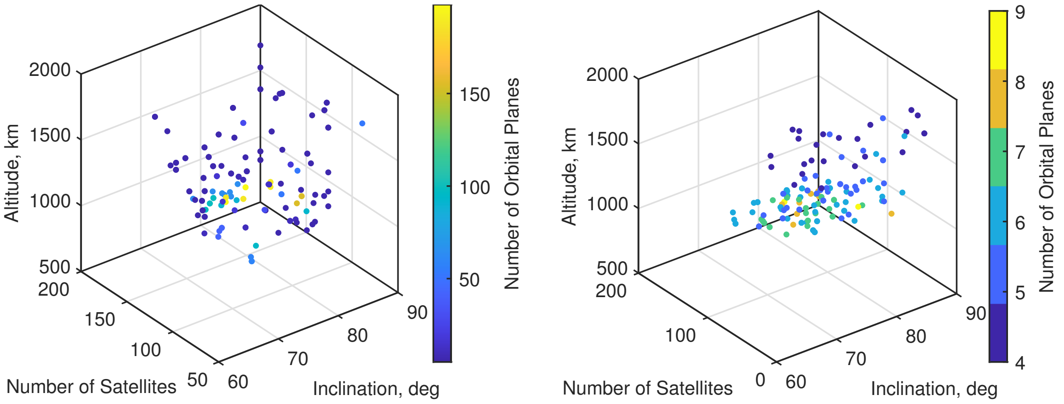

(a) Optimal Walker constellations. (b) Optimal SoC constellations.

Figure 3.19: *Pareto-front solutions for the 1-fold LEO mission (the number of orbital planes increasing as the colour from dark to light).*

As presented in Sec. 3.3.8, there exist various trade-offs between properties, and these trade-offs are also demonstrated here by the multi-objective optimisation results. Fig. 3.20 shows as example two pairs of objectives: J_1 versus J_2 and J_6 versus $(J_7)_{\text{LEO}}$, corresponding to the trade-off between the coverage and robustness properties and the trade-off between the station-keeping and EoL disposal properties. It can be seen that the different objectives do weigh against each other depending on their dimensions and scaling, and a small increase in one objective will lead to an increase in the other objective, and vice-versa.

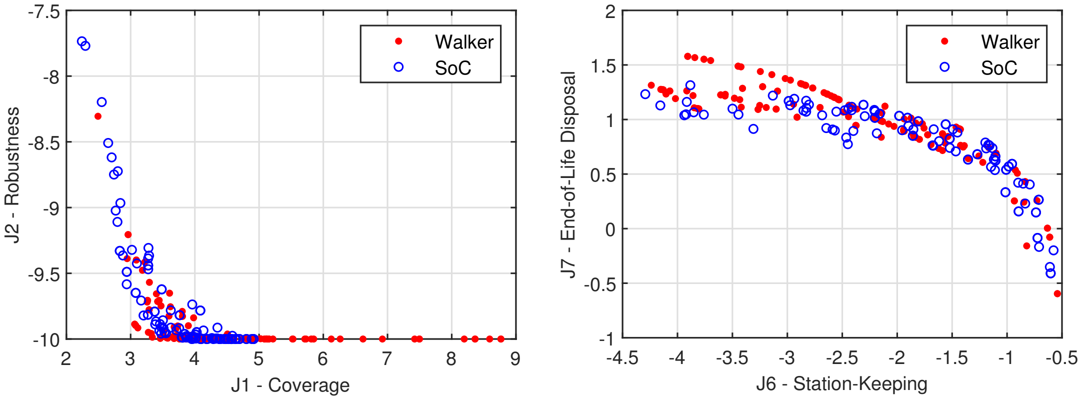

(a) J_1 versus J_2.

(b) J_6 versus $(J_7)_{\text{LEO}}$.

Figure 3.20: *Sensitivity analysis of objectives for the 1-fold LEO mission (dot: Walker, circle: SoC).*

Among the optimal constellations, we select two constellations at the similar altitudes of the Iridium constellation as the alternatives to Iridium, and another two new constellations at the altitudes between $1,200$ and $1,400$ km, where the space debris density is relatively low. In addition to the altitude constraints, the following issues should also be considered during the selection.

- The selected constellations should have relatively fewer satellites, as the number of satellites is traditionally the prime cost driver for small- and middle-sized constellations [2, Tabel 13-2];
- The selected constellations should have relatively larger constellation angular miss distance, considering the snowball effect which not only destroying the constellation itself but also posing severe safety threat to the other operational spacecraft in the already congested LEO region.

Table 3.6 presents the results of the Iridium constellation and of the selected optimal constellations. Here are some discussion about the results.

- Compared to the alternatives, the Iridium constellation shows excellent performances in terms of most of the properties apart from the robustness. For the Iridium constellation, once a satellite fails, on average only 57.72% of the Earth's surface can be offered with normal services. Considering that a replenishment operation will take some time, such an outage may cause a huge profit loss for both the ground users and the telecom operators. This represents a business trade-off that might not have been taken into account in the design of the Iridium constellation.
- Comparing the two new constellations, the SoC constellation is better than the Walker one in terms of most of the properties apart from the robustness. This is because the SoC constellation has fewer satellites and orbital planes, which, according to Table 3.4, benefits to all properties except the robustness.

Fig. 3.21 and Fig. 3.22 show the configurations of the selected optimal constellations for the 1-fold LEO mission in the ECI coordinate system, where the round

Table 3.6: *Results of the Iridium constellation and of the selected optimal constellations for the 1-fold LEO mission.*

		Alternative Iridium		New	
Symbol	Iridium	Walker	SoC	Walker	SoC
N	66	126	126	72	48
P	6	7	7	24	6
F		3		8	
i, deg	86.4	87.0	79.6	77.2	82.4
h, km	780	776	773	$1,321$	$1,286$
J_1	1.74	3.29	3.27	3.46	2.24
J_2	-5.77	-9.57	-9.39	-10.00	-7.70
J_3	1.48	1.44	1.72	1.55	1.35
J_4	1.31	1.51	1.43	1.38	1.32
J_5	6	7	7	24	6
J_6	-2.00	-1.69	-1.67	-3.19	-3.31
$(J_7)_{\text{LEO}}$	0.50	0.77	0.76	1.11	0.91
cov	1.74	3.29	3.27	3.46	2.24
pct, %	57.72	95.69	93.91	99.95	77.05
opp, s^{-1}	0.11	0.25	0.25	0.49	0.07
K, deg	0.30	1.89	0.58	0.29	0.76
lch_h, $\times 10^4$ km	5.15	9.78	9.73	9.51	6.17
lch_i, deg	80.40	80.98	73.64	71.21	76.43
bld	6	7	7	24	6
Δv_{keep}, km/s	0.01	0.02	0.02	6.43×10^{-4}	4.91×10^{-4}
$(\Delta v_{\text{eol}})_{\text{LEO}}$, km/s	3.16	5.89	5.76	12.89	8.20

markers and lines indicate the satellites and orbital planes, respectively.

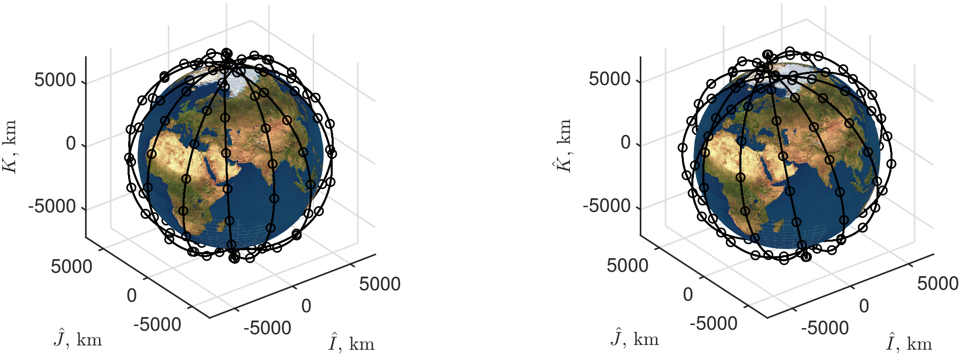

(a) Walker.

(b) SoC.

Figure 3.21: *Alternatives to the Iridium constellation.*

3.5.2 4-Fold MEO Mission

Fig. 3.23 shows the Pareto-front solutions for the 4-fold MEO mission, each point representing an optimal constellation. In the plots, the three axes indicate the number of satellites, the inclination, and the altitude, and the colour bar indicates the number of orbital planes. An interesting result is that all the optimal SoC constellations have only two orbital planes. One possible reason is that a high-

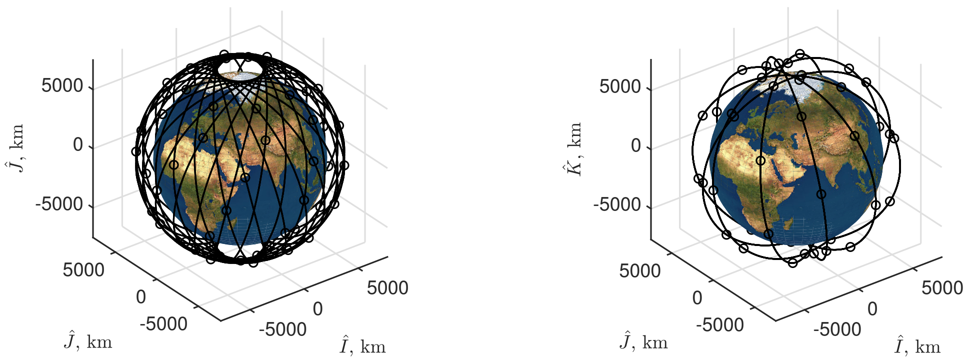

(a) Walker.

(b) SoC.

Figure 3.22: *New constellations for the 1-fold LEO mission.*

altitude mission in MEO usually requires fewer satellites, while a 4-fold MEO mission with small number of satellites can lead to a high-demanding constraint on the number of orbital planes, as demonstrated by Eq. (3.13).

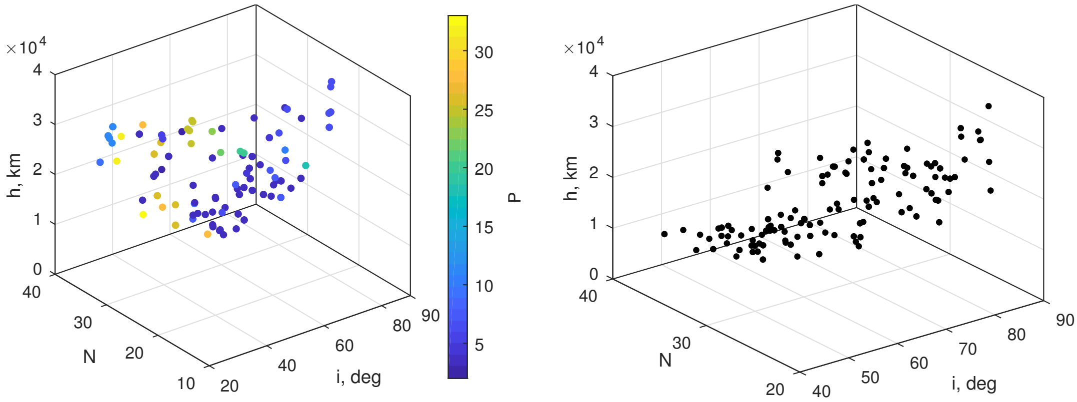

(a) Optimal Walker constellations.

(b) Optimal SoC constellations ($P = 2$).

Figure 3.23: *Pareto-front solutions for the 4-fold MEO mission (the number of orbital planes increasing as the colour from dark to light).*

Fig. 3.24 shows as example two pairs of objectives: J_1 versus J_2 and J_1 versus $(J_7)_{\text{MEO}}$, corresponding to the trade-off between the coverage and robustness properties and the trade-off between the coverage and EoL disposal properties. It can be seen that the different objectives do weigh against each other depending on their dimensions and scaling, and a small increase in one objective will lead to an increase in the other objective, and vice-versa.

Among the optimal constellations, we select four constellations at the similar altitudes of the GPS and Galileo constellations as the alternatives to GPS and Galileo, two for each, and another two new constellations at the altitudes above $25,000$ km so as not to interfere with the GPS and Galileo constellations. Apart from the altitude constraints, the following issues should also be considered during

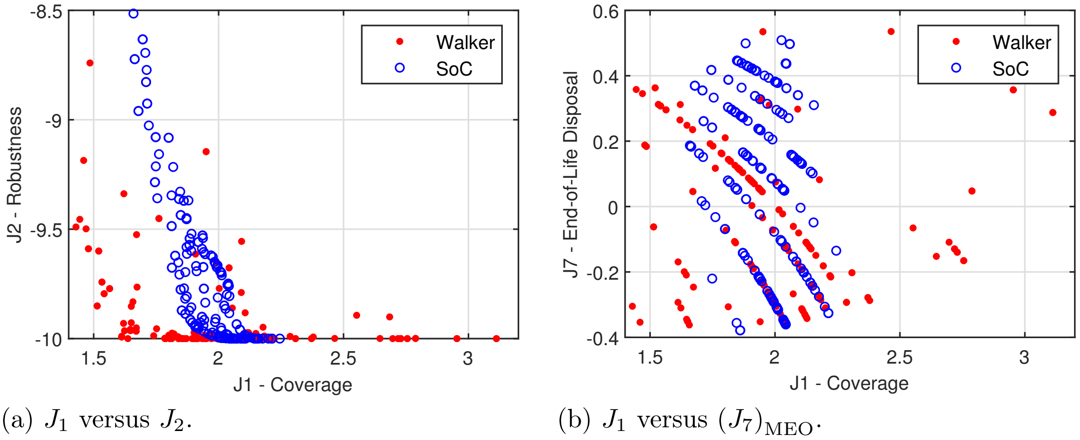

(a) J_1 versus J_2.

(b) J_1 versus $(J_7)_{\text{MEO}}$.

Figure 3.24: *Sensitivity analysis of objectives for the 4-fold MEO mission (dot: Walker, circle: SoC).*

the selection.

- The selected constellations should have relatively fewer satellites, as the number of satellites is traditionally the prime cost driver for small- and middle-sized constellations [2, Table 13-2].
- The selected Walker constellations should have relatively fewer numbers of orbital planes, in order to speed up the build-up process to start the revenue flow as early as possible.

Table 3.7 presents the results of the GPS and Galileo constellations and of the selected optimal constellations. These results show that the selected constellations have advantages and disadvantages from different aspects, demonstrating again the need of trade-off for constellation design.

Figs. 3.25 – 3.27 show the configurations of the selected optimal constellations for the 4-fold MEO mission in the ECI coordinate system, where the round markers and lines indicate the satellites and orbital planes, respectively.

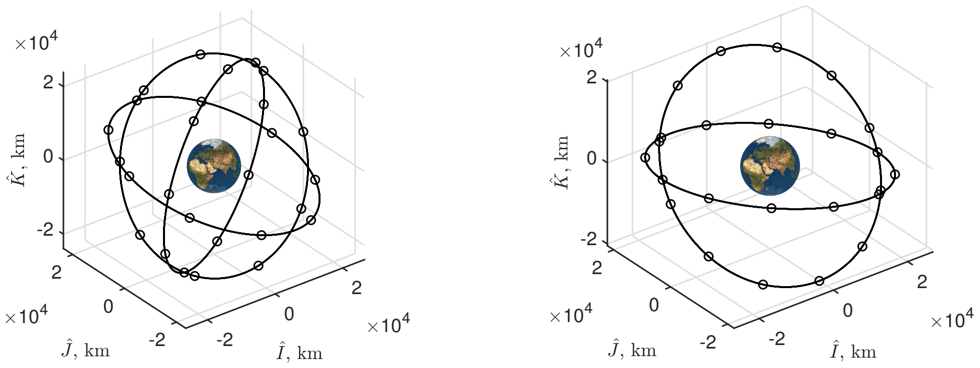

(a) Walker.

(b) SoC.

Figure 3.25: *Alternatives to the GPS constellation.*

Table 3.7: *Results of the GPS and Galileo constellations and of the selected optimal constellations for the 4-fold MEO mission.*

Symbol	GPS	Alternative GPS		Galileo	Alternative Galileo		New	
		Walker	SoC		Walker	SoC	Walker	SoC
N	24	27	24	24	27	24	18	24
P	6	3	2	3	3	2	3	2
F	2	1		1	1		2	
i, deg	55	64.6	49.8	56	62.4	78.5	61.3	76.4
h, km	$20,200$	$20,065$	$20,379$	$23,222$	$23,122$	$23,588$	$27,903$	$26,177$
J_1	1.80	2.02	1.80	1.86	2.09	1.87	1.46	1.92
J_2	-9.98	-10	-9.11	-10	-10	-9.48	-9.19	-9.59
J_3	1.27	1.15	1.01	1.06	1.10	0.98	1.11	0.96
J_4	1.09	1.23	0.99	1.13	1.23	1.36	1.17	1.36
J_5	6	3	2	3	3	2	3	2
$(J_7)_{\mathrm{MEO}}$	-0.06	-0.01	-0.07	-0.13	-0.08	-0.14	-0.35	-0.20
cov	1.80	2.02	1.80	1.86	2.09	1.87	1.46	1.92
pct, %	99.83	100	91.08	100	100	94.79	91.86	95.88
opp, $\times 10^{-3}$ s^{-1}	5.57	2.52	1.10	1.89	2.14	0.93	1.14	0.82
K, deg	0	4.02	10.54	9.16	6.96	10.54	0.29	10.54
lch_h, $\times 10^5$ km	4.85	5.42	4.89	5.57	6.24	5.66	5.02	6.28
lch_i, deg	49	58.65	43.79	50	56.38	72.48	55.27	70.43
bld	6	3	2	3	3	2	3	2
$(\Delta v_{\mathrm{eol}})_{\mathrm{MEO}}$, km/s	0.86	0.98	0.85	0.73	0.83	0.72	0.44	0.64

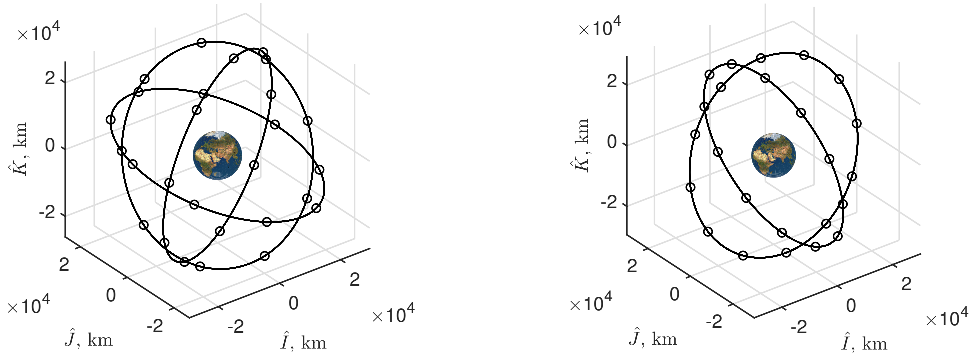

(a) Walker.

(b) SoC.

Figure 3.26: *Alternatives to the Galileo constellation.*

3.6 Summary

This chapter presented the multi-criteria constellation design, by taking seven critical constellation properties as design criteria. In the subsequent chapters, we will perform detailed analyses and design for the phases related to some of the constellation properties investigated by this chapter, that are:

- deployment, which is related to the launch and build-up properties;
- de-orbiting, which is related to the EoL disposal property of LEO constellations;
- planar transfer considering self-induced collision avoidance, which is related to the self-induced collision avoidance property.

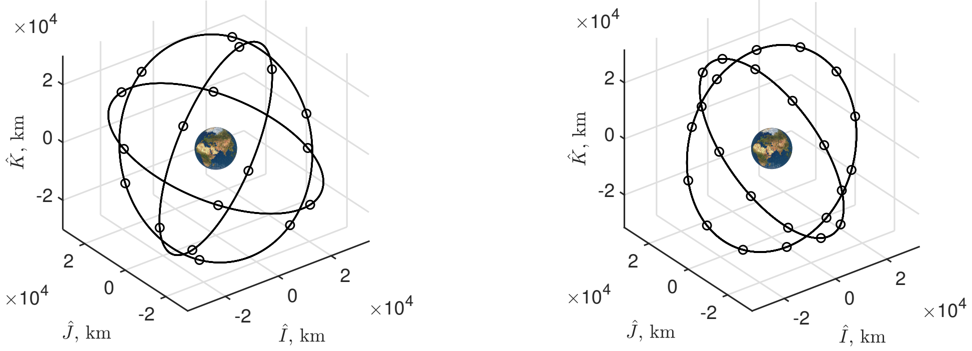

(a) Walker.

(b) SoC.

Figure 3.27: *New constellations for the 4-fold MEO mission.*

It has to be noted that in Sec. 3.3.6 and Sec. 3.3.7 when evaluating the Δv-budget for the station-keeping and EoL disposal properties, we assume an impulsive manoeuvre, but in the following chapters we focus on low-thrust. Actually they are not conflicting because the Δv-budget is an approach to estimate the propellant usage, while the relationship between the propellant usage and the characteristic parameters is not affected by the type of thrusting; that is to say, if using the low-thrust propulsion, the influence of the characteristic parameters on the Δv-budget will still be the one presented in Table 3.4. Besides, although the study scope of this chapter is Walker and SoC types, the following chapters are focused on general circular-orbit constellations and not limited to constellation types.

CHAPTER 4

Constellation Low-Thrust Deployment Through Earth Oblateness

This chapter proposes a four-phase scheme for low-thrust deployment of circular-orbit constellations through the Earth J_2 perturbations, in which an out-of-plane thrusting phase is introduced to accelerate the deployment. With the objective to reduce the computational effort for the integrated design of a deployment mission under low-thrust control, an analytical method is developed to allocate the times taken for the four phases. In this method, two design parameters, which are used to adjust the fuel consumption for the inherently expensive out-of-plane thrusting phase, are optimised, allowing the total time and fuel consumption for RAAN separation to be minimised at the same time. In order to carry out the analytical time-allocation, two sets of analytical solutions are first derived for low-thrust circular transfer subject to an in-plane tangential thrusting and an out-of-plane yaw thrusting. Finally, two case studies of large constellation deployment are presented to show how the proposed approach is used.

4.1 Description of Deployment Scheme

In this thesis, the goal of the deployment is to distribute a set of satellites from the same parking orbit into multiple desired operational orbits through the RAAN separation and within each operational orbit, to distribute the satellites into their desired positions through the AoL separation. As a preliminary study, it is assumed that the inclinations of the parking and operational orbits are the same, and all satellites remain in circular orbits during the deployment; the justification for circular assumption is presented in Sec. 7.2. The deployment includes the following four phases:

- phase 1: waiting
- phase 2: orbit raising
- phase 3: out-of-plane phasing
- phase 4: in-plane phasing

In phase 1, satellites will pause at the parking orbit to wait for raising the orbit at predetermined time intervals. For satellites to be deployed into separate planes, the times of phase 1 are different. That is to say, when some satellites are still pausing at the parking orbit, the others are being or have been raised to the operational altitude. As indicated by the RAAN drift rate due to J_2 [93, Sec. 9.6.1]:

$$\dot{\Omega} = -\frac{3\sqrt{\mu}J_2 R_\oplus \cos i}{2a^{7/2}} \tag{4.1}$$

different semi-major axes can induce different RAAN drift rates, thus further separating the RAANs of satellites.

In phase 2, satellites will be raised to the operational altitude with a continuously applied tangential thrusting (see Sec. 2.4.1).

In phase 3, satellites will perform an out-of-plane phasing manoeuvre to actively change the RAAN with an intermittently applied yaw thrusting (see Sec. 2.4.4), for predetermined time intervals, until the desired RAAN separation is achieved. From the RAAN change rate due to the yaw thrusting [43]:

$$\dot{\Omega} = \sqrt{\frac{a}{\mu}}\frac{\sin u}{\sin i} f_h \tag{4.2}$$

it is clear that satellites in a higher orbit will experience a faster RAAN change rate, and this is the reason why phase 3 is performed after raising the orbit.

In phase 4, satellites will perform an in-plane phasing manoeuvre to reach their desired in-plane positions. For circular orbits, the satellite's in-plane position can be described by the AoL. Analogous to some previous work such as Refs. [34,44,104,105], the AoL separation in this study will be achieved through a three-subphase manoeuvre: a thrusting phase to raise or lower the orbit, a coasting phase, and another thrusting phase to return to the original orbit; the two thrusting phases will use the continuous tangential thrusting. As indicated by the AoL change rate due to the Earth gravitational and J_2 effects [93, Sec. 9.6.1]:

$$\dot{u} = \frac{\sqrt{\mu}}{a^{3/2}} + \frac{3\sqrt{\mu}J_2 R_\oplus (3 - 4\sin^2 i)}{2a^{7/2}} \tag{4.3}$$

different semi-major axes can induce different AoL change rates, thus further separating the AoLs of satellites. Note that, although the change in semi-major axis is for the AoL separation only, the RAAN will be accordingly changed and thus will deviate a bit from the desired value; such inevitable change in the RAAN is called by Ref. [34] as the "parasitic RAAN drift". Ref. [34] examined the parasitic RAAN drift by assessing a worst-case scenario in which a 360 deg AoL separation at the altitude of 200 km and the inclination of 10 deg was considered, obtaining a maximum parasitic RAAN drift of 1.261 deg.

For clarity, Table 4.1 summarises the aims and perturbing forces (i.e. J_2 or thrust) for the four phases. Basically, the RAAN separation will be fulfilled in the first three phases, and the AoL separation will be fulfilled in the last phase.

Table 4.1: *Summary of the aims and perturbing forces for phase 1 to phase 4.*

Phase	Description	Aim	Perturbing force
1	Waiting	RAAN separation	J_2
2	Orbit raising	Orbit raising and RAAN separation	J_2 and thrust (tangential)
3	Out-of-plane phasing	RAAN separation	J_2 and thrust (yaw)
4	In-plane phasing	AoL separation	J_2 and thrust (tangential)

In this study, the separation in the RAANs and AoLs of satellites is measured relative to a reference satellite, which is the first one to be raised to the final orbit and does not perform the out-of-plane or in-plane phasing manoeuvre. For satellites to be deployed into the same plane as the reference satellite, only phase 2 and phase 4 are required. For clarity, Table 4.2 summarises the phases required by different satellites, where the phrase "yes" and "no" indicate that if the specific phase is required or not.

Table 4.2: *Summary of the required phases for different satellites.*

Satellite	Phase 1	Phase 2	Phase 3	Phase 4
Reference satellite	No	Yes	No	No
Satellites to be deployed into reference satellite's plane	No	Yes	No	Yes
Other satellites	Yes	Yes	Yes	Yes

4.2 Analytical Solutions for Circular Low-Thrust Transfer

In this section, analytical solutions will be derived for circular low-thrust transfer subject to two different types of thrusting: the continuous tangential thrusting and the intermittent yaw thrusting; the former will be used in phase 2 and phase 4, and the latter will be used in phase 3. The validation of these analytical solutions will be presented in Sec. 4.5 by two case studies.

Due to the fact that the influence on eccentricity by these two types of thrusting is so small that can be neglected, all satellites can therefore be assumed to remain in circular orbits throughout the deployment, as long as the initial orbit, i.e., the parking orbit, is circular. The validation of this circular assumption will be presented in Sec. 7.2. For constantly circular transfer, the dynamics system can be described in terms of four orbital elements: a, i, Ω, and u, and the equations of motion due to low-thrust and J_2 can be stated as [43]

$$\dot{a} = \frac{2f_\theta}{n} \tag{4.4a}$$

$$\dot{i} = \frac{f_h}{na}\cos u \tag{4.4b}$$

$$\dot{\Omega} = \frac{f_h}{na}\frac{\sin u}{\sin i} - \frac{3nJ_2R_\oplus^2}{2a^2}\cos i \tag{4.4c}$$

$$\dot{u} = n + \frac{2f_r}{na} - \frac{f_h}{na}\frac{\sin u}{\tan i} + \frac{3nJ_2R_\oplus^2}{2a^2}(3 - 4\sin^2 i) \tag{4.4d}$$

Besides, as presented in Sec. 2.4, the loss of the spacecraft mass m is governed by $\dot{m}$ given in Eq. (2.7), and recall that in this thesis, the thrust F, the specific impulse I_{sp}, and the mass flow rate $\dot{m}$ are assumed constant.

4.2.1 Continuous Tangential Thrusting

When applying the tangential thrusting to circular transfer, only the transversal thrust component

$$f_\theta = \mathrm{sgn}_{\Delta a}\,(F/m) \tag{4.5}$$

which in this case is tangent to the trajectory, is applied, where Δa represents the desired change in a, and $\mathrm{sgn}_{\Delta a}$ returns the sign of Δa, with which a will be increased if $\Delta a > 0$ and will be decreased if $\Delta a < 0$. Thus, Eqs. (4.4) can be reduced to

$$\dot{a} = \frac{2f_\theta}{n} \tag{4.6a}$$

$$\dot{\Omega} = -\frac{3nJ_2R_\oplus^2}{2a^2}\cos i \tag{4.6b}$$

$$\dot{u} = n + \frac{3nJ_2R_\oplus^2}{2a^2}(3 - 4\sin^2 i) \tag{4.6c}$$

where i is constant.

As the thrust is continuously applied, the solution to m is

$$m = m_0 + \dot{m}\,(t - t_0) \tag{4.7}$$

With $n = (\mu/a^3)^{1/2}$, Eq. (4.6a) can be rewritten into the form

$$a^{-3/2}\mathrm{d}a = \frac{2f_\theta}{\sqrt{\mu}}\mathrm{d}t \tag{4.8}$$

Then using f_θ from Eq. (4.5) and replacing m with Eq. (4.7), Eq. (4.8) for a can be integrated by the means of

$$\int_{a_0}^{a} a^{-3/2}\mathrm{d}a = \frac{2\mathrm{sgn}_{\Delta a}}{\sqrt{\mu}}\int_{t_0}^{t}\frac{F}{m_0 + \dot{m}\,(t - t_0)}\mathrm{d}t \tag{4.9}$$

which yields

$$a = \left[\frac{1}{\sqrt{a_0}} - \frac{\mathrm{sgn}_{\Delta a}F}{\sqrt{\mu}\dot{m}}\ln\frac{m_0 + \dot{m}\,(t - t_0)}{m_0}\right]^{-2} \tag{4.10}$$

For convenience of expression, a can also be written as a function of m:

$$a = \left(\frac{1}{\sqrt{a_0}} - \frac{\mathrm{sgn}_{\Delta a}F}{\sqrt{\mu}\dot{m}}\ln\frac{m}{m_0}\right)^{-2} \tag{4.11}$$

With $n = (\mu/a^3)^{1/2}$, Eq. (4.6b) and Eq. (4.6c) become

$$\dot{\Omega} = -\frac{3\sqrt{\mu}J_2R_\oplus^2\cos i}{2}a^{-7/2} \tag{4.12a}$$

$$\dot{u} = \sqrt{\mu}a^{-3/2} + \frac{3\sqrt{\mu}J_2R_\oplus^2(3 - 4\sin^2 i)}{2}a^{-7/2} \tag{4.12b}$$

Then using a from Eq. (4.10), the preceding equations can be integrated as

$$\Omega = \Omega_0 - \frac{3\sqrt{\mu}J_2R_\oplus^2\cos i}{2}\int_{t_0}^{t}\left[\frac{1}{\sqrt{a_0}} - \frac{\mathrm{sgn}_{\Delta a}F}{\sqrt{\mu}\dot{m}}\ln\frac{m_0 + \dot{m}\,(t - t_0)}{m_0}\right]^{7}\mathrm{d}t \tag{4.13}$$

$$
\begin{aligned}
u = u_0 + \sqrt{\mu}\int_{t_0}^{t}\left[\frac{1}{\sqrt{a_0}} - \frac{\mathrm{sgn}_{\Delta a}F}{\sqrt{\mu}\dot{m}}\ln\frac{m_0+\dot{m}\left(t-t_0\right)}{m_0}\right]^3\mathrm{d}t \\
+\frac{3\sqrt{\mu}J_2R_{\oplus}^2(3-4\sin^2 i)}{2}\int_{t_0}^{t}\left[\frac{1}{\sqrt{a_0}} - \frac{\mathrm{sgn}_{\Delta a}F}{\sqrt{\mu}\dot{m}}\ln\frac{m_0+\dot{m}\left(t-t_0\right)}{m_0}\right]^7\mathrm{d}t
\end{aligned}
\tag{4.14}
$$

For convenience of expression, the solution to Ω is written as a function of m and a, and the solution to u is written as a function of m, a, and Ω:

$$
\Omega = \Omega_0 - \frac{3\sqrt{\mu}J_2R_{\oplus}^2\cos i}{2\dot{m}}\sum_{k=0}^{7}\frac{7!}{(7-k)!}\left(\frac{\mathrm{sgn}_{\Delta a}F}{\sqrt{\mu}\dot{m}}\right)^k\left[ma^{(k-7)/2} - m_0a_0^{(k-7)/2}\right] \tag{4.15}
$$

$$
u = u_0 + \frac{\sqrt{\mu}}{\dot{m}}\sum_{k=0}^{3}\frac{3!}{(3-k)!}\left(\frac{\mathrm{sgn}_{\Delta a}F}{\sqrt{\mu}\dot{m}}\right)^k\left[ma^{(k-3)/2} - m_0a_0^{(k-3)/2}\right] - \frac{3-4\sin^2 i}{\cos i}\left(\Omega-\Omega_0\right) \tag{4.16}
$$

where $\circ!$ returns the factorial of the generic variable $\circ$.

4.2.2 Intermittent Yaw Thrusting

When using the yaw thrusting, only the out-of-plane thrust component f_h is applied. Here we introduce a parameter $0 < \eta \leq \pi/2$ and let

$$
f_h = \begin{cases} -\mathrm{sgn}_{\cos i}\left(F/m\right), & \text{if} \quad \pi/2-\eta \leq u \leq \pi/2+\eta \\ \mathrm{sgn}_{\cos i}\left(F/m\right), & \text{if} \quad -\pi/2-\eta \leq u \leq -\pi/2+\eta \\ 0, & \text{otherwise} \end{cases} \tag{4.17}
$$

where $\mathrm{sgn}_{\cos i}$ returns the sign of $\cos i$, with which the thrust effect on Ω is the same as J_2; that is to say, Ω will be decreased for prograde orbits with $i < 90$ deg and will be increased for retrograde orbits with $i > 90$ deg. Fig. 4.1 illustrates the intermittent yaw thrusting, where the y-axis is $\sin u$ because $\dot{\Omega}$ is a function of $\sin u$.

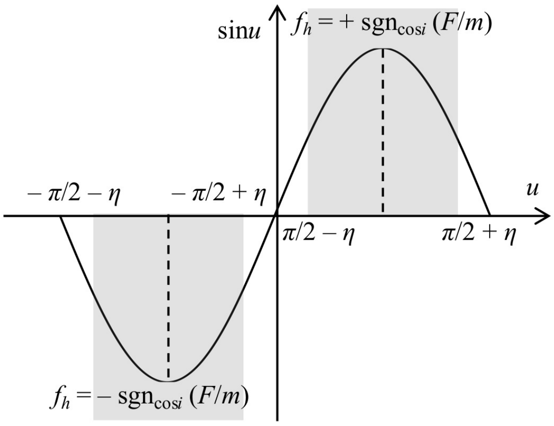

Figure 4.1: *Illustration of the intermittent yaw thrusting.*

As shown in Fig. 4.1, η defines the length of burning arcs per revolution as 4η. The reason why we introduce this parameter is because the out-of-plane thrusting is usually very expensive in terms of changing i or Ω, and η allows us to adjust the time and fuel consumption of the out-of-plane thrusting phase. Later in Sec. 4.3, we will show how η can be used to minimise the time and fuel consumption for the RAAN separation. Moreover, because applying the yaw thrusting over the orbital arcs around $u = \pm\pi/2$ can efficiently change Ω while results in a nearly null change in i, Eqs. (4.4) can be reduced to

$$\dot{\Omega} = \frac{f_h}{na}\frac{\sin u}{\sin i} - \frac{3nJ_2R_\oplus^2}{2a^2}\cos i \tag{4.18a}$$

$$\dot{u} = n - \frac{f_h}{na}\frac{\sin u}{\tan i} + \frac{3nJ_2R_\oplus^2}{2a^2}(3 - 4\sin^2 i) \tag{4.18b}$$

where a and i are constant.

Eqs. (4.18) includes the thrust, J_2, and gravitational effects. Let $\circ_T$ denote the thrust effect on the generic variable $\circ$, with the subscript T representing thrust. From Eqs. (4.18), the thrust effects on Ω and u are

$$\dot{\Omega}_T = \frac{f_h}{na}\frac{\sin u}{\sin i} \tag{4.19a}$$

$$\dot{u}_T = -\frac{f_h}{na}\frac{\sin u}{\tan i} \tag{4.19b}$$

Eqs. (4.19) involve the short-term oscillations associated with u, making it difficult to carry out the analytical integration for Ω_T and u_T. In order to address this problem, we employ the orbital averaging technique on Ω_T to obtain the averaged time rate of change of Ω_T.

As presented in Sec. 2.5, the incremental change in Ω_T over one revolution due to a small thrust can be computed by integrating $\mathrm{d}\Omega_T/\mathrm{d}u$ in u, taking the thrust acceleration and all orbital elements except u as constant. Because the perturbing effects (i.e. thrust and J_2) are very small compared to the gravitational effect, Eq. (4.18b) can be approximated as

$$\dot{u} \approx n \tag{4.20}$$

Dividing Eq. (4.19a) by Eq. (4.20), $\mathrm{d}\Omega_T/\mathrm{d}u$ is accordingly approximated as

$$\frac{\mathrm{d}\Omega_T}{\mathrm{d}u} \approx \frac{f_h}{n^2a}\frac{\sin u}{\sin i} \tag{4.21}$$

Using f_h from Eq. (4.17), the incremental change in Ω_T after every revolution can be computed by the means of

$$(\Delta\Omega_T)_{\mathrm{rev}} = \frac{\mathrm{sgn}_{\cos i}F}{mn^2a\sin i}\left(-\int_{\frac{\pi}{2}-\eta}^{\frac{\pi}{2}+\eta}\sin u\mathrm{d}u + \int_{-\frac{\pi}{2}-\eta}^{-\frac{\pi}{2}+\eta}\sin u\mathrm{d}u\right) = -\frac{4\mathrm{sgn}_{\cos i}F\sin\eta}{mn^2a\sin i} \tag{4.22}$$

The above change occur during a time period of $2\pi/\dot{u} \approx 2\pi/n$. The averaged time rate of change of Ω_T is therefore

$$\dot{\bar{\Omega}}_T = \frac{n}{2\pi}(\Delta\Omega_T)_{\mathrm{rev}} = -\frac{2\mathrm{sgn}_{\cos i}F\sin\eta}{\pi mna\sin i} \tag{4.23}$$

Similarly, we can also employ the orbital averaging technique on m, and the averaged time rate of change of m can be obtained by the means of

$$\dot{\bar{m}} = \frac{n}{2\pi}\frac{\dot{m}}{n}\left(\int_{\frac{\pi}{2}-\eta}^{\frac{\pi}{2}+\eta}\mathrm{d}u + \int_{-\frac{\pi}{2}-\eta}^{-\frac{\pi}{2}+\eta}\mathrm{d}u\right) = \frac{2\dot{m}\eta}{\pi} \tag{4.24}$$

Note that the approximation for $\dot{u}$ is used to obtain $\dot{\bar{m}}$ and $\dot{\bar{\Omega}}_T$ only.

Observing from Eq. (4.24) that $\dot{\bar{m}}$ is independent of t, so the solution to m is

$$m = m_0 + \dot{\bar{m}}\left(t - t_0\right) = m_0 + \frac{2\dot{m}\eta}{\pi}\left(t - t_0\right) \tag{4.25}$$

Substituting Eq. (4.25) into Eq. (4.23), the integration for Ω_T can be carried out as

$$\begin{aligned}\Omega_T &= \Omega_0 - \frac{2\mathrm{sgn}_{\cos i}\sin\eta}{\pi n a \sin i}\int_{t_0}^{t}\frac{F}{m_0 + \frac{2\dot{m}\eta}{\pi}\left(t - t_0\right)}\mathrm{d}t \\ &= \Omega_0 - \frac{\mathrm{sgn}_{\cos i}F}{\dot{m}na\sin i}\frac{\sin\eta}{\eta}\ln\frac{m_0 + \frac{2\dot{m}\eta}{\pi}\left(t - t_0\right)}{m_0}\end{aligned} \tag{4.26}$$

For convenience of expression, Ω_T can also be written as a function of m:

$$\Omega_T = \Omega_0 - \frac{\mathrm{sgn}_{\cos i}F}{\dot{m}na\sin i}\frac{\sin\eta}{\eta}\ln\frac{m}{m_0} \tag{4.27}$$

Observing from Eqs. (4.19) that

$$\dot{u}_T = -\cos i\dot{\Omega}_T \tag{4.28}$$

where i is constant, so u_T can be solved as

$$u_T = u_0 - \cos i\left(\Omega_T - \Omega_0\right) = u_0 + \frac{\mathrm{sgn}_{\cos i}F}{\dot{m}na\tan i}\frac{\sin\eta}{\eta}\ln\frac{m}{m_0} \tag{4.29}$$

Adding the J_2 and gravitational effects, the complete solutions to Ω and u are given by

$$\Omega = \Omega_0 - \frac{\mathrm{sgn}_{\cos i}F}{\dot{m}na\sin i}\frac{\sin\eta}{\eta}\ln\frac{m}{m_0} - \frac{3nJ_2R_\oplus^2}{2a^2}\cos i\left(t - t_0\right) \tag{4.30}$$

$$u = u_0 + n\left(t - t_0\right) + \frac{\mathrm{sgn}_{\cos i}F}{\dot{m}na\tan i}\frac{\sin\eta}{\eta}\ln\frac{m}{m_0} + \frac{3nJ_2R_\oplus^2}{2a^2}\left(3 - 4\sin^2 i\right)\left(t - t_0\right) \tag{4.31}$$

4.3 Right Ascension of the Ascending Node Separation

In this section, an analytical method will be developed to optimise the times allocated to the first three phases, such that the time and fuel consumption for the RAAN separation can be minimised at the same time. Note that the RAAN separation analysed here is for a single manoeuvring satellite, but the analytical method proposed can be readily applied to the others.

4.3.1 Description of Right Ascension of the Ascending Node Separation

As reported in Table 4.1, the RAAN separation consists of three phases, viz., phase 1 – waiting in the parking orbit, phase 2 – orbit raising to the operational altitude with the continuous tangential thrusting, and phase 3 – out-of-plane phasing with the intermittent yaw thrusting to make the RAAN separation completed.

Fig. 4.2 and Fig. 4.3 illustrate the time histories of a and $\dot{\Omega}$, respectively, for the reference and manoeuvring satellites during the RAAN separation, recalling that the reference satellite is the first one to be raised and for it, there is no phase 1 or phase 3. In the figures, Δt_1, Δt_2, and Δt_3 are the times of the three phases; a_0 and a_f are the initial and final semi-major axes, respectively, that correspond to the parking and operational orbits; $\dot{\Omega}_T$ is the time rate of change of Ω due to thrust; $\dot{\Omega}_{J_2}(a_0)$ and $\dot{\Omega}_{J_2}(a_f)$ are the time rates of change of Ω due to J_2 at $a = a_0$ and $a = a_f$.

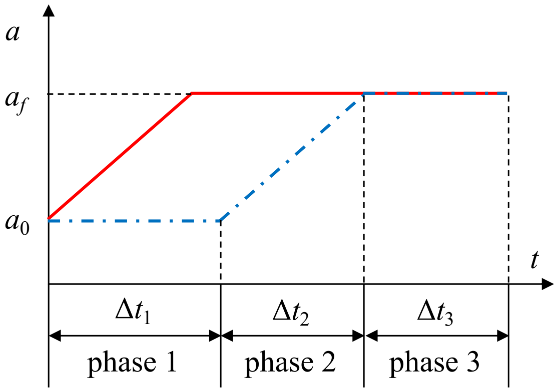

Figure 4.2: *Illustration of the time history of a for the reference satellite (solid line) and for the manoeuvring satellite (dash-dotted line) during the RAAN separation.*

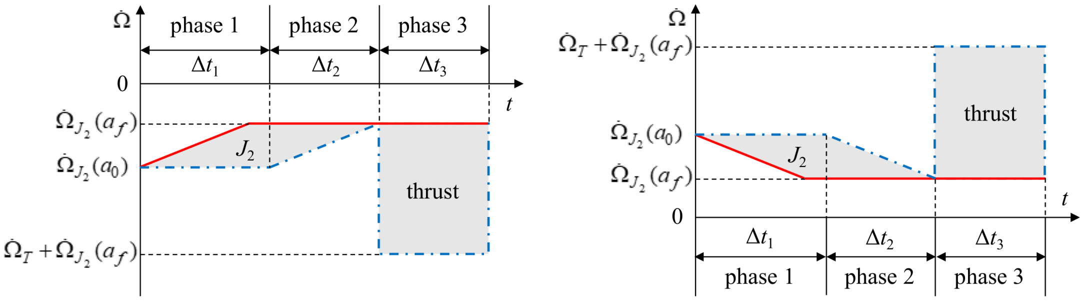

(a) Prograde orbit, $i < 90$ deg.

(b) Retrograde orbit, $i > 90$ deg.

Figure 4.3: *Illustration of the time history of $\dot{\Omega}$ for the reference satellite (solid line) and for the manoeuvring satellite (dash-dotted line) during the RAAN separation.*

From the figures, it can be seen that the J_2 effect on $\dot{\Omega}$ varies with a. In Fig. 4.3, the sudden change in $\dot{\Omega}$ is caused by the use of the intermittent yaw thrusting, and the two shadowed areas indicate the contributions of J_2 and thrust effects to the RAAN separation, which will be optimised in the remainder of this section.

4.3.2 Analytical Expressions for Times of Three Phases

In order to optimise the time allocation through an analytical approach, the first step is to derive the analytical expressions of the times taken for the three phases.

For phase 2, given the initial spacecraft mass m_0, using Eq. (4.10), a_f can be written as

$$a_f = \left(\frac{1}{\sqrt{a_0}} - \frac{F}{\sqrt{\mu}\dot{m}} \ln \frac{m_0 + \dot{m}\Delta t_2}{m_0} \right)^{-2} \tag{4.32}$$

from which, Δt_2 can be solved as

$$\Delta t_2 = \frac{m_0}{\dot{m}} \left\{ \exp\left[\frac{\dot{m}}{F} \left(\sqrt{\frac{\mu}{a_0}} - \sqrt{\frac{\mu}{a_f}} \right) \right] - 1 \right\} \tag{4.33}$$

For phase 1 and phase 3, the analytical expressions of Δt_1 and Δt_3 are to be derived by analysing the total RAAN separation between the manoeuvring and reference satellites over the three phases.

By using the analytical solutions derived in Sec. 4.2, the total RAAN change of the manoeuvring satellite can be written as

$$\begin{aligned} \Delta\Omega_{\text{man}} = &- \frac{3 n_0 J_2 R_\oplus^2 \cos i}{2 a_0^2} \Delta t_1 \\ &- \frac{3\sqrt{\mu} J_2 R_\oplus^2 \cos i}{2\dot{m}} \sum_{k=0}^{7} \frac{7!}{(7-k)!} \left(\frac{F}{\sqrt{\mu}\dot{m}} \right)^k \left[(m_2)_f a_f^{(k-7)/2} - m_0 a_0^{(k-7)/2} \right] \\ &- \frac{\text{sgn}_{\cos i} F}{\dot{m} n_f a_f \sin i} \frac{\sin\eta}{\eta} \ln \frac{(m_3)_f}{(m_2)_f} - \frac{3 n_f J_2 R_\oplus^2 \cos i}{2 a_f^2} \Delta t_3 \end{aligned} \tag{4.34}$$

where $n_0 = (\mu/a_0^3)^{1/2}$ and $n_f = (\mu/a_f^3)^{1/2}$; $(m_2)_f$ and $(m_3)_f$ are the spacecraft masses at the ends of phase 2 and phase 3, respectively, with $(m_2)_f$ given by

$$(m_2)_f = m_0 + \dot{m}\Delta t_2 = m_0 \exp\left[\frac{\dot{m}}{F} \left(\sqrt{\frac{\mu}{a_0}} - \sqrt{\frac{\mu}{a_f}} \right) \right] \tag{4.35}$$

In Eq. (4.34), the first term indicates the RAAN change of phase 1, the second term indicates the RAAN change of phase 2, obtained from Eq. (4.15), and the last two terms indicate the RAAN change of phase 3, obtained from Eq. (4.30).

If the mission parameters, i.e., a_0, a_f, i, m_0, F, and $\dot{m}$, are identical for all satellites, the time and final spacecraft mass of phase 2, i.e., Δt_2 and $(m_2)_f$, for the reference satellite will be the same as the manoeuvring satellite. So the total RAAN change of the reference satellite is

$$\begin{aligned} \Delta\Omega_{\text{ref}} = &- \frac{3\sqrt{\mu} J_2 R_\oplus^2 \cos i}{2\dot{m}} \sum_{k=0}^{7} \frac{7!}{(7-k)!} \left(\frac{F}{\sqrt{\mu}\dot{m}} \right)^k \left[(m_2)_f a_f^{(k-7)/2} - m_0 a_0^{(k-7)/2} \right] \\ &- \frac{3 n_f J_2 R_\oplus^2 \cos i}{2 a_f^2} (\Delta t_1 + \Delta t_3) \end{aligned} \tag{4.36}$$

where the first term is the RAAN change over the orbit raising which lasts Δt_2, and the second term is the RAAN change after reaching the operational orbit for an interval of $(\Delta t_1 + \Delta t_3)$.

Thus, the total RAAN separation between the manoeuvring and reference satellites can be described by

$$\begin{aligned} \delta\Omega &= \Delta\Omega_{\text{man}} - \Delta\Omega_{\text{ref}} \\ &= -\frac{3}{2} J_2 R_\oplus^2 \cos i \left(\frac{n_0}{a_0^2} - \frac{n_f}{a_f^2} \right) \Delta t_1 - \frac{\text{sgn}_{\cos i} F}{\dot{m} n_f a_f \sin i} \frac{\sin\eta}{\eta} \ln \frac{(m_3)_f}{(m_2)_f} \end{aligned} \tag{4.37}$$

where the two separate terms respectively represent the J_2 and thrust contributions to the RAAN separation, corresponding to the two shadowed areas in Fig. 4.3. Here we introduce a parameter $0 \leq \gamma \leq 1$ and let

$$-\frac{3}{2} J_2 R_{\oplus}^2 \cos i \left(\frac{n_0}{a_0^2} - \frac{n_f}{a_f^2}\right) \Delta t_1 = (1-\gamma)\, \delta\Omega_{\mathrm{des}}, \quad -\frac{\mathrm{sgn}_{\cos i} F}{\dot{m} n_f a_f \sin i} \frac{\sin\eta}{\eta} \ln \frac{(m_3)_f}{(m_2)_f} = \gamma \delta\Omega_{\mathrm{des}} \tag{4.38}$$

where $\delta\Omega_{\mathrm{des}}$ is the desired RAAN separation, such that $(1-\gamma)$ of the RAAN separation will be achieved by J_2 and γ of the RAAN separation will be achieved by thrust.

From Eq. (4.38), Δt_1 and $(m_3)_f$ can be analytically expressed as

$$\Delta t_1 = \frac{(1-\gamma)\, \delta\Omega_{\mathrm{des}}}{-\dfrac{3}{2} J_2 R_{\oplus}^2 \cos i \left(\dfrac{n_0}{a_0^2} - \dfrac{n_f}{a_f^2}\right)} \tag{4.39}$$

$$(m_3)_f = (m_2)_f \exp\left(-\mathrm{sgn}_{\cos i} n_f a_f \sin i \frac{\dot{m}}{F} \frac{\eta}{\sin\eta} \gamma \delta\Omega_{\mathrm{des}}\right) \tag{4.40}$$

Then substituting Eq. (4.40) into Eq. (4.25), Δt_3 can be solved:

$$\Delta t_3 = \frac{(m_3)_f - (m_2)_f}{\dot{\tilde{m}}} = \frac{\pi\, (m_2)_f}{2\dot{m}\eta} \left[\exp\left(-\mathrm{sgn}_{\cos i} n_f a_f \sin i \frac{\dot{m}}{F} \frac{\eta}{\sin\eta} \gamma \delta\Omega_{\mathrm{des}}\right) - 1\right] \tag{4.41}$$

where $(m_2)_f$ is given by Eq. (4.35).

As indicated in Eqs. (4.33), (4.39), and (4.41), Δt_2 can be directly determined if the mission parameters a_i, a_f, i, m_i, F, and $\dot{m}$ are given, while Δt_1 and Δt_3 cannot; instead, Δt_1 and Δt_3 are functions two variables: γ and η. γ evaluates the J_2 and thrust contributions to the RAAN separation; the higher the value of γ, the greater the thrust contribution, and thus the higher the fuel consumption. η, which defines the length of burning arcs per revolution, can be used to adjust the time and fuel consumption of phase 3; the higher the value of η, the shorter the time, while the higher the fuel consumption.

4.3.3 Time and Fuel Consumption Minimisation

Using Eqs. (4.39) – (4.41), the total time and fuel consumption of the three phases for the RAAN separation, denoted by Δt and Δm_p, can be analytically expressed in the form of

$$\begin{aligned} \Delta t &= \Delta t_1 + \Delta t_2 + \Delta t_3 \\ &= c_1 \delta\Omega_{\mathrm{des}} (1-\gamma) + \Delta t_2 + \frac{c_2\, (m_2)_f}{\eta} \left[\exp\left(c_3 \delta\Omega_{\mathrm{des}} \frac{\gamma\eta}{\sin\eta}\right) - 1\right] \end{aligned} \tag{4.42}$$

$$\Delta m_p = m_0 - (m_3)_f = m_0 - (m_2)_f \exp\left(c_3 \delta\Omega_{\mathrm{des}} \frac{\gamma\eta}{\sin\eta}\right) \tag{4.43}$$

where

$$c_1 = \left[-\frac{3}{2} J_2 R_{\oplus}^2 \cos i \left(\frac{n_0}{a_0^2} - \frac{n_f}{a_f^2}\right)\right]^{-1}, \quad c_2 = \frac{\pi}{2\dot{m}}, \quad c_3 = -\mathrm{sgn}_{\cos i} n_f a_f \sin i \frac{\dot{m}}{F} \tag{4.44}$$

In the preceding equations, Δt_2, $(m_2)_f$, c_1, c_2, and c_3 are constant parameters for a given mission, while γ and η are unknown variables. Now the optimal time-allocation problem can be converted to a multi-objective optimisation problem, that is, to find the optimal design variables γ and η such that the objectives Δt and Δm_p can be minimised. Table 4.3 gives the lower and upper bounds for the design variables, where the lower bound for η is set to 5 deg to avoid phase 3 being too long, and the upper bound for η is 90 deg because η equals a quarter of the length of burning arcs per revolution in phase 3.

Table 4.3: *Bounds for the design variables.*

Parameter	Lower bound	Upper bound
γ	0	1
η	5 deg	90 deg

Fig. 4.4 shows the evolution of Δt and Δm_p with η for different values of γ, taking as example the FORMOSAT-3/COSMIC mission to achieve a 30 deg RAAN separation. All the parameters involved in the computation are presented in Table 4.4, where the first seven are the original data of the FORMOSAT-3/COSMIC mission [32] and the last six are computed based on the original one[1]. Note that the real thrust and specific impulse of the FORMOSAT-3/COSMIC mission vary from 1.1 N to 0.2 N and from 217 s to 194 s, respectively [32]; however, this thesis assumes constant thrust and specific impulse, so we use their average values for the computation.

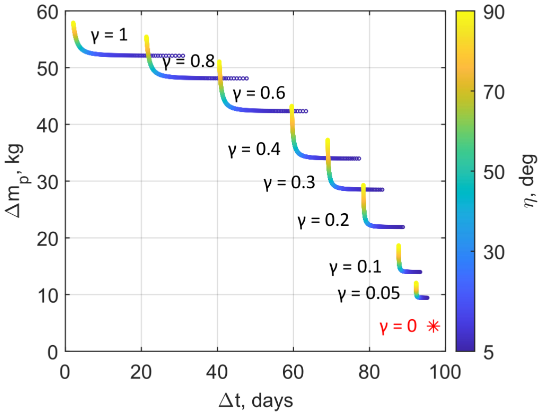

Figure 4.4: *Evolution of Δt and Δm_p with η for different γ, for the FORMOSAT-3/COSMIC mission to achieve a 30 deg RAAN separation (the value of η increasing as the colour from dark to light).*

It can be seen from Fig. 4.4 that: as γ increases, i.e., as the thrust contribution increases, the fuel consumption increases while the time decreases; for a given γ, as η increases, i.e., as the length of burning arcs per revolution in phase 3 increases, the fuel consumption increases while the time decreases. In other words, there exists a trade-off between the time and fuel consumption. Particularly, if $\gamma = 0$, the thrust effect will have a null contribution to the RAAN separation, and phase 3

---

[1] The mass flow rate $\dot{m}$ is computed using Eq. (2.7)

Table 4.4: *Parameters involved in the computation for the FORMOSAT-3/COSMIC mission.*

Parameter	Symbol	Value	Unit
Desired RAAN separation	$\delta\Omega_{\text{des}}$	-30	deg
Initial semi-major axis	a_0	6893	km
Final semi-major axis	a_f	7178	km
Inclination	i	71.992	deg
Initial spacecraft mass	m_0	61.05	kg
Thrust	F	0.65	N
Specific impulse	I_{sp}	205.5	s
Mass flow rate	$\dot{m}$	-3.2254×10^{-4}	kg/s
Time of phase 2	Δt_2	0.16	days
Spacecraft mass at the end of phase 2	$(m_2)_f$	56.601	kg
Mission-related parameter	c_1	-1.5951×10^{7}	s
Mission-related parameter	c_2	-4.8701×10^{3}	s/kg
Mission-related parameter	c_3	3.5166	

will vanish; in this case, the proposed three-phase RAAN separation will reduce to the traditional two-phase RAAN separation that exploits J_2 only.

In order to identify the optimal design variables, a mapping from the design variable space to the objective space is performed, as shown in Fig. 4.5.

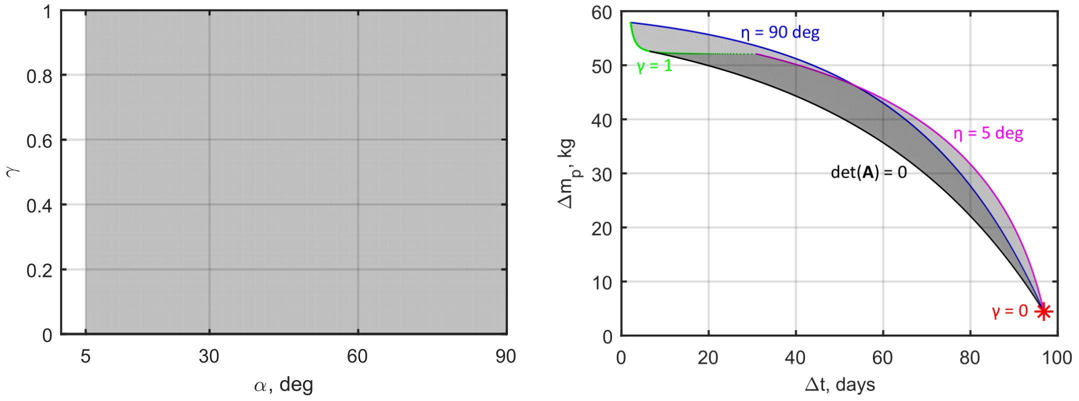

(a) Design variable space.

(b) Objective space.

Figure 4.5: *Mapping from the design variable space to the objective space, for the FORMOSAT-3/COSMIC mission to achieve a 30 deg RAAN separation.*

As shown in Fig. 4.5 (b), the edge of the objective space is composed of the following boundaries.

- $\gamma = 0$:
  the thrust effect has a null contribution to the RAAN separation, and thus $\Delta t_3 = 0$.
- $\gamma = 1$, 5 deg $\leq \eta \leq 90$ deg:
  the J_2 effect has a null contribution to the RAAN separation, and thus $\Delta t_1 = 0$.
- $\eta =$ 5 deg, $0 \leq \gamma \leq 1$:
  the length of burning arcs per revolution in phase 3 is $4 \times$ 5 $=$ 20 deg.
- $\eta = 90$ deg, $0 \leq \gamma \leq 1$:
  the length of burning arcs per revolution in phase 3 is $4 \times 90 = 360$ deg.

- $\det(\boldsymbol{A}) = 0$:
  the determinant of the transformation matrix

$$\boldsymbol{A} = \begin{Bmatrix} \partial\Delta t/\partial\gamma & \partial\Delta m_p/\partial\gamma \\ \partial\Delta t/\partial\eta & \partial\Delta m_p/\partial\eta \end{Bmatrix} \tag{4.45}$$

  is zero, implying a singular transformation from the design variables to the objectives; that is to say, the objectives do not change with the design variables. Thanks to the analytical expressions of Δt and Δm_p, we can derive the analytical expressions of the partial derivatives in $\boldsymbol{A}$, and further, derive the analytical expression of $\det(\boldsymbol{A})$:

$$\begin{aligned} \det(\boldsymbol{A}) = &- c_2 c_3 \left(m_2\right)_f^2 \delta\Omega_{\mathrm{des}} \frac{\exp\left(c_3 \delta\Omega_{\mathrm{des}} \dfrac{\gamma\eta}{\sin\eta}\right)}{\eta \sin\eta} \\ &\left[\exp\left(c_3\delta\Omega_{\mathrm{des}}\frac{\gamma\eta}{\sin\eta}\right) - 1 - \frac{c_1\delta\Omega_{\mathrm{des}}}{c_2\left(m_2\right)_f}\gamma\eta\left(1-\frac{\eta}{\tan\eta}\right)\right] \end{aligned} \tag{4.46}$$

As indicated in Fig. 4.5 (b), the Pareto-front solutions of this multi-objective optimisation problem lie on the left edge of the objective space, corresponding to

- $\gamma = 0$
- $\gamma = 1$
- $\det(\boldsymbol{A}) = 0$

Due to the fact that the out-of-plane manoeuvre is inherently expensive, the boundary $\gamma = 1$, which indicates that the RAAN separation is fully achieved by thrust, is therefore excluded. This decision is justified through two case studies in Fig. 4.7 and Fig. 4.12, which show that if $\gamma = 1$, a small decrease in Δt will be at the price of a large increase in Δm_p. Finally, the optimal design variables $(\gamma^*,\ \eta^*)$ are analytically described by $\det(\boldsymbol{A}) = 0$, since $\gamma = 0$ is a solution of $\det(\boldsymbol{A}) = 0$. From Eq. (4.46), $\det(\boldsymbol{A}) = 0$ can be further reduced to

$$\exp\left(c_3\delta\Omega_{\mathrm{des}}\frac{\gamma^*\eta^*}{\sin\eta^*}\right) - 1 - \frac{c_1\delta\Omega_{\mathrm{des}}}{c_2\left(m_2\right)_f}\gamma^*\eta^*\left(1-\frac{\eta^*}{\tan\eta^*}\right) = 0 \tag{4.47}$$

4.3.4 Optimal Time Allocation with Time and Fuel Consumption Requirements

Having the analytical expressions of the time and fuel consumption and the analytical description of the optimal design variables, the optimal times allocated to phase 1 and phase 3 can now be determined for the mission either with a given time requirement or with a fuel consumption requirement.

If a time requirement Δt_{req} is given, by combining Eq. (4.42) and Eq. (4.47), the optimal design variables that minimise the fuel consumption can be derived:

$$\exp\left[\frac{c_3\delta\Omega_{\mathrm{des}}}{\cos\eta^*}\left(1-\frac{\Delta t_{\mathrm{req}}-\Delta t_2}{c_1\delta\Omega_{\mathrm{des}}}\right)\right] - 1 - \frac{c_1\delta\Omega_{\mathrm{des}}}{c_2\left(m_2\right)_f}\left(1-\frac{\Delta t_{\mathrm{req}}-\Delta t_2}{c_1\delta\Omega_{\mathrm{des}}}\right)\left(\tan\eta^*-\eta^*\right) = 0 \tag{4.48a}$$

$$\gamma^* = \left(1-\frac{\Delta t_{\mathrm{req}}-\Delta t_2}{c_1\delta\Omega_{\mathrm{des}}}\right)\frac{\tan\eta^*}{\eta^*} \tag{4.48b}$$

If a fuel consumption requirement $(\Delta m_p)_{\text{req}}$ is given, by combining Eq. (4.43) and Eq. (4.47), the optimal design variables that minimise the time can be derived:

$$\exp\left\{\frac{c_2 c_3\left[m_0-(\Delta m_p)_{\text{req}}-(m_2)_f\right]}{c_1\cos\eta^*(\tan\eta^*-\eta^*)}\right\}-\frac{m_0-(\Delta m_p)_{\text{req}}}{(m_2)_f}=0 \tag{4.49a}$$

$$\gamma^*=\frac{c_2\left[m_0-(\Delta m_p)_{\text{req}}-(m_2)_f\right]}{c_1\delta\Omega_{\text{des}}}\frac{\tan\eta^*}{\eta^*(\tan\eta^*-\eta^*)} \tag{4.49b}$$

Eq. (4.48a) and Eq. (4.49a) for η^* can be rapidly solved with the support of numerical optimisers such as the MATLAB nonlinear equation solver *fsolve* [100]. Then from Eq. (4.48b) and Eq. (4.49b), γ^* can be obtained. Finally, substituting γ^* and η^* into Eq. (4.39) and Eq. (4.41), the optimal times allocated to phase 1 and phase 3 can be determined.

4.4 Argument of Latitude Separation

In this section, an analytical method will be presented to determine the times allocated to the three subphases of the AoL separation. Note that the AoL separation analysed here is for a single manoeuvring satellite, but the analytical method proposed can be readily applied to the others.

4.4.1 Description of Argument of Latitude Separation

Analogous to the previous work [34,44,104,105], the AoL separation in this study is composed of three subphases:

- a thrusting phase, beginning in the final orbit, to either raise or lower the orbit;
- a coasting phase during which the thrust is not applied;
- another thrusting phase to return to the final orbit.

Note that only the manoeuvring satellite performs the manoeuvres, while the reference satellite stays in its final orbit.

To achieve the desired AoL separation, the AoL changes of the reference and manoeuvring satellites in phase 4 must satisfy

$$\Delta u_{\text{ref}}-\Delta u_{\text{man}}=\delta u \tag{4.50}$$

where

$$\delta u=(\delta u_4)_0-\delta u_{\text{des}} \tag{4.51}$$

is the phase angle to be made up, with the positive sense in the direction of satellite motion. In the preceding equation, $(\delta u_4)_0$ is the AoL difference of the manoeuvring satellite relative to the reference satellite at the beginning of phase 4, which can be known once phase 1 to phase 3 have been solved, and δu_{des} is the desired AoL separation between the manoeuvring and reference satellites.

To make up the phase angle, the manoeuvring satellite can move into a higher coasting orbit with a longer period if $0 < \delta u \leq \pi$, or move into a lower coasting orbit with a shorter period if $-\pi \leq \delta u < 0$ [93, pp. 345-352].

4.4.2 Time Allocation for Three Subphases

Let $(\Delta t_{\text{thrust}})_1$, $(\Delta t_{\text{thrust}})_2$, and Δt_{coast} be the times taken for the two thrusting phases and the coasting phase.

For the two thrusting phases, because the thrust is continuously applied, we have

$$(\Delta t_{\text{thrust}})_1 = \frac{m_{\text{coast}} - (m_4)_0}{\dot{m}}, \quad (\Delta t_{\text{thrust}})_2 = \frac{(m_4)_f - m_{\text{coast}}}{\dot{m}} \tag{4.52}$$

where m_{coast} is the spacecraft mass in the coasting phase, $(m_4)_0$ and $(m_4)_f$ are the spacecraft masses at the beginning and end of phase 4; $(m_4)_0$ can be known once phase 1 to phase 3 have been solved.

For the coasting phase, it is assumed in this study that the manoeuvring satellite revolves χ revolutions in the coasting orbit, where χ is a non-negative integer. Then we have

$$\Delta t_{\text{coast}} = \frac{2\chi\pi}{\dot{u}_{\text{coast}}} \tag{4.53}$$

where

$$\dot{u}_{\text{coast}} = n_{\text{coast}} + \frac{3 n_{\text{coast}} J_2 R_\oplus^2}{2 a_{\text{coast}}^2}(3 - 4\sin^2 i) \tag{4.54}$$

with a_{coast} being the semi-major axis of the coasting orbit, and $n_{\text{coast}} = (\mu / a_{\text{coast}}^3)^{1/2}$.

As shown in Eqs. (4.52) – (4.54), to determine the times of the three subphases, it is necessary to solve for the unknown parameters a_{coast}, m_{coast}, and $(m_4)_f$, which in turn can be done by solving Eq. (4.50).

In Eq. (4.50), the AoL change of the reference satellite is

$$\Delta u_{\text{ref}} = \dot{u}_f \left[(\Delta t_{\text{thrust}})_1 + (\Delta t_{\text{thrust}})_2 + \Delta t_{\text{coast}}\right] \quad = \dot{u}_f \left[\frac{(m_4)_f - (m_4)_0}{\dot{m}} + \frac{2\chi\pi}{\dot{u}_{\text{coast}}}\right] \tag{4.55}$$

where

$$\dot{u}_f = n_f + \frac{3 n_f J_2 R_\oplus^2}{2 a_f^2}(3 - 4\sin^2 i) \tag{4.56}$$

and the AoL change of the manoeuvring satellite is

$$\Delta u_{\text{man}} = 2\chi\pi + \Delta u_{\text{thrust}} \tag{4.57}$$

where $2\chi\pi$ is the AoL change of the coasting phase, and Δu_{thrust} is the sum of the AoL changes of the two thrusting phases. Using u from Eq. (4.16), Δu_{thrust} can be written as

$$\begin{aligned} \Delta u_{\text{thrust}} = & \frac{3\sqrt{\mu} J_2 R_\oplus^2}{2\dot{m}}(3 - 4\sin^2 i) \sum_{k=0}^{7} \left[\frac{7!}{(7-k)!}\left(\frac{F}{\sqrt{\mu}\dot{m}}\right)^k w_1\right] \\ & + \frac{\sqrt{\mu}}{\dot{m}} \sum_{k=0}^{3} \left[\frac{3!}{(3-k)!}\left(\frac{F}{\sqrt{\mu}\dot{m}}\right)^k w_2\right] \end{aligned} \tag{4.58}$$

where

$$\begin{aligned} w_1 &= (\ \ \mathrm{sgn}_{\delta u})^k \left[m_{\mathrm{coast}} a_{\mathrm{coast}}^{(k-7)/2} - (m_4)_0\, a_f^{(k-7)/2} \right] \\ &\quad + (-\mathrm{sgn}_{\delta u})^k \left[(m_4)_f\, a_f^{(k-7)/2} - m_{\mathrm{coast}} a_{\mathrm{coast}}^{(k-7)/2} \right] \\ w_2 &= (\ \ \mathrm{sgn}_{\delta u})^k \left[m_{\mathrm{coast}} a_{\mathrm{coast}}^{(k-3)/2} - (m_4)_0\, a_f^{(k-3)/2} \right] \\ &\quad + (-\mathrm{sgn}_{\delta u})^k \left[(m_4)_f\, a_f^{(k-3)/2} - m_{\mathrm{coast}} a_{\mathrm{coast}}^{(k-3)/2} \right] \end{aligned} \tag{4.59}$$

with $\mathrm{sgn}_{\delta u}$ returning the sign of δu.

Replacing Δu_{ref} and Δu_{man} with Eq. (4.55) and Eq. (4.57), Eq. (4.50) can now be written as a function of a_{coast}, m_{coast}, and $(m_4)_f$. Let us then use a from Eq. (4.11), which gives

$$a_{\mathrm{coast}} = \left[\frac{1}{\sqrt{a_f}} - \frac{\mathrm{sgn}_{\delta u} F}{\sqrt{\mu}\dot{m}} \ln \frac{m_{\mathrm{coast}}}{(m_4)_0} \right]^{-2} \tag{4.60a}$$

$$a_f = \left[\frac{1}{\sqrt{a_{\mathrm{coast}}}} + \frac{\mathrm{sgn}_{\delta u} F}{\sqrt{\mu}\dot{m}} \ln \frac{(m_4)_f}{m_{\mathrm{coast}}} \right]^{-2} \tag{4.60b}$$

and substitute a_f into a_{coast}, which yields

$$(m_4)_f = \frac{m_{\mathrm{coast}}^2}{(m_4)_0} \tag{4.61}$$

Both a_{coast} and $(m_4)_f$ can now be expressed in terms of m_{coast}. Consequently, Eq. (4.50)'s only unknown parameter is m_{coast}. This equation can be rapidly solved with the support of numerical optimisers such as the MATLAB nonlinear system solver *fsolve* [100].

Once m_{coast} is obtained, a_{coast} and $(m_4)_f$ can then be known from Eq. (4.60a) and Eq. (4.61). Finally, substituting m_{coast}, a_{coast}, and $(m_4)_f$ into Eq. (4.52) and Eq. (4.53), the times allocated to the three subphases can be determined.

4.5 Case Studies and Discussion

This section will investigate the deployment of two large constellations – a OneWeb-like constellation and a sun-synchronous constellation – to demonstrate how the proposed analytical methods can be fast implemented. For these two case studies, a Hall Effect thruster, which produces a thrust of 154 mN and a specific impulse of 2035 s, is used [106].

For convenience of description, in the following sections, the RAAN separation method that exploits the J_2 effect only is called the J_2-only strategy, and the method that also exploits the thrust effect is called the J_2-thrust strategy.

4.5.1 OneWeb-Like Constellation

Mission Scenario

Table 4.5 gives the geometrical information of the OneWeb-like constellation. Note that the OneWeb-like constellation is not a typical Walker or SoC constellation investigated in Sec. 3, because the orbital planes are not evenly space over the equator or unevenly spaced over half of the equator, although they are equally separated by 10.2 deg.

Table 4.5: *Geometrical information of the OneWeb-like constellation.*

Parameter	Symbol	Value	Unit
Number of satellites	N	720	
Number of orbital planes	P	18	
Number of satellites per orbital plane	S	40	
Inclination	i	87.9	deg
Altitude	h	1200	km
RAAN spacing	$\delta\Omega$	10.2	deg
Intra-plane AoL spacing	δu_{intra}	9	deg
Inter-plane AoL spacing	δu_{inter}	4.5	deg

According to the letter of intent [107], the real OneWeb constellation will use 18 Soyuz launchers, one for each plane. In this case study we assume a large launcher (e.g. Falcon 9 [108]) to deploy 80 satellites into two planes by each launch, as the study scope of this thesis is multi-plane deployment. Fig. 4.6 shows the desired separation in the RAAN and AoL, where the reference satellite is the first one in the first plane.

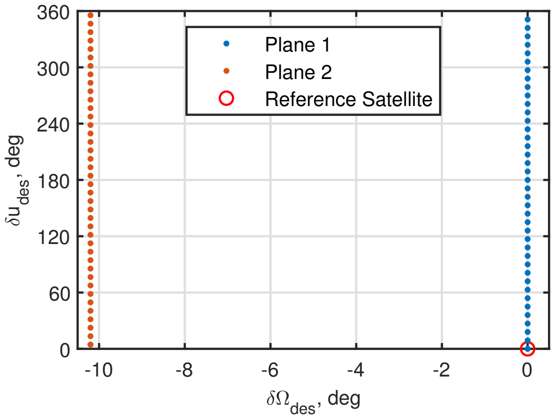

Figure 4.6: *Desired separation in the RAAN and AoL for 80 OneWeb-like satellites deployed into two planes.*

Table 4.6 presents the simulation parameters for the case study of the OneWeb-like constellation, where it is assumed that all the 80 satellites, with an initial spacecraft mass of 150 kg, are launched into a 500-km-high parking orbit and are initially separated from each other by an along-track distance of 200 km, which is equivalent to an initial AoL separation of 1.666 deg.

Minimum-Time RAAN Separation with Fuel Consumption Requirement

In this case study we will present a minimum-time RAAN separation given a fuel consumption requirement, for the purpose of starting revenue flow as early as possible with a limited propellant budget. Note that satellites in the first plane will directly reach the final orbit together with the reference satellite, so the following analysis of the RAAN separation is performed for the second plane only.

Table 4.6: *Simulation parameters for the OneWeb-like constellation.*

Parameter	Symbol	Value	Unit
Initial semi-major axis	a_0	$R_\oplus +\ \ 500$	km
Final semi-major axis	a_f	$R_\oplus + 1200$	km
Inclination	i	87.9	deg
Initial AoL separation between adjacent satellites	δu_0	1.666	deg
Desired separation in the RAAN and AoL	$\delta\Omega_{\text{des}}$, δu_{des}	Fig. 4.6	deg
Initial spacecraft mass	m_0	150	kg
Thrust	F	154	mN
Specific impulse	I_{sp}	2035	s
Mass flow rate	$\dot{m}$	-7.7168×10^{-6}	kg
Number of revolutions in the coasting orbit	χ	100	

Table 4.7 presents the constant parameters that will be used in the subsequent computation, where Δt_2 and $(m_2)_f$ are obtained from Eq. (4.33) and Eq. (4.35), c_1, c_2, and c_3 are obtained from Eq. (4.44).

Table 4.7: *Constant parameters for the OneWeb-like constellation.*

Parameter	Symbol	Value	Unit
Time of phase 2	Δt_2	4.02	days
Spacecraft mass at the end of phase 2	$(m_2)_f$	147.318	kg
Mission-related parameter	c_1	-6.1380×10^7	s
Mission-related parameter	c_2	-2.0356×10^5	s/kg
Mission-related parameter	c_3	0.3632	

With Eq. (4.42) and Eq. (4.43), the mapping from the design variable space to the objective space can be performed. Fig. 4.7 shows the time and fuel consumption for the RAAN separation of a single satellite, considering $0 \leq \gamma \leq 1$ and $5 \text{ deg} \leq \eta \leq 90$ deg, where the shadowed area indicates the objective space of the second plane. In the figure, the Pareto-optimal time and fuel consumption are highlighted by the solid line, and the triangle indicates the time and fuel consumption corresponding to the J_2-only strategy, that are, 130.49 days and 3.628 kg.

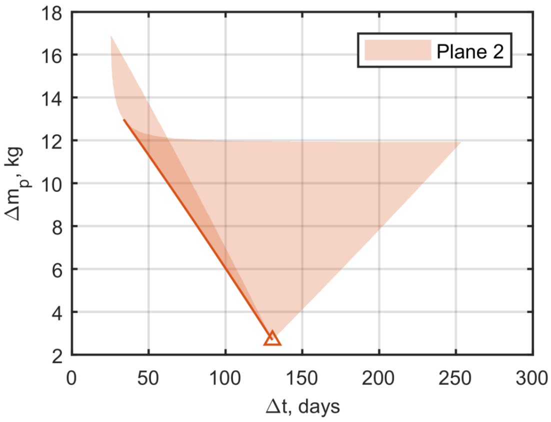

Figure 4.7: *Time and fuel consumption for the RAAN separation of a single OneWeb-like satellite, considering $0 \leq \gamma \leq 1$ and $5 \text{ deg} \leq \eta \leq 90$ deg.*

Let us suppose that 5% of the initial spacecraft mass is reserved for the RAAN separation of a single satellite, i.e. $(\Delta m_p)_{\text{req}} = 7.5$ kg. Given such a fuel consumption requirement, the optimal design variables that minimise the time for RAAN separation can be obtained from Eq. (4.49). Then the optimal times allocated to phase 1 and phase 3 can be determined using Eq. (4.39) and Eq. (4.41). These optimal results are reported in Table 4.8.

Table 4.8: *Optimal results for the minimum-time RAAN separation of a single OneWeb-like satellite.*

Plane	γ^*	η^*, rad	Δt_1, days	Δt_3, days	Δt, days
2	0.4579	0.8246	68.56	13.76	86.34

Compared to the J_2-only strategy, the fuel consumption using the J_2-thrust strategy is increased by 3.872 kg per satellite, but the RAAN separation can be completed 44.15 days earlier, which means that the revenue flow can start earlier by approximately 1.5 months. This implies the need of a trade-off between the revenue of a quicker deployment and the cost of higher fuel consumption.

Figs. 4.8 (a) – (c) show the time histories of $\dot{\Omega}$, $\dot{u}$, and h for the entire deployment, including also the AoL separation, where $h = a - R_{\oplus}$. For clarity, only three satellites are presented: the reference satellite, the 25th satellite in the first plane and the 23rd satellite in the second plane. As shown in the figures, both $\dot{\Omega}$ and $\dot{u}$ vary with a, and the sudden change in $\dot{\Omega}$ is caused by the use of the intermittent yaw thrusting. In Fig. 4.8 (c), the semi-major axis is modified after reaching the final orbit to induce the AoL separation, where the semi-major axis of the coasting orbit and the times allocated to the three subphases of the AoL separation can be rapidly determined using the analytical method presented in Sec. 4.4.

Figs. 4.9 (a) and (b) show the errors of the final separation in the RAAN and AoL relative to the desired values for all the 80 satellites. As indicated in the figures, the AoL separation can be accurately fulfilled, while due to the interaction between RAAN and AoL [34] in phase 4, the final separation in the RAAN deviates a bit from the desired values.

Finally, comparisons with the numerical results by integrating the exact dynamics model Eqs. (4.4) are performed to validate the accuracy of the analytical solutions derived in Sec. 4.2. Figs. 4.10 (a) – (e) show the time histories of a, i, Ω, u, and m, taking as example the 23rd satellite in the second plane. Good agreement can be seen between the analytical and numerical results. Note that the variation in i of the numerical results is due to the short-term oscillations when applying the intermittent yaw thrusting, but the net effect on i is nearly null.

4.5.2 Sun-Synchronous Constellation Deployment

Mission Scenario

A sun-synchronous constellation with retrograde orbits is considered. It has the same configuration as the OneWeb-like constellation but at different altitude and inclination of 959.889 km and 99.3 deg, respectively. Table 4.9 gives the geometrical information of the sun-synchronous constellation.

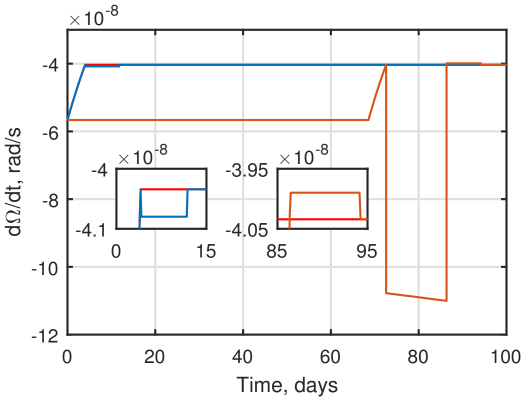

(a) Time history of $\dot{\Omega}$.

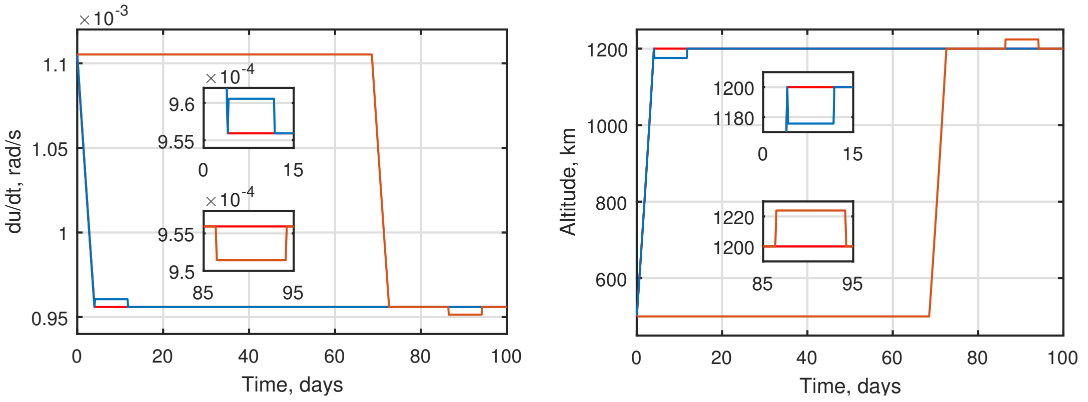

(b) Time history of $\dot{u}$.

(c) Time history of h.

Figure 4.8: *Deployment profiles (red: reference satellite, blue: satellite 25 in plane 1, orange: satellite 23 in plane 2), with magnification indicating the profiles of phase 4.*

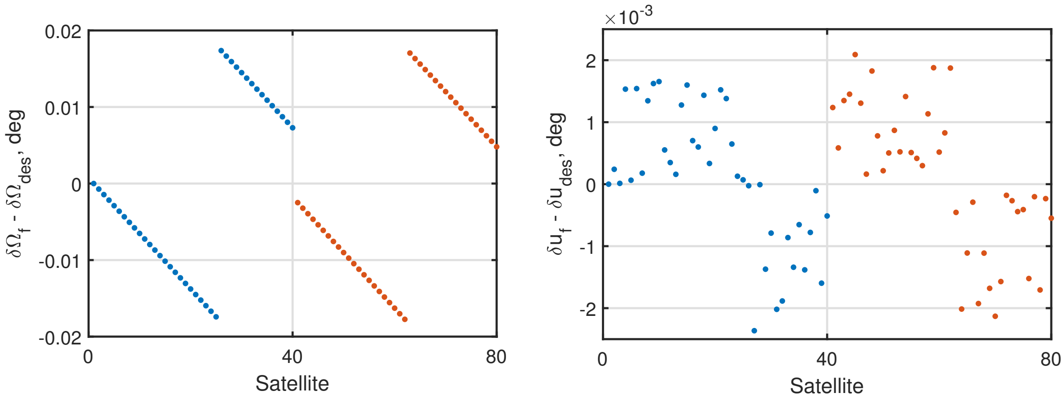

(a) Final errors of the RAAN separation.

(b) Final errors of the AoL separation.

Figure 4.9: *Final errors for the deployment of 80 OneWeb-like satellite (blue: plane 1, orange: plane 2).*

In this case study we assume that the initial spacecraft mass of the sun-synchronous satellite is 50 kg, that is, one third of the OneWeb-like satellite,

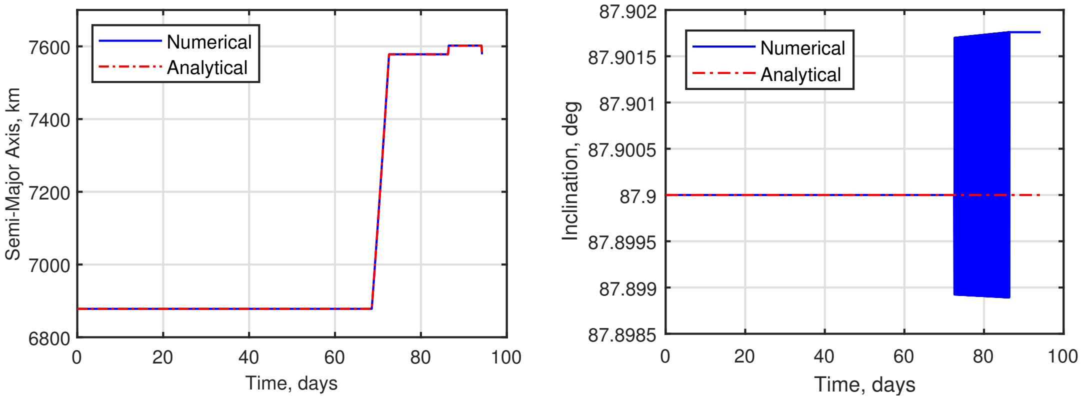

(a) Time history of a. (b) Time history of i.

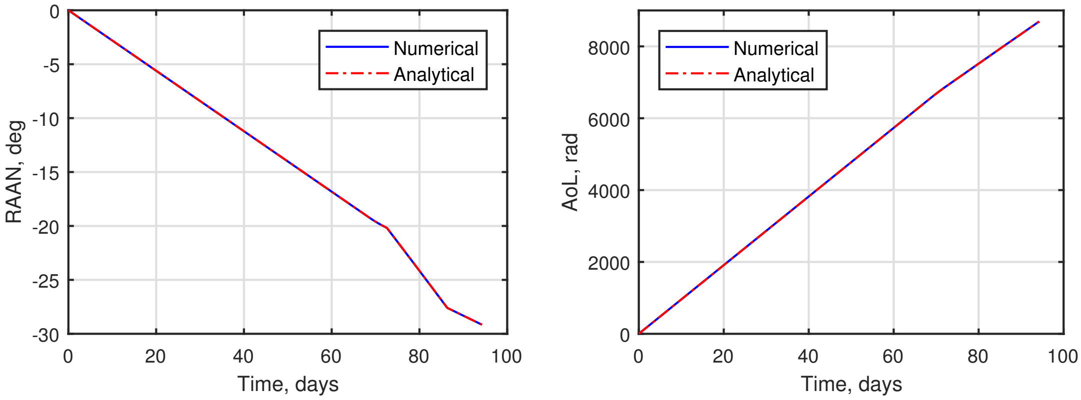

(c) Time history of Ω. (d) Time history of u.

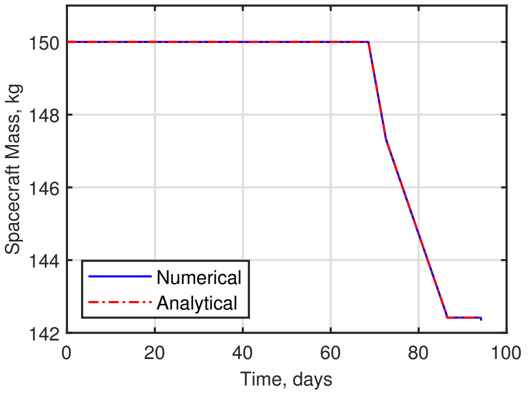

(e) Time history of m.

Figure 4.10: *Validation of the analytical solutions (dashed line) versus the numerical results (solid line), for satellite 23 in plane 2.*

such that 240 satellites can be deployed into six planes by each launch, if using the same launcher as the OneWeb-like constellation. Fig. 4.11 shows the desired separation in the RAAN and AoL, where the reference satellite is the first one in the first plane.

Table 4.10 presents the simulation parameters for the case study of the sun-synchronous constellation, where it is assumed that all the 240 satellites are

Table 4.9: *Geometrical information of the sun-synchronous constellation.*

Parameter	Symbol	Value	Unit
Number of satellites	N	720	
Number of orbital planes	P	18	
Number of satellites per orbital plane	S	40	
Inclination	i	99.3	deg
Altitude	h	959.889	km
RAAN spacing	$\delta\Omega$	10.2	deg
Intra-plane AoL spacing	δu_{intra}	9	deg
Inter-plane AoL spacing	δu_{inter}	4.5	deg

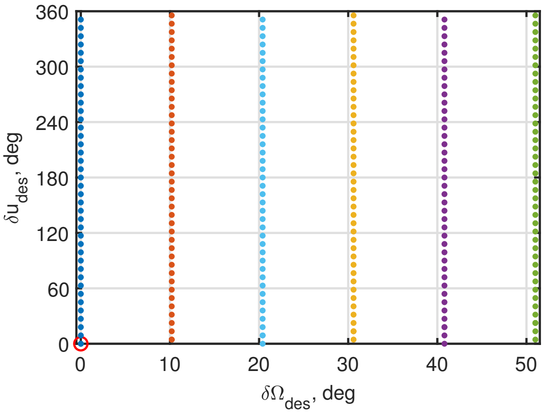

Figure 4.11: *Desired separation in the RAAN and AoL for 240 sun-synchronous satellites deployed into six planes (blue: plane 1, orange: plane 2, light blue: plane 3, yellow: plane 4, purple: plane 5, green: plane 6).*

launched into a 759.889-km-high parking orbit and are initially separated from each other by an along-track distance of 200 km, which is equivalent to an initial AoL separation of 1.605 deg.

Table 4.10: *Simulation parameters for the sun-synchronous constellation.*

Parameter	Symbol	Value	Unit
Initial semi-major axis	a_0	$R_\oplus + 759.889$	km
Final semi-major axis	a_f	$R_\oplus + 959.889$	km
Inclination	i	99.3	deg
Initial AoL separation between adjacent satellites	δu_0	1.605	deg
Desired separation in the RAAN and AoL	$\delta\Omega_{\text{des}}$, δu_{des}	Fig. 4.11	deg
Initial spacecraft mass	m_0	50	kg
Thrust	F	154	mN
Specific impulse	I_{sp}	2035	s
Mass flow rate	$\dot{m}$	-7.7168×10^{-06}	kg/s
Number of revolutions in the coasting orbit	χ	100	

Minimum-Fuel RAAN Separation with Time Requirement

In this case study we will present a minimum-fuel RAAN separation given a time requirement, for the purpose of reducing the propellant budget as much as possible with a limited time budget. Note that satellites in the first plane will directly reach the final orbit together with the reference satellite, so the following analysis of the RAAN separation is performed for the second to sixth planes.

Table 4.11 presents the constant parameters that will be used in the subsequent computation, where Δt_2 and $(m_2)_f$ are obtained from Eq. (4.33) and Eq. (4.35), c_1, c_2, and c_3 are obtained from Eq. (4.44).

Table 4.11: *Constant parameters for the sun-synchronous constellation.*

Parameter	Symbol	Value	Unit
Time of phase 2	Δt_2	0.38	days
Spacecraft mass at the end of phase 2	$(m_2)_f$	49.744	kg
Mission related parameter	c_1	4.9451×10^7	s
Mission related parameter	c_2	$-2.0356e \times 10^5$	s/kg
Mission related parameter	c_3	-0.3645	

With Eq. (4.42) and Eq. (4.43), the mapping from the design variable space to the objective space can be performed. Fig. 4.12 shows the time and fuel consumption for the RAAN separation of a single satellite, considering $0 \leq \gamma \leq 1$ and 5 deg $\leq \eta \leq 90$ deg, where the shadowed areas with different colours indicate the objective spaces of separate planes. In the figure, the Pareto-optimal time and fuel consumption are highlighted by the solid lines, and the triangles indicate the time and fuel consumption corresponding to the J_2-only strategy. For the J_2-only strategy, the fuel consumption is at a very low level of 0.256 kg, but the total time to separate all the six planes is 1.4 years, which is a significant period of time for small satellites whose lifetime is around five years.

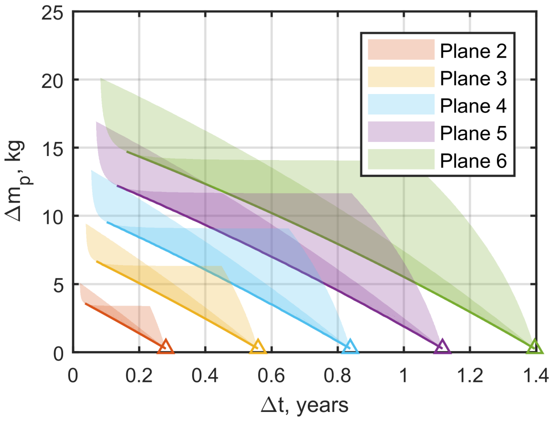

Figure 4.12: *Time and fuel consumption for the RAAN separation of a single sun-synchronous satellite, considering $0 \leq \gamma \leq 1$ and 5 deg $\leq \eta \leq 90$ deg.*

Let us suppose that the RAAN separation must be completed in 0.5 years, i.e., $\Delta t_{\text{req}} = 0.5$ years. From Fig. 4.12, the second plane can still use the J_2-only strategy, while the third to sixth planes will have to use the J_2-thrust strategy. Given such a time requirement, the optimal design variables that can minimise the fuel consumption for RAAN separation can be obtained from Eq. (4.48). Then the optimal times allocated to phase 1 and phase 3 can be determined using Eq. (4.39) and Eq. (4.41). These optimal results are reported in Table 4.12.

Compared to the J_2-only strategy, the fuel consumption using the J_2-thrust

Table 4.12: *Optimal results for the minimum-fuel RAAN separation of a single sun-synchronous satellite.*

Plane	γ^*	η^*, rad	Δt_1, days	Δt_3, days	Δm_p, kg
3	0.1213	0.6132	179.06	3.18	1.084
4	0.4616	0.6051	164.59	17.65	4.790
5	0.6296	0.5972	150.98	31.26	8.180
6	0.7288	0.5897	138.17	44.07	11.287

strategy is increased by 1.084 kg, 4.534 kg, 7.924 kg, and 11.287 kg for a single satellite in the third, fourth, fifth, and sixth planes, respectively; although a bit high, they are the optimal solutions yet for such a high-demanding time requirement.

Figs. 4.13 (a) – (c) show the time histories of $\dot{\Omega}$, $\dot{\omega}$, and h for the entire deployment, including also the AoL separation, where $h = a - R_\oplus$. For clarity, only five satellites are presented: the reference satellite, the second satellite in the first plane, the 34th satellite in the fourth plane, the 10th satellite in the fifth plane, and the first satellite in the sixth plane. As shown in the figures, both $\dot{\Omega}$ and $\dot{u}$ vary with a, and the sudden change in $\dot{\Omega}$ is caused by the use of the intermittent yaw thrusting. In Fig. 4.13 (c), the semi-major axis is modified after reaching the final orbit in order to induce the AoL separation, where the semi-major axis of the coasting orbit and the times allocated to the three subphases of the AoL separation can be rapidly determined using the analytical method presented in Sec. 4.4.

Figs. 4.14 (a) and (b) show the errors of the final separation in the RAAN and AoL relative to the desired values for all the 240 satellites. As indicated in the figures, the AoL separation can be accurately fulfilled, while due to the interaction between RAAN and AoL [34] in phase 4, the final separation in the RAAN deviates a bit from the desired values.

Finally, comparisons with the numerical results by integrating the exact dynamics model Eqs. (4.4) are performed to validate the accuracy of the analytical solutions derived in Sec. 4.2. Figs. 4.15 (a) – (e) show the time histories of a, i, Ω, u, and m, taking as example the first satellite in the sixth plane. Good agreement can be seen between the analytical and numerical results. Note that the variation in i of the numerical results is due to the short-term oscillations when applying the intermittent yaw thrusting, but the net effect on i is nearly null.

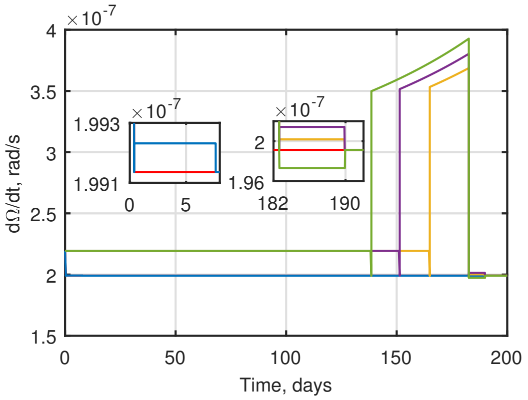

(a) Time history of $\dot{\Omega}$.

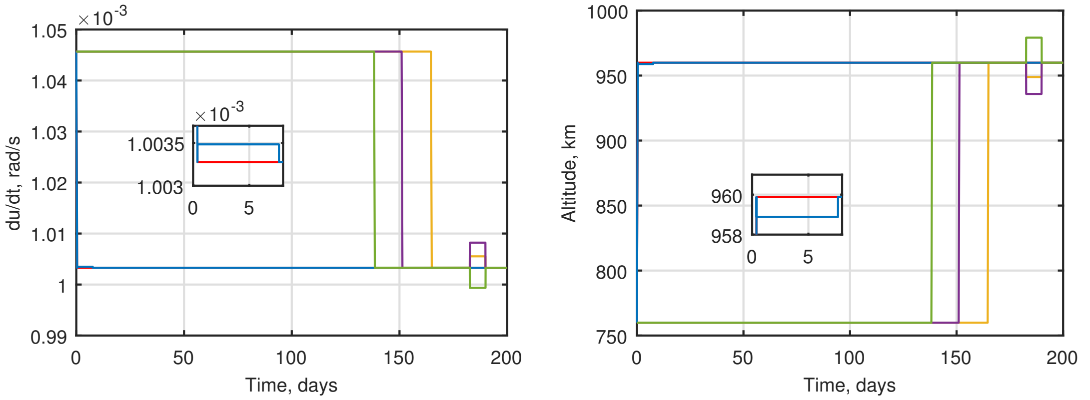

(b) Time history of $\dot{u}$.

(c) Time history of h.

Figure 4.13: *Deployment profiles (red: reference satellite, blue: satellite 2 in plane 1, yellow: satellite 34 in plane 4, purple: satellite 10 in plane 5, green: satellite 1 in plane 6), with magnification indicating the profiles of phase 4.*

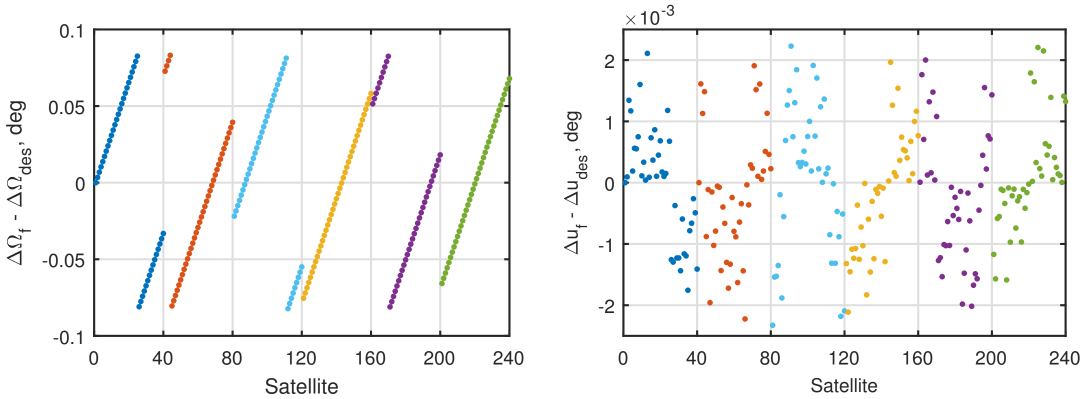

(a) Final errors of the RAAN separation.

(b) Final errors of the AoL separation.

Figure 4.14: *Final errors for the deployment of 240 sun-synchronous satellites (blue: plane 1, orange: plane 2, yellow: plane 3, light blue: plane 4, purple: plane 5, green: plane 6).*

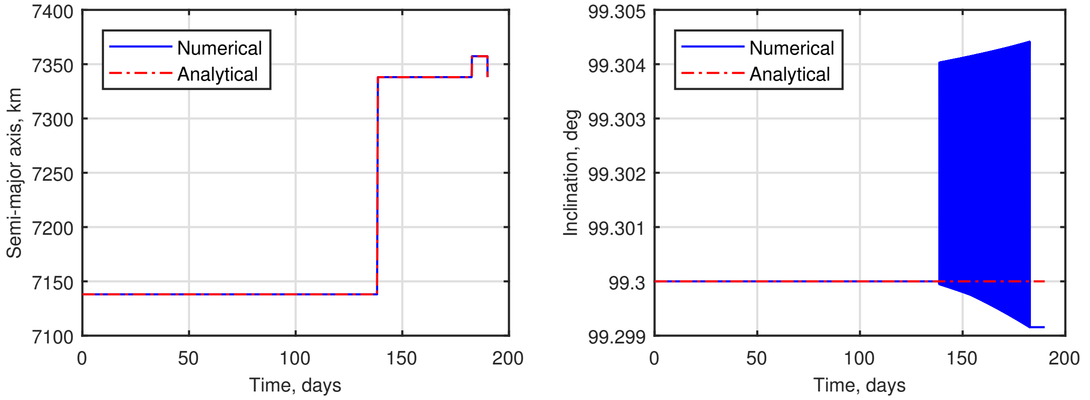

(a) Time history of a.

(b) Time history of i.

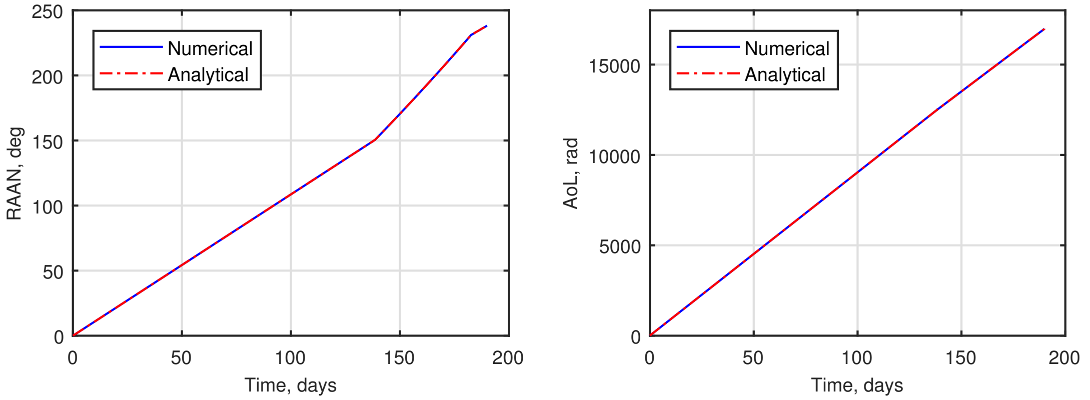

(c) Time history of Ω.

(d) Time history of u.

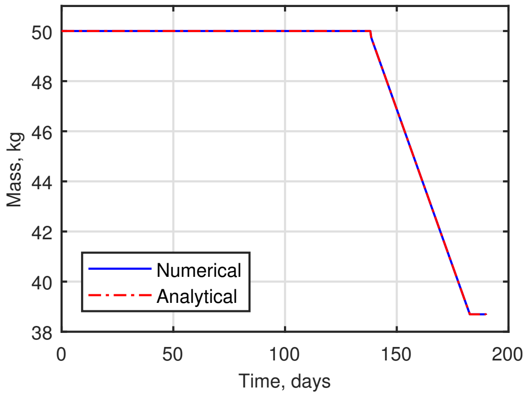

(e) Time history of m.

Figure 4.15: *Validation of the analytical solutions (dashed line) versus the numerical results (solid line), satellite 1 plane 6.*

CHAPTER 5

Low Earth Orbit Constellation Low-Thrust De-Orbiting Through Natural Perturbations

This chapter investigates the low-thrust de-orbiting through natural perturbations for LEO constellations. Two strategies that would be applicable to de-orbiting from LEO are considered. The first strategy uses the control thrust to lower the perigee altitude to achieve drag-induced re-entry. The second strategy uses the control thrust to reach a specific condition to then provoke natural orbital decay due to the coupled effect of the Earth oblateness and SRP. Two closed-loop control laws, one for each strategy, are developed by using the Lyapunov method. Given the control laws, maps that represent the Δv-budget and de-orbiting time for de-orbiting from any near-circular LEO using the two strategies can be obtained, based on which, the application conditions of the two strategies can be identified. In order to reduce the computational load of propagating the initial conditions over the entire LEO region, the averaged low-thrust dynamics models are firstly derived. Note that, as the scope of this chapter is LEO constellation, the eccentricity is therefore less than 0.2, and the inclination ranges between 30 deg and 120 deg, because most LEO constellations are located in this region.

5.1 Description of De-Orbiting Strategies

In this section, the two de-orbiting strategies, which are named as the perigee decrease strategy and the de-orbiting corridor strategy, will be introduced, and the terminal conditions of low-thrust transfer for these two strategies will be presented.

Briefly speaking, both strategies are aiming to lower the perigee altitude to achieve the drag-induced re-entry. However, in the perigee decrease strategy, the perigee altitude is actively lowered by the thrust, whereas in the de-orbiting corridor strategy, the perigee altitude is passively lowered by the coupled effect of natural perturbations with the aid of passive de-orbiting device, and the thrust is used to reach the de-orbiting corridor that can provoke a natural decrease in the perigee altitude. Fig. 5.1 gives the illustration of these two strategies.

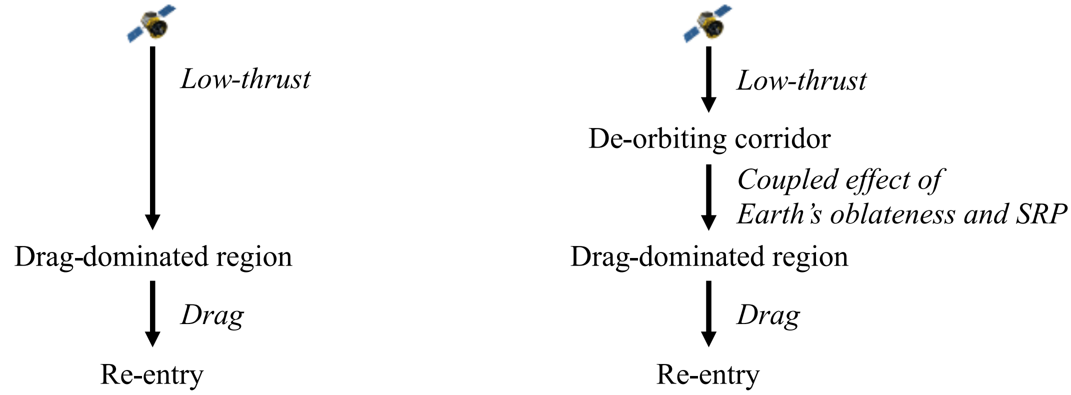

(a) Perigee decrease strategy.

(b) De-orbiting corridor strategy.

Figure 5.1: *Illustration of the de-orbiting strategies.*

5.1.1 Perigee Decrease Strategy

In the perigee decrease strategy, low-thrust manoeuvres will be performed to lower the perigee altitude to the drag-dominated region, after which the drag effect will be strong enough to lower the apogee altitude until re-entry happens [46]. Thus, the terminal condition of the low-thrust transfer for the perigee decrease strategy is given by

$$\psi^{\mathrm{str1}}\big|_{t=t_f} = r_p\big|_{t=t_f} - (h_{pf} + R_\oplus) = 0 \tag{5.1}$$

where r_p is the perigee radius and h_{pf} is the target perigee altitude. Generally speaking, the selection of h_{pf} depends on the area-to-mass ratio and required re-entry time; the smaller the area-to-mass ratio and the shorter the required re-entry time, the lower the target perigee altitude will be.

Considering the expression for r_p:

$$r_p = a\,(1 - e) \tag{5.2}$$

the terminal condition can be expressed in terms of the semi-major axis and eccentricity as

$$\psi^{\mathrm{str1}}\big|_{t=t_f} = a\,(1 - e)\,\big|_{t=t_f} - (h_{pf} + R_\oplus) = 0 \tag{5.3}$$

5.1.2 De-Orbiting Corridor Strategy

A mapping of the LEO region was obtained in Ref. [109], revealing the existence of specific initial conditions in semi-major axis, eccentricity, and inclination that can lead to orbital decay beyond the drag-dominated region. As a matter of fact, the decay, which lowers the perigee altitude, is caused by an increase in eccentricity. Such behaviour in the LEO region is mainly due to the coupled effect of the Earth oblateness and SRP, provided a large enough area-to-mass ratio. In principle, if the initial conditions for the decay are satisfied, then driven by the coupled effect, the natural decrease in the perigee altitude will either follow the libration curves or the hyperbolic curves associated with the hyperbolic equilibrium points [51, 110]. Hereinafter, the initial conditions that can provoke the natural decrease in the perigee altitude are referred to as the de-orbiting corridors [54].

As presented in Ref. [51], the location of the de-orbiting corridors can be approximated as a resonant condition which has six different forms

$$\dot{\Omega}_{J_2} \pm \dot{\omega}_{J_2} \pm n_S = 0, \quad \dot{\omega}_{J_2} \pm n_S = 0 \tag{5.4}$$

where $\dot{\Omega}_{J_2}$ and $\dot{\omega}_{J_2}$ are the time rates of change of Ω and ω, respectively, due to the secular effects of J_2, and $n_S \approx 2\pi/365.25$ rad/day is the apparent mean motion of the Sun measured on the ecliptic plane.

Replacing $\dot{\Omega}_{J_2}$ and $\dot{\omega}_{J_2}$ with Eq. (2.6b) and Eq. (2.6c), Eq. (5.4) can be expressed in terms of the semi-major axis, eccentricity, and inclination as

$$\frac{3\sqrt{\mu}J_2R_\oplus^2}{4a^{7/2}\left(1-e^2\right)^2}\left(5n_2\cos^2 i - 2n_1\cos i - n_2\right) + n_3 n_S = 0 \tag{5.5}$$

where $n_1 = (0,\ 1)$, $n_2 = \pm 1$, and $n_3 = \pm 1$ are the coefficients in front of $\dot{\Omega}_{J_2}$, $\dot{\omega}_{J_2}$, and n_S, respectively, that correspond to the six de-orbiting corridors. Fig. 5.2 shows the location of the six de-orbiting corridors as a function of a and i, assuming $e = 0.001$.

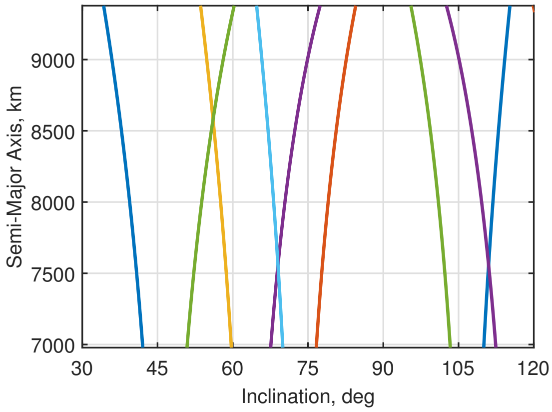

Figure 5.2: *Location of the six de-orbiting corridors, assuming e = 0.001 (blue: $\dot{\Omega}_{J_2} + \dot{\omega}_{J_2} - n_S = 0$, orange: $\dot{\Omega}_{J_2} - \dot{\omega}_{J_2} - n_S = 0$, yellow: $\dot{\omega}_{J_2} - n_S = 0$, purple: $\dot{\omega}_{J_2} + n_S = 0$, green: $\dot{\Omega}_{J_2} + \dot{\omega}_{J_2} + n_S = 0$, light blue: $\dot{\Omega}_{J_2} - \dot{\omega}_{J_2} + n_S = 0$).*

In the de-orbiting corridor strategy, low-thrust manoeuvres will be performed to move the spacecraft towards the closest de-orbiting corridor, and then the passive de-orbiting device, such as solar sail or de-orbiting balloon, will be deployed to artificially increase the area-to-mass ratio to enhance the subsequent natural decrease in the perigee altitude. Thus, the terminal condition of the low-thrust transfer for the de-orbiting corridor strategy is given by

$$\psi^{\text{str2}}\big|_{t=t_f} = \frac{3\sqrt{\mu}J_2R_\oplus^2}{4a^{7/2}\left(1-e^2\right)^2}\left(5n_2\cos^2 i - 2n_1\cos i - n_2\right)\big|_{t=t_f} + n_3 n_S = 0 \tag{5.6}$$

5.2 Control Law Design

In this section, two closed-loop control laws will be developed for the two de-orbiting strategies by using the Lyapunov method, and the stability analyses of the control laws will be presented.

5.2.1 Perigee Decrease Strategy

For the perigee decrease strategy aiming to decrease the perigee altitude, the candidate Lyapunov function is defined as

$$\begin{aligned} V^{\mathrm{str1}} &= \psi^{\mathrm{str1}} \\ &= a\,(1-e) - (h_{pf} + R_{\oplus}) \end{aligned} \tag{5.7}$$

The time rate of change of V^{str1} is

$$\frac{\mathrm{d}V^{\mathrm{str1}}}{\mathrm{d}t} = (1-e)\,\frac{\mathrm{d}a}{\mathrm{d}t} - a\frac{\mathrm{d}e}{\mathrm{d}t} \tag{5.8}$$

Because $\dot{a}$ and $\dot{e}$ are governed by the in-plane thrust components f_r and f_θ, only the in-plane control law for the pitch angle α is to be developed, while the yaw angle β is zero; the definition of the pitch and yaw angles are shown in Fig. 2.3. Thus, the thrust components of the perigee decrease strategy are given in the form of

$$\begin{aligned} f_r^{\mathrm{str1}} &= f\sin\alpha \\ f_\theta^{\mathrm{str1}} &= f\cos\alpha \\ f_h^{\mathrm{str1}} &= 0 \end{aligned} \tag{5.9}$$

Then substituting Eq. (2.5a) and Eq. (2.5b) into Eq. (5.8) and replacing the thrust components with Eq. (5.9), $\dot{V}^{\mathrm{str1}}$ becomes

$$\dot{V}^{\mathrm{str1}} = f\sqrt{\frac{\mu}{a^3}}\frac{1}{1-e\cos E}\left(p_\alpha\sin\alpha + q_\alpha\cos\alpha\right) \tag{5.10}$$

where

$$\begin{aligned} p_\alpha &= -\left(1-e\right)^2\sin E \\ q_\alpha &= \sqrt{1-e^2}\left[2\left(1-\cos E\right) - e\sin^2 E\right] \end{aligned} \tag{5.11}$$

It is clear from the definition of the candidate Lyapunov function in Eq. (5.7) that for an initially near-circular orbit whose initial altitude is higher than the target perigee altitude, V^{str1} is zero at the final state and positive elsewhere. Thus, the goal of low-thrust transfer is to drive V^{str1} to zero. In this study we choose the pitch angle that minimises V^{str1} at the fastest rate to make V^{str1} being sent to zero as quickly as possible at any instant. By solving

$$\begin{cases} \partial\ \dot{V}^{\mathrm{str1}}/\partial\alpha \ = 0 \\ \partial^2\dot{V}^{\mathrm{str1}}/\partial\alpha^2 \geq 0 \end{cases} \tag{5.12}$$

the in-plane control law that minimises $\dot{V}^{\mathrm{str1}}$ can be obtained:

$$\sin\alpha = -\frac{p_\alpha}{\sqrt{p_\alpha^2+q_\alpha^2}}, \qquad \cos\alpha = -\frac{q_\alpha}{\sqrt{p_\alpha^2+q_\alpha^2}} \tag{5.13}$$

where p_α and q_α are given in Eq. (5.11). Fig. 5.3 shows α as a function of e and E. As indicated in the figure, the influence of low values of eccentricities on the pitch angle is small.

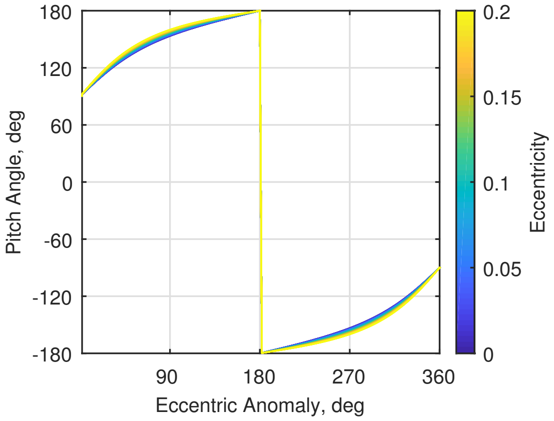

Figure 5.3: *Pitch angle in Eq. (5.13).*

Based on the sensitivity analysis, let us modify Eq. (5.13) by setting $e = 0$, and there is

$$\sin\alpha = \frac{\sin E}{\sqrt{\sin^2 E + 4\left(1-\cos E\right)^2}}, \qquad \cos\alpha = -\frac{2\left(1-\cos E\right)}{\sqrt{\sin^2 E + 4\left(1-\cos E\right)^2}} \tag{5.14}$$

With this control law, the rates of change of orbital elements with E can be analytically integrated, as presented in Sec. 5.3.1, thus making it possible to derived the averaged dynamics model. Substituting Eq. (5.14) into Eq. (5.9), the thrust components of the perigee decrease strategy are finally given as

$$\begin{aligned} f_r^{\mathrm{str1}} &= f\frac{\sin E}{\sqrt{\sin^2 E + 4\left(1-\cos E\right)^2}} \\ f_\theta^{\mathrm{str1}} &= -f\frac{2\left(1-\cos E\right)}{\sqrt{\sin^2 E + 4\left(1-\cos E\right)^2}} \\ f_h^{\mathrm{str1}} &= 0 \end{aligned} \tag{5.15}$$

Proposition 1: Let a satellite be in the LEO region where 30 deg $\leq i \leq$ 120 deg and $e \leq 0.2$. Using the control law Eq. (5.15), all solutions governed by the dynamics model Eq. (2.5) converge to any predefined target perigee altitude h_{pf}.

Proof: Substituting Eq. (5.14) into Eq. (5.10) yields

$$\dot{V}^{\mathrm{str1}} = -f\sqrt{\frac{\mu}{a^3}}\frac{1}{1-e\cos E}\frac{-p_\alpha \sin E + 2q_\alpha\left(1-\cos E\right)}{\sqrt{\sin^2 E + 4\left(1-\cos E\right)^2}}$$

In the preceding equation, the low-thrust acceleration $f > 0$, and there are

$$\sqrt{\frac{\mu}{a^3}}\frac{1}{1-e\cos E} > 0, \qquad \sqrt{\sin^2 E + 4\left(1-\cos E\right)^2} \geq 0$$

Replacing p_α and q_α with Eq. (5.11) gives

$$\begin{gathered}-p_\alpha \sin E + 2q_\alpha (1-\cos E) = \\ (1-e)^2 \sin^2 E + 2\sqrt{1-e^2}\,(1-\cos E)\left[2(1-e\cos E) - e\sin^2 E\right] \geq 0\end{gathered}$$

because

$$2(1-e\cos E) - e\sin^2 E = 2(1-e) + e(1-\cos E)^2 > 0$$

Thus, $\dot{V}^{\text{str1}} \leq 0$, where the equal sign does not hold indefinitely as E changes over time. So V^{str1} always converges to zero. □

5.2.2 De-orbiting Corridor Strategy

For the de-orbiting corridor strategy aiming to reach the target de-orbiting corridor, the candidate Lyapunov function is defined as

$$\begin{aligned}V^{\text{str2}} &= \left(\psi^{\text{str2}}\right)^2 \\ &= \left[\frac{3\sqrt{\mu}J_2R_\oplus^2}{4a^{7/2}\left(1-e^2\right)^2}\left(5n_2\cos^2 i - 2n_1\cos i - n_2\right) + n_3 n_S\right]^2\end{aligned} \tag{5.16}$$

The time rate of change of V^{str2} is

$$\frac{\mathrm{d}V^{\text{str2}}}{\mathrm{d}t} = \psi^{\text{str2}}\frac{3\sqrt{\mu}J_2R_\oplus^2}{4a^{9/2}\left(1-e^2\right)^3}\left[\left(1-e^2\right)c_a\frac{\mathrm{d}a}{\mathrm{d}t} + 2aec_e\frac{\mathrm{d}e}{\mathrm{d}t} + 2a\left(1-e^2\right)c_i\frac{\mathrm{d}i}{\mathrm{d}t}\right] \tag{5.17}$$

where c_a, c_e, and c_i are functions of i:

$$\begin{aligned}c_a &= -7\left(5n_2\cos^2 i - 2n_1\cos i - n_2\right) \\ c_e &= 4\left(5n_2\cos^2 i - 2n_1\cos i - n_2\right) \\ c_i &= 2n_1\sin i - 5n_2\sin 2i\end{aligned} \tag{5.18}$$

The control law design is conducted via two steps. The first step is selecting a proper in-plane control law which can efficiently change a. The second step is developing an out-of-plane control law to drive i, together with a and e, to reach the terminal condition as quickly as possible.

As presented in Sec. 2.4, two types of control laws can efficiently change a: the tangential thrusting and the transversal thrusting. Substituting Eq. (2.10) and Eq. (2.11) into Eq. (2.5a), the time rates of change of a due to the tangential and transversal thrusting are respectively given by

$$\dot{a}_{\tan} = \pm 2f\sqrt{\frac{a^3}{\mu}}\frac{1}{1-e\cos E}\sqrt{1-e^2\cos^2 E} \tag{5.19a}$$

$$\dot{a}_{\text{tra}} = \pm 2f\sqrt{\frac{a^3}{\mu}}\frac{1}{1-e\cos E}\sqrt{1-e^2} \tag{5.19b}$$

where the sign + and − represent the cases of semi-major increase and decrease, respectively.

In this study we adopt the transversal thrusting for the following reasons.

- If irrespective of the out-of-plane control law, the efficiency to change a with these two types of thrusting is almost the same for small e. From Eq. (5.19), the ratio of $\dot{a}$
$$\dot{a}_{\text{tra}}/\dot{a}_{\tan} = \sqrt{\left(1-e^2\right)/\left(1-e^2\cos^2 E\right)} \tag{5.20}$$
is greater than 0.9798 for $e \leq 0.2$.
- Compared to the tangential thrusting, the dynamics model governed by the transversal thrusting is in a simpler fashion, making it easier to carry out the analytical integration for orbital elements when employing the orbital averaging technique in Sec. 5.3.

When the transversal thrusting serves as the in-plane control law, the thrust direction projected on the orbital plane is perpendicular to the orbital radius vector, and there is

$$\sin\alpha = 0, \quad \cos\alpha = 1 \tag{5.21}$$

So the thrust components of the de-orbiting corridor strategy can be written in the form of

$$\begin{aligned} f_r^{\text{str2}} &= 0 \\ f_\theta^{\text{str2}} &= f\cos\beta \\ f_h^{\text{str2}} &= f\sin\beta \end{aligned} \tag{5.22}$$

By substituting Eqs. (2.5a), (2.5b), and (2.5c) into Eq. (5.17) and replacing the thrust components with Eq. (5.22), $\dot{V}^{\text{str2}}$ becomes

$$\dot{V}^{\text{str2}} = \psi^{\text{str2}} f \frac{3J_2R_\oplus^2}{2a^3\left(1-e^2\right)^{5/2}}\left(q_\beta\cos\beta + p_\beta\sin\beta\right) \tag{5.23}$$

where

$$\begin{aligned} q_\beta &= \frac{c_a\left(1-e^2\right) + c_e e\left(2\cos E - e - e\cos^2 E\right)}{1-e\cos E} \\ p_\beta &= c_i\left[\left(\cos E - e\right)\cos\omega - \sqrt{1-e^2}\sin E\sin\omega\right] \end{aligned} \tag{5.24}$$

It is clear from the definition of the candidate Lyapunov function in Eq. (5.16) that V^{str2} is zero at the final state and positive elsewhere. Thus, the goal of low-thrust transfer is to drive V^{str2} to zero. In this study we choose the yaw angle that minimises V^{str2} at the fastest rate to make V^{str2} being sent to zero as quickly as possible at any instant. By solving

$$\begin{cases} \partial\ \dot{V}^{\text{str2}}/\partial\beta &= 0 \\ \partial^2\dot{V}^{\text{str2}}/\partial\beta^2 &\geq 0 \end{cases} \tag{5.25}$$

the out-of-plane control law that minimises $\dot{V}^{\text{str2}}$ can be obtained:

$$\cos\beta = -\frac{\text{sgn}_{\psi^{\text{str2}}} q_\beta}{\sqrt{q_\beta^2 + p_\beta^2}}, \quad \sin\beta = -\frac{\text{sgn}_{\psi^{\text{str2}}} p_\beta}{\sqrt{q_\beta^2 + p_\beta^2}} \tag{5.26}$$

where q_β and p_β are given in Eq. (5.24), and $\text{sgn}_{\psi^{\text{str2}}}$ returns the sign of ψ^{str2}, with ψ^{str2} given in Eq. (5.6). Fig. 5.4 shows β as a function of e and $(\omega + E)$ (i.e. the latitude of eccentric anomaly) for different values of ω, assuming $i = 87.9$ deg. As

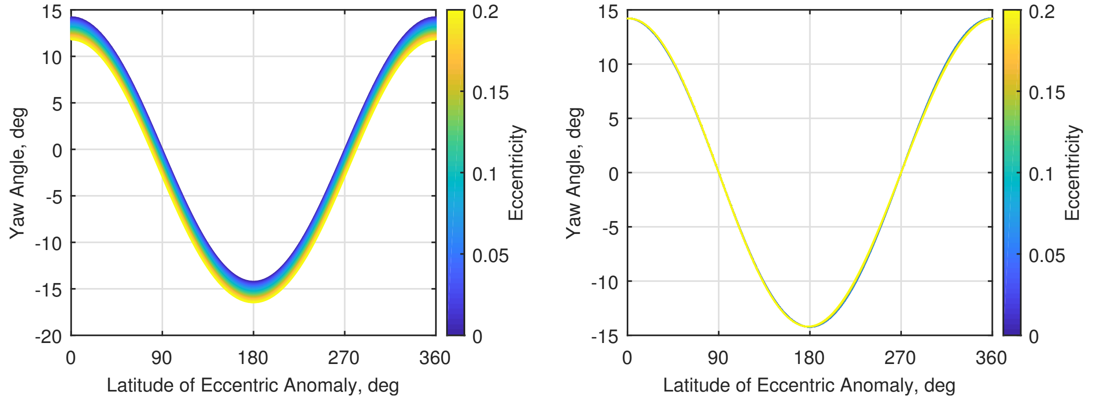

(a) $\omega = 0$ deg. (b) $\omega = 90$ deg.

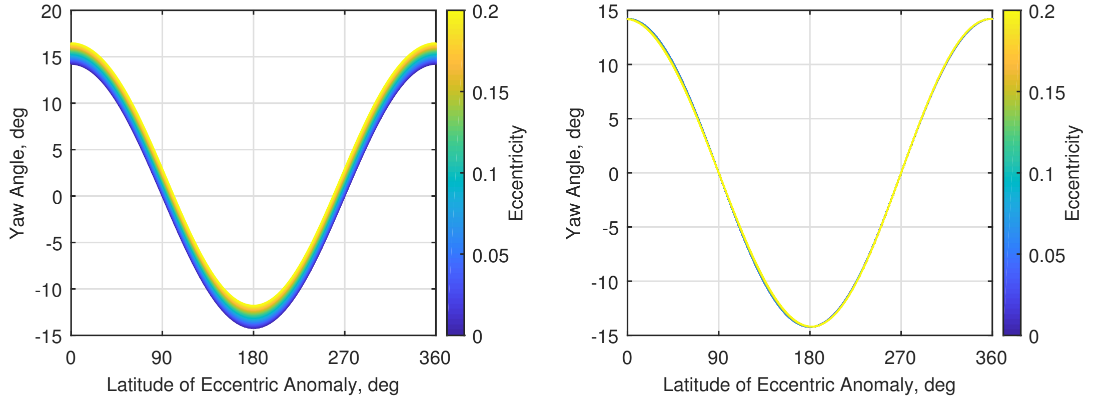

(c) $\omega = 180$ deg. (d) $\omega = 270$ deg.

Figure 5.4: *Yaw angle in Eq. (5.26), assuming $i = 87.9$ deg.*

indicated in the figure, the influence of low values of eccentricities on the yaw angle is small; the similar phenomenon can be observed if changing the inclination.

Based on the sensitivity analysis, let us modify Eq. (5.26) by setting $e = 0$, and there is

$$\cos\beta = -\frac{\mathrm{sgn}_{\psi^{\mathrm{str2}}} c_a}{\sqrt{c_a^2 + c_i^2 \cos^2(\omega + E)}}, \quad \sin\beta = -\frac{\mathrm{sgn}_{\psi^{\mathrm{str2}}} c_i \cos(\omega + E)}{\sqrt{c_a^2 + c_i^2 \cos^2(\omega + E)}} \tag{5.27}$$

Substituting Eq. (5.27) into Eq. (5.22), the thrust components of the de-orbiting corridor strategy are finally given as

$$\begin{aligned} f_r^{\mathrm{str2}} &= 0 \\ f_\theta^{\mathrm{str2}} &= -\mathrm{sgn}_{\psi^{\mathrm{str2}}} f \frac{c_a}{\sqrt{c_a^2 + c_i^2 \cos^2(\omega + E)}} \\ f_h^{\mathrm{str2}} &= -\mathrm{sgn}_{\psi^{\mathrm{str2}}} f \frac{c_i \cos(\omega + E)}{\sqrt{c_a^2 + c_i^2 \cos^2(\omega + E)}} \end{aligned} \tag{5.28}$$

Proposition 2: Let a satellite be in the LEO region where 30 deg $\leq i \leq$ 120 deg and $e \leq 0.2$. Using the control law Eq. (5.28), all solutions governed by the dynamics model Eq. (2.5) converge to any predefined target de-orbiting corridor.

Proof: Substituting Eq. (5.27) into Eq. (5.23) yields

$$\dot{V}^{\mathrm{str2}} = -\mathrm{sgn}_{\psi^{\mathrm{str2}}}\psi^{\mathrm{str2}} f \frac{3J_2R_\oplus^2}{2a^3\left(1-e^2\right)^{5/2}} \frac{q_\beta c_a + p_\beta c_i \cos\left(\omega+E\right)}{\sqrt{c_a^2+c_i^2\cos^2\left(\omega+E\right)}}$$

In the preceding equation, $\mathrm{sgn}_{\mathrm{str2}}\psi^{\mathrm{str2}}$ is zero at the final state and positive elsewhere, the low-thrust acceleration $f > 0$, and there are

$$\frac{3J_2R_\oplus^2}{2a^3\left(1-e^2\right)^{5/2}} > 0, \qquad \sqrt{c_a^2+c_i^2\cos^2\left(\omega+E\right)} \geq 0$$

where the equal sign in the latter term holds only if both c_a and $\cos\left(\omega+E\right)$ are zero; however, $\cos\left(\omega+E\right)$ does not stay at zero indefinitely as E changes over time.

It is observed from Eq. (5.18) that $c_e = -(4/7)c_a$. Then using this relationship and replacing q_β and p_β with Eq. (5.24), after some manipulations, gives

$$q_\beta c_a + p_\beta c_i \cos\left(\omega+E\right) = c_a^2\sigma + c_i^2\varsigma$$

where

$$\sigma = \frac{3\left(1-e^2\right)+4\left(1-e\cos E\right)^2}{7\left(1-e\cos E\right)}$$

$$\varsigma = \left[\left(\cos E - e\right)\cos\omega - \sqrt{1-e^2}\sin E\sin\omega\right]\cos\left(\omega+E\right)$$

Thus, to show that V^{str2} always converges to zero, it is necessary to show that

$$\begin{cases} \sigma + \dfrac{c_i^2}{c_a^2}\varsigma \geq 0 \text{ for } e \leq 0.2, & \text{if } c_a \neq 0 \\ \qquad c_i^2\varsigma \geq 0 \text{ for } e \leq 0.2, & \text{if } c_a = 0 \end{cases}$$

where the equal sign does not hold indefinitely.

For σ, there are the following partial derivatives:

$$\frac{\partial\sigma}{\partial E} = \frac{e}{7}\left[4 - \frac{3\left(1-e^2\right)}{\left(1-e\cos E\right)^2}\right]\sin E$$

$$\frac{\partial^2\sigma}{\partial E^2} = \frac{e}{7}\left[4\cos E - \frac{3\left(1-e^2\right)\cos E}{\left(1-e\cos E\right)^2} + \frac{6e\left(1-e^2\right)\sin^2 E}{\left(1-e\cos E\right)^3}\right]$$

By solving

$$\begin{cases} \partial\ \sigma/\partial E &= 0 \\ \partial^2\sigma/\partial E^2 &\geq 0 \end{cases}$$

we can get E that minimises σ for any e, given in the form of

$$\cos E = \frac{2-\sqrt{3\left(1-e^2\right)}}{2e}$$

Substituting the preceding equation into the expression of σ yields

$$\min_E \sigma = \frac{4\sqrt{3(1-e^2)}}{7}$$

which monotonically decreases with e, and therefore

$$\sigma_{\min} = \min_{e,\ E} \sigma = 0.9697 \text{ for } e \leq 0.2$$

For ς, there are the following partial derivatives:

$$\begin{aligned}
\frac{\partial \varsigma}{\partial \omega} &= \frac{1}{2}\left[(\sqrt{1-e^2}-1)\sin 2\omega - (\sqrt{1-e^2}+1)\sin(2\omega+2E) + 2e\sin(2\omega+E)\right] \\
\frac{\partial \varsigma}{\partial E} &= \left[(e-\cos E)\cos\omega + \sqrt{1-e^2}\sin\omega\sin E\right]\sin(\omega+E) \\
&\quad -(\cos\omega\sin E + \sqrt{1-e^2}\sin\omega\cos E)\cos(\omega+E) \\
\frac{\partial^2 \varsigma}{\partial\omega\partial E} &= e\cos(2\omega+E) - (1+\sqrt{1-e^2})\cos(2\omega+2E)
\end{aligned}$$

By solving

$$\begin{cases} \partial\ \varsigma/\partial\omega &= 0 \\ \partial\ \varsigma/\partial E &= 0 \\ \partial^2\varsigma/\partial\omega\partial E &\geq 0 \end{cases}$$

we can get ω and E that minimise ς for any e:

$$\omega = \frac{1}{2}\tan^{-1}\frac{\sqrt{1-e^2}}{e} + \frac{3\pi}{4}, \quad E = \frac{\pi}{2}$$

Substituting the preceding equation into the expression of ς yields

$$\min_{\omega,\ E} \varsigma = \frac{\sqrt{1-e^2}-1}{2}$$

which monotonically decreases with e, and therefore

$$\varsigma_{\min} = \min_{e,\ \omega,\ E} \varsigma = -0.0101 \text{ for } e \leq 0.2$$

For the case $c_a \neq 0$, because c_a and c_i are functions of i, we can compute the minimum value of c_i^2/c_a^2 for the six de-orbiting corridors, considering 30 deg $\leq i \leq$ 120 deg, as presented in Table 5.1. For all the de-orbiting corridors, there is

$$\sigma_{\min} + \left(\frac{c_i^2}{c_a^2}\right)_{\min} \varsigma_{\min} > 0 \text{ for } e \leq 0.2$$

Thus, V^{str2} always converges to zero if $c_a \neq 0$.

Table 5.1: *Minimum value of c_i^2/c_a^2 for 30 deg $\leq i \leq$ 120 deg.*

De-orbiting corridor	$(c_i^2/c_a^2)_{\min}$
$\dot{\Omega}_{J_2} + \dot{\omega}_{J_2} - n_S = 0$	0.1492
$\dot{\Omega}_{J_2} - \dot{\omega}_{J_2} - n_S = 0$	0.0601
$\dot{\omega}_{J_2} - n_S = 0$	0.0980
$\dot{\omega}_{J_2} + n_S = 0$	0.0980
$\dot{\Omega}_{J_2} + \dot{\omega}_{J_2} + n_S = 0$	0.1492
$\dot{\Omega}_{J_2} - \dot{\omega}_{J_2} + n_S = 0$	0.0601

For the case $c_a = 0$, because $\varsigma_{\min} < 0$, there is

$$(c_i^2)_{\min}\varsigma_{\min} \leq 0$$

Thus, V^{str2} cannot converge to zero if $c_a = 0$. For the six de-orbiting corridors, the values of i that result in a zero c_a are (in degrees): 46.378, 63.435, 73.148, 106.852, and 116.565. Therefore, to ensure that V^{str2} converges to zero, the initial inclination must be always specified to be outside of a small region surrounding these values. □

5.3 Averaged Low-Thrust Dynamics Model

In this section, the averaged low-thrust dynamics models governed by the proposed control laws will be derived by using the orbital averaging technique. It is of note that the application of orbital averaging is motivated by the need to reduce the computational load in Sec. 5.4.2, where a series of initial conditions over the whole LEO region, with a total number of $6,946$, will be propagated.

Let x denote any of the orbital elements to be averaged, i.e. $x \in (a,\ e,\ i,\ \Omega,\ \omega)$. Recalling the orbital averaging technique presented in Sec. 2.5, the averaged time rate of change of x can be derived by dividing the incremental change in x over one revolution by the orbit period $T = 2\pi/n$, i.e.:

$$\frac{\mathrm{d}\tilde{x}}{\mathrm{d}t} = \frac{n}{2\pi}\Delta x_{\text{rev}} \tag{5.29}$$

Supposing a burning arc from E_{on} to E_{off}, Δx_{rev} can be obtained by the means of

$$\Delta x_{\text{rev}} = \int_{E_{\text{on}}}^{E_{\text{off}}} \frac{\mathrm{d}x}{\mathrm{d}E}\mathrm{d}E = \text{fun}_x\left(E_{\text{off}}\right) - \text{fun}_x\left(E_{\text{on}}\right) \tag{5.30}$$

where fun_x is the primitive function of $\mathrm{d}x/\mathrm{d}E$ and will be presented later in Sec. 5.3.1 and Sec. 5.3.2 for the perigee decrease and de-orbiting-corridor strategies, respectively.

Analogously, the time rate of change of the spacecraft mass can also be averaged, given by [71]

$$\frac{\mathrm{d}\tilde{m}}{\mathrm{d}t} = -\dot{m}\frac{E_{\text{off}} - e\sin E_{\text{off}} - E_{\text{on}} + e\sin E_{\text{on}}}{2\pi} \tag{5.31}$$

recalling that $\dot{m}$ is the constant mass flow rate.

5.3.1 Perigee-Decrease Strategy

Substituting the control law Eq. (5.15) into the equations of motion Eqs. (2.5a) – (2.5e) and divided by $\dot{E}$ Eq. (2.5f), the rates of change of orbital elements with

E for the perigee decrease strategy are given by

$$
\begin{aligned}
&\left\{\left(\frac{\mathrm{d}a}{\mathrm{d}E}\right)^{\mathrm{str1}}, \left(\frac{\mathrm{d}e}{\mathrm{d}E}\right)^{\mathrm{str1}}, \left(\frac{\mathrm{d}\omega}{\mathrm{d}E}\right)^{\mathrm{str1}}\right\}^{\top} \\
=&\frac{f}{\sqrt{\sin^2 E + 4\left(1-\cos E\right)^2}} \\
&\left\{\begin{array}{c}
\dfrac{2a^3}{\mu}\left[e\sin^2 E - 2\sqrt{1-e^2}\left(1-\cos E\right)\right] \\
\dfrac{a^2\sqrt{1-e^2}}{\mu}\left[\sqrt{1-e^2}\sin^2 E - 2\left(2\cos E - e - e\cos^2 E\right)\left(1-\cos E\right)\right] \\
\dfrac{a^2}{\mu e}\left[\sqrt{1-e^2}\left(e-\cos E\right)\sin E - 2\left(2-e^2-e\cos E\right)\sin E\left(1-\cos E\right)\right]
\end{array}\right\}
\end{aligned}
\tag{5.32}
$$

Note that $\left(\mathrm{d}i/\mathrm{d}E\right)^{\mathrm{str1}} = \left(\mathrm{d}\Omega/\mathrm{d}E\right)^{\mathrm{str1}} = 0$ because $f_h^{\mathrm{str1}} = 0$.

Carrying out the integration of Eq. (5.32), after some manipulations, the primitive functions for the perigee decrease strategy can be obtained:

$$
\begin{aligned}
\mathrm{fun}_a^{\mathrm{str1}} &= \frac{2fa^3}{\mu}\left[\frac{\sqrt{2}}{3}e\cos\frac{E}{2}\sqrt{5-3\cos E} - \frac{4\sqrt{3}}{9}\left(3\sqrt{1-e^2}-2e\right)\tan^{-1}\frac{\sqrt{5-3\cos E}}{\sqrt{6}\cos\dfrac{E}{2}}\right] \\
\mathrm{fun}_e^{\mathrm{str1}} &= \frac{fa^2\sqrt{1-e^2}}{\mu}\left[\frac{\sqrt{2}}{3}\left(\sqrt{1-e^2}+e-4+e\cos E\right)\cos\frac{E}{2}\sqrt{5-3\cos E}\right. \\
&\qquad\left. + \frac{8\sqrt{3}}{9}\left(\sqrt{1-e^2}+3e-1\right)\tan^{-1}\frac{\sqrt{5-3\cos E}}{\sqrt{6}\cos\dfrac{E}{2}}\right] \\
\mathrm{fun}_\omega^{\mathrm{str1}} &= \frac{fa^2}{\mu e}\left[\frac{\sqrt{2}}{3}\left(\sqrt{1-e^2}+2e^2+2e-4+e\cos E\right)\sin\frac{E}{2}\sqrt{5-3\cos E}\right. \\
&\qquad\left. - \frac{2\sqrt{3}}{9}\left(\sqrt{1-e^2}\left(4-3e\right)+2e^2+3e-4\right)\tanh^{-1}\frac{\sqrt{6}\sin\dfrac{E}{2}}{\sqrt{5-3\cos E}}\right]
\end{aligned}
\tag{5.33}
$$

where $\tan^{-1}\circ$ and $\tanh^{-1}\circ$ return the *four-quadrant* inverse tangent and the inverse hyperbolic tangent, respectively, of the generic variable $\circ$.

Eq. (5.33) is derived with the support of Wolfram Mathematica 11.2, the results given by which contain a complex term, making the primitive functions impossible to be evaluated in the field of real number. To address this problem, we perform an analysis for the complex term, as presented in Appendix A.1, and finally rewrite it as

$$
\mathbb{i}\ln\left(\sqrt{6}\cos\frac{E}{2} + \mathbb{i}\sqrt{5-3\cos E}\right) = -\tan^{-1}\frac{\sqrt{5-3\cos E}}{\sqrt{6}\cos\dfrac{E}{2}} + \mathbb{i}\ln\sqrt{8}
\tag{5.34}
$$

where $\mathbb{i}$ is the imaginary unit, and the imaginary part $\mathbb{i}\ln\sqrt{8}$ is the integration constant that can be removed.

In the case of continuous thrusting, the burning arc in every revolution is from 0 to 2π, and the expressions of the incremental changes in orbital elements over one revolution for the perigee decrease strategy can be further reduced to

$$\begin{aligned}
\Delta a_{\text{rev}}^{\text{str1}} &= -\frac{8fa^3}{\mu}\left[\frac{1}{3}e+\frac{\sqrt{3}}{9}\left(3\sqrt{1-e^2}-2e\right)\left(\pi-2\tan^{-1}\frac{1}{\sqrt{3}}\right)\right] \\
\Delta e_{\text{rev}}^{\text{str1}} &= \frac{4fa^2\sqrt{1-e^2}}{\mu}\left[\frac{1}{3}\left(4-\sqrt{1-e^2}-2e\right)\right. \\
&\quad \left.+\frac{2\sqrt{3}}{9}\left(\sqrt{1-e^2}+3e-1\right)\left(\pi-2\tan^{-1}\frac{1}{\sqrt{3}}\right)\right] \\
\Delta\omega_{\text{rev}}^{\text{str1}} &= 0
\end{aligned} \tag{5.35}$$

5.3.2 De-orbiting Corridor Strategy

Substituting the control law Eq. (5.28) into the equations of motion Eqs. (2.5a) – (2.5e) and divided by $\dot{E}$ Eq. (2.5f), the rates of change of orbital elements with E for the de-orbiting corridor strategy are

$$\begin{aligned}
&\left\{\left(\frac{\mathrm{d}a}{\mathrm{d}E}\right)^{\text{str2}}, \left(\frac{\mathrm{d}e}{\mathrm{d}E}\right)^{\text{str2}}, \left(\frac{\mathrm{d}i}{\mathrm{d}E}\right)^{\text{str2}}, \left(\frac{\mathrm{d}\Omega}{\mathrm{d}E}\right)^{\text{str2}}, \left(\frac{\mathrm{d}\omega}{\mathrm{d}E}\right)^{\text{str2}}\right\}^{\top} \\
=&\frac{-\mathrm{sgn}_{\psi^{\text{str2}}}f}{\sqrt{c_a^2+c_i^2\cos^2(\omega+E)}} \\
&\left\{\begin{array}{c}
\dfrac{2c_a a^3\sqrt{1-e^2}}{\mu} \\
\dfrac{c_a a^2\sqrt{1-e^2}}{\mu}\left(2\cos E-e-e\cos^2 E\right) \\
\dfrac{c_i a^2}{\mu}\left(\dfrac{\cos E-e}{\sqrt{1-e^2}}\cos\omega-\sin E\sin\omega\right)(1-e\cos E)\cos(\omega+E) \\
\dfrac{c_i a^2}{\mu}\left(\dfrac{\cos E-e}{\sqrt{1-e^2}}\sin\omega+\sin E\cos\omega\right)\dfrac{1-e\cos E}{\sin i}\cos(\omega+E) \\
\dfrac{c_a a^2}{\mu e}\left(2-e^2-e\cos E\right)\sin E
\end{array}\right\} \\
+&\left\{0,\ 0,\ 0,\ 0,\ -\left(\frac{\mathrm{d}\Omega}{\mathrm{d}E}\right)^{\text{str2}}\cos i\right\}^{\top}
\end{aligned} \tag{5.36}$$

Unfortunately, Eq. (5.36) can not be integrated analytically. Observing that the term $\cos(\omega+E)$ is periodic, let us expand the following term in Fourier series up to 8^{th}-order before carrying out the integration:

$$\frac{1}{\sqrt{c_a^2+c_i^2\cos^2(\omega+E)}} \approx \frac{2}{\pi\sqrt{c_a^2+c_i^2}}\sum_{k=0}^{4} b_k\cos\left[2k(\omega+E)\right] \tag{5.37}$$

where b_k ($k=0$ to 4) are the Fourier series coefficients, given in the form of

$$b_k = b_k^F \mathrm{ellipticF}(\rho) + b_k^E \mathrm{ellipticE}(\rho) \tag{5.38}$$

with b_k^F and b_k^E dependent on c_a and c_i, given in Appendix A.2. Note that the reason to choose the 8th-order Fourier series expansion is for the sake of achieving good accuracy with a reasonable computational effort. For an 8th-order Fourier series expansion, there should have been 17 coefficients, among which only five coefficients, i.e. b_0 to b_4, are non-zero in the current problem.

In Eq. (5.37), the complete elliptic integrals of the first and second kinds [94, Sec. 1.5]

$$\begin{aligned} \text{elliptic}F\,(\rho) &= \int_0^{\pi/2} \left(1 - \rho \sin^2 \varphi\right)^{-1/2} \mathrm{d}\varphi \\ \text{elliptic}E\,(\rho) &= \int_0^{\pi/2} \left(1 - \rho \sin^2 \varphi\right)^{\;1/2} \mathrm{d}\varphi \end{aligned} \tag{5.39}$$

are to be evaluated, where the modulus ρ is

$$\rho = \frac{c_i^2}{c_a^2 + c_i^2} \tag{5.40}$$

Then substituting Eq. (5.37) into Eq. (5.36) and carrying out the integration, after considerable manipulations, the primitive functions for the de-orbiting corridor strategy can be obtained:

$$\begin{aligned} &\left\{\text{fun}_a^{\text{str2}},\ \text{fun}_e^{\text{str2}},\ \text{fun}_i^{\text{str2}},\ \text{fun}_\Omega^{\text{str2}},\ \text{fun}_\omega^{\text{str2}}\right\}^\top \\ &= \frac{-\text{sgn}_{\psi^{\text{str2}}} f}{\pi \mu \sqrt{c_a^2 + c_i^2}} \left\{ \begin{array}{l} \left[\sum_{k=0}^{4} b_k \left(\text{fun}_k\right)_a\right] c_a a^3 \sqrt{1 - e^2} \\ \left[\sum_{k=0}^{4} b_k \left(\text{fun}_k\right)_e\right] c_a a^2 \sqrt{1 - e^2} \\ \left[\sum_{k=0}^{4} b_k \left(\text{fun}_k\right)_i\right] c_i a^2 \\ \left[\sum_{k=0}^{4} b_k \left(\text{fun}_k\right)_\Omega\right] \dfrac{c_i a^2}{\sin i} \\ \left[\sum_{k=0}^{4} b_k \left(\text{fun}_k\right)_\omega\right] \dfrac{c_a a^2}{e} \end{array} \right\} + \left\{0,\ 0,\ 0,\ 0,\ \ -\text{fun}_\Omega^{\text{str2}} \cos i\right\}^\top \end{aligned} \tag{5.41}$$

where $\left(\text{fun}_k\right)_x$ ($k = 0$ to 4 and $x = a,\ e,\ i,\ \Omega,\ \omega$) are dependent on e, ω, and E, given in Appendix A.3.

In the case of continuous thrusting, the burning arc in every revolution is from 0 to 2π, and the expressions of the incremental changes in orbital elements over one revolution for the de-orbiting corridor strategy can be further reduced to

$$
\begin{aligned}
&\left\{\Delta a_{\text{rev}}^{\text{str2}},\ \Delta e_{\text{rev}}^{\text{str2}},\ \Delta i_{\text{rev}}^{\text{str2}},\ \Delta \Omega_{\text{rev}}^{\text{str2}},\ \Delta \omega_{\text{rev}}^{\text{str2}}\right\}^{\top}\\
&=\frac{-\operatorname{sgn}_{\psi^{\text{str2}}} f}{\mu\sqrt{c_a^2+c_i^2}}\left\{\begin{array}{c}
8 c_a a^3 \sqrt{1-e^2} b_0\\
-c_a a^2 e \sqrt{1-e^2}\left(6 b_0+b_1 \cos 2\omega\right)\\
c_i a^2\left(b_0+\frac{1}{2} b_1\right)\left[\frac{1+e^2}{\sqrt{1-e^2}}+1+\left(\frac{1+e^2}{\sqrt{1-e^2}}-1\right)\cos 2\omega\right]\\
\frac{c_i a^2}{\sin i}\left(b_0+\frac{1}{2} b_1\right)\left(\frac{1+e^2}{\sqrt{1-e^2}}-1\right)\sin 2\omega\\
c_a a^2 b_1 \sin 2\omega
\end{array}\right\}\\
&+\left\{0,\ 0,\ 0,\ 0,\ -\Delta \Omega_{\text{rev}}^{\text{str2}} \cos i\right\}^{\top}
\end{aligned}
\tag{5.42}
$$

5.4 Simulation Results and Discussion

In this section, numerical simulations will be performed to validate the performance of the control laws and averaged low-thrust dynamics models, and several maps that depict the de-orbiting cost for the whole LEO region will be obtained, based on which, the application conditions of the two de-orbiting strategies will be identified. Table 5.2 presents the parameters that are fixed for all the simulations.

Table 5.2: *Simulation parameters.*

Parameter	Symbol	Value	Unit
Initial eccentricity	e_0	0.001	
Initial RAAN	Ω_0	0	rad
Initial argument of perigee	ω_0	1	rad
Initial eccentric anomaly	E_0	2	rad
Initial spacecraft mass	m_0	150	kg
Low-thrust engine input power	P_{eng}	200	W
Low-thrust engine efficiency	η_{eng}	50	%
Low-thrust engine specific impulse	I_{sp}	1500	s

5.4.1 Numerical Validations

In this part, a test transfer for the OneWeb satellite is presented to demonstrate the optimality of the proposed control laws and the accuracy of the averaged low-thrust dynamics models. The following simulation parameters and force model are considered:

- the initial semi-major axis and inclination are $a_0 = R_{\oplus} + 1200$ km and $i_0 = 87.9$ deg, respectively [111];
- the target perigee altitude for the perigee decrease strategy is 250 km, following the study in Ref. [46], such that the satellite can quickly re-enter;
- the secular effects of J_2 Eq. (2.6) are considered.

Validation for Control Laws

The optimality of the proposed closed-loop control laws is validated by comparing with the time-minimum open-loop control laws in terms of the Time of Flight (ToF). Here the time-minimum open-loop control laws are obtained by using the indirect method, as presented in Appendix A.4. Table 5.3 gives the initial costates of the open-loop control laws for the two strategies.

Table 5.3: *Initial costates.*

Strategy	$(\lambda_a)_0$, s/km	$(\lambda_e)_0$, s	$(\lambda_i)_0$, s/rad	$(\lambda_\Omega)_0$, s/rad
Perigee decrease	4.2662×10^3	-3.6820×10^7	0	0
De-orbiting corridor	4.7356×10^3	-9.6343×10^4	2.7379×10^7	0
	$(\lambda_\omega)_0$, s/rad	$(\lambda_E)_0$, s/rad	$(\lambda_m)_0$, s/kg	
Perigee decrease	0	303.86	3.0798×10^4	
De-orbiting corridor	17.342	15.063	6.1801×10^4	

Comparisons of ToFs for the closed- and open-loop control laws are presented in Table 5.4 for the two strategies. As indicated in the table, for both strategies, the ToFs of the closed-loop control laws are very close to the optimal solutions.

Table 5.4: *Comparison of ToFs for the closed- and open-loop control laws.*

Strategy	ToF of closed-loop control law, days	ToF of open-loop control law, days
Perigee decrease	56.392	56.105
De-orbiting corridor	108.577	108.576

Validation for Averaged Low-Thrust Dynamics Model

The accuracy of the averaged dynamics models is validated by comparing with the exact dynamics model in terms of the numerical integration results. In this study, the numerical integration is carried out using MATLAB R2020b running on a computer with Intel Core i7-8550U and 8GB RAM; the ODE solver is *ode45*, where the absolute and relative error tolerances are specified as 10^{-13}.

Comparisons of the exact and averaged results in terms of the final state variables, ToF, and CPU time are presented in Table 5.5 and Table 5.6 for the perigee decrease and de-orbiting corridor strategies, respectively. As indicated in the tables, the averaged dynamics models can significantly reduce the computational load while maintain good accuracy.

Table 5.5: *Comparison of the exact and averaged results for the perigee decrease strategy.*

Model	a_f, km	e_f, $\times 10^{-2}$	ω_f, rad	m_f, kg	ToF, days	CPU time, s
Exact	6910.432	4.0847	−2.1275	145.496	56.4011	6.237
Averaged	6910.399	4.0843	−2.1515	145.496	56.4030	0.007

Table 5.6: *Comparison of the exact and averaged results for the de-orbiting corridor strategy.*

Model	a_f, km	e_f, $\times 10^{-4}$	i_f, deg	Ω_f, rad	ω_f, rad	m_f, kg	ToF, days	CPU time, s
Exact	9705.773	7.6915	86.515	0.3242	−2.4849	141.329	108.5776	5.770
Averaged	9705.759	8.3046	86.515	0.3242	−2.4589	141.329	108.5773	0.039

5.4.2 De-Orbiting Mapping

In this part, several maps of the LEO region that show the Δv-budget and de-orbiting time are obtained for the two strategies, by propagating a series of initial conditions. Here, the Δv-budget refers to the change in velocity of low-thrust transfer, and the de-orbiting time refers to the total time to de-orbit, including the time of active de-orbiting with low-thrust propulsion and the time of passive de-orbiting due to natural perturbations. Particularly the numerical simulations for passive de-orbiting are performed by Dr. Elisa Maria Alessi.

Here are the force models considered for the active and passive de-orbiting. In the simulations for active de-orbiting, the averaged low-thrust dynamics models are used, and the secular effects of J_2 are considered. In the simulations for passive de-orbiting, the orbital propagator developed for the ReDSHIFT software tool [53, 112, 113] is applied. It considers

- Earth zonal harmonics up to degree 5
- SRP with the cannonball model
- lunisolar perturbations
- atmospheric drag with the Jacchia-Roberts atmospheric density model, assuming an exospheric temperature of 1000 K and a variable solar flux at 2800 MHz

For the perigee decrease strategy, the area-to-mass ratio is $A/m = 0.012$ m^2/kg, which is the average value of the orbiting intact population [114]. For the de-orbiting corridor strategy, the area-to-mass ratios are $A/m = 1$ m^2/kg and 3 m^2/kg; the former is a feasible value achievable for small satellites [109], whereas the latter has a potential application for quick re-entry. For both strategies, the drag and reflectivity coefficients are set to $C_D = 2.1$ and $C_R = 1$, respectively, and the re-entry is assumed to happen whenever the perigee altitude is decreased to a demise value of 78 km.

Table 5.7 defines the grids of initial altitude h_0 for both strategies, of initial inclination i_0 for the de-orbiting corridor strategy, and of target perigee altitude h_{pf} for the perigee decrease strategy. In the following simulations, the initial inclination for the perigee decrease strategy, which has ignorable influence on the simulation results compared to h_0 and h_{pf}, is fixed as 63.435 deg.

Table 5.7: *Initial grids.*

h_0, km	Δh_0, km	i_0, deg	Δi_0, deg	h_{pf}, km	Δh_{pf}, km
[500, 2000]	10	[30, 120]	2	[200, 600]	10

Perigee Decrease Strategy

Fig. 5.5 shows the Δv-budget for the perigee decrease strategy as a function of h_0 and h_{pf}, where the white area means $h_0 < h_{pf}$. Here the Δv-budget is the change in velocity required to move a spacecraft from given h_0 to h_{pf}. As shown Fig. 5.5, the lower the initial altitude and the higher the target perigee altitude, the less the Δv-budget will be. Fig. 5.6 shows the ToF of low-thrust transfer; it is proportional to Δv because the thrust is continuously applied.

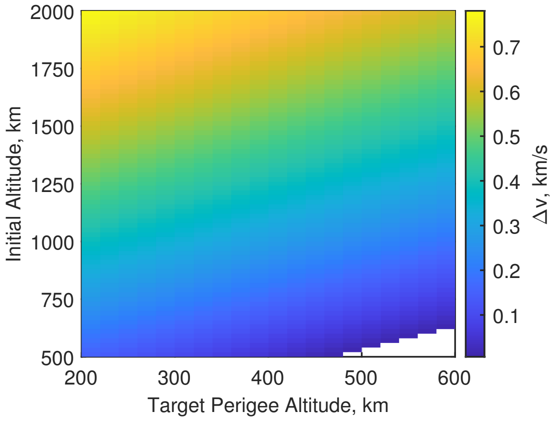

Figure 5.5: *Δv-budget for the perigee decrease strategy as a function of h_0 and h_{pf}.*

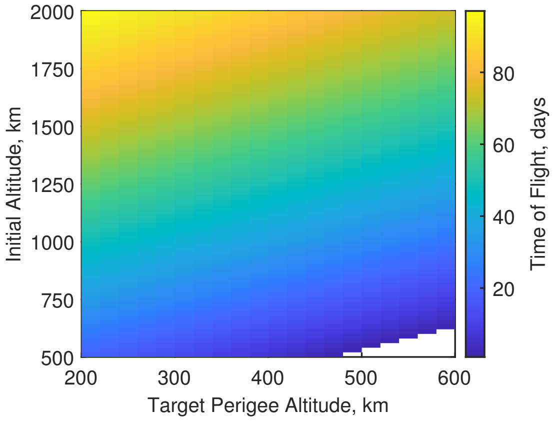

Figure 5.6: *ToF of low-thrust transfer for the perigee decrease strategy as a function of h_0 and h_{pf}.*

Figs. 5.7 (a) and (b) show the de-orbiting time for the perigee decrease strategy as a function of h_0 and h_{pf}, given the requirements to de-orbit within 25 years and 5 years, respectively. Here the de-orbiting time is the total time to de-orbit that accounts for the active de-orbiting from given h_0 to h_{pf} and the passive de-orbiting from that h_{pf}. In the maps, the coloured areas denote the conditions in (h_0, h_{pf}) that can lead to re-entry within the required de-orbiting times. Note that the requirement of 25 years is the guidance from the International-Agency Space Debris Coordination Committee (IADC) for satellites in LEO, and the requirement of 5 years is a guideline that has been considered by some large constellations, such as the Starlink constellation [115] and the OneWeb constellation [111], to reduce the negative impact on the space environment as much as possible.

As shown in Fig. 5.7, generally, the lower the initial altitude and the lower the target perigee altitude, the faster the de-orbiting will be. If there is no limit on Δv-budget, the perigee decrease strategy can achieve re-entry within 5 years from any initial altitudes up to $2,000$ km.

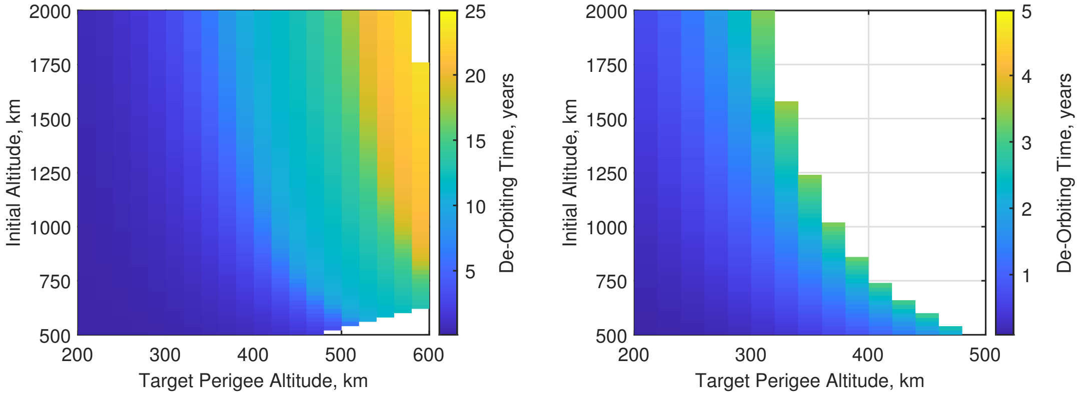

(a) De-orbiting within 25 years.

(b) De-orbiting within 5 years.

Figure 5.7: *De-orbiting time for the perigee decrease strategy as a function of* h_0 *and* h_{pf}.

De-Orbiting Corridor Strategy

Fig. 5.8 shows the Δv-budget for the de-orbiting corridor strategy as a function of h_0 and i_0, where the black curves indicate the location of de-orbiting corridors, assuming $e = 0.001$. Here the Δv-budget is the change in velocity required to move a spacecraft from a given $(h_0,\ i_0)$ to the closest de-orbiting corridor. As shown in Fig. 5.8, the closer the initial state to the corresponding target de-orbiting corridor, the less the Δv-budget will be. Fig. 5.9 shows the ToF of low-thrust transfer; it is proportional to Δv because the thrust is continuously applied.

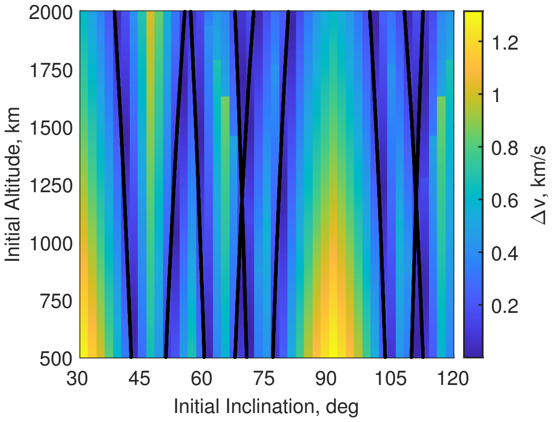

Figure 5.8: Δv*-budget for the de-orbiting corridor strategy as a function of* h_0 *and* i_0.

Fig. 5.10 and Fig. 5.11 show the de-orbiting time for the de-orbiting corridor strategy as a function of h_0 and i_0, for $A/m = 1\ \mathrm{m^2/kg}$ and $3\ \mathrm{m^2/kg}$, respectively. Here the de-orbiting time is the total time to de-orbit that accounts for the active de-orbiting from a given $(h_0,\ i_0)$ to the closest de-orbiting corridor and the passive de-orbiting from that de-orbiting corridor. In the maps, the coloured areas denote the conditions in $(h_0,\ i_0)$ that can lead to re-entry within 25 years and 5 years.

As indicated in Fig. 5.10 and Fig. 5.11, the de-orbiting corridor located in the inclination between 30 and 45 deg is more effective than the others in terms of the

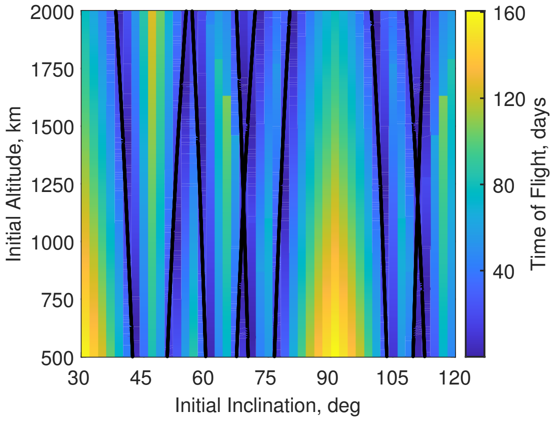

Figure 5.9: *ToF for the de-orbiting corridor strategy as a function of* h_0 *and* i_0.

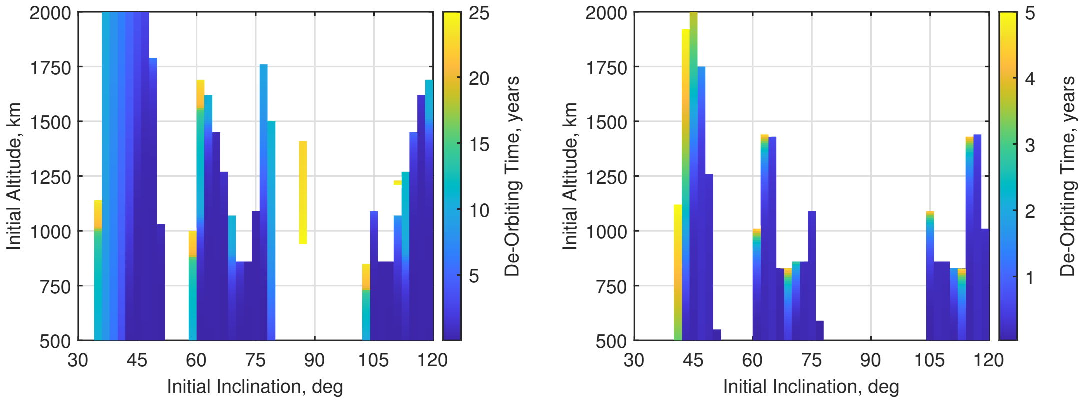

(a) De-orbiting within 25 years.

(b) De-orbiting within 5 years.

Figure 5.10: *De-orbiting time for the de-orbiting corridor strategy as a function of* h_0 *and* i_0, *for* $A/m = 1\ m^2/kg$.

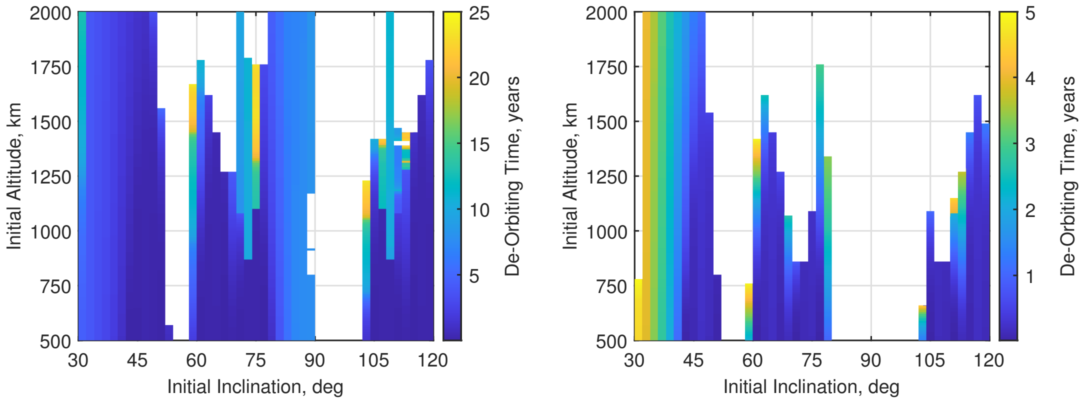

(a) De-orbiting within 25 years.

(b) De-orbiting within 5 years.

Figure 5.11: *De-orbiting time for the de-orbiting corridor strategy as a function of* h_0 *and* i_0, *for* $A/m = 3\ m^2/kg$.

passive de-orbiting. Besides, the low and middle LEO altitudes show a relatively wider region for exploitable initial conditions. This is due to the fact the passive de-orbiting device with an augmentation area can also act as a drag sail [54]. Also, the ability of the de-orbiting corridor strategy depends on the area-to-mass ratio of the passive de-orbiting device; the larger the area-to-mass ratio, the faster the de-orbiting will be.

De-orbiting Strategy Comparison

Finally, the two strategies are compared in terms of the Δv-budget to identify the feasible regions for the two strategies with given de-orbiting time requirements (i.e. 25 years and 5 years), as shown in Fig. 5.12 and Fig. 5.13, where the area-to-mass ratios considered for the de-orbiting corridor strategy are $A/m = 1$ m^2/kg and 3 m^2/kg, respectively. In the maps, the green areas denote the regions where the Δv-budgets by the de-orbiting corridor strategy are smaller than those by the perigee decrease strategy, and thus for these regions, the de-orbiting corridor strategy is superior. Accordingly, the remaining blue areas denote the feasible regions for the perigee decrease strategy. Note that for the perigee decrease strategy, the Δv-budget used in the comparison is the minimum value to de-orbit from a given h_0 within a given de-orbiting time requirement (i.e. 25 years or 5 years), and this value is assumed identical for all the initial inclination, recalling that the initial inclination has ignorable influence on the simulation results for the perigee decrease strategy.

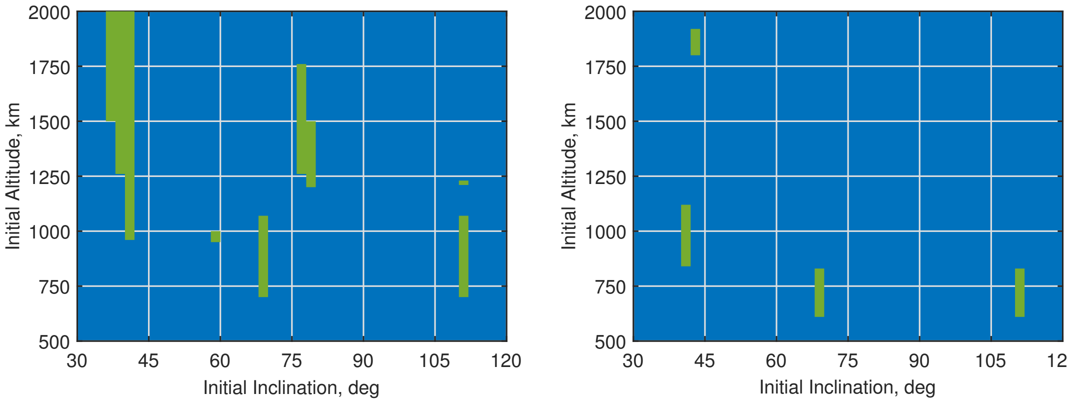

(a) De-orbiting within 25 years.

(b) De-orbiting within 5 years.

Figure 5.12: *Feasible regions for the perigee decrease strategy (blue) and for the de-orbiting corridor strategy (green), for* $A/m = 1$ *m*^{2}*/kg.*

As indicated in Fig. 5.12 and Fig. 5.13, the de-orbiting corridor strategy spends more Δv-budget than the perigee decrease strategy in most of the LEO region because of the expensive inclination change. However, there still exist many cases, especially in the high-altitude LEO region, where the de-orbiting corridor strategy is more attractive. By reading the maps, the mission operators can choose their preferable strategy according to mission conditions and requirements.

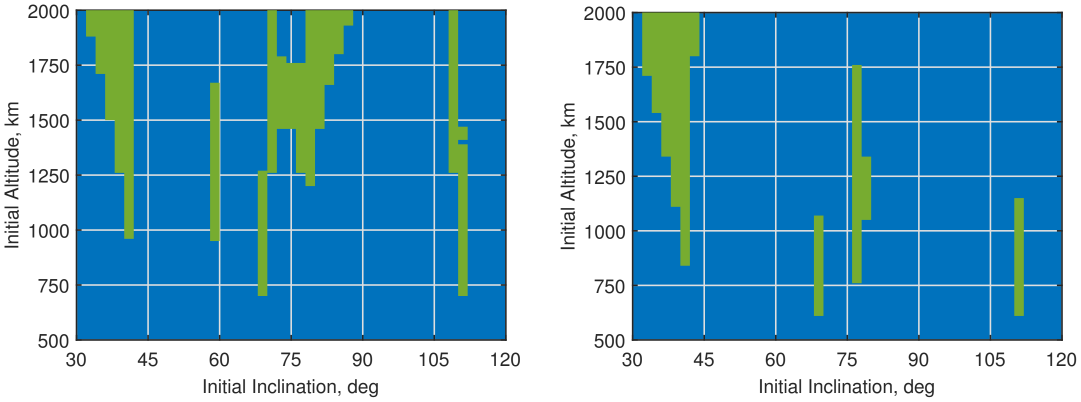

(a) De-orbiting within 25 years.

(b) De-orbiting within 5 years.

Figure 5.13: *Feasible regions for the perigee decrease strategy (blue) and for the de-orbiting corridor strategy (green), for* $A/m = 3\ m^2/kg$.

CHAPTER 6

Low Earth Orbit Co-Planar Satellites Low-Thrust Planar Transfer Considering Self-Induced Collision Avoidance

This chapter deals with the planar transfer problem (orbit raising and de-orbiting) for co-planar satellites with low-thrust propulsion, taking the self-induced collision avoidance into consideration at the mission design stage. A Blended Error-Correction (BEC) control law, with which the thrust direction changes in a self-adaptive way, is developed by blending two types of efficient control laws and offsetting the errors of the osculating orbit with respect to the target orbit. The semi-analytical solutions for orbital elements, which reduce the computational load of propagating long-duration trajectories, are derived by computing the analytical incremental changes in orbital elements after every revolution with an orbital averaging technique. Based on the analytical BEC control law and semi-analytical solutions, transfers can be computed quickly for any starting times. Finally, the self-induced collision, which is modelled by miss distance, is avoided by properly scheduling the timing to start transfer for every satellite.

Note that the scope of this study is only the propulsive phase. For orbit raising, it is the phase from the parking orbit to the final orbit at the nominal altitude, while excluding the final phasing angle adjustment. For de-orbiting, it is the active disposal phase, from the initial orbit to the re-entry perigee under which the atmospheric drag will lead the spacecraft to natural re-entry. Within this scope, the atmospheric drag can be neglected compared with the effects of low-thrust and Earth's gravity, and the self-induced collision is discussed between the active satellites.

6.1 Control Law Design

In this study, two control laws are used for planar transfer: the tangential thrusting and the inertial thrusting. Here are the reasons for this choice:

- the tangential and inertial thrusting are the local- and near-optimal control laws to change a and e, respectively, as introduced in Sec. 2.4;
- the dynamics model governed by these two control laws is in a simple fashion, making it possible to carry out the analytical integration for variations in orbital elements, as will be presented in Sec. 6.2.

It has to be noted that the idea of "error-correction" was proposed by Ruggiero et. al [77], where the authors used a local-optimal control law to change e. Here are the pitch angles for inertial thrusting and local-optimal control law:

$$\alpha_i \quad = \pm\nu \tag{6.1a}$$

$$\alpha_{\text{local}} = \pm\tan^{-1}\left(\frac{\sin\nu}{\cos\nu+\cos E}\right) \tag{6.1b}$$

where the sign + and − represents the cases of eccentricity increase and decrease, respectively. Apparently, the expression of α_i is more concise than that of α_{local}, thus leading to a simpler dynamics model. Fig. 6.1 shows the efficiency of inertial thrusting as a function of E and e, where the y-axis is the ratio between $\dot{e}$ governed by inertial thrusting and local-optimal control law. As shown in the figure, the ratio is higher than 0.92 for LEO transfer where $e \leq 0.2$, implying high efficiency of inertial thrusting.

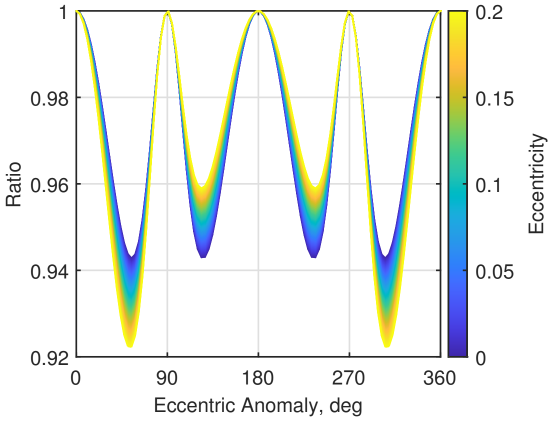

Figure 6.1: *Efficiency of inertial thrusting (the eccentricity increasing as the colour from dark to light).*

Using the expression of tangential thrusting in Eq. (2.10), the rates of change of planar orbital elements with E subject to tangential thrusting are given by

$$\frac{\mathrm{d}a}{\mathrm{d}E} = \pm f\frac{2a^3}{\mu}\sqrt{1-e^2\cos^2 E} \tag{6.2a}$$

$$\frac{\mathrm{d}e}{\mathrm{d}E} = \pm f\frac{2a^2\left(1-e^2\right)}{\mu}\sqrt{\frac{1-e\cos E}{1+e\cos E}}\cos E \tag{6.2b}$$

$$\frac{\mathrm{d}\omega}{\mathrm{d}E} = \pm f\frac{2a^2\sqrt{1-e^2}}{\mu e}\sqrt{\frac{1-e\cos E}{1+e\cos E}}\sin E \tag{6.2c}$$

where the sign + and − represents the cases of semi-major axis increase and decrease, respectively.

Using the expression of inertial thrusting in Eq. (2.13), the rates of change of planar orbital elements with E subject to inertial thrusting are given by

$$\frac{\mathrm{d}a}{\mathrm{d}E} = \pm f \frac{2a^3\sqrt{1-e^2}}{\mu} \cos E \tag{6.3a}$$

$$\frac{\mathrm{d}e}{\mathrm{d}E} = \pm f \frac{a^2\sqrt{1-e^2}}{\mu} \left(\cos^2 E - 2e\cos E + 1\right) \tag{6.3b}$$

$$\frac{\mathrm{d}\omega}{\mathrm{d}E} = \pm f \frac{a^2}{\mu e} \left(\cos E - e\right) \sin E \tag{6.3c}$$

where the sign + and − represents the cases of eccentricity increase and decrease, respectively.

In order to change a and e at the same time, the thrust acceleration vector is defined as

$$\boldsymbol{f} = c_t \boldsymbol{f}_t + c_i \boldsymbol{f}_i = f(c_t \hat{\boldsymbol{f}}_t + c_i \hat{\boldsymbol{f}}_i) \tag{6.4}$$

where $\boldsymbol{f}_t$ and $\boldsymbol{f}_i$ are the thrust acceleration vectors of tangential and inertial thrusting, respectively, with a magnitude of f, c_t and c_i are the weighting factors allocated to tangential and inertial thrusting, respectively, and $\hat{\circ}$ represents the unit vector of the generic variable $\circ$.

Recalling that the tangential and inertial thrusting are the local- and near-optimal control laws to change a and e, respectively, c_t and c_i are therefore set to be proportional to the instantaneous errors of a and e, respectively, towards the desired target values, such that thrust direction can change in a self-adaptive way. The instantaneous errors in a and e, denoted by k_a and k_e, respectively, are defined by the means of [77]

$$k_a = \frac{a_d - a}{|a_d - a_0|}, \quad k_e = \frac{e_d - e}{|e_d - e_0|} \tag{6.5}$$

where $\circ_0$ and $\circ_d$ represent the initial and desired target values, respectively, of the generic variable $\circ$, and $|\circ|$ represents the absolute value of $\circ$. Note that Eq. (6.5) can eliminate the dimensional difference between a and e, where a is on the order of 10^3–10^5 km and e is less than 1.

For orbit raising mission, a_d and e_d are the orbital elements of the final orbit, while for de-orbiting mission, a_d and e_d are set to satisfy

$$h_{pf} = a_d\left(1 - e_d\right) - R_\oplus \tag{6.6}$$

where h_{pf} is the final perigee altitude below which the atmospheric drag will lead the spacecraft to natural re-entry. To lower the perigee as fast as possible, a_d and e_d in de-orbiting mission are chosen as

$$a_d = h_{pf} + R_\oplus, \quad e_d = 1 \tag{6.7}$$

After defining the instantaneous errors, c_t and c_i can be stated as

$$c_t = s k_a, \quad c_i = s k_e \tag{6.8}$$

where s is a scale factor that ensures

$$\|c_t\hat{\boldsymbol{f}}_t + c_i\hat{\boldsymbol{f}}_r\| = \|\hat{\boldsymbol{f}}\| = 1 \tag{6.9}$$

with $\|\circ\|$ representing the magnitude of the generic vector $\circ$. By using the cosine law, the left-hand side of Eq. (6.9) becomes

$$\|c_t\hat{\boldsymbol{f}}_t + c_i\hat{\boldsymbol{f}}_r\| = c_t^2\|\hat{\boldsymbol{f}}_t\|^2 + c_i^2\|\hat{\boldsymbol{f}}_i\|^2 - 2|c_t||c_i|\|\hat{\boldsymbol{f}}_t\|\|\hat{\boldsymbol{f}}_i\|\cos\zeta \tag{6.10}$$

where ζ is the angle between $\hat{\boldsymbol{f}}_t$ and $\hat{\boldsymbol{f}}_i$. Because $\hat{\boldsymbol{f}}_t$ and $\hat{\boldsymbol{f}}_i$ are unit vectors, there is

$$\|\hat{\boldsymbol{f}}_t\| = \|\hat{\boldsymbol{f}}_i\| = 1 \tag{6.11}$$

Thus, Eq. (6.10) becomes

$$\|c_t\hat{\boldsymbol{f}}_t + c_i\hat{\boldsymbol{f}}_r\| = c_t^2 + c_i^2 - 2|c_t||c_i|\cos\zeta \tag{6.12}$$

Then substituting Eq. (6.12) into Eq. (6.9) and replacing c_t, c_i with Eq. (6.8), s can be solved:

$$s = \frac{1}{\sqrt{k_a^2 + k_e^2 - 2|k_a||k_e|\cos\zeta}} \tag{6.13}$$

and accordingly,

$$c_t = \frac{k_a}{\sqrt{k_a^2 + k_e^2 - 2|k_a||k_e|\cos\zeta}}, \quad c_i = \frac{k_e}{\sqrt{k_a^2 + k_e^2 - 2|k_a||k_e|\cos\zeta}} \tag{6.14}$$

From the definitions of tangential and inertial thrusting in Sec. 2.4, there is

$$\zeta = \alpha_i - \alpha_t \tag{6.15}$$

where α_t and α_i are the pitch angles for tangential and inertial thrusting, respectively, given by

$$\alpha_t = \begin{cases} \phi_{\text{fpa}}, & \text{if } k_a \geq 0 \\ \phi_{\text{fpa}} + \pi, & \text{if } k_a < 0 \end{cases} \tag{6.16a}$$

$$\alpha_i = \begin{cases} \nu, & \text{if } k_e \geq 0 \\ \nu - \pi, & \text{if } k_e < 0 \end{cases} \tag{6.16b}$$

with ϕ_{fpa} being the flight path angle, a satellite-based angle from the direction of the $\hat{\theta}$-axis of the Gauss coordinate system to the direction of velocity vector [93, pp. 18]; ϕ_{fpa} and E are related by

$$\sin\phi_{\text{fpa}} = \frac{e\sin E}{\sqrt{1-e^2\cos^2 E}}, \quad \cos\phi_{\text{fpa}} = \frac{\sqrt{1-e^2}}{\sqrt{1-e^2\cos^2 E}} \tag{6.17}$$

From Eq. (6.16), there is

$$\cos\zeta = \text{sgn}_{k_a}\text{sgn}_{k_e}\cos(\nu - \phi_{\text{fpa}}) = \text{sgn}_{k_a}\text{sgn}_{k_e}\frac{\sqrt{1-e^2}\cos E}{\sqrt{1-e^2\cos^2 E}} \tag{6.18}$$

where sgn_{k_a} and sgn_{k_e} return the signs of k_a and k_e, respectively.

Finally, substituting Eq. (6.18) into Eq. (6.14), c_t and c_i are written as functions of the instantaneous errors k_a, k_e and the eccentric anomaly E:

$$c_t = \frac{k_a}{\sqrt{k_a^2 + k_e^2 + 2k_a k_e \dfrac{\sqrt{1-e^2}\cos E}{\sqrt{1-e^2\cos^2 E}}}}, \quad c_i = \frac{k_e}{\sqrt{k_a^2 + k_e^2 + 2k_a k_e \dfrac{\sqrt{1-e^2}\cos E}{\sqrt{1-e^2\cos^2 E}}}} \tag{6.19}$$

The proposed control law is named here as the Blended Error-Correction (BEC) control law, the blend of tangential thrusting and inertial thrusting, based on the offsets in the instantaneous errors in semi-major axis and eccentricity, and hence enabling the thrust direction to self-adaptively adjust according to the deviation of the instantaneous orbit towards the desired target orbit.

By using the BEC control law, the rates of change of planar orbital elements with E are given by

$$\frac{\mathrm{d}\boldsymbol{x}}{\mathrm{d}E} = c_t \left(+\frac{\mathrm{d}\boldsymbol{x}}{\mathrm{d}E}\right)_t + c_i \left(+\frac{\mathrm{d}\boldsymbol{x}}{\mathrm{d}E}\right)_i \tag{6.20}$$

where $\boldsymbol{x} = \{a,\ e,\ \omega\}^\top$, $(+\mathrm{d}\boldsymbol{x}/\mathrm{d}E)_t$ and $(+\mathrm{d}\boldsymbol{x}/\mathrm{d}E)_i$ are given by Eq. (6.2) and Eq. (6.3), respectively, with the sign $+$ representing that the signs of sub-equations are positive, because the increase and decrease of a and e depend on c_t and c_i.

6.2 Averaged Low-Thrust Dynamics Model

It is of high importance in the present study to further speed up the computation process of low-thrust trajectories because in the next section, in every trial to find the transfer starting times, we need to propagate the orbit motion for all satellites. To reduce the computational load, in this section, the orbital averaging technique will be used to derive two sets of averaged dynamics models for orbit raising and de-orbiting missions, and the numerical validations will be conducted to prove the accuracy of the averaged dynamics models.

Recalling the use of the orbital averaging technique presented in Sec. 2.5, the variations in the orbital elements (semi-major axis, eccentricity, and argument of perigee) over one revolution can be evaluated by integrating Eq. (6.20) in the eccentric anomaly from 0 to 2π:

$$\int_0^{2\pi} \frac{\mathrm{d}\boldsymbol{x}}{\mathrm{d}E}\mathrm{d}E = \int_0^{2\pi} \left[c_t \left(+\frac{\mathrm{d}\boldsymbol{x}}{\mathrm{d}E}\right)_t + c_i \left(+\frac{\mathrm{d}\boldsymbol{x}}{\mathrm{d}E}\right)_i\right] \mathrm{d}E \tag{6.21}$$

Being this a preliminary study, the Earth's shadow effect is not considered. No analytical solutions exist for Eq. (6.21). Noting that the eccentricity of LEO orbits is small (≤ 0.2), in this study we compute a Taylor expansion in power of the eccentricity for the inverse of the denominator of c_t and c_i up to $O(e^2)$.

6.2.1 Orbit Raising

The orbit raising mission in this study is assumed to raise the satellites from the parking orbits to the final circular orbits at the nominal altitude, i.e., $e_f = 0$; the final phasing angle adjustment is excluded from this preliminary study. According to Eq. (6.5), the errors in semi-major axis and eccentricity are given by

$$k_a = \frac{\Delta a}{a_f - a_0}, \quad k_e = -\frac{e}{e_0} \tag{6.22}$$

where $\Delta a = a_f - a$.

Then substituting Eq. (6.22) into Eq. (6.19) and carrying out the expansion, c_t and c_i can be approximated as

$$c_t \approx R, \quad c_i \approx -\frac{a_f - a_0}{\Delta a e_0} e R \tag{6.23}$$

where R is a binomial in the eccentricity, given by

$$R = 1 + \frac{a_f - a_0}{\Delta a e_0} \cos E e + \left(\frac{a_f - a_0}{\Delta a e_0}\right)^2 \frac{3\cos^2 E - 1}{2} e^2 \tag{6.24}$$

Substituting Eq. (6.23) into Eq. (6.20), and then carrying out the integration in E from 0 to 2π, after some manipulations, the variations in the orbital elements over one revolution can be derived:

$$\Delta a_{\text{rev}} = \frac{4\pi a^3}{\mu} \left[1 - \frac{(a_f - a_0)^2 + \Delta a^2 e_0^2}{4\Delta a^2 e_0^2} e^2\right] f \tag{6.25a}$$

$$\Delta e_{\text{rev}} = -\frac{\pi a^2}{\mu} \frac{a_f - a_0 + 2\Delta a e_0}{\Delta a e_0} e f \tag{6.25b}$$

$$\Delta \omega_{\text{rev}} = -\frac{\pi a^2}{\mu} \frac{a_f - a_0}{\Delta a e_0} e f \tag{6.25c}$$

6.2.2 De-Orbiting

According to Eqs. (6.5) – (6.7), the errors in semi-major axis and eccentricity are given by

$$k_a = \frac{\Delta a}{a_0 - a_{pf}}, \quad k_e = \Delta e \tag{6.26}$$

where, $a_{pf} = h_{pf} + R_\oplus$, $\Delta a = a_{pf} - a$, and $\Delta e = 1 - e$.

Similar to orbit raising, substituting Eq. (6.26) into Eq. (6.19) and carrying out the expansion, c_t and c_i can be approximated as

$$c_t \approx \Delta a D, \quad c_i \approx (a_0 - a_{pf}) \Delta e D \tag{6.27}$$

where D is a binomial in the eccentricity, given by

$$\begin{aligned} D = &\frac{D_0}{\left[(a_0 - a_{pf})^2 + \Delta a^2 + 2(a_0 - a_{pf}) \Delta a \cos E\right]^{1/2}} \\ &+ \frac{D_1}{\left[(a_0 - a_{pf})^2 + \Delta a^2 + 2(a_0 - a_{pf}) \Delta a \cos E\right]^{3/2}} e \\ &+ \frac{D_2}{\left[(a_0 - a_{pf})^2 + \Delta a^2 + 2(a_0 - a_{pf}) \Delta a \cos E\right]^{5/2}} e^2 \end{aligned} \tag{6.28}$$

with D_0, D_1 and D_2 being

$$\begin{aligned} D_0 &= 1 \\ D_1 &= (a_0 - a_{pf})\left[(a_0 - a_{pf}) + \Delta a \cos E\right] \\ D_2 &= \frac{a_0 - a_{pf}}{4}\{(a_0 - a_{pf})\left[4{(a_0 - a_{pf})}^2 + 3\Delta a^2\right] \\ &\quad + 2\left[5{(a_0 - a_{pf})}^2 + \Delta a^2\right]\Delta a \cos E + 3\,(a_0 - a_{pf})\,\Delta a^2 \cos 2E \\ &\quad - 2\left[{(a_0 - a_{pf})}^2 + \Delta a^2\right])\Delta a \cos 3E - 2\,(a_0 - a_{pf})\,\Delta a^2 \cos 4E\} \end{aligned} \tag{6.29}$$

Substituting Eq. (6.27) into Eq. (6.20), and then carrying out the integration in E from 0 to 2π, after some manipulations, the variations in the orbital elements over one revolution can be derived:

$$\begin{aligned} \Delta a_{\mathrm{rev}} = \frac{2a^3}{\mu}[\frac{1}{a_0 - a}\left(a_t^{elliF}\Delta a + a_i^{elliF}\sqrt{1-e^2}\Delta e\right) elliF \\ + (a_0 - a)\left(a_t^{elliE}\Delta a + a_t^{elliF}\sqrt{1-e^2}\Delta e\right) elliE]f \end{aligned} \tag{6.30}$$

$$\begin{aligned} \Delta e_{\mathrm{rev}} = f\left[\frac{1}{a_0 - a} + (a_0 - a)\right]\frac{a^2\sqrt{1-e^2}}{\mu}[e_t^{elliF}\sqrt{1-e^2}\Delta a \\ + e_i^{elliF}\,(a_0 - a_{pf})\,\Delta e]elliF \end{aligned} \tag{6.31}$$

$$\Delta\omega_{\mathrm{rev}} = \frac{3\pi R_E^2 J_2}{2a^2{(1-e^2)}^2}\left(5{\cos}^2 i - 1\right) \tag{6.32}$$

where a_t^{elliF}, a_i^{elliF}, a_t^{elliE} , e_t^{elliF} , e_i^{elliF} , e_t^{elliE} , e_i^{elliE} and are the binomials in the eccentricity, reported in Appendix B.1.

Eqs. (6.30) and (6.31) contain some elliptic integrals to be evaluated once per revolution:

$$elliF = \mathrm{elliptic}F\left(\pi,\ \frac{4\,(a_0 - a_{pf})\,\Delta a}{{\left[(a_0 - a_{pf}) + \Delta a\right]}^2}\right) \tag{6.33}$$

where

$$\mathrm{elliptic}F\,(\phi,\ \rho) = \int\limits_0^\phi \frac{1}{\sqrt{1 - \rho{\sin}^2\varphi}}\mathrm{d}\varphi \tag{6.34}$$

is the first kind of incomplete elliptic integral [94, Sec. 1.5], and

$$elliE = \mathrm{elliptic}E\left(\pi,\ \frac{4\,(a_0 - a_{pf})\,\Delta a}{{\left[(a_0 - a_{pf}) + \Delta a\right]}^2}\right) \tag{6.35}$$

where

$$\mathrm{elliptic}E\,(\phi,\ \rho) = \int\limits_0^\phi \sqrt{1 - \rho{\sin}^2\varphi}\mathrm{d}\varphi \tag{6.36}$$

is the second kind of incomplete elliptic integral [94, Sec. 1.5].

6.2.3 Numerical Validation

To verify the accuracy of the semi-analytical solutions, a comparison is conducted between the full dynamics integration and the semi-analytical solutions. Table 6.1 gives the characteristics of a stationary plasma thruster [116]. The mission parameters are presented in Table 6.2. Note that, for the full dynamics integration, the lower boundary for the eccentricity is set to 10^{-4} in order to avoid the singularity during the integration of the argument of perigee. In this study, the numerical integration is carried out using MATLAB R2020b running on a computer with Intel Core i7-8550U and 8GB RAM; the ODE solver is *ode45*, where the absolute and relative error tolerances are specified as 10^{-13}.

Table 6.1: *Thruster characteristics.*

P_{eng}, W	η_{eng}, %	I_{sp},s
150	39.23	1500

Table 6.2: *Mission parameters.*

	Initial conditions							
	m_0, kg	a_0, km	e_0		i_0, deg	ω_0, deg	ν_0, deg	
Mission			Full	Semi				Final conditions
Orbit raising	120	$R_\oplus +$ 500	10^{-2}	10^{-2}	87.9	0	30	$a_f = (R_\oplus + 1200)$ km, $e_f \leq 10^{-4}$
De-orbiting	120	$R_\oplus + 1200$	10^{-4}	0	87.9	0	30	$h_{pf} = 300$ km

Fig. 6.2 to Fig. 6.4 present the time histories of the orbital elements obtained by the full dynamics integration and the semi-analytical solutions for both missions.

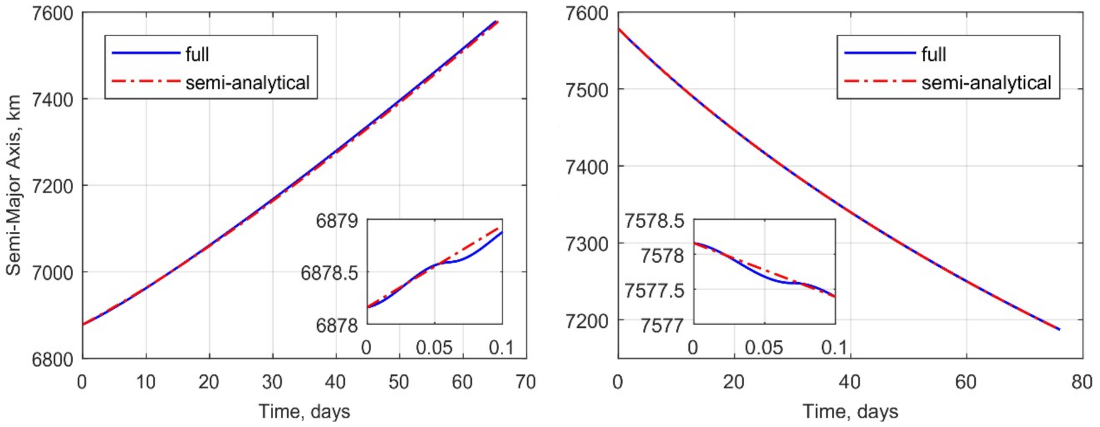

(a) *Orbit raising* **(b)** *De-orbiting*

Figure 6.2: *Time history of the semi-major axis.*

It can be seen from the figures that the semi-analytical solutions can eliminate the short period effects and give the averaged orbital elements. Fig. 6.2 – Fig. 6.4 show good agreement between the full dynamics integration and semi-analytical

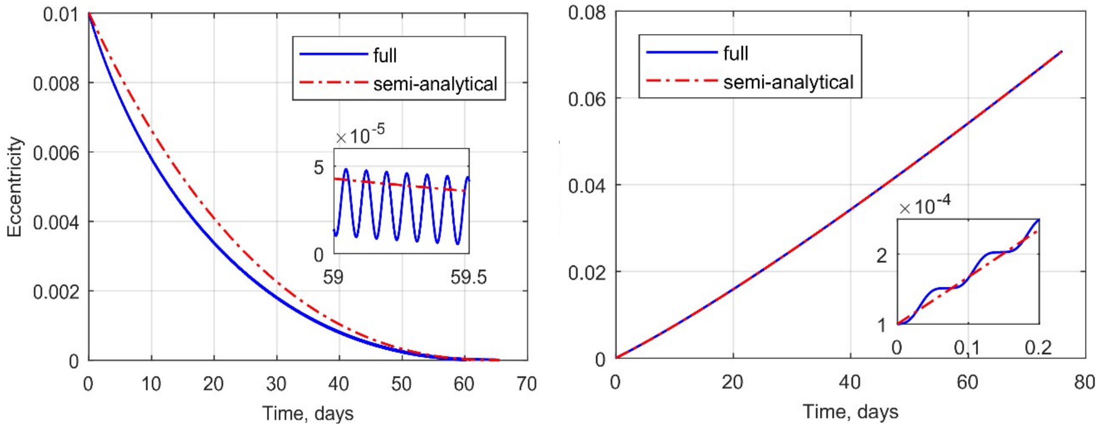

(a) *Orbit raising* **(b)** *De-orbiting*

Figure 6.3: *Time history of the eccentricity.*

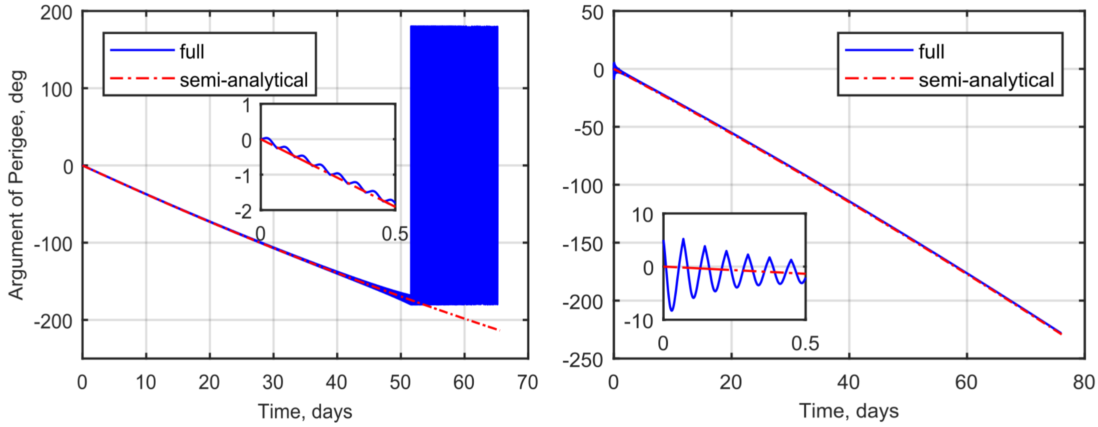

(a) *Orbit raising* **(b)** *De-orbiting*

Figure 6.4: *Time history of the argument of perigee.*

solutions. Although there exists a maximum error of less than 10^{-3} for the eccentricity in the orbit raising mission, which is introduced by the Taylor expansion, the semi-analytical results gradually convergence to the numerical integration and the final travel time is the same.

The results at the final time are presented in Table 6.3, again, showing good agreement.

Table 6.3: *Results at the final time.*

Mission	Full dynamics integration				Semi-analytical solutions			
	a_f, km	e_f	t_f, days	Δm_f, kg	a_f, km	e_f	t_f, days	Δm_f, kg
Orbit raising	7578.16	1.00×10^{-8}	65.20	3.06	7578.12	3.95×10^{-10}	65.55	3.08
De-orbiting	7187.32	7.08×10^{-2}	76.01	3.57	7186.82	7.10×10^{-2}	76.12	3.58

The computation time of the full dynamics integration and the semi-analytical

Table 6.4: *Computation time.*

Mission	Full dynamic integration	Semi-analytical solutions
Orbit raising	2.9739 s	0.0072 s
De-orbiting	3.1563 s	0.1706 s

solutions are compared in Table 6.4, in which the relative and absolute tolerance for the full dynamics integration are 10^{-6} and 10^{-9}, respectively. It can be seen that the computation load can be drastically reduced by using the semi-analytical solutions.

6.3 Self-Induced Collision Avoidance

With the analytical BEC control law and semi-analytical solutions, the orbital transfers from any starting times can be computed in short time. The next step is to deal with the transfer problem for multiple satellites, in which the problem of self-induced collision arises. In this section, the self-induced collision risk is quantitatively evaluated by miss distance, and then the problem of self-induced collision is solved by scheduling properly the timing to start transfer for every satellite for orbit raising and de-orbiting missions.

6.3.1 Miss Distance

The notion of miss distance in this study is redefined on two levels.

The first level is the miss distance between two satellites, the minimum relative distance between two satellites over the entire transfer, referred to as the satellite-pair miss distance, and denoted by d_{miss}. The satellite-pair miss distance between satellites Ath and Bth is given by

$$d_{\text{miss}}^{AB} = \min \delta r_{AB}\left(t\right), \quad t \in \left[t_0^{AB}, t_f^{AB}\right] \tag{6.37}$$

where, $\left[t_0^{AB}, t_f^{AB}\right]$ is the time interval within which both the Ath and Bth satellite are in the propulsive transfer phase, t_0^{AB} and t_f^{AB} are given by

$$t_0^{AB} = \max\left\{t_0^A, t_0^B\right\}, \quad t_f^{AB} = \min\left\{t_f^A, t_f^B\right\} \tag{6.38}$$

with t_0^A and t_f^A being the transfer starting and ending time of the Ath satellite, respectively,t_0^B and t_f^B being the transfer starting and ending time of the Bth satellite, respectively.

The second level is the miss distance of the constellation, the minimum satellite-pair miss distance of all satellite pairs from the constellation, referred to as the constellation miss distance, and denoted by D_{miss}. Supposing a constellation of N satellites, the constellation miss distance is given by

$$D_{\text{miss}} = \min_{1 \leq A < B \leq N} d_{\text{miss}}^{AB} \tag{6.39}$$

Through this assessment approach, the problem of avoiding the self-induced collision can be quantitatively transformed into increasing the constellation miss distance, which is equivalent to increasing the satellite-pair miss distance, whereas the satellite-pair miss distance is dependent on the relative motions of the satellites. Reminding that we are discussing planar transfer for co-planar satellites, the relative distance can be written as

$$\delta r_{AB} = \sqrt{r_A^2 + r_B^2 - 2 r_A r_B \cos\left(\phi_A - \phi_B\right)} \tag{6.40}$$

where $\phi = \omega + \nu$, referred to in this study as the true latitude.

Observing from Eq. (6.40), for given r_A and r_B, δr_{AB} will reach its minimum, i.e., $\delta r_{AB} = |r_A - r_B|$, when $\phi_A - \phi_B = 2k\pi$, where k is an integer. This implies that the satellite-pair miss distance is associated to the orbit radius difference when the latitude difference is a multiple of 2π. In this study, such an event is referred to as latitude resonance.

Since the transfer trajectories have been predefined for every satellite, the possible way to increase the miss distance is by properly scheduling the timing to start transfer for every satellite in the constellation. For no doubts the optimal solution for timing scheduling is to let all satellites start to transfer at the same timing, such that all satellites follow the same orbital path, and hence no collision will happen. However, in practical applications, the satellites may not be allowed to transfer at the same time; for example, the command for manoeuvring cannot be delivered to all satellites at the same time due to the distribution of ground stations. So, in this study, the transfer starting time is scheduled within the scope that the satellites do not start to transfer at the same time.

6.3.2 Transfer Starting Time Scheduling for Orbit Raising Mission

This section will schedule the transfer starting times for orbit raising mission.

Fig. 6.5 shows the satellite-pair miss distance as a function of the transfer starting time difference for two satellites with the initial true anomaly difference of $2\pi/20$ rad. The mission conditions are given by Table 6.1 and Table 6.2. The red crosses indicate that the latitude resonance does not happen, i.e., the latitude difference never reaches 2π. The blue dots and black circles indicate that the latitude resonance happens for one or multiple times. The difference is that, for the blue dots, the miss distance equals to the relative distance at one of the latitude resonances, while for the black circles, the miss distance equals to the relative distance at the first latitude resonance. The detailed interpretation on these three cases is reported in Appendix B.2. Note that for the case that the latitude resonance does not happen, a small increase in the transfer starting time difference will lead to a sharp decline in the miss distance.

Fig. 6.6 shows in detail for the blue dots and black circles of Fig. 6.5. In Fig. 6.6, all blue dots and black circles from Fig. 6.5 are replaced with black dots, and the x coordinates for the blue cross and red asterisk are equal to the critical transfer starting time differences δt_0^{safe} and $\delta t_0^{\text{safest}}$. δt_0^{safe} denotes the safe time interval between two successive transfers. If the transfer starting time difference between two satellites is equal to or larger than δt_0^{safe} , then the satellite-pair miss distance of these two satellites can be ensured higher than a given threshold (10 km for the present problem), and thus the transfers can be ensured safely enough. $\delta t_0^{\text{safest}}$ stands for the safest time interval between two successive transfers. If the

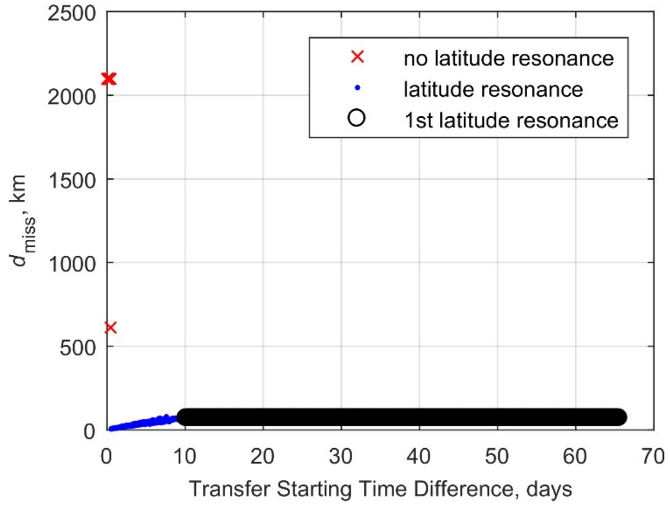

Figure 6.5: *Satellite-pair miss distance versus transfer starting time difference ($\delta\nu_0 = 2\pi/20$ rad).*

transfer starting time difference between two satellites is equal to or larger than $\delta t_0^{\text{safest}}$, then the satellite-pair miss distance of these two satellites will increase to a constant number (70.5 km for the present problem), in which case the transfers can be ensured safest.

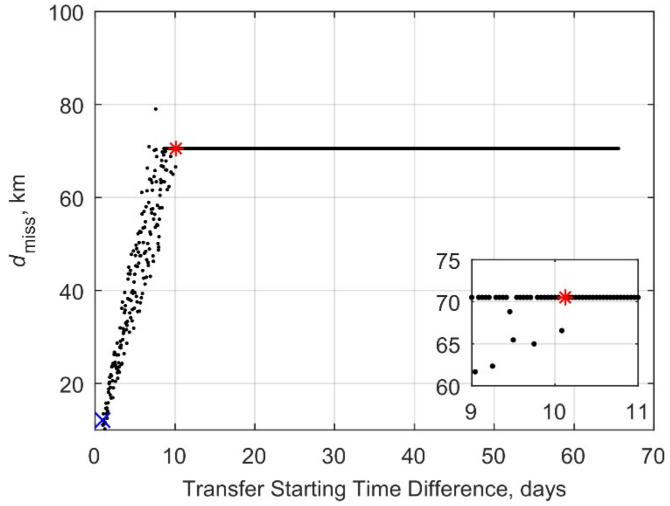

Figure 6.6: *Critical transfer starting time differences (cross: safe transfer starting time difference, asterisk: safest transfer starting time difference).*

By checking the satellite-pair miss distance for the satellite pairs with different initial relative phases and identifying the critical transfer starting time difference, the mission designers can preliminary estimate the self-induced collision risk and can have an idea about the safe time interval to do the next transfer.

Take as example 20 evenly spaced co-planar satellites. The mission conditions are given in Table 6.1 and Table 6.2. The critical transfer starting time difference is identified for the satellite pairs with different initial relative phases, presented

Table 6.5: *Critical transfer starting time difference for different satellite pairs ($d_{\text{miss}} \geq$ 10 km).*

	Critical transfer starting time	
$\delta\nu_0$, rad	δt_0^{safe}, *days*	$\delta t_0^{\text{safest}}$, *days*
$2\pi/20$	0.92	10.13
$4\pi/20$	0.92	12.42
$6\pi/20$	1.13	9.71
$8\pi/20$	1.04	11.58
$10\pi/20$	0.96	7.58
$12\pi/20$	0.96	10.13
$14\pi/20$	1.13	10.46
$16\pi/20$	1.25	7.58
$18\pi/20$	1.17	6.71
$20\pi/20$	1.21	9.42
$22\pi/20$	1.08	8.96
$24\pi/20$	1.25	8.54
$26\pi/20$	1.25	6.13
$28\pi/20$	1.29	7.38
$30\pi/20$	1.33	5.50
$32\pi/20$	1.54	5.46
$34\pi/20$	1.75	4.08
$36\pi/20$	1.83	3.83
$38\pi/20$	1.62	2.38

in Table 6.5. The figures of the satellite-pair miss distance versus the transfer starting time difference are presented in Appendix B.3.

6.3.3 Transfer Starting Time Scheduling for De-Orbiting Mission

This section will schedule the transfer starting times for de-orbiting mission.

Fig. 6.7 (a) shows the satellite-pair miss distance as a function of the transfer starting time difference for two satellites with the initial true anomaly difference of $2\pi/8$ rad; the red crosses and black dots indicate the cases that the latitude resonance does not happen and does happen, respectively. Fig. 6.7 (b) is the magnification for Fig. 6.7 (a) in terms of the cases that the latitude resonance happens. The mission conditions are given in Table 6.1 and Table 6.2. Similarly to Fig. 6.5, for the case that the latitude resonance does not happen, a small increase in the transfer starting time difference will lead to a sharp decline in the miss distance.

As shown in Fig. 6.7, for de-orbiting missions, the influence of the transfer starting time difference on the satellite-pair miss distance is not as clear as orbit raising missions (shown in Fig. 6.5 and Fig. 6.6). This is due to the fact that the de-orbiting trajectories are elliptical and hence the relative geometry of two de-orbiting trajectories are more complicated than the near-circular orbit raising trajectories. Therefore, we are not able to identify the critical transfer starting time difference for the de-orbiting missions in this preliminary study. Instead, the timing scheduling is done with the aid of multi-objective optimisation.

The first objective is maximising the constellation miss distance, i.e. minimising the self-induced collision risk. The second objective is minimising the total transfer time, from the first satellite starting the transfer to the last satellite

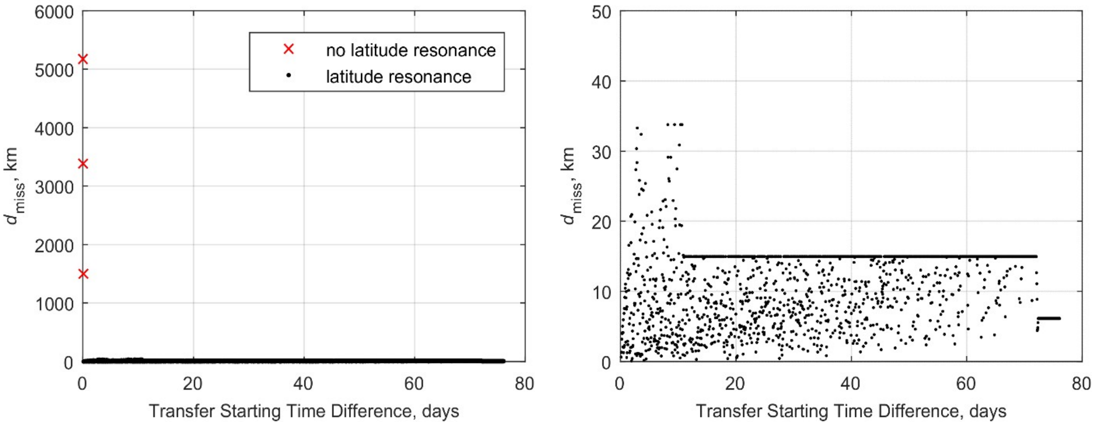

(a) *All cases.* **(b)** *Cases that the latitude resonance happens.*

Figure 6.7: *Satellite-pair miss distance versus transfer starting time difference* ($\delta\nu_0 = 2\pi/8$ *rad).*

finishing the transfer. This multi-objective optimisation problem is modelled as

$$J_1 = -D_{\mathrm{miss}} \tag{6.41a}$$

$$J_2 = \quad t_{\mathrm{total}} \tag{6.41b}$$

where the objective functions J_1 and J_2 are to be minimised, and t_{total} is the total transfer time, given by

$$t_{\mathrm{total}} = \max_{1 \leq B \leq N} \left\{ t_f^B \right\} - \min_{1 \leq A \leq N} \left\{ t_0^A \right\} \tag{6.42}$$

with N being the number of satellites in the constellation, t_0^A and t_f^B being the transfer starting and ending time of the Ath and Bth satellite, respectively.

Take as an example of 8 evenly spaced co-planar satellites. The mission conditions are given in Table 6.1 and Table 6.2. A de-orbiting strategy is also considered to remove the satellites in four groups, two satellites in each group, as shown in Fig. 6.8. In this figure, the satellites from different groups are represented by different colours; $t_{00} - t_{03}$ indicate the transfer starting time of each group, and the satellites from the same group start to de-orbit at the same timing. The reason to propose such a strategy is because the satellite-pair miss distance of the satellites in opposite positions is maximum if they start to de-orbit at the same time. A multi-objective global optimiser is used to search for the Pareto-front solutions through a multi-agent-based search approach hybridized with a domain decomposition technique [85]. The lower and upper bounds for the design variables, i.e. transfer starting time, are given in Table 6.6. Here, t_{00} is set to 0 and the minimum acceptable constellation miss distance is set to 5 km.

The optimisation results are presented in Fig. 6.9 and Table 6.7, implying that a trade-off consideration for the constellation miss distance and the total transfer time is needed. Note that the constellation miss distance considering the RAAN shift due to J_2 perturbation is also verified a posteriori and presented in Table 6.7. In general, the constellation miss distance considering the RAAN shift satisfies

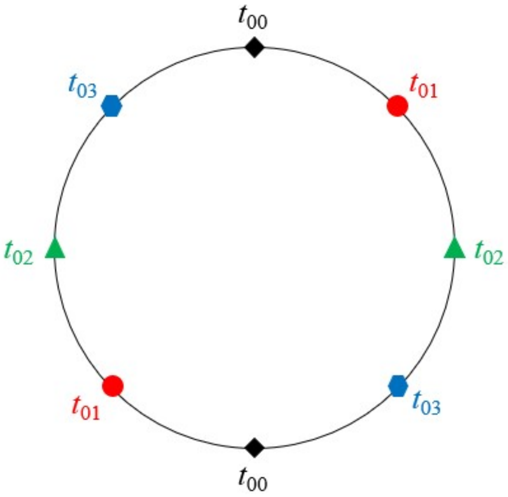

Figure 6.8: *De-orbiting strategy.*

Table 6.6: *Lower and upper bounds for the transfer starting time.*

	Lower bounds, days	Upper bounds, days
t_{00}	0	0
t_{01}	15	60
t_{02}	30	60
t_{03}	45	60

the lower bound for D_{miss} ($\geq$ 5 km) and it is larger than the constellation miss distance that does not consider the RAAN shift, except for few cases.

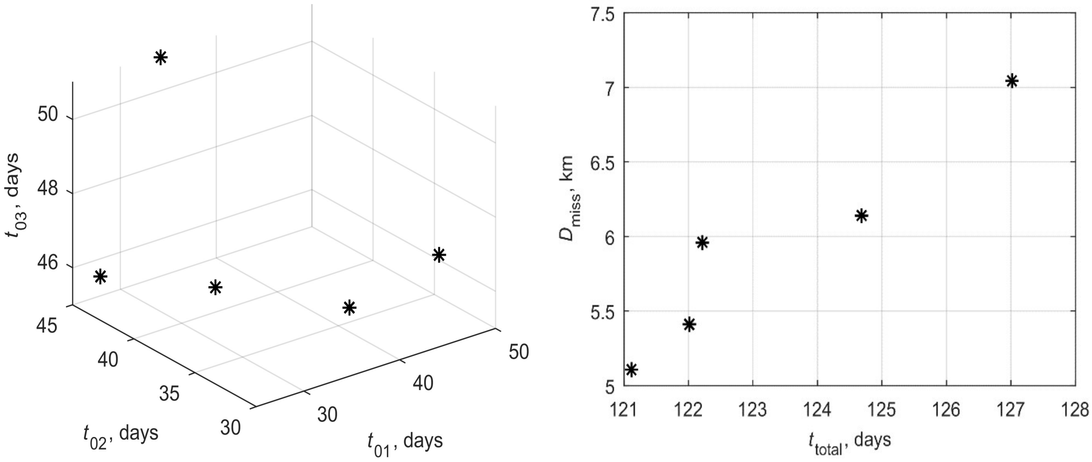

(a) *Transfer starting time.*

(b) *Pareto-front solutions – constellation miss distance versus total transfer time.*

Figure 6.9: *Optimization results ($D_{\text{miss}} \geq$ 5 km).*

Table 6.7: *Optimization results ($D_{\text{miss}} \geq 5$ km).*

t_{01}, days	t_{02}, days	t_{03}, days	t_{total}, days	D_{miss}, km	A posteriori D_{miss}, km
36.46	42.30	45	121.12	5.11	9.65
38.92	33.28	45.90	122.01	5.41	5.51
25.34	43.00	46.10	122.22	5.96	9.65
48.57	33.50	46.47	124.69	6.14	3.16
34.19	44.99	50.90	127.02	7.04	9.65

CHAPTER 7

Conclusions

As constellations with large numbers of satellites become more achievable and appealing, critical challenges in terms of cost, safety threat, computational effort, etc., have been posed to constellation studies. This thesis responds to the challenges brought by the surge in constellations by performing mission analysis and design for four key phases of constellation life cycle.

In this chapter the main results of this thesis are summarised and commented. On the base of the findings of this study, the limitations and future work are given.

7.1 Summary and Findings

In the following the major findings and advancements are discussed separately along with a summary of the methods and applications developed.

7.1.1 Constellation Design

A part of the main contents of this thesis is constellation design, as presented in Chap. 3. It is an imperative pre-mission phase that strongly affects the system cost and performance [2, pp. 673]. Given the objective to reduce cost, a systematic method was developed for multi-criteria design of continuous global coverage Walker and SoC constellations, allowing seven critical constellation properties to be optimised in a traded off way, where the constellation properties refer to constellation performances or costs. Particularly, the self-induced collision property was considered as a design criterion to respond to the challenge of safety threat. In this method, the quantitative relationship between constellation configuration and properties was established. To be specific:

- the constellation configuration was represented by a set of characteristic parameters, with which all the configuration-related parameters of a Walker or SoC constellation can be determined;
- the constellation properties were quantitatively assessed by a series of indexes, where the indexes were modelled as functions of the characteristic parameters.

Moreover, this quantitative relationship also revealed the influence of constellation configuration on properties and thus helped analyse the trade-offs between properties. Based on the quantitative relationship, a multi-objective optimisation problem was formulated and then solved with the support of a multi-objective global optimiser [85]. By replacing the mission-related parameters of the multi-objective optimisation problem with required values, the proposed method can be promptly applied to the multi-criteria design for any mission. As an implementation of the proposed method, some globally optimal constellations were found for a 1-fold LEO mission and for a 4-fold MEO mission; compared to the existing constellations (Iridium, GPS, and Galileo), the new designed constellations showed advantages and disadvantages from different aspects, demonstrating the need of trade-off for constellation design.

7.1.2 Constellation Deployment

The second topic of this thesis is constellation low-thrust deployment through J_2 perturbations, as presented in Chap. 4, which corresponds to the launch and build-up properties in constellation design. Given a first objective to increase revenue, a four-phase deployment scheme was proposed, in which an out-of-plane thrusting phase was introduced to accelerate the deployment. Given a second objective to reduce computational effort for the integrated design of a deployment mission using low-thrust propulsion, analytical time-allocation methods were developed to determine the times taken for separate phases, allowing the RAAN and AoL separation completed at the ends of phase 3 and phase 4, respectively. Especially, the times of the first three phases were optimised, allowing the time and fuel consumption for RAAN minimised at the same time. Finally, two case studies of large constellation deployment – a OneWeb-like constellation and a sun-synchronous constellation – were presented, showing how the proposed approach was implemented for missions with time and fuel consumption requirements. In general, the fuel consumption of the proposed J_2-thrust strategy is higher than the traditional J_2-only strategy, due to the out-of-plane thrusting, but the time is shorter and thus the revenue flow can start earlier. This provides mission designers a fresh thinking to reduce cost by trading off the revenue of a faster deployment and the cost of higher fuel consumption.

7.1.3 Low Earth Orbit Constellation De-Orbiting

The third topic of this thesis is LEO constellation low-thrust de-orbiting through natural perturbations, as presented in Chap. 5, which corresponds to the EoL disposal property in constellation design. Given the objective to reduce negative impact on LEO environment, two de-orbiting strategies for EoL disposal from LEO were investigated: the perigee decrease strategy and the de-orbiting corridor strategy. With the closed-loop control laws and semi-analytical solutions derived, a series of initial conditions over the entire LEO region were rapidly propagated, and subsequently, a set of maps were obtained, showing the Δv-budget and de-orbiting time for de-orbiting from LEO with the two strategies. From the maps, it was observed that if there was no limit on Δv-budget, the perigee decrease strategy was able to achieve re-entry within 5 years from any initial altitudes up to 2000 km, while the ability of the de-orbiting corridor strategy depended on the initial altitude and inclination, as well as the area-to-mass ratio of passive de-orbiting device. By comparing the Δv-budget, another set of maps were obtained, showing the application conditions of the two strategies to de-orbit within given time requirements. From the maps, it was concluded that mostly the perigee decrease strategy was superior, because the de-orbiting corridor strategy was involved in an expensive inclination change; however, there still existed many cases, especially in high-altitude LEO region, where the de-orbiting corridor strategy was more attractive.

7.1.4 Low Earth Orbit Co-Planar Satellites Planar Transfer Phases Considering Self-Induced Collision Avoidance

The last key phase is the planar low-thrust orbit raising and de-orbiting for LEO coplanar satellites, by taking into account the self-induced collision avoidance which is crucial to the safety operation of a constellation, as presented in Chap. 6. The design was conducted via two layers: the first layer was the low-thrust trajectory design for a single satellite; the second layer was the transfer starting time design for all satellites. In the first layer a closed-loop Blended Error-Correction Control law and the corresponding semi-analytical solutions were derived in Sec. 6.1 and Sec. 6.2, respectively. In the second layer, the problem of reducing the self-induced collision risk was quantitatively converted to increasing the miss distance, and it was solved by designing the transfer starting time for each satellite. For the orbit raising mission, thanks to the near-circular transfer trajectories, we were able to identify the safe time interval between two successive transfers, and the miss distance could be ensured larger than a given safety threshold. For the de-orbiting mission, with the help of a multi-objective optimiser [85], we obtained the optimal transfer starting times of all satellites, which corresponded to a set of Pareto-front solutions of miss distance maximisation and total transfer time minimisation. Although the test transfers were solved for 20 satellites for orbit raising and 8 satellites for de-orbiting, the same approach could be followed to address a similar problem.

7.1.5 Closed-Loop Control Law Design

Given the objective to reduce computational effort for the integrated design of constellation missions using low-thrust propulsion, throughout the research we were pursuing closed-loop control laws to directly apply to every satellite in the constellation. In order to achieve this goal, we resorted to heuristic methods.

In Sec. 5.2, two closed-loop control laws were developed by using the Lyapunov method. Given the objective to reduce negative impact on LEO environment as much as possible, constellations were desired to be fast removed, and thus the control laws were selected to send the candidate Lyapunov functions to zero at the fastest rate. Subsequently, stability analyses were performed, proving that the proposed control laws were stable and thus robust to any initial conditions. By comparing against the minimum-time open-loop control laws obtained with indirect methods, the proposed control laws were demonstrated to be sub-optimal. It has to be noted that for the perigee decrease strategy, although it was proposed many years ago and have been widely used in real missions, we did not find any similar work on this topic; in this context, our work filled the gap in the study of this strategy.

In Sec. 6.1, a Blended Error-Correction control law was developed. Two simple but efficient in-plane control laws were considered and blended: the tangential thrusting to change the semi-major axis and the inertial thrusting to change the eccentricity. A weighting parameter was assigned to each control law in order to offset the error of the osculating orbit towards the target orbit. A normalisation procedure was then performed to make the thrust direction along the desired one. Although not optimal, the proposed control law had a clear physical meaning, able to adjust the thrust direction in a self-adaptive way.

7.1.6 Analytical and Semi-Analytical Solutions of Low-Thrust Motion

In parallel, a considerable effort was devoted to the reduction of the computational load required to propagate the orbital motion under the effect of a low-thrust acceleration.

In Sec. 4.2, two sets of analytical solutions were derived for circular low-thrust transfer subject to the continuous tangential thrusting and the intermittent yaw thrusting. Comparing with the other analytical techniques by previous authors, the scope of application of the formulae presented here was not restricted to constant thrust acceleration. Especially, to make the analytical integration for orbital elements achievable, we made use of the orbital averaging technique to filter out the short-term oscillations related to AoL.

In Sec. 5.3 and Sec. 6.2, the semi-analytical solutions for low-thrust transfer, i.e. the averaged low-thrust dynamics models, were derived by using the orbital averaging technique. In particular, to make the analytical integration for variations in orbital elements achievable, some approximations were introduced to the exact dynamics model by means of the Fourier series expansion and the Taylor expansion.

The numerical tests, presented in this dissertation (see Sec. 4.5, Sec. 5.4 and Sec. 6.2), have shown that the combination of accuracy and computational cost of these analytical and semi-analytical solutions renders them advantageous compared to numerical integration schemes.

7.2 Limitations and Future Work

Despite the achievements of the research presented in this thesis, some limitations remain. They are discussed here including possible future work to address them.

In Chap. 3, the proposed constellation design method has shown its ability to optimise multiple constellation performances and costs. However, it has to be noted that this study is focused on circular Walker and SoC constellations, which have been widely applied in practical applications (e.g. GPS [99], Galileo [82], and Iridium [83, 84]); in the meanwhile, there still exists other beautiful design, such as elliptical Draim [117], Flower [20], etc. Moreover, the Flower constellation has been proved able to encompass many symmetric constellations, apart from SoC because it is asymmetric. So in future research the Flower constellation can be used as a more general case. Another limitation is that the proposed constellation design method is not suitable for large constellations, but only for small- and middle-sized constellations, because the constellation properties considered here may not be priority for large constellations. For example, the coverage and robustness properties are no more important design criteria for large constellations containing hundreds to thousands of satellites. So in future research other design criteria for large constellations can be investigated and added.

In Chap. 4, the proposed deployment scheme has shown its advantage of accelerating the RAAN separation. However, it has to be noted that the prerequisite of applying this deployment scheme is that the low-thrust engine has to be powerful enough; that is to say, the thrust force and specific impulse require to be large enough, otherwise the it will be meaningless to add the out-of-plane thrusting phase. For example in the FORMOSAT-3/COSMIC mission [32], the thrust acceleration is on the order of 10^{-5} km/s^2, which is relatively large compared to those very low thrust missions. If we reduce the thrust acceleration to 10^{-7} km/s^2, the optimal solution will always be $\gamma^* = 0$, i.e. the traditional J_2-based method, as shown in Fig 7.1. Another limitation of the proposed deployment scheme is that the final separation in RAAN slightly deviates from the desired value, as shown in Fig. 4.9 and Fig. 4.14, due to the interaction between RAAN and AoL in phase 4. Such error is inevitable as long as the separation in RAAN and AoL is performed separately [34]. For future research, it would be of interest to address a coupled control problem to simultaneously separate the RAAN and AoL. A third limitation is that in this study, all satellites are assumed to remain in circular orbits throughout the deployment, and the analytical solutions are valid for circular low-thrust transfer. To examine this circular assumption, here we per-

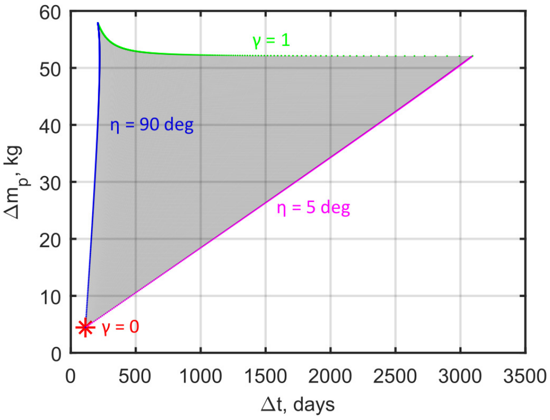

Figure 7.1: *Objective space, for the FORMOSAT-3/COSMIC mission to achieve a 30 deg RAAN separation with a thrust acceleration of 10^{-7} km/s^2.*

form a comparison between analytical and numerical solutions for different initial eccentricities, taking as example the fifth satellite in the sixth plane of the sun-synchronous constellation, given 1 year time requirement for RAAN separation. Note that the analytical solutions assume constantly zero eccentricity. Table 7.1 presents the final errors of the analytical solutions relative to the numerical solutions in terms of the semi-major axis, inclination, RAAN, AoL, and spacecraft mass. As indicated in the table, the errors remain very small until $e_0 = 10^{-2}$, higher than which the analytical solution to AoL cannot keep enough accuracy.

Table 7.1: *Final errors for different initial eccentricity, for satellite 5 in plane 6, sun-synchronous constellation.*

e_0	ϵ_a, km	ϵ_i, deg	ϵ_Ω, deg	ϵ_u, deg	ϵ_m, kg
0	−0.0799	−0.0005	0.0087	0.4806	−0.0008
10^{-4}	−0.0793	−0.0005	0.0087	0.4546	−0.0008
10^{-3}	−0.0738	−0.0005	0.0079	0.2217	−0.0008
10^{-2}	−0.0179	−0.0004	−0.0718	−2.0000	−0.0007

In Chap. 5, the application conditions of the two de-orbiting strategies have been identified and clearly described with maps. However, it has to be noted that the control laws in this study are designed to be minimum-time in order to reduce negative impact on LEO environment as much as possible. For future research, to better compare the two strategies in terms of the Δv-budget, a minimum-fuel de-orbiting can also be investigated, and in this case, the averaged low-thrust dynamics model derived would be helpful to reduce the computational load if using numerical optimisation methods. In addition to LEO constellations, one possible research topic is the EoL disposal design for MEO and geosynchronous constellations; the possible de-orbiting strategies could be removing to graveyard orbit or exploiting the de-orbiting corridors with the aid of passive de-orbiting devices. Zuiani [118] has performed a preliminary study on the combined use of low-thrust and SRP for EoL disposal from MEO. The results showed that the contribution of SRP consistently helped in reducing thrust and propellant requirements. Another idea for future research is that the deployment and control of a passive de-orbiting device with large enough area-to-mass ratio (that for a 150 kg spacecraft would translate into 450 m^2 of reflective surface with $A/m = 3$ m^2/kg) implies a higher level of complexity and mass of the mechanisms onboard. Such increase in the complexity and spacecraft mass is not considered in this study although one could argue that the saving in propellant mass or de-orbiting time. But the point which can be ensured is that such passive de-orbiting device will not cause additional negative impact on space environment due to the material it uses, in the sense that no fragment will generate if an object penetrates the augmentation area.

Concerning the work of Chap. 6, two open points remain for future research. The first one is the RAAN drifting due to J_2. In order to focus on analysing the planar behaviour only, this study did not consider the RAAN drifting. However, by checking a posteriori, in some cases the RAAN drifting did have negative influence on self-induced collision. The second problem to address is the transfer of non-planar satellites, i.e. multi-satellite and multi-plane. The two-layer-study methodology proposed in this study, i.e. first designing trajectory and then solving collision avoidance, can be used to address a more general problem.

In addition to the open points above mentioned, some other possible topics are the studies of elliptical-orbit constellations providing intermittent or local coverage, as they are out of the scope of this thesis.

APPENDIX $\mathcal{A}$

Appendix for Chapter 5

The appendix for Chapter 5 is shown here.

A.1 Derivation of Eq. (5.34)

The derivation of Eq. (5.34) is presented as follows.

Let $x = \sqrt{6}\cos(E/2)$ and $y = \sqrt{5 - 3\cos E}$. We do not know yet if the term $\mathbb{i}\ln(x + \mathbb{i}y)$ is real or complex.

Let us start by assuming $\mathbb{i}\ln(x + \mathbb{i}y)$ equal to a real number z. Then there will be

$$x + \mathbb{i}y = \exp(-\mathbb{i}z) = \cos z - \mathbb{i}\sin z \tag{A.1}$$

Thus, the following equalities hold

$$x = \cos z, \quad y = -\sin z \tag{A.2}$$

However, because $\cos^2 z + \sin^2 z = 1$, while

$$x^2 + y^2 = 6\cos^2\frac{E}{2} + 5 - 3\cos E = 3 + 3\cos E + 5 - 3\cos E = 8 \neq 1 \tag{A.3}$$

the term $\mathbb{i}\ln(x + \mathbb{i}y)$ is complex.

Let $\mathbb{i}\ln(x + \mathbb{i}y) = \sigma + \mathbb{i}\varsigma$, where σ and $\mathbb{i}\varsigma$ are the real and imaginary parts, respectively. Then there will be

$$x + \mathbb{i}y = \exp(\varsigma - \mathbb{i}\sigma) = \exp\varsigma\,(\cos\sigma - \mathbb{i}\sin\sigma) \tag{A.4}$$

Thus, the following equalities hold

$$x = \exp\varsigma\cos\sigma, \quad y = -\exp\varsigma\sin\sigma \tag{A.5}$$

from which, σ and ς can be solved in terms of x and y as

$$\sigma = -\tan^{-1}\frac{y}{x}, \quad \varsigma = \ln\sqrt{x^2+y^2} \tag{A.6}$$

Recalling from Eq. (A.3) that $x^2+y^2=8$, so we have

$$\mathbb{i}\ln\left(x+\mathbb{i}y\right) = -\tan^{-1}\frac{y}{x} + \mathbb{i}\ln\sqrt{8} \tag{A.7}$$

namely,

$$\mathbb{i}\ln\left(\sqrt{6}\cos\frac{E}{2} + \mathbb{i}\sqrt{5-3\cos E}\right) = -\sin\frac{E}{2}\tan^{-1}\frac{\sqrt{6}\cos\frac{E}{2}}{\sqrt{5-3\cos E}} + \mathbb{i}\ln\sqrt{8} \tag{A.8}$$

A.2 Expressions in Eq. (5.38)

The expressions of b_k^F and b_k^E (with $k=0$ to 4) in Eq. (5.38) are given as follows.

$$b_0^F = 1 \tag{A.9a}$$

$$b_1^F = -\frac{2}{c_i^2}\left(2c_a^2 + c_i^2\right) \tag{A.9b}$$

$$b_2^F = \frac{2}{3c_i^4}\left(16c_a^4 + 16c_a^2c_i^2 + 3c_i^4\right) \tag{A.9c}$$

$$b_3^F = -\frac{2}{15c_i^6}\left(256c_a^6 + 384c_a^4c_i^2 + 158c_a^2c_i^4 + 15c_i^6\right) \tag{A.9d}$$

$$b_4^F = \frac{2}{105c_i^8}\left(6144c_a^8 + 12288c_a^6c_i^2 + 8000c_a^4c_i^4 + 1856c_a^2c_i^6 + 105c_i^8\right) \tag{A.9e}$$

$$b_0^E = 0 \tag{A.10a}$$

$$b_1^E = \frac{4}{c_i^2}\left(c_a^2 + c_i^2\right) \tag{A.10b}$$

$$b_2^E = -\frac{16}{3c_i^4}\left(2c_a^4 + 3c_a^2c_i^2 + c_i^4\right) \tag{A.10c}$$

$$b_3^E = \frac{4}{15c_i^6}\left(128c_a^6 + 256c_a^4c_i^2 + 151c_a^2c_i^4 + 23c_i^6\right) \tag{A.10d}$$

$$b_4^E = -\frac{64}{105c_i^8}\left(192c_a^8 + 480c_a^6c_i^2 + 406c_a^4c_i^4 + 129c_a^2c_i^6 + 11c_i^8\right) \tag{A.10e}$$

A.3 Expressions in Eq. (5.38)

The expressions of $(\text{fun}_k)_x$ ($k = 0$ to 4 and $x = a, e, i, \Omega, \omega$) that appear in Eq. (5.38) are given as follows.

$$(\text{fun}_0)_a = 4E \tag{A.11a}$$

$$(\text{fun}_1)_a = 2\sin(2\omega + 2E) \tag{A.11b}$$

$$(\text{fun}_2)_a = \sin(4\omega + 4E) \tag{A.11c}$$

$$(\text{fun}_3)_a = \frac{2}{3}\sin(6\omega + 6E) \tag{A.11d}$$

$$(\text{fun}_4)_a = \frac{1}{2}\sin(8\omega + 8E) \tag{A.11e}$$

$$(\text{fun}_0)_e = \frac{1}{2}(8\sin E - e\sin 2E - 6eE) \tag{A.12a}$$

$$\begin{aligned}(\text{fun}_1)_e = \frac{1}{24}[\; & 48\sin(2\omega + E) - 36e\sin(2\omega + 2E) \\ & +16\sin(2\omega + 3E) - 3e\sin(2\omega + 4E) - 12eE\cos 2\omega]\end{aligned} \tag{A.12b}$$

$$\begin{aligned}(\text{fun}_2)_e = \frac{1}{60}[& -15e\sin(4\omega + 2E) + 40\sin(4\omega + 3E) \\ & - 45e\sin(4\omega + 4E) + 24\sin(4\omega + 5E) - 5e\sin(4\omega + 6E)]\end{aligned} \tag{A.12c}$$

$$\begin{aligned}(\text{fun}_3)_e = \frac{1}{560}[& -\;70e\sin(6\omega + 4E) + 224\sin(6\omega + 5E) \\ & - 280e\sin(6\omega + 6E) + 160\sin(6\omega + 7E) - 35e\sin(6\omega + 8E)]\end{aligned} \tag{A.12d}$$

$$\begin{aligned}(\text{fun}_4)_e = \frac{1}{2520}[& -210e\sin(8\omega + 6E) + 720\sin(8\omega + 7E) \\ & - 945e\sin(8\omega + 8E) + 560\sin(8\omega + 9E) - 126e\sin(8\omega + 10E)]\end{aligned} \tag{A.12e}$$

$$\begin{aligned}(\text{fun}_0)_i = \frac{1}{12}[\; & -3e\left(\frac{7}{\sqrt{1-e^2}} + 1\right)\sin E + 3\left(\frac{1+e^2}{\sqrt{1-e^2}} - 1\right)\sin 2E \\ & - e\left(\frac{1}{\sqrt{1-e^2}} - 1\right)\sin 3E + 3e\left(\frac{1}{\sqrt{1-e^2}} - 1\right)\sin(2\omega - E) \\ & - \frac{18e}{\sqrt{1-e^2}}\sin(2\omega + E) + 3\left(\frac{1+e^2}{\sqrt{1-e^2}} + 1\right)\sin(2\omega + 2E) \\ & - e\left(\frac{1}{\sqrt{1-e^2}} + 1\right)\sin(2\omega + 3E) + 6\left(\frac{1+e^2}{\sqrt{1-e^2}} + 1\right)E \\ & + 6\left(\frac{1+e^2}{\sqrt{1-e^2}} - 1\right)E\cos 2\omega\;]\end{aligned} \tag{A.13a}$$

$$
\begin{aligned}
(\mathrm{fun}_1)_i = \frac{1}{120}\{&[-30e\cos(\omega - E) + 30\cos(\omega + 2E) \\
&- 10e\cos(\omega + 3E) + 30e\cos(3\omega + E) \\
&- 30\cos(3\omega + 2E) + 15\cos(3\omega + 4E) \\
&- 6e\cos(3\omega + 5E)]\sin\omega + [30e\sin(\omega - E) \\
&+ 30\left(1 + e^2\right)\sin(\omega + 2E) - 10e\sin(\omega + 3E) \\
&- 30e\sin(3\omega + E) + 30\left(1 + e^2\right)\sin(3\omega + 2E) \\
&+ 15\left(1 + e^2\right)\sin(3\omega + 4E) - 6e\sin(3\omega + 5E) \\
&- 180e\sin(\omega + E) - 60e\sin(3\omega + 3E)]\frac{\cos\omega}{\sqrt{1 - e^2}} \\
&+ 30\left(\frac{1 + e^2}{\sqrt{1 - e^2}} + 1\right)E + 30\left(\frac{1 + e^2}{\sqrt{1 - e^2}} - 1\right)E\cos 2\omega\}
\end{aligned}
\tag{A.13b}
$$

$$
\begin{aligned}
(\mathrm{fun}_2)_i = \frac{1}{840}\{&[210e\cos(3\omega + E) - 210\cos(3\omega + 2E) \\
&+ 105\cos(3\omega + 4E) - 42e\cos(3\omega + 5E) \\
&+ 70e\cos(5\omega + 3E) - 105\cos(5\omega + 4E) \\
&+ 70\cos(5\omega + 6E) - 30e\cos(5\omega + 7E)]\sin\omega \\
&+ [-210e\sin(3\omega + E) + 210\left(1 + e^2\right)\sin(3\omega + 2E) \\
&+ 105\left(1 + e^2\right)\sin(3\omega + 4E) - 42e\sin(3\omega + 5E) \\
&- 70e\sin(5\omega + 3E) + 105\left(1 + e^2\right)\sin(5\omega + 4E) \\
&+ 70\left(1 + e^2\right)\sin(5\omega + 6E) - 30e\sin(5\omega + 7E) \\
&- 420e\sin(3\omega + 3E) - 252e\sin(5\omega + 5E)]\frac{\cos\omega}{\sqrt{1 - e^2}}\}
\end{aligned}
\tag{A.13c}
$$

$$\begin{aligned}
(\mathrm{fun}_3)_i = \frac{1}{5040}\{&[420e\cos(5\omega+3E) - 630\cos(5\omega+4E) \\
&+ 420\cos(5\omega+6E) - 180e\cos(5\omega+7E) \\
&+ 252e\cos(7\omega+5E) - 420\cos(7\omega+6E) \\
&+ 315\cos(7\omega+8E) - 140e\cos(7\omega+9E)]\sin\omega \\
&+ [-420e\sin(5\omega+3E) + 630\left(1+e^2\right)\sin(5\omega+4E) \\
&+ 420\left(1+e^2\right)\sin(5\omega+6E) - 180e\sin(5\omega+7E) \\
&- 252e\sin(7\omega+5E) + 420\left(1+e^2\right)\sin(7\omega+6E) \\
&+ 315\left(1+e^2\right)\sin(7\omega+8E) - 140e\sin(7\omega+9E) \\
&- 1512e\sin(5\omega+5E) - 1080e\sin(7\omega+7E)]\frac{\cos\omega}{\sqrt{1-e^2}}\}
\end{aligned} \tag{A.13d}$$

$$\begin{aligned}
(\mathrm{fun}_4)_i = \frac{1}{55440}\{&[2772e\cos(7\omega+5E) - 4620\cos(7\omega+6E) \\
&+ 3465\cos(7\omega+8E) - 1540e\cos(7\omega+9E) \\
&+ 1980e\cos(9\omega+7E) - 3465\cos(9\omega+8E) \\
&+ 2772\cos(9\omega+10E) - 1260e\cos(9\omega+11E)]\sin\omega \\
&+ [-2772e\sin(7\omega+5E) + 4620\left(1+e^2\right)\sin(7\omega+6E) \\
&+ 3465\left(1+e^2\right)\sin(7\omega+8E) - 1540e\sin(7\omega+9E) \\
&- 1980e\sin(9\omega+7E) + 3465\left(1+e^2\right)\sin(9\omega+8E) \\
&+ 2772\left(1+e^2\right)\sin(9\omega+10E) - 1260e\sin(9\omega+11E) \\
&- 11880e\sin(7\omega+7E) - 9240e\sin(9\omega+9E)]\frac{\cos\omega}{\sqrt{1-e^2}}\}
\end{aligned} \tag{A.13e}$$

$$\begin{aligned}
(\mathrm{fun}_0)_\Omega = \frac{1}{12}[&-3e\left(\frac{5}{\sqrt{1-e^2}}-1\right)\cos E + 3\left(\frac{1+e^2}{\sqrt{1-e^2}}-1\right)\cos 2E \\
&- e\left(\frac{1}{\sqrt{1-e^2}}-1\right)\cos 3E - 3e\left(\frac{1}{\sqrt{1-e^2}}-1\right)\cos(2\omega-E) \\
&+ \frac{18e}{\sqrt{1-e^2}}\cos(2\omega+E) - 3\left(\frac{1+e^2}{\sqrt{1-e^2}}+1\right)\cos(2\omega+2E) \\
&+ e\left(\frac{1}{\sqrt{1-e^2}}+1\right)\cos(2\omega+3E) + 6\left(\frac{1+e^2}{\sqrt{1-e^2}}-1\right)E\sin 2\omega\ ]
\end{aligned} \tag{A.14a}$$

$$
\begin{aligned}
(\mathrm{fun}_1)_\Omega = \frac{1}{120}\{&[30e\cos(\omega - E) - 30\cos(\omega + 2E) + 10e\cos(\omega + 3E) \\
&- 30e\cos(3\omega + E) + 30\cos(3\omega + 2E) - 15\cos(3\omega + 4E) \\
&+ 6e\cos(3\omega + 5E)]\cos\omega + [30e\sin(\omega - E) \\
&+ 30\left(1 + e^2\right)\sin(\omega + 2E) - 10e\sin(\omega + 3E) \\
&- 30e\sin(3\omega + E) + 30\left(1 + e^2\right)\sin(3\omega + 2E) \\
&+ 15\left(1 + e^2\right)\sin(3\omega + 4E) - 6e\sin(3\omega + 5E) \\
&- 180e\sin(\omega + E) - 60e\sin(3\omega + 3E)]\frac{\sin\omega}{\sqrt{1 - e^2}} \\
&+ 30\left(\frac{1 + e^2}{\sqrt{1 - e^2}} - 1\right)E\sin 2\omega\}
\end{aligned}
\tag{A.14b}
$$

$$
\begin{aligned}
(\mathrm{fun}_2)_\Omega = \frac{1}{840}\{&[-210e\cos(3\omega + E) + 210\cos(3\omega + 2E) \\
&- 105\cos(3\omega + 4E) + 42e\cos(3\omega + 5E) \\
&- 70e\cos(5\omega + 3E) + 105\cos(5\omega + 4E) \\
&- 70\cos(5\omega + 6E) + 30e\cos(5\omega + 7E)]\cos\omega \\
&+ [-210e\sin(3\omega + E) + 210\left(1 + e^2\right)\sin(3\omega + 2E) \\
&+ 105\left(1 + e^2\right)\sin(3\omega + 4E) - 42e\sin(3\omega + 5E) \\
&- 70e\sin(5\omega + 3E) + 105\left(1 + e^2\right)\sin(5\omega + 4E) \\
&+ 70\left(1 + e^2\right)\sin(5\omega + 6E) - 30e\sin(5\omega + 7E) \\
&- 420e\sin(3\omega + 3E) - 252e\sin(5\omega + 5E)]\frac{\sin\omega}{\sqrt{1 - e^2}}\}
\end{aligned}
\tag{A.14c}
$$

$$\begin{aligned}(\mathrm{fun}_3)_\Omega = \frac{1}{5040}\{[&-420e\cos(5\omega+3E)+630\cos(5\omega+4E)\\
&-420\cos(5\omega+6E)+180e\cos(5\omega+7E)\\
&-252e\cos(7\omega+5E)+420\cos(7\omega+6E)\\
&-315\cos(7\omega+8E)+140e\cos(7\omega+9E)]\cos\omega\\
&+[-420e\sin(5\omega+3E)+630\left(1+e^2\right)\sin(5\omega+4E)\\
&+420\left(1+e^2\right)\sin(5\omega+6E)-180e\sin(5\omega+7E)\\
&-252e\sin(7\omega+5E)+420\left(1+e^2\right)\sin(7\omega+6E)\\
&+315\left(1+e^2\right)\sin(7\omega+8E)-140e\sin(7\omega+9E)\\
&-1512e\sin(5\omega+5E)-1080e\sin(7\omega+7E)]\frac{\sin\omega}{\sqrt{1-e^2}}\}\end{aligned} \tag{A.14d}$$

$$\begin{aligned}(\mathrm{fun}_4)_\Omega = \frac{1}{55440}\{[&-2772e\cos(7\omega+5E)+4620\cos(7\omega+6E)\\
&-3465\cos(7\omega+8E)+1540e\cos(7\omega+9E)\\
&-1980e\cos(9\omega+7E)+3465\cos(9\omega+8E)\\
&-2772\cos(9\omega+10E)+1260e\cos(9\omega+11E)]\cos\omega\\
&+[-2772e\sin(7\omega+5E)+4620\left(1+e^2\right)\sin(7\omega+6E)\\
&+3465\left(1+e^2\right)\sin(7\omega+8E)-1540e\sin(7\omega+9E)\\
&-1980e\sin(9\omega+7E)+3465\left(1+e^2\right)\sin(9\omega+8E)\\
&+2772\left(1+e^2\right)\sin(9\omega+10E)-1260e\sin(9\omega+11E)\\
&-11880e\sin(7\omega+7E)-9240e\sin(9\omega+9E)]\frac{\sin\omega}{\sqrt{1-e^2}}\}\end{aligned} \tag{A.14e}$$

$$(\mathrm{fun}_0)_\omega = [\ -2\left(2-e^2\right)\cos E+e\cos^2 E\ ] \tag{A.15a}$$

$$\begin{aligned}(\mathrm{fun}_1)_\omega = \frac{1}{24}[\ &24\left(2-e^2\right)\cos(2\omega+E)-8\left(2-e^2\right)\cos(2\omega+3E)\\
&+3e\cos(2\omega+4E)+12eE\sin 2\omega\ ]\end{aligned} \tag{A.15b}$$

$$\begin{aligned}(\mathrm{fun}_2)_\omega = \frac{1}{60}[\ &-15e\cos(4\omega+2E)+20\left(2-e^2\right)\cos(4\omega+3E)\\
&-12\left(2-e^2\right)\cos(4\omega+5E)+5e\cos(4\omega+6E)\ ]\end{aligned} \tag{A.15c}$$

$$
\begin{aligned}
(\mathrm{fun}_3)_\omega = \frac{1}{560}[&-70e\cos(6\omega+4E)+112\left(2-e^2\right)\cos(6\omega+5E) \\
&-80\left(2-e^2\right)\cos(6\omega+7E)+35e\cos(6\omega+8E)]
\end{aligned}
\tag{A.15d}
$$

$$
\begin{aligned}
(\mathrm{fun}_4)_\omega = \frac{1}{1260}[&-105e\cos(8\omega+6E)+180\left(2-e^2\right)\cos(8\omega+7E) \\
&-140\left(2-e^2\right)\cos(8\omega+9E)+63e\cos(8\omega+10E)]
\end{aligned}
\tag{A.15e}
$$

A.4 Minimum-Time Open-Loop Control Law Design

The minimum-time open-loop control law design is presented as follows.

The equations of motion due to low-thrust and J_2-effect are stated as

$$\dot{\boldsymbol{x}} = \boldsymbol{g}(\boldsymbol{x},\ \hat{\boldsymbol{f}}) = \boldsymbol{A}(\boldsymbol{x})\,\hat{\boldsymbol{f}} + \boldsymbol{b}(\boldsymbol{x}) \tag{A.16}$$

where $\boldsymbol{x} = \{a,\ e,\ i,\ \Omega,\ \omega,\ E,\ m\}^\top$ is the vector of state variables; $\hat{\boldsymbol{f}} = \{\hat{f}_r,\ \hat{f}_\theta,\ \hat{f}_h\}^\top$ is the vector of control variables, which in the current problem is the unit vector of the low-thrust acceleration, i.e. the thrust direction; the matrix $\boldsymbol{A}$ and the vector $\boldsymbol{b}$ are functions of $\boldsymbol{x}$.

The minimum-time low-thrust transfer problem is formulated as follows. Find the optimal control $\hat{\boldsymbol{f}}^*$ that minimises

$$J = \int_{t_0}^{t_f} \mathrm{d}t \tag{A.17}$$

with the initial condition

$$\boldsymbol{x}\big|_{t=t_0} = \boldsymbol{x}_{\boldsymbol{0}} \tag{A.18}$$

and the terminal condition

$$\psi(\boldsymbol{x})\,\big|_{t=t_f} = 0 \tag{A.19}$$

where the terminal conditions for the two strategies have been given in Eq. (5.3) and Eq. (5.6).

The Hamiltonian function for a minimum-time problem reads [119]

$$H = 1 + \boldsymbol{\lambda}^\top\dot{\boldsymbol{x}} = 1 + \boldsymbol{\lambda}^\top(\boldsymbol{A}\hat{\boldsymbol{f}} + \boldsymbol{b}) \tag{A.20}$$

where $\boldsymbol{\lambda} = \{\lambda_a,\ \lambda_e,\ \lambda_i,\ \lambda_\Omega,\ \lambda\omega,\ \lambda_E,\ \lambda_m\}^\top$ is the vector of costates.

The optimal solutions $(\boldsymbol{x}^*,\ \boldsymbol{\lambda}^*,\ \hat{\boldsymbol{f}}^*)$ satisfy the Euler-Lagrange equations [119]

$$
\begin{aligned}
\dot{\boldsymbol{x}} &= \quad H_{\boldsymbol{\lambda}} \\
\dot{\boldsymbol{\lambda}} &= -H_{\boldsymbol{x}}
\end{aligned}
\tag{A.21}
$$

along with the transversality conditions [119]

$$\boldsymbol{\Psi}(\boldsymbol{y})\,\big|_{t=t_f} = \left\{\begin{matrix} H \\ \boldsymbol{\lambda} - \upsilon\psi_{\boldsymbol{x}} \\ \psi \end{matrix}\right\}_{t=t_f} = \boldsymbol{0} \tag{A.22}$$

where $\boldsymbol{y}$ denotes the vector consisting of the states and costates, and υ is the terminal multiplier, which can be eliminated by hand in the current problem. For the two strategies, $\boldsymbol{\Psi}(\boldsymbol{y})$ can be reduced to

$$\boldsymbol{\Psi}^{\mathrm{str1}}(\boldsymbol{y}) = \begin{Bmatrix} 1 + \lambda_a \dot{a} + \lambda_e \dot{e} \\ \lambda_a a + \lambda_e (1 - e) \\ \lambda_i \\ \lambda_\Omega \\ \lambda_\omega \\ \lambda_E \\ \lambda_m \\ a(1-e) - (h_{pf} + R_\oplus) \end{Bmatrix}$$

$$\boldsymbol{\Psi}^{\mathrm{str2}}(\boldsymbol{y}) = \begin{Bmatrix} 1 + \lambda_a \dot{a} + \lambda_e \dot{e} + \lambda_i \dot{i} \\ 8\lambda_a a e + 7\lambda_e \left(1 - e^2\right) \\ 2\lambda_a a \left(2n_1 \sin i - 5n_2 \sin 2i\right) + 7\lambda_i \left(5n_2 \cos^2 i - 2n_1 \cos i - n_2\right) \\ \lambda_\Omega \\ \lambda_\omega \\ \lambda_E \\ \lambda_m \\ \dfrac{3\sqrt{\mu} J_2 R_\oplus^2}{4a^{7/2}\left(1-e^2\right)^2}\left(5n_2 \cos^2 i - 2n_1 \cos i - n_2\right) + n_3 n_S \end{Bmatrix}$$

According to the Pontryagin Minimum Principle [120], the optimal thrust direction that minimises H is anti-parallel to $\boldsymbol{A}^\top \boldsymbol{\lambda}$:

$$\hat{\boldsymbol{f}}^* = -\frac{\boldsymbol{A}^\top \boldsymbol{\lambda}}{\left\|\boldsymbol{A}^\top \boldsymbol{\lambda}\right\|} \tag{A.23}$$

with which, the dynamics including both the states and costates becomes

$$\dot{\boldsymbol{y}} = \boldsymbol{G}(\boldsymbol{y}) \quad \Rightarrow \quad \begin{Bmatrix} \dot{\boldsymbol{x}} \\ \dot{\boldsymbol{\lambda}} \end{Bmatrix} = \begin{Bmatrix} -\dfrac{\boldsymbol{A}\boldsymbol{A}^\top \boldsymbol{\lambda}}{\left\|\boldsymbol{A}^\top \boldsymbol{\lambda}\right\|} + \boldsymbol{b} \\ \dfrac{\partial\left(\dfrac{\boldsymbol{\lambda}^\top \boldsymbol{A}\boldsymbol{A}^\top \boldsymbol{\lambda}}{\left\|\boldsymbol{A}^\top \boldsymbol{\lambda}\right\|} - \boldsymbol{\lambda}^\top \boldsymbol{b}\right)}{\partial \boldsymbol{x}} \end{Bmatrix} \tag{A.24}$$

Now the minimum-time problem has been converted to a Two-Point Boundary Value Problem (TPBVP), stated as follows. Find $(\boldsymbol{\lambda_0},\ t_f)$ such that $\boldsymbol{y}(t)$, which is subject to Eq. (A.24), satisfies Eq. (A.22) at $t = t_f$. This TPBVP can be solved by means of the shooting method.

In order to increase the accuracy and robustness of the shooting procedure, the state transition matrix

$$\boldsymbol{\Phi}(t_0,\ t) = \partial \boldsymbol{y}(t) / \partial \boldsymbol{y}(t_0), \quad \boldsymbol{\Phi}(t_0,\ t_0) = \boldsymbol{I}_{14\times14} \tag{A.25}$$

which maps the variations in states $\delta\boldsymbol{y}(t)$ with respect to the variations in initial conditions $\delta\boldsymbol{y}(t_0)$ over $t_0 \to t$, i.e., $\delta\boldsymbol{y}(t) = \boldsymbol{\Phi}(t_0,\ t)\,\delta\boldsymbol{y}(t_0)$, is provided [121]. The time derivative of $\boldsymbol{\Phi}\left(t_0,\ t\right)$ is given by

$$\dot{\boldsymbol{\Phi}}\left(t_0,\ t\right) = \boldsymbol{J}\boldsymbol{\Phi}\left(t_0,\ t\right) \tag{A.26}$$

where $\boldsymbol{J}$ is the Jacobian of $\boldsymbol{G}\left(\boldsymbol{y}\right)$.

Eq. (A.26) contains 196 differential equations which are required to be evaluated along $\boldsymbol{y}\left(t\right)$. Let $\boldsymbol{z}$ denotes the vector consisting of the elements in $\boldsymbol{y}$ and $\boldsymbol{\Phi}$. The integrated dynamics is

$$\dot{\boldsymbol{z}} = \mathcal{G}\left(\boldsymbol{z}\right) \quad \Rightarrow \quad \begin{Bmatrix} \dot{\boldsymbol{y}} \\ \mathrm{vec}(\dot{\boldsymbol{\Phi}}) \end{Bmatrix} = \begin{Bmatrix} \boldsymbol{G}\left(\boldsymbol{y}\right) \\ \mathrm{vec}(\boldsymbol{J}\boldsymbol{\Phi}) \end{Bmatrix} \tag{A.27}$$

Besides, to eliminate dependence on a specific central attracting body and to allow global mapping of solutions [93, pp. 363], the time and distance units are scaled as

$$1\ \mathrm{TU} = \sqrt{R_{\oplus}^3/\mu}, \quad 1\ \mathrm{DU} = R_{\oplus} \tag{A.28}$$

APPENDIX $\mathcal{B}$

Appendix for Chapter 6

The appendix for Chapter 6 is shown here.

B.1 Expressions in Eq. (6.30) and Eq. (6.31)

The expressions of the coefficients that appear in Eq. (6.30) and Eq. (6.31) are as follows.

$$a_t^{elliF} = 2 + e - \frac{3(a_0 - a_{pf})^4 + 3(a_0 - a_{pf})^2 \Delta a^2 + 3\Delta a^4}{2(a_0 - a_{pf})^2 \Delta a^2} e^2 \tag{B.1}$$

$$\begin{aligned} a_i^{elliF} = &- \frac{(a_0 - a_{pf})^2 + \Delta a^2}{\Delta a} - \Delta a e \\ &+ \frac{4(a_0 - a_{pf})^6 + 6(a_0 - a_{pf})^4 \Delta a^2 + (a_0 - a_{pf})^2 \Delta a^4 + 4\Delta a^6}{5(a_0 - a_{pf})^2 \Delta a^3} e^2 \end{aligned} \tag{B.2}$$

$$a_t^{elliE} = \frac{1}{(a_0 - a_{pf})^2 - \Delta a^2} e + \frac{3(a_0 - a_{pf})^6 - 4(a_0 - a_{pf})^2 \Delta a^4 + 3\Delta a^6}{2(a_0 - a_{pf})^2 \Delta a^2 \left((a_0 - a_{pf})^2 - \Delta a^2\right)^2} e^2 \tag{B.3}$$

$$\begin{aligned}
a_i^{elliE} = {} & \frac{1}{\Delta a} - \frac{\Delta a}{{(a_0 - a_{pf})}^2 - \Delta a^2} e \\
& - \frac{4{(a_0 - a_{pf})}^8 - 2{(a_0 - a_{pf})}^6 \Delta a^2}{5{(a_0 - a_{pf})}^2 \Delta a^3 \Big({(a_0 - a_{pf})}^2 - \Delta a^2\Big)^2} e^2 \\
& - \frac{6{(a_0 - a_{pf})}^4 \Delta a^4 - 7{(a_0 - a_{pf})}^2 \Delta a^6 + 4\Delta a^8}{5{(a_0 - a_{pf})}^2 \Delta a^3 \Big({(a_0 - a_{pf})}^2 - \Delta a^2\Big)^2} e^2
\end{aligned} \tag{B.4}$$

$$\begin{aligned}
e_t^{elliF} = {} & -\frac{{(a_0 - a_{pf})}^2 + \Delta a^2}{(a_0 - a_{pf})\,\Delta a} \\
& - \frac{{(a_0 - a_{pf})}^4 + 4{(a_0 - a_{pf})}^2 \Delta a^2 + 3\,(a_0 - a_{pf})\,\Delta a^3 + \Delta a^4}{3{(a_0 - a_{pf})}^2 \Delta a^2} e \\
& + \frac{22{(a_0 - a_{pf})}^6 + 10{(a_0 - a_{pf})}^5 \Delta a + 23{(a_0 - a_{pf})}^4 \Delta a^2 - 22\Delta a^6}{30{(a_0 - a_{pf})}^3 \Delta a^3} e^2 \\
& - \frac{20{(a_0 - a_{pf})}^3 \Delta a^3 + 7{(a_0 - a_{pf})}^2 \Delta a^4 + 20\,(a_0 - a_{pf})\,\Delta a^5}{30{(a_0 - a_{pf})}^3 \Delta a^3} e^2
\end{aligned} \tag{B.5}$$

$$\begin{aligned}
e_i^{elliF} = {} & \frac{{(a_0 - a_{pf})}^4 + 10{(a_0 - a_{pf})}^2 \Delta a^2 + \Delta a^4}{3{(a_0 - a_{pf})}^2 \Delta a^2} \\
& - \frac{{(a_0 - a_{pf})}^4 - 6{(a_0 - a_{pf})}^3 \Delta a}{3{(a_0 - a_{pf})}^2 \Delta a^2} e \\
& + \frac{5{(a_0 - a_{pf})}^2 \Delta a^2 + 6\,(a_0 - a_{pf})\,\Delta a^3 + 2\Delta a^4}{3{(a_0 - a_{pf})}^2 \Delta a^2} e \\
& - \frac{48{(a_0 - a_{pf})}^8 + 250{(a_0 - a_{pf})}^6 \Delta a^2 + 139{(a_0 - a_{pf})}^4 \Delta a^4}{105{(a_0 - a_{pf})}^4 \Delta a^4} e^2 \\
& - \frac{210{(a_0 - a_{pf})}^3 \Delta a^5 - 145{(a_0 - a_{pf})}^2 \Delta a^6 - 48\Delta a^8}{105{(a_0 - a_{pf})}^4 \Delta a^4} e^2
\end{aligned} \tag{B.6}$$

$$
\begin{aligned}
e_t^{elliE} = {} & \frac{1}{\left(a_0 - a_{pf}\right)\Delta a} + \frac{\left(a_0 - a_{pf}\right)^4 - 3\left(a_0 - a_{pf}\right)\Delta a^3 - \Delta a^4}{3\left(a_0 - a_{pf}\right)^2 \Delta a^2 \left(\left(a_0 - a_{pf}\right)^2 - \Delta a^2\right)} e \\
& - \frac{22\left(a_0 - a_{pf}\right)^8 + 10\left(a_0 - a_{pf}\right)^7 \Delta a}{30\left(a_0 - a_{pf}\right)^3 \Delta a^3 \left(\left(a_0 - a_{pf}\right)^2 - \Delta a^2\right)^2} e^2 \\
& + \frac{21\left(a_0 - a_{pf}\right)^6 \Delta a^2 + 10\left(a_0 - a_{pf}\right)^5 \Delta a^3}{30\left(a_0 - a_{pf}\right)^3 \Delta a^3 \left(\left(a_0 - a_{pf}\right)^2 - \Delta a^2\right)^2} e^2 \\
& - \frac{58\left(a_0 - a_{pf}\right)^4 \Delta a^4 + 20\left(a_0 - a_{pf}\right)^3 \Delta a^5}{30\left(a_0 - a_{pf}\right)^3 \Delta a^3 \left(\left(a_0 - a_{pf}\right)^2 - \Delta a^2\right)^2} e^2 \\
& + \frac{51\left(a_0 - a_{pf}\right)^2 \Delta a^6 + 20\left(a_0 - a_{pf}\right)\Delta a^7 - 22\Delta a^8}{30\left(a_0 - a_{pf}\right)^3 \Delta a^3 \left(\left(a_0 - a_{pf}\right)^2 - \Delta a^2\right)^2} e^2
\end{aligned}
\tag{B.7}
$$

$$
\begin{aligned}
e_i^{elliE} = {} & -\frac{\left(a_0 - a_{pf}\right)^2 + \Delta a^2}{3\left(a_0 - a_{pf}\right)^2 \Delta a^2} \\
& + \frac{\left(a_0 - a_{pf}\right)^4 - 6\left(a_0 - a_{pf}\right)^3 \Delta a}{3\left(a_0 - a_{pf}\right)^2 \Delta a^2 \left(\left(a_0 - a_{pf}\right)^2 - \Delta a^2\right)} e \\
& + \frac{3\left(a_0 - a_{pf}\right)^2 \Delta a^2 + 6\left(a_0 - a_{pf}\right)\Delta a^3 + 2\Delta a^4}{3\left(a_0 - a_{pf}\right)^2 \Delta a^2 \left(\left(a_0 - a_{pf}\right)^2 - \Delta a^2\right)} e \\
& + \frac{48\left(a_0 - a_{pf}\right)^{10} + 154\left(a_0 - a_{pf}\right)^8 \Delta a^2}{105\left(a_0 - a_{pf}\right)^4 \Delta a^4 \left(\left(a_0 - a_{pf}\right)^2 - \Delta a^2\right)^2} e^2 \\
& + \frac{8\left(a_0 - a_{pf}\right)^6 \Delta a^4 + 210\left(a_0 - a_{pf}\right)^5 \Delta a^5}{105\left(a_0 - a_{pf}\right)^4 \Delta a^4 \left(\left(a_0 - a_{pf}\right)^2 - \Delta a^2\right)^2} e^2 \\
& - \frac{97\left(a_0 - a_{pf}\right)^4 \Delta a^6 + 210\left(a_0 - a_{pf}\right)^3 \Delta a^7}{105\left(a_0 - a_{pf}\right)^4 \Delta a^4 \left(\left(a_0 - a_{pf}\right)^2 - \Delta a^2\right)^2} e^2 \\
& + \frac{49\left(a_0 - a_{pf}\right)^2 \Delta a^8 + 48\Delta a^{10}}{105\left(a_0 - a_{pf}\right)^4 \Delta a^4 \left(\left(a_0 - a_{pf}\right)^2 - \Delta a^2\right)^2} e^2
\end{aligned}
\tag{B.8}
$$

B.2 Interpretation of Fig. 6.5

This appendix provides the interpretation on the three cases shown in Fig. 6.5 (latitude resonance does not happen; latitude resonance happens; satellite-pair miss distance is always given by the relative distance at the first latitude resonance).

If the transfer starting time difference is small, then the latitude difference will be accordingly small over the entire transfer, as the satellites follow an orbital path with the same geometry, such that the latitude resonance will not happen.

Fig. B.1 presents the time histories of the latitude difference and relative distance for the transfer starting time difference of 2 hours. It can be seen that the latitude resonance does not happen.

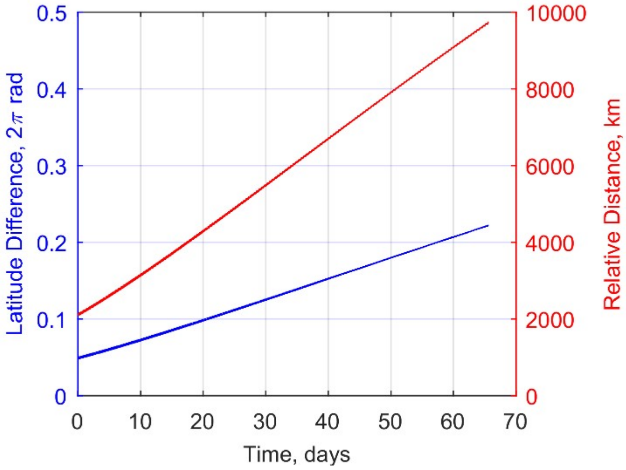

Figure B.1: *Time histories of the latitude difference and relative distance for the transfer starting time difference of 2 hours (d_{miss} = 2096.9 km).*

Once the transfer starting time difference increases to a minimum threshold, the latitude difference will accumulate to be larger than 2π – the latitude resonance happens. Fig. B.2 presents the time histories of the latitude difference and relative distance for the transfer starting time difference of 12 hours. It can be seen that the satellite-pair miss distance equals to the relative distance at the latitude resonance.

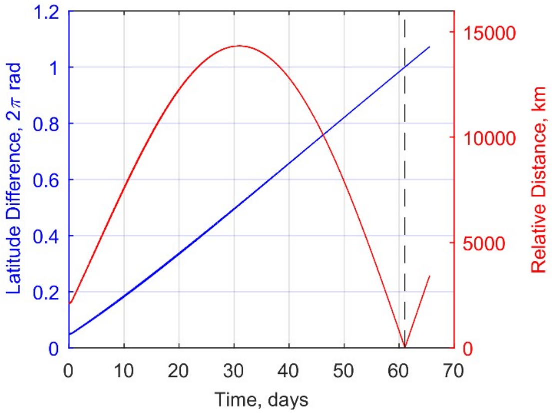

Figure B.2: *Time histories of the latitude difference and relative distance for the transfer starting time difference of 12 hours (d_{miss} = 5.2 km).*

As the transfer starting time difference increases, the latitude difference accumulates faster and faster, and the frequency of the latitude difference accordingly increases. Figs. B.3 (a) and (b) present the time histories of the latitude difference and relative distance for the transfer starting time difference of 3 days and 6 days, respectively. The satellite-pair miss distance equals to the relative distance at the first and the second latitude resonance, respectively.

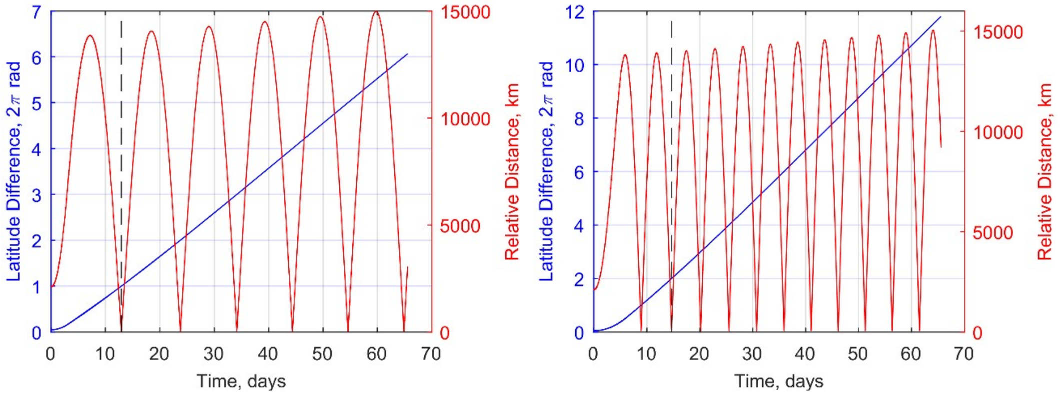

(a) *Transfer starting time difference of 3 days (d_{miss} = 23.6 km).* **(b)** *Transfer starting time difference of 6 days (d_{miss} = 53.4 km).*

Figure B.3: *Time histories of the relative distance and latitude difference.*

Once the transfer starting time difference increases to a high enough value, the satellite-pair miss distance will always be the orbital radius difference at the first fly-by, or the first latitude resonance. Fig. B.4 presents the time histories of the latitude difference and relative distance for the transfer starting time difference of 20 days.

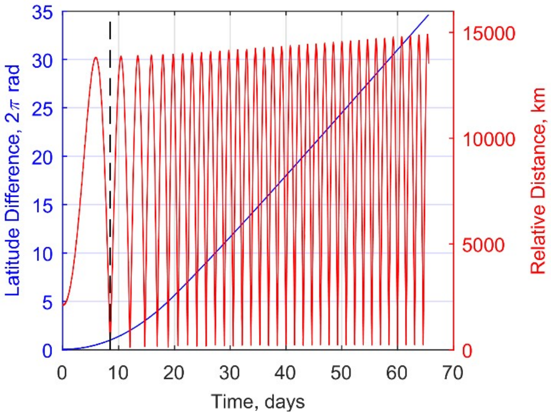

Figure B.4: *Time histories of the latitude difference and relative distance for the transfer starting time difference of 20 days (d_{miss} = 70.5 km).*

B.3 Satellite-Pair Miss Distance versus Transfer Starting Time Difference

Fig. B.5, Fig. B.6 and Fig. B.7 show the satellite-pair miss distance versus the transfer starting time difference for the satellite pairs with different initial relative phases. The critical transfer starting time difference δt_0^{safe} and $\delta t_0^{\text{safest}}$ are highlighted by the blue cross and red asterisk, respectively.

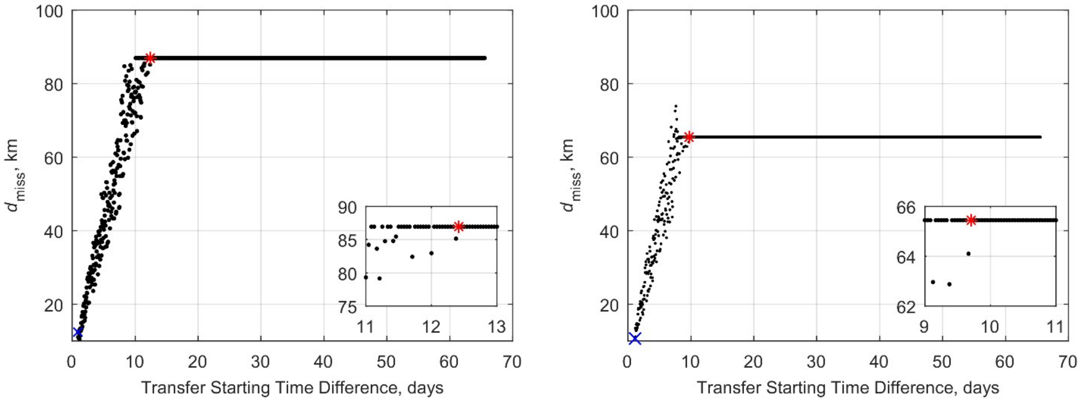

(a) $\delta\nu_0 = 4\pi/20$ rad.

(b) $\delta\nu_0 = 6\pi/20$ rad.

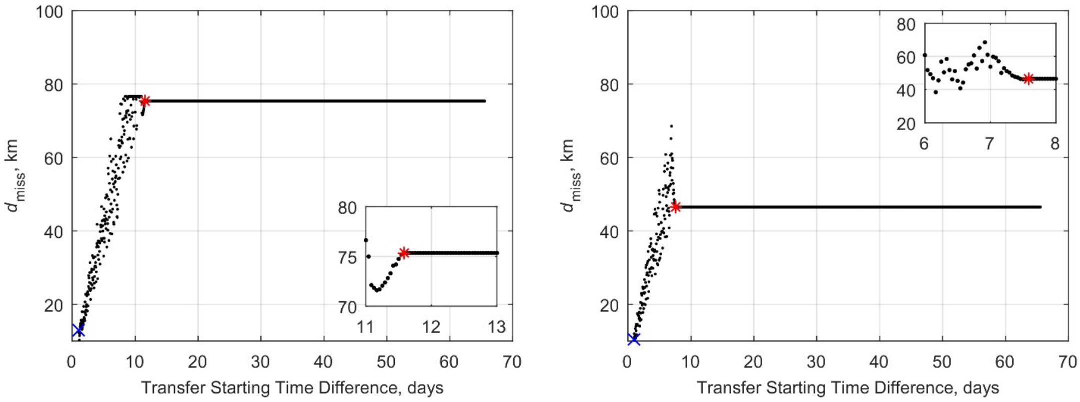

(c) $\delta\nu_0 = 8\pi/20$ rad.

(d) $\delta\nu_0 = 10\pi/20$ rad.

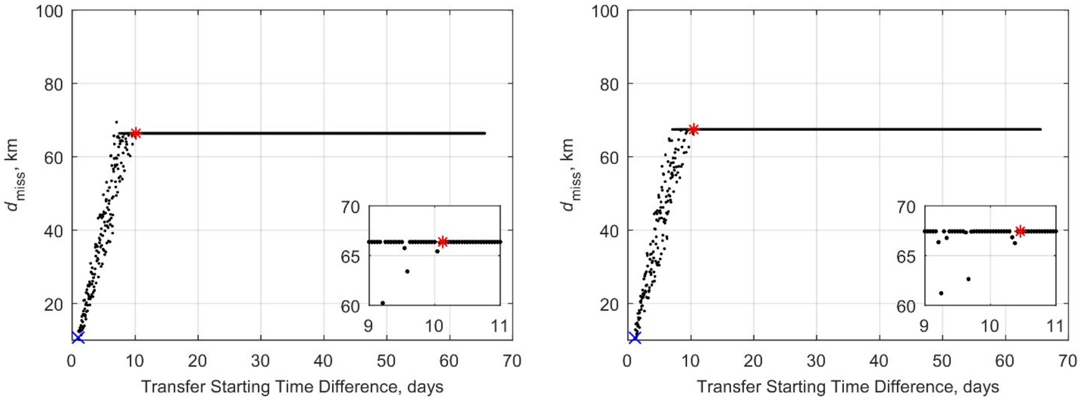

(e) $\delta\nu_0 = 12\pi/20$ rad.

(f) $\delta\nu_0 = 14\pi/20$ rad.

Figure B.5: *Satellite-pair miss distance versus transfer starting time difference for different satellite pairs with initial true anomaly differences of* $\delta\nu_0 = 4\pi/20,\ 6\pi/20,\ 8\pi/20,\ 10\pi/20,\ 12\pi/20,\ 14\pi/20$.

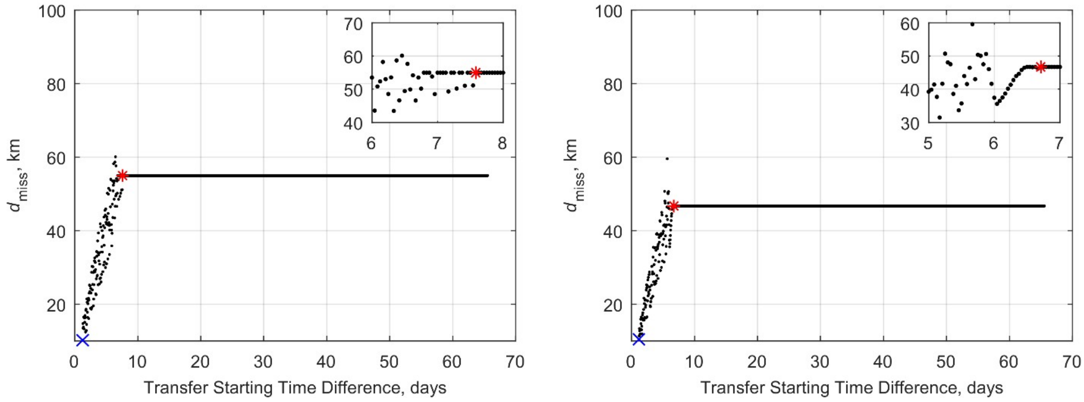

(g) $\delta\nu_0 = 16\pi/20$ rad.

(h) $\delta\nu_0 = 18\pi/20$ rad.

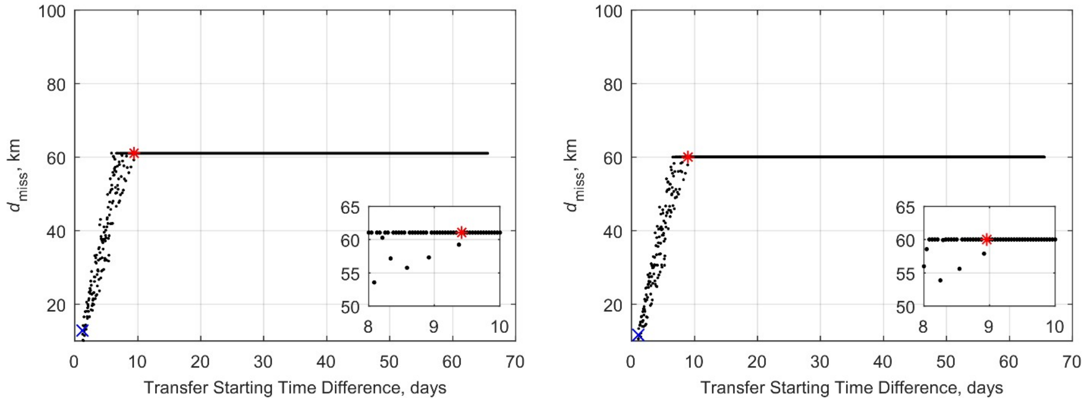

(i) $\delta\nu_0 = 20\pi/20$ rad.

(j) $\delta\nu_0 = 22\pi/20$ rad.

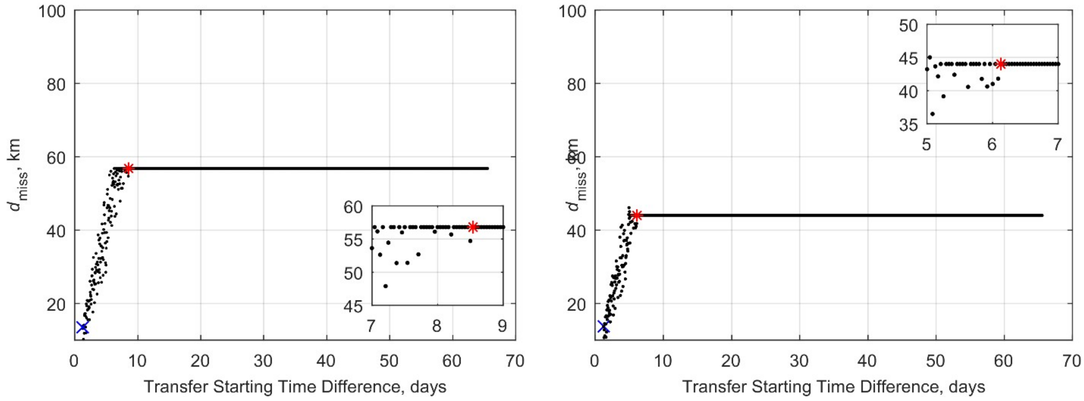

(k) $\delta\nu_0 = 24\pi/20$ rad.

(l) $\delta\nu_0 = 26\pi/20$ rad.

Figure B.6: *Satellite-pair miss distance versus transfer starting time difference for different satellite pairs with initial true anomaly differences of* $\delta\nu_0 = 16\pi/20,\ 18\pi/20,\ 20\pi/20,\ 22\pi/20,\ 24\pi/20,\ 26\pi/20$.

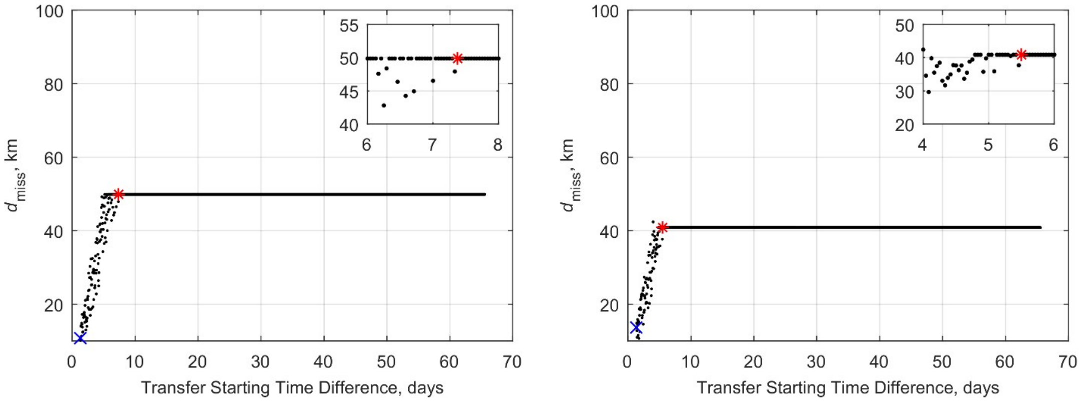

(m) $\delta\nu_0 = 28\pi/20$ rad.

(n) $\delta\nu_0 = 30\pi/20$ rad.

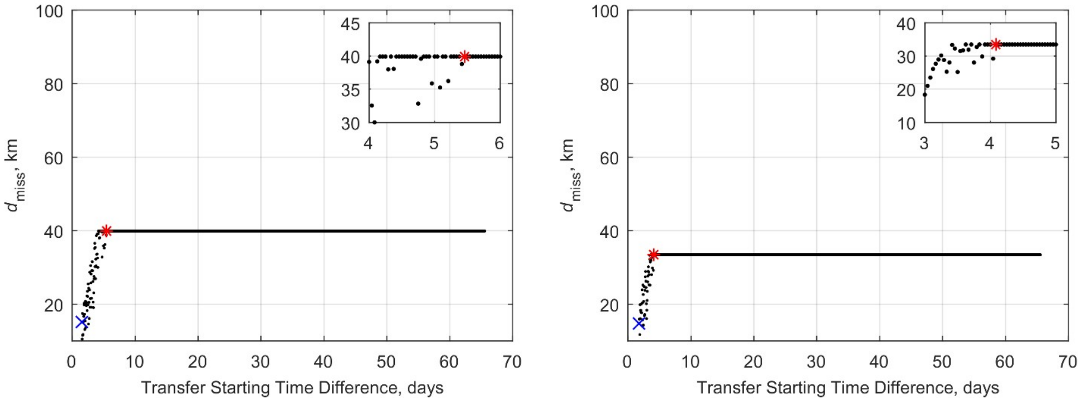

(o) $\delta\nu_0 = 32\pi/20$ rad.

(p) $\delta\nu_0 = 34\pi/20$ rad.

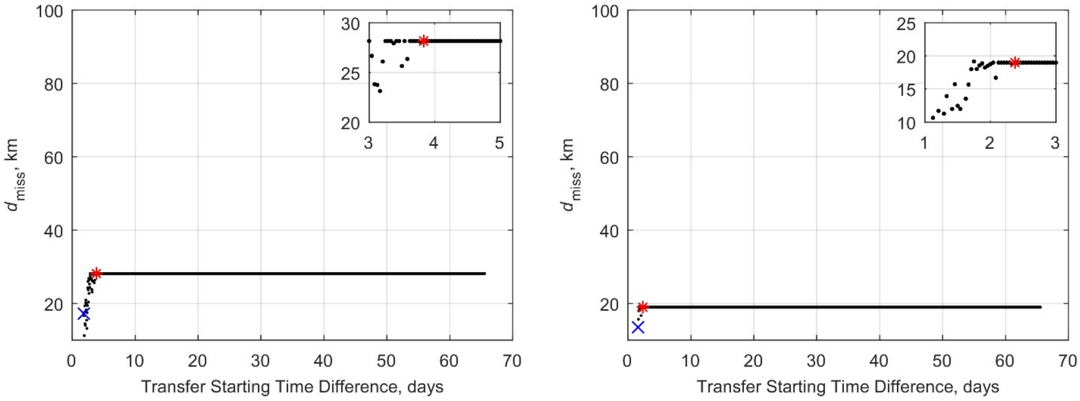

(q) $\delta\nu_0 = 36\pi/20$ rad.

(r) $\delta\nu_0 = 38\pi/20$ rad.

Figure B.7: *Satellite-pair miss distance versus transfer starting time difference for different satellite pairs with initial true anomaly differences of* $\delta\nu_0 = 28\pi/20,\ 30\pi/20,\ 32\pi/20,\ 34\pi/20,\ 36\pi/20,\ 38\pi/20$.

Bibliography

[1] Wood, L., “Satellite Constellation Networks,” *Internetworking and Computing over Satellite Networks*, 2003, pp. 13–34.

[2] Wertz, J. R., editor, *Mission Geometry; Orbit and Constellation Design and Management*, Microcosm Press and Kluwer Academic Publishers, 2001.

[3] Cornara, S., Beech, T. W., Belló-Mora, M., and Martinez de Aragon, A., “Satellite Constellation Launch, Deployment, Replacement and End-of-Life Strategies,” *Proceedings of the Small Satellite Conference*, 1999, Technical Session X: New Approaches To Space Launch, SSC99-X-1, https://digitalcommons.usu.edu/smallsat/1999/all1999/71/.

[4] Walker, J. G., “Circular Orbit Patterns Providing Continuous Whole Earth Coverage,” Tech. rep., Royal Aircraft Establishment Farnborough (United Kingdom), 1 November 1970, https://apps.dtic.mil/sti/pdfs/AD0722776.pdf.

[5] Walker, J. G., “Continuous Whole-Earth Coverage by Circular-Orbit Satellite Patterns,” Tech. rep., Royal Aircraft Establishment Farnborough (United Kingdom), 24 March 1977, https://apps.dtic.mil/sti/pdfs/ADA044593.pdf.

[6] Walker, J. G., “Satellite Patterns for Continuous Multiple Whole-Earth Coverage,” *International Conference on Maritime and Aeronautical Satellite Communication and Navigation*, London, England, 7-9 March 1978, pp. 119–122.

[7] Walker, J. G., “Coverage Predictions and Selection Criteria for Satellite Constellations,” Tech. rep., Royal Aircraft Establishment Farnborough (United Kingdom), 1 December 1982, https://apps.dtic.mil/sti/pdfs/ADA129792.pdf.

[8] Ulybyshev, Y., “Near-Polar Satellite Constellations for Continuous Global Coverage,” *Journal of Spacecraft and Rockets*, Vol. 36, No. 1, 1999, pp. 92–99, doi: 10.2514/2.3419.

[9] Mozhaev, G. V., “The Problem of the Continuous Earth Coverage and the Kinematically Regular Satellite Networks, I,” *Kosmicheskie Issledovaniya*, Vol. 10, No. 6, 1972, pp. 833–840.

[10] Mozhaev, G. V., “The Problem of the Continuous Earth Coverage and the Kinematically Regular Satellite Networks, II,” *Kosmicheskie Issledovaniya*, Vol. 11, No. 1, 1973, pp. 59–69.

[11] Ballard, A. H., “Rosette Constellations of Earth Satellites,” *IEEE Transactions on Aerospace and Electronic System*, Vol. AES-16, No. 5, September 1980, pp. 656–673.

[12] Lang, T. J., “Symmetric Circular Orbit Satellite Constellations for Continuous Global Coverage,” *AAS/AIAA Astrodynamics Specialist Conference*, Kalispell, Montana, United States of America, 10-13 August 1987, pp. 1111–1132.

[13] Lang, T. J., “Optimal Low Earth Orbit Constellations for Continuous Global Coverage,” *AAS/AIAA Astrodynamics Specialist Conference*, Victoria, British Columbia, Canada, 16-19 August 1993, pp. 1199–1216, AAS 93-597.

[14] Lang, T. J. and Adams, W. S., "A Comparison of Satellite Constellations for Continuous Global Coverage," *Mission Design & Implementation of Satellite Constellations*, Toulouse, France, November 1997, pp. 51–62, doi: 10.1007/978-94-011-5088-0_5.

[15] Lüders, R. D., "Satellite Networks for Continuous Zonal Coverage," *American Rocket Society Journal*, Vol. 31, No. 2, 1961, pp. 179–184, doi: 10.2514/8.5422.

[16] Lüders, R. D. and Ginsberg, L. J., "Continuous Zonal Coverage – A Generalized Analysis," *AIAA Mechanics and Control of Flight Conference*, Anaheim, California, United States of America, 5-9 August 1974, AIAA paper No. 74-842, doi: 10.2514/6.1974-842.

[17] Rider, L., "Analytic Design of Satellite Constellations for Zonal Earth Coverage Using Inclined Circular Orbits," *Journal of the Astronautical Sciences*, Vol. 34, 1986, pp. 31–64.

[18] Beste, D. C., "Design of Satellite Constellations for Optimal Continuous Coverage," *IEEE Transactions on Aerospace and Electronic Systems*, Vol. AES-14, No. 3, 1978, pp. 466–473, doi: 10.1109/TAES.1978.308608.

[19] Rider, L., "Optimized Polar Orbit Constellations for Redundant Earth Coverage," *Journal of the Astronautical Sciences*, Vol. 33, 1985, pp. 147–161.

[20] Mortari, D., Wilkins, M. P., and Bruccoleri, C., "The Flower Constellations," *Journal of Astronautical Sciences*, Vol. 52, March 2004, pp. 107–127, doi: 10.1007/BF03546424.

[21] Avendaño, M. E., Davis, J. J., and Mortari, D., "The 2-D Lattice Theory of Flower Constellations," *Celestial Mechanics and Dynamical Astronomy*, Vol. 116, 2013, pp. 325–337, doi: 10.1007/s10569-013-9493-8.

[22] Davis, J. J., Avendaño, M. E., and Mortari, D., "The 3-D Lattice Theory of Flower Constellations," *Celestial Mechanics and Dynamical Astronomy*, Vol. 116, 2013, pp. 339–356, doi: 10.1007/s10569-013-9494-7.

[23] Draim, J. E. and Kacena, T. J., "Populating the Abyss - Investigating More Efficient Orbits," *Proceedings of the Small Satellite Conference*, 1992, Technical Session III: New Missions & Applications/Military, 16, https://digitalcommons.usu.edu/smallsat/1992/all1992/16/.

[24] Lansard, E. and Palmade, J., "Satellite Constellation Design: Searching for Global Cost-Efficiency Trade-Offs," *Mission Design & Implementation of Satellite Constellations*, Toulouse, France, November 1997, pp. 23–31, doi: 10.1007/978-94-011-5088-0_3.

[25] Lansard, E., Frayssinhes, E., and Palmade, J., "Global Design of Satellite Constellations: A Multi-Criteria Performance Comparison of Classical Walker Patterns and New Design Patterns," *Acta Astronautica*, Vol. 42, No. 9, 1998, pp. 555–564, doi: 10.1016/S0094-5765(98)00043-5.

[26] Keller, H., Salzwedel, H., Schorcht, G., and Zerbe, V., "Geometric Aspects of Polar and Near Polar Circular Orbits for the Use of Intersatellite Links for Global Communication," *48th IEEE Vehicular Technology Conference. Pathway to Global Wireless Revolution (Cat. No. 98CH36151)*, Ottawa, Ontario, Canada, 21-21 May 1998, pp. 199–203, doi: 10.1109/VETEC.1998.686526.

[27] Ferringer, M. P. and Spencer, D. B., "Satellite Constellation Design Tradeoffs Using Multiple-Objective Evolutionary Computation," *Journal of Spacecraft and Rockets*, Vol. 43, No. 6, 2006, pp. 1404–1411, doi: 10.2514/1.18788.

[28] Li, Y., Zhao, S., and Wu, J., "A General Evaluation Criterion for the Coverage Performance of LEO Constellations," *Aerospace Science and Technology*, Vol. 48, 2012, pp. 94–101, doi: 10.1016/j.ast.2015.11.003.

[29] Shtark, T. and Gurfil, P., "Regional Positioning Using a Low Earth Orbit Satellite Constellation," *Celestial Mechanics and Dynamical Astronomy*, Vol. 130, No. 2, 2018, pp. 1–28, doi: 10.1007/s10569-017-9811-7.

[30] Buzzi, P. G., Selva, D., Hitomi, N., and Blackwell, W. J., "Assessment of Constellation Designs for Earth Observation: Application to the TROPICS Mission," *Acta Astronautica*, Vol. 161, 2019, pp. 166–182, doi: 10.1016/j.actaastro.2019.05.007.

[31] King, J. A. and Beidleman, N. J., "Method and Apparatus for Deploying a Satellite Network," 6 April 1993, US Patent 5,199,672, https://patentimages.storage.googleapis.com/24/f3/30/ed8e54c6336203/US5199672.pdf.

[32] Fong, C., Shiau, W., Lin, C., Kuo, T., Chu, C., Yang, S., Yen, N. L., Chen, S., Kuo, Y., Liou, Y., and Chi, S., "Constellation Deployment for the FORMOSAT-3/COSMIC Mission," *IEEE Transactions on Geoscience and Remote Sensing*, Vol. 46, No. 11, 2008, pp. 3367–3379, doi: 10.1109/TGRS.2008.2005202.

[33] Jenkins, M. G., Krejci, D., and Lozano, P., "CubeSat Constellation Management Using Ionic Liquid Electrospray Propulsion," *Acta Astronautica*, Vol. 151, 2018, pp. 243–252, doi: 10.1016/j.actaastro.2018.06.007.

[34] McGrath, C. N. and Macdonald, M., "General Perturbation Method for Satellite Constellation Deployment Using Nodal Precession," *Journal of Guidance, Control, and Dynamics*, Vol. 43, No. 4, 2020, pp. 814–824, doi: 10.2514/1.G004443.

[35] Cerf, M., "Low-Thrust Transfer Between Circular Orbits Using Natural Precession," *Journal of Guidance, Control, and Dynamics*, Vol. 39, No. 10, 2016, pp. 2232–2239, doi: 10.2514/1.G001331.

[36] Chow, N., Gralla, E., and Kasdin, N. J., "Low Earth Orbit Constellation Design Using the Earth-Moon L1 Point," *14th AAS/AIAA Space Flight Mechanics Conference*, Maui, Hawaii, United States of America, 8-12 February 2004, AAS 04-248, https://trs.jpl.nasa.gov/handle/2014/37921.

[37] Chase, J., Chow, N., Gralla, E., and Kasdin, N. J., "LEO Constellation Design Using the Lunar L1 Point," *14th AAS/AIAA Space Flight Mechanics Conference*, Maui, Hawaii, United States of America, 8-12 February 2004, https://trs.jpl.nasa.gov/handle/2014/8036.

[38] Nadoushan, M. J. and Novinzadeh, A. B., "Satellite Constellation Build-Up via Three-Body Dynamics," *Proceedings of the Institution of Mechanical Engineers, Part G: Journal of Aerospace Engineering*, Vol. 228, No. 1, 2013, pp. 155–160, doi: 10.1177/0954410013476615.

[39] Crisp, N. H., Smith, K., and Hollingsworth, P., "Launch and Deployment of Distributed Small Satellite Systems," *Acta Astronautica*, Vol. 114, 2015, pp. 65–78, doi: 10.1016/j.actaastro.2015.04.015.

[40] de Weck, O., de Neufville, R., and Chaize, M., "Staged Deployment of Communications Satellite Constellations in Low Earth Orbit," *Journal of Aerospace Computing, Information, and Communication*, Vol. 1, No. 3, 2004, pp. 119–136, doi: 10.2514/1.6346.

[41] Appel, L., Guelman, M., and Mishne, D., "Optimization of Satellite Constellation Reconfiguration Maneuvers," *Acta Astronautica*, Vol. 99, 2014, pp. 166–174, doi: 10.1016/j.actaastro.2014.02.016.

[42] de Weck, O. L., Scialom, U., and Siddiqi, A., "Optimal Reconfiguration of Satellite Constellations with the Auction Algorithm," *Acta Astronautica*, Vol. 62, No. 2-3, 2008, pp. 112–130, doi: 10.1016/j.actaastro.2007.02.008.

[43] Kechichian, J. A., "Orbit Raising with Low-Thrust Tangential Acceleration in Presence of Earth Shadow," *Journal of Spacecraft and Rockets*, Vol. 35, No. 4, 1998, pp. 516–525, doi: 10.2514/2.3361.

[44] McGrath, C. N. and Macdonald, M., "General Perturbation Method for Satellite Constellation Reconfiguration Using Low-Thrust Maneuvers," *Journal of Guidance, Control, and Dynamics*, Vol. 42, No. 8, 2019, pp. 1676–1692, doi: 10.2514/1.G003739.

[45] Burt, E. G. C., "On Space Manoeuvres with Continuous Thrust," *Planetary and Space Science*, Vol. 15, No. 1, 1967, pp. 103–122, doi: 10.1016/0032-0633(67)90070-0.

[46] Pollard, J. E., "Evaluation of Low-Thrust Orbital Maneuvers," *34th AIAA/ASME/SAE/ASEE Joint Propulsion Conference and Exhibit*, Cleveland, Ohio, United States of America, 13-15 July 1998, AIAA-98-3486, doi: 10.2514/6.1998-3486.

[47] Lücking, C., Colombo, C., and McInnes, C. R., "A Passive Satellite Deorbiting Strategy for Medium Earth Orbit Using Solar Radiation Pressure and the J2 Effect," *Acta Astronautica*, Vol. 77, 2012, pp. 197–206, doi: 10.1016/j.actaastro.2012.03.026.

[48] Colombo, C., Lücking, C., and McInnes, C. R., "Orbital Dynamics of High Area-to-Mass Ratio Spacecraft with J2 and Solar Radiation Pressure for Novel Earth Observation and Communication Services," *Acta Astronautica*, Vol. 81, No. 1, 2012, pp. 137–150, doi: 10.1016/j.actaastro.2012.07.009.

[49] Lücking, C., Colombo, C., and McInnes, C. R., "Solar Radiation Pressure-Augmented Deorbiting: Passive End-of-Life Disposal from High-Altitude Orbits," *Journal of Spacecraft and Rockets*, Vol. 50, No. 6, 2013, pp. 1256–1267, doi: 10.2514/1.A32478.

[50] Colombo, C. and De Fer, T. d. B., "Assessment of Passive and Active Solar Sailing Strategies for End-of-Life Re-Entry," *67th International Astronautical Congress*, Guadalajara, Mexico, 26-30 September 2016, IAC-16-A6.4.4.

[51] Alessi, E. M., Schettino, G., Rossi, A., and Valsecchi, G. B., "Solar Radiation Pressure Resonances in Low Earth Orbits," *Monthly Notices of the Royal Astronomical Society*, Vol. 473, 2018, pp. 2407–2414, doi: 10.1093/mnras/stx2507.

[52] Alessi, E. M. and Colombo, C., "Dynamical System Description of the Solar Radiation Pressure and J2 Phase Space for End-of-Life Design and Frozen Orbit Design," *69th International Astronautical Congress*, Bremen, Germany, 1-5 October 2018, IAC-18,A6,10-C1.7,11,x45107, http://redshift-h2020.eu/wp-content/uploads/2019/02/AlessiColombo_IAC-18A610-C1.711x45107.pdf.

[53] Schettino, G., Alessi, E. M., Rossi, A., and Valsecchi, G. B., "Exploiting Dynamical Perturbations for the End-of-Life Disposal of Spacecraft in LEO," *Astronomy and Computing*, Vol. 27, 2019, pp. 1–10, doi: 10.1016/j.ascom.2019.02.001.

[54] Rossi, A., Alessi, E. M., Schettino, G., Schaus, V., and Valsecchi, G. B., "How An Aware Usage of the Long-Term Dynamics Can Improve the Long-Term Situation in the LEO Region," *Acta Astronautica*, Vol. 174, 2020, pp. 159–165, doi: 10.1016/j.actaastro.2020.05.005.

[55] Radtke, J., Kebschull, C., and Stoll, E., "Interactions of the Space Debris Environment with Mega Constellations Using the Example of the OneWeb Constellation," *Acta Astronautica*, Vol. 131, 2017, pp. 55–68, doi: 10.1016/j.actaastro.2016.11.021.

[56] Lewis, H., Radtke, J., Beck, J., Bastida Virgili, B., and Krag, H., "Self-Induced Collision Risk Analysis for Large Constellations," *7th European Conference on Space Debris*, 2017, https://conference.sdo.esoc.esa.int/proceedings/sdc7/paper/723/SDC7-paper723.pdf.

[57] Somma, G. L., Lewis, H. G., Colombo, C., et al., "Space Debris: Analysis of a Large Constellation at 1200 km Altitude," *69th International Astronautical Congress*, Bremen, Germany, 1-5 October 2018.

[58] Lee, K., Park, H., Park, C., and Park, S., "Sub-Optimal Cooperative Collision Avoidance Maneuvers of Multiple Active Spacecraft via Discrete-Time Generating Functions," *Aerospace Science and Technology*, Vol. 93, 2019, doi: 10.1016/j.ast.2019.07.031.

[59] von Stryk, O. and Bulirsch, R., "Direct and Indirect Methods for Trajectory Optimization," *Annals of Operations research*, Vol. 37.

[60] Betts, J. T., "Survey of Numerical Methods for Trajectory Optimization," *Journal of Guidance, Control, and Dynamics*, Vol. 21, No. 2, 1998, pp. 193–207, doi: 10.2514/2.4231.

[61] Haberkorn, T., Martinon, P., and Gergaud, J., "Low Thrust Minimum-Fuel Orbital Transfer: A Homotopic Approach," *Journal of Guidance, Control, and Dynamics*, Vol. 27, No. 6, 2004, pp. 1046–1060, doi: 10.2514/1.4022.

[62] Jiang, F., Baoyin, H., and Li, J., "Practical Techniques for Low-Thrust Trajectory Optimization with Homotopic Approach," *Journal of Guidance, Control, and Dynamics*, Vol. 35, No. 1, 2012, pp. 245–258, doi: 10.2514/1.52476.

[63] Guo, T., Jiang, F., and Li, J., "Homotopic Approach and Pseudospectral Method Applied Jointly to Low Thrust Trajectory Optimization," *Acta Astronautica*, Vol. 71, 2012, pp. 38–50, doi: 10.1016/j.actaastro.2011.08.008.

[64] Scheel, W. A. and Conway, B. A., "Optimization of Very-Low-Thrust, Many-Revolution Spacecraft Trajectories," *Journal of Guidance, Control, and Dynamics*, Vol. 17, No. 6, 1994, pp. 1185–1192, doi: 10.2514/3.21331.

[65] Betts, J. T., "Very Low-Thrust Trajectory Optimization Using a Direct SQP Method," *Journal of Computational and Applied Mathematics*, Vol. 120, No. 1-2, 2000, pp. 27–40, doi: 10.1016/S0377-0427(00)00301-0.

[66] Petropoulos, A. E., "Low-Thrust Orbit Transfers Using Candidate Lyapunov Functions with a Mechanism for Coasting," *AIAA/AAS Astrodynamics Specialist Conference and Exhibit*, Providence, Rhode Island, United States of America, 16-19 August 2004, AIAA 2004-5089, doi: 10.2514/6.2004-5089.

[67] Spencer, D. B. and Culp, R. D., "Designing Continuous-Thrust Low-Earth-Orbit to Geosynchronous-Earth-Orbit Transfers," *Journal of Spacecraft and Rockets*, Vol. 32, No. 6, 1995, pp. 1033–1038, doi: 10.2514/3.26726.

[68] Kluever, C. A. and Oleson, S. R., "Direct Approach for Computing Near-Optimal Low-Thrust Earth-Orbit Transfers," *Journal of Spacecraft and Rockets*, Vol. 35, No. 4, 1998, pp. 509–515, doi: 10.2514/2.3360.

[69] Kluever, C. A., "Simple Guidance Scheme for Low-Thrust Orbit Transfers," *Journal of Guidance, Control, and Dynamics*, Vol. 21, No. 6, 1998, pp. 1015–1017, doi: 10.2514/2.4344.

[70] Kluever, C. A. and O'Shaughnessy, D. J., "Trajectory-Tracking Guidance Law for Low-Thrust Earth-Orbit Transfers," *Journal of Guidance, Control, and Dynamics*, Vol. 23, No. 4, 2000, pp. 754–756, doi: 10.2514/2.4597.

[71] Gao, Y., "Near-Optimal Very Low-Thrust Earth-Orbit Transfers and Guidance Schemes," *Journal of Guidance, Control, and Dynamics*, Vol. 30, No. 2, 2007, pp. 529–539, doi: 10.2514/1.24836.

[72] Petropoulos, A. E., "Simple Control Laws for Low-Thrust Orbit Transfers," *AAS/AIAA Astrodynamics Specialist Conference*, Big Sky, Montana, United States of America, 3-7 August 2003, AAS 03-630, https://trs.jpl.nasa.gov/handle/2014/38468.

[73] Hernandez, S. and Akella, M. R., "Lyapunov-Based Guidance for Orbit Transfers and Rendezvous in Levi-Civita Coordinates," *Journal of Guidance, Control, and Dynamics*, Vol. 37, No. 4, 2014, pp. 1170–1181, doi: 10.2514/1.62305.

[74] Gao, Y. and Li, X., "Optimization of Low-Thrust Many-Revolution Transfers and Lyapunov-Based Guidance," *Acta Astronautica*, Vol. 66, No. 1-2, 2010, pp. 117–129, doi: 10.1016/j.actaastro.2009.05.013.

[75] Pontani, M. and Conway, B., "Optimal Low-Thrust Orbital Maneuvers via Indirect Swarming Method," *Journal of Optimization Theory and Applications*, Vol. 162, 2014, pp. 272–292, doi: 10.1007/s10957-013-0471-9.

[76] Yang, D., Xu, B., and Gao, Y., "Optimal Strategy for Low-Thrust Spiral Trajectories Using Lyapunov-Based Guidance," *Advances in Space Research*, Vol. 56, 2015, pp. 865–878, doi: 10.1016/j.asr.2015.05.030.

[77] Ruggiero, A., Pergola, P., Marcuccio, S., and Andrenucci, M., "Low-thrust Maneuvers for the Efficient Correction of Orbital Elements," *32nd International Electric Propulsion Conference*, Wiesbaden, Germany, 11-15 September 2011, IEPC-2011-102, http://electricrocket.org/IEPC/IEPC-2011-102.pdf.

[78] Zhang, L., Xu, B., Li, M., and Zhang, F., "Semi-Analytical Approach for Computing Near-Optimal Low-Thrust Transfers to Geosynchronous Orbit," *Aerospace Science and Technology*, Vol. 55, 2016, pp. 482–493, doi: 10.1016/j.ast.2016.06.022.

[79] Ceriotti, M. and McInnes, C. R., "Generation of Optimal Trajectories for Earth Hybrid Pole Sitters," *Journal of Guidance, Control, and Dynamics*, Vol. 34, No. 3, 2011, pp. 847–859, doi: 10.2514/1.50935.

[80] Mengali, G. and Quarta, A. A., "Near-Optimal Solar-Sail Orbit-Raising from Low Earth Orbit," *Journal of Spacecraft and Rockets*, Vol. 42, No. 5, 2005, pp. 954–958, doi: 10.2514/1.14184.

[81] Gao, Y. and Kluever, C. A., "Analytic Orbital Averaging Technique for Computing Tangential-Thrust Trajectories," *Journal of Guidance, Control, and Dynamics*, Vol. 28, No. 6, 2005, pp. 1320–1323, doi: 10.2514/1.14698.

[82] https://www.esa.int/Applications/Navigation/Galileo/What_is_Galileo, Retrieved: 15 July 2020.

[83] Hubbel, Y. C., "A Comparison of the IRIDIUM and AMPS Systems," *IEEE Network*, Vol. 11, No. 2, 1997, pp. 52–59, doi: 10.1109/65.580922.

[84] https://earth.esa.int/web/eoportal/satellite-missions/i/iridium-next, Retrieved: 10 December 2020.

[85] Vasile, M., "Robust Mission Design Through Evidence Theory and Multi-Agent Collaborative Search," *Annals of the New York Academy of Science*, Vol. 1065, No. 1, 2005, pp. 152–173, doi: 10.1196/annals.1370.024.

[86] Edelbaum, T. N., "Propulsion Requirements for Controllable Satellites," *ARS Journal*, Vol. 31, No. 8, 1961, pp. 1079–1089, doi: 10.2514/8.5723.

[87] Spitzer, A., "Near Optimal Transfer Orbit Trajectory Using Electric Propulsion," *Space Flight Mechanics*, 1995, pp. 1031–1044.

[88] Huang, S., Colombo, C., and Bernelli-Zazzera, F., "Comparative Assessment Of Different Constellation Geometries for Space-Based Application," *68th International Astronautical Congress*, Adelaide, Australia, 25-29 September 2017, pp. 887–903, IAC-17,C1,IP,31,x41252, https://re.public.polimi.it/retrieve/handle/11311/1044169/258856/HUANS_OA_01-17.pdf.

[89] Huang, S., Colombo, C., Alessi, E. M., and Hou, Z., "Large Constellation De-Orbiting with Low-Thrust Propulsion," *29th AAS/AIAA Space Flight Mechanics Meeting*, Ka'anapali, Hawaii, United States of America, 13-17 January 2019, AAS 19-480, https://re.public.polimi.it/retrieve/handle/11311/1076637/342256/HUANS01-19.pdf.

[90] Huang, S., Colombo, C., and Alessi, E. M., "Trade-Off Study on Large Constellation De-Orbiting Using Low-Thrust and De-Orbiting Balloons," *10th International Workshop on Satellite Constellations and Formation Flying*, Glasgow, United Kingdom, 16-19 July 2019, IWSCFF 19-1953, https://re.public.polimi.it/retrieve/handle/11311/1120861/466787/HUANS02-19.pdf.

[91] Huang, S., Colombo, C., and Bernelli-Zazzera, F., "Orbit Raising and De-Orbit for Coplanar Satellite Constellations with Low-Thrust Propulsion," *4th IAA Conference on Dynamics and Control of Space Systems*, Changsha, China, 21-13 May 2018, pp. 95–122, IAA-AAS-DyCoSS4-1-15, AAS 18-508, https://re.public.polimi.it/retrieve/handle/11311/1056552/342245/HUANS02-18.pdf.

[92] Huang, S., Colombo, C., and Bernelli-Zazzera, F., "Low-Thrust Planar Transfer for Co-Planar Low Earth Orbit Satellites Considering Self-Induced Collision Avoidance," *Aerospace Science and Technology*, Vol. 106, November 2020, doi: 10.1016/j.ast.2020.106198.

[93] Vallado, D. A., editor, *Fundamentals of Astrodynamics and Applications*, Microcosm Press and Kluwer Academic Publishers, 2nd ed., 2004.

[94] Battin, R. H., editor, *An Introduction to the Mathematics and Methods of Astrodynamics*, American Institute of Aeronautics and Astronautics, Inc., revised ed., 1999.

[95] Pollard, J. E., "Simplified Approach for Assessment of Low-Thrust Elliptical Orbit Transfers," *25th International Electric Propulsion Conference*, Cleveland, Ohio, United States of America, 24-28 August 1997, pp. 979–986, IEPC-97-106, http://electricrocket.org/IEPC/7160.pdf.

[96] Marec, J. P., *Optimal Space Trajectories*, Elsevier, 1979.

[97] Colombo, C., Vasile, M., and Radice, G., "Semi-Analytical Solution for the Optimal Low-Thrust Deflection of Near-Earth Objects," *Journal of Guidance, Control, and Dynamics*, Vol. 32, No. 3, 2009, pp. 796–809, doi: 10.2514/1.40363.

[98] Colombo, C., *Optimal Trajectory Design for Interception and Deflection of Near Earth Objects*, Ph.D. thesis, University of Glasgow, 2010, http://theses.gla.ac.uk/1819/.

[99] https://www.nasa.gov/directorates/heo/scan/communications/policy/GPS.html, Retrieved: 15 July 2020.

[100] https://uk.mathworks.com/help/optim/ug/fsolve.html, Retrieved: 15 November 2020.

[101] Speckman, L. E., Lang, T. J., and Boyce, W. H., "An Analysis of the Line of Sight Vector Between Two Satellites in Common Altitude Circular Orbits," *AIAA/AAS Astrodynamics Conference*, Portland, Oregon, United States of America, 20-22 August 1990, pp. 866–874, AIAA-90-2988, doi: 10.2514/6.1990-2988.

[102] Wertz, J. R. and Larson, W. J., editors, *Space Mission Analysis and Design*, Microcosm Press and Kluwer Academic Publishers, 3rd ed., 1999.

[103] https://en.wikipedia.org/wiki/PSLV-C37, Retrieved: 10 December 2020.

[104] McGrath, C. and Macdonald, M., "Design of a Reconfigurable Satellite Constellation," *66th International Astronautical Congress*, Jerusalem, Israel, 12-16 October 2015, https://strathprints.strath.ac.uk/55049/.

[105] McGrath, C., Kerr, E., and Macdonald, M., "An Analytical, Low-Cost Deployment Strategy for Satellite Constellations," *13th Reinventing Space Conference*, Oxford, United Kingdom, 2015, pp. 107–116, BIS-RS-2015-45, doi: 10.1007/978-3-319-32817-1_11.

[106] http://www.busek.com/index_htm_files/70000702A.pdf, Retrieved: 11 August 2020.

[107] https://fcc.report/IBFS/SAT-LOI-20160428-00041/1134939, Retrieved: 11 August 2020.

[108] https://www.spacex.com/vehicles/falcon-9/, Retrieved: 11 August 2020.

[109] Alessi, E. M., Schettino, G., Rossi, A., and Valsecchi, G. B., “Natural Highways for End-of-Life Solutions in the LEO Region,” *Celestial Mechanics and Dynamical Astronomy*, Vol. 130, No. 34, 2018, doi: 10.1007/s10569-018-9822-z.

[110] Alessi, E. M., Colombo, C., and Rossi, A., “Phase Space Description of the Dynamics due to the Coupled Effect of the Planetary Oblateness and the Solar Radiation Pressure Perturbations,” *Celestial Mechanics and Dynamical Astronomy*, Vol. 131, No. 43, 2019, doi: 10.1007/s10569-019-9919-z.

[111] https://www.oneweb.world/, Retrieved: 11 August 2020.

[112] Rossi, A., Colombo, C., Tsiganis, K., et al., “ReDSHIFT: A Global Approach to Space Debris Mitigation,” *Aerospace*, Vol. 5, No. 2, 2018, pp. 64, doi: 10.3390/aerospace5020064.

[113] Letterio, F., Alessi, E. M., Gkolias, I., et al., “ReDSHIFT Software Tool for the Design and Computation of Mission End-of-Life Disposal,” *7th International Conference on Astrodynamics Tools and Techniques*, 2018, http://redshift-h2020.eu/wp-content/uploads/2019/01/ICATT-7-2018-ReDSHIFT.pdf.

[114] Colombo, C. and Gkolias, I., “Analysis of Orbit Stability in the Geosynchronous Region for End-of-Life Disposal,” *7th European Conference on Space Debris*, Darmstadt, Germany, 18-21 April 2017, http://redshift-h2020.eu/wp-content/uploads/2018/03/1-Colombo-Gkolias-SpaceDebrisConf2017.pdf.

[115] https://www.starlink.com/https://www.starlink.com/https://www.starlink.com/, Retrieved: 11 August 2020.

[116] Gaudel, A., Hourtolle, C., Goester, J.-F., Fuentes, N., and Ottaviani, M., “De-orbit Strategies with Low-Thrust Propulsion,” *Space Safety is No Accident*, Springer, Cham, 2015, pp. 59–68, doi: 10.1007/978-3-319-15982-9_7.

[117] Draim, J. E., “A Common-Period Four-Satellite Continuous Global Coverage Constellation,” *Journal of Guidance, Control, and Dynamics*, Vol. 10, No. 5, 1987, pp. 492–499, doi: 10.2514/3.20244.

[118] Zuiani, F., *Multi-Objective Optimisation of Low-Thrust Trajectories*, Ph.D. thesis, University of Glasgow, 2015, http://theses.gla.ac.uk/6311/.

[119] Bryson, A. and Ho, Y., *Applied Optimal Control*, Wiley, New York, 1975.

[120] Pontryagin, L. S., Boltyanskii, V. G., Gamkrelidze, R. V., and Mishenko, E. F., *Mathematical Theory of Optimal Processes*, Wiley (Interscience), New York, 1962.

[121] Zhang, C., Topputo, F., Bernelli-Zazzera, F., and Zhao, Y., “Low-Thrust Minimum-Fuel Optimization in the Circular Restricted Three-Body Problem,” *Journal of Guidance, Control, and Dynamics*, Vol. 38, No. 8, pp. 1501–1510, doi: 10.2514/1.G001080.